Potential Vorticity Conserving Flows and Vortex-Wave Interaction: the Role of Vertical Velocity and Isopycnal Diffusion on Plankton Heterogeneity

Mariona Claret

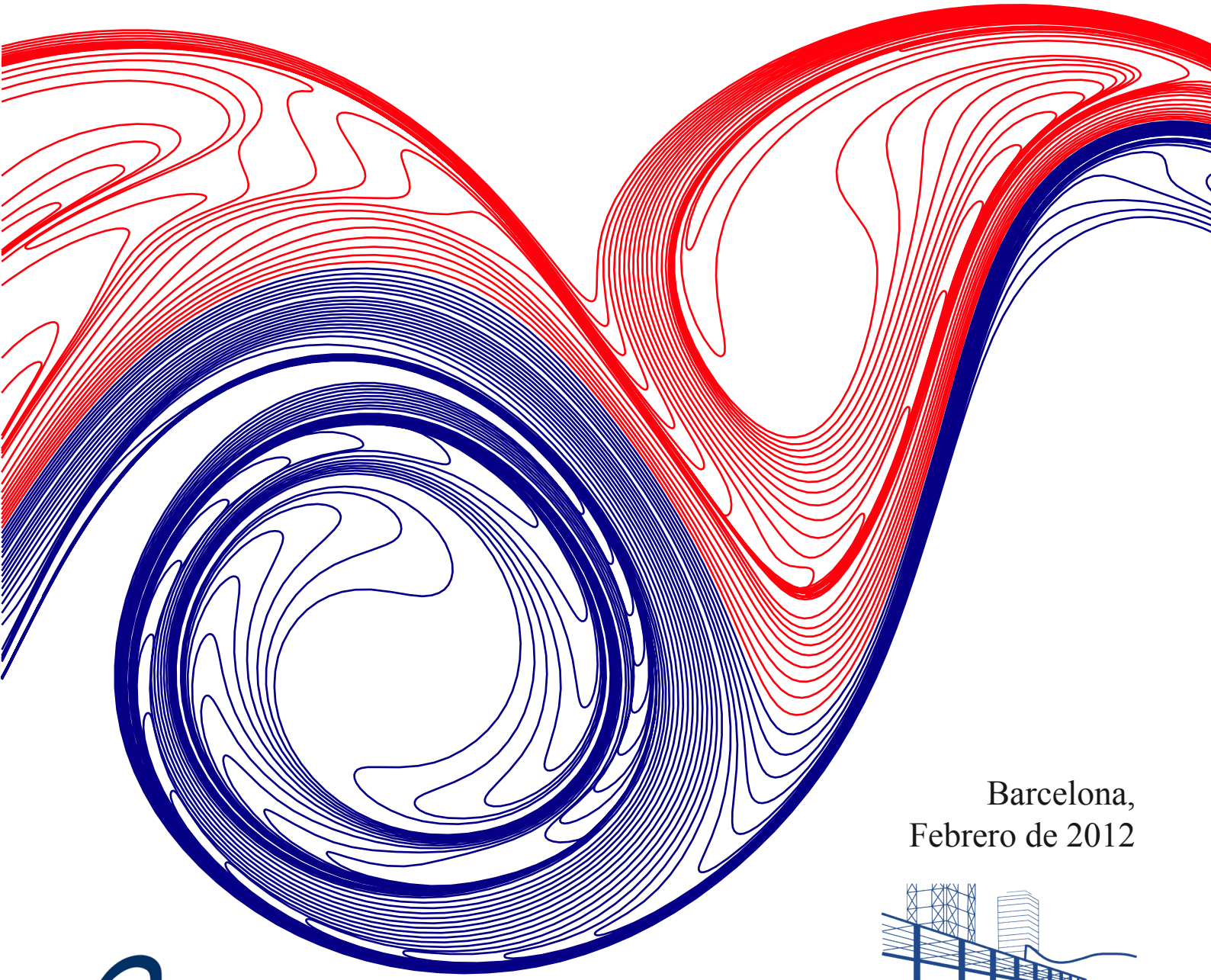

Barcelona,
Febrero de 2012

UNIVERSIDAD DE LAS PALMAS DE GRAN CANARIA
Departamento de Física

CSIC

Institut de Ciències del Mar

Ilustración de la contraportada realizada por Marc Gasser Rubinat.

Anexo I

D/Dª.....SECRETARIO/A DEL DEPARTAMENTO DE FISICA DE LA UNIVERSIDAD DE LAS PALMAS DE GRAN CANARIA,

CERTIFICA,

Que el Consejo de Doctores del Departamento en su sesión de fecha.....tomó el acuerdo de dar el consentimiento para su tramitación, a la tesis doctoral titulada “Potential vorticity conserving flows and vortex-wave interaction: the role of vertical velocity and isopycnal diffusion on plankton heterogeneity” presentada por la doctoranda Dª Mariona Claret Cortés y dirigida por el Doctor Álvaro Viúdez Lomba y la Doctora Yvette H. Spitz.

Y para que así conste, y a efectos de lo previsto en el Artº 73.2 del Reglamento de Estudios de Doctorado de esta Universidad, firmo la presente en Las Palmas de Gran Canaria, a…….de.....de dos mil doce.

UNIVERSIDAD DE LAS PALMAS DE GRAN CANARIA
Departamento de Física

Institut de Ciències del Mar

CSIC
Consejo Superior de Investigaciones Científicas

Potential vorticity conserving flows and vortex-wave interaction: the role of vertical velocity and isopycnal diffusion on plankton heterogeneity

(Flujos que conservan la vorticidad potencial e interacción onda-vórtice: el efecto de la velocidad vertical y la difusión isopicna en la heterogeneidad planctónica)

Tesis doctoral presentada por
Mariona Claret Cortés

dirigida por el Dr.
Álvaro Viúdez Lomba

y codirigida por la Dra.
Yvette H. Spitz

para obtener el grado de Doctora por la
Universidad de Las Palmas de Gran Canaria,
Departamento de Física,
Programa en Oceanografía (Bienio 2006-2008).

En Barcelona, a febrero de 2012

La Doctoranda | El Director | La Codirectora

Per a la meva àvia,

única en su especie.

Per tenir un bombó sempre a punt,

per viure el dia a dia amb ironia,

per la il·lusió dels seus ulls.

THESIS ABSTRACT

This thesis investigates physical-ecological and vortex-wave interactions through *potential vorticity* (PV) considering a stratified and oligotrophic ocean. To this end, a NPZ (Nutrients-Phytoplankton-Zooplankton) model is coupled to a physical one that conserves PV explicitly on isopycnals. The physical-ecological coupled model is initialized using stationary NPZ solutions numerically stable with the fluid at rest. These solutions are implemented homogeneous both on horizontal and isopycnals levels to quantify the effect of horizontal and vertical advection caused by *mesoscale* and *submesoscale vortex structures*, and isopycnal mixing. At the interior of the vortex separatrix, plankton and PV distributions translate in phase at vortex propagation speed. Within cyclones, isopycnal doming enhances plankton biomass at the vortex center in different trophic conditions. Furthermore, isopycnal mixing associated to small-scale motions maximizes the phytoplankton (P) biomass in cyclones through a resonant response between P and diffusive timescales. This P increase is significant in mesotrophic conditions and occurs where the vertical displacement of isopycnals is maximum, and hence where vertical gradients of PV are large. At the separatrix outer, horizontal and vertical advection are of the same order of magnitude than the ecological forcing and enhance P through different mechanisms. Firstly, vertical velocity w uplifts nutrients and P to better lit levels. P responds with some time lag to this perturbation and the associated increase in biomass occurs far from the upwelling location due to the action of horizontal advection. As a result, P correlates with w, and thus with horizontal gradients of PV, only at initial times. In the particular case of translating cyclones, this mechanism explains the development of a P trail at their wake. And secondly, the horizontal advection of a surface ecosystem patch by *subsurface* vortices decreases P self-shading at the patch front in benefit of P growth. Finally, interactions between vortex structures and pure inertial and gravity large amplitude waves are investigated. The advection of PV by waves causes vortices to be unsteady and modifies the upper and lower bounds of the wave frequency band. The advection of waves by vortices Doppler shifts the local wave frequency. When inertial waves are involved, a near-inertial right-handed helical wave is developed due to a non-linear interaction. As a result, total w increases one order of magnitude and correlates with horizontal gradients of PV. These results aim to shed further light on the ecological impact of long-lived coherent vortices in the open ocean.

RESUMEN DE LA TESIS

Esta tesis investiga interacciones físico-biológicas y onda-vórtice a través de la *vorticidad potencial* (VP) considerando un océano estratificado y oligotrófico. Un modelo NPZ (Nutrientes-Fitoplancton-Zooplancton) ha sido acoplado a uno físico que conserva la VP explícitamente en isopicnas. El modelo acoplado se inicializa utilizando soluciones NPZ estacionarias y numéricamente estables con el fluido en reposo. Estas soluciones se implementan como distribuciones homogéneas en niveles horizontales y en isopicnos para cuantificar el efecto de la advección horizontal y vertical debidas a estructuras submesoescalares y mezcla isopicna. En el interior de la separatriz del vórtice, las distribuciones de plancton y VP se trasladan en fase a la velocidad de propagación del vórtice. En ciclones, el abombamiento de las isopicnas incrementa la biomasa de fitoplancton (P) en el centro del vórtice en diferentes condiciones tróficas. Además, la mezcla isopicna asociada al movimiento de pequeña escala maximiza la biomasa de P en ciclones mediante una respuesta resonántica entre la escala temporal de P y la difusiva. Este incremento de P es significante en condiciones mesotróficas y ocurre donde el desplazamiento vertical de las isopicnas es máximo, y por tanto donde los gradientes verticales de VP son grandes. Fuera de la separatriz, la advección horizontal y vertical son del mismo orden de magnitud que el forzamiento ecológico, e incrementan el P mediante diferentes mecanismos. En primer lugar, la velocidad vertical w eleva nutrientes y P a niveles más iluminados. En consecuencia, el P se correlaciona con la w, y por tanto con gradientes horizontales de VP, sólo inicialmente. En el caso particular de vórtices en traslación, este mecanismo genera una cola de P en la estela de éstos. En segundo lugar, la advección horizontal de un ecosistema superficial por vórtices *subsuperficiales* disminuye el apantallamiento del P en el frente del ecosistema aumentando el crecimiento del P. Finalmente, se investigan interacciones entre estructuras vorticales y ondas inerciales y gravitatorias de gran amplitud. La advección de la VP por las ondas fuerza los vórtices a un estado inestable y modifica los límites del rango frecuencial de la onda. La advección de ondas por los vórtices, modifica la frecuencia de onda local por efecto Doppler. Si se consideran ondas inerciales, se genera una onda en hélice dextrógira de frecuencia casi-inercial debido a una interacción no lineal. Como resultado, la w total se incrementa un orden de magnitud y se correlaciona con gradientes horizontales de VP. Estos resultados contribuyen a una mayor comprensión del impacto ecológico ejercido por vórtices coherentes de larga duración.

Contents

LIST OF SYMBOLS

Physics

ρ	mass density
ρ'	density anomaly
ρ_0	constant density
α_0	constant specific volume
p	pressure
p'	pressure anomaly
ϱ_z	stratification constant
$d(\mathbf{x}, t)$	depth in the reference density configuration of isopycnal located at $(\mathbf{x}, t)$
$\mathcal{D}(\mathbf{x}, t)$	vertical displacement of isopycnals in the spatial description
$\overline{\mathcal{D}}(s, d)$	vertical displacement of isopycnals in the isopycnal description
f	Coriolis frequency
f_e	*effective* Coriolis frequency
N	background buoyancy frequency
$\mathcal{N}$	*total* buoyancy frequency
c	Prandtl ratio
ω_l	*local* wave frequency
ω_p	particle wave frequency
$\mathbf{u} = (u, v, w)$	velocity vector
$\mathbf{u}^g$	geostrophic velocity
w^q	QG vertical velocity
$\mathbf{Q}_h^g$	geostrophic $\mathbf{Q}$-vector
U_d	dipole speed
$\boldsymbol{\omega} \equiv \boldsymbol{\omega}_h + \zeta \mathbf{k}$	relative vorticity
$\boldsymbol{\omega}^g$	geostrophic vorticity
$\boldsymbol{\omega}'$	ageostrophic vorticity
ϖ	PV *anomaly*
Π	*total* PV
$\boldsymbol{\varphi} = (\varphi, \psi, \phi)$	vector potential
$\mathcal{F}$	Froude number
$\mathcal{R}$	Rossby number
κ	dimensional diffusion coefficient
$\mathcal{K}$	non-dimensional diffusion coefficient
$\mathcal{Z}_{\min}$	minimum dimensional vertical coordinate z
$\mathcal{L}$	spatial conversion factor
$\mathcal{T}$	temporal conversion factor

Ecology

P	phytoplankton
Z	zooplankton
N	nutrients
N_T	total nitrogen
G_P	phytoplankton production rate
G_Z	zooplankton production rate
K_0	half-saturation for P uptake
L	photosynthetic rate
I	available radiation
I_0	surface available radiation
A_w	light attenuation by sea water
A_p	light attenuation by P
Ψ_0	initial slope P-I curve
V_0	P maximum uptake rate
M_P	phytoplankton mortality
M_Z	zooplankton mortality
Ξ_0	P specific mortality rate
R	zooplankton grazing rate
R_0	zooplankton maximum
Λ_0	Ivlev constant
Γ_0	fraction of Z grazing egested
Ψ_0	Z excretion/mortality rate
Θ_0	Z *specific* excretion/mortality rate

Chapter 1

Introduction

Marine ecosystems are highly sensitive to ocean physics. Pelagic organisms are embedded in the fluid and thus they are explicitly affected by its dynamics. Since most of these individuals are non-motile, they drift in the vast ocean. These wanderers owe their name to the Greek equivalent, *plankton*. Two microscopic groups are enclosed within plankton, autotrophs and heterotrophs. The formers are called *phytoplankton*, where *phyto* denotes its *plant*-like character due to the performance of photosynthesis. The latters are the *animal*-like plankton, the *zooplankton*, since they feed from phytoplankton or the smallest zooplankton. Phytoplankton is of great importance because is the basis of the oceanic food web. Its growth is affected by fluid motion because growth limiting factors, light and nutrients, are vertically segregated in the ocean. On the one hand, the well-lit layer is akin to the tip of an iceberg, it is the upper fraction of an ocean which is on average twenty times deeper. On the other hand, nutrients slowly and incessantly sediment into the dark deep ocean. As a result, vertical velocities in the ocean play an implicit role in ecosystems by fertilizing the well-lit zone.

Many works have been conducted to characterize the ecological patterns associated to specific physical structures. In this regard, Haury et al. (1978) first drew an ecological counterpart of the *Stommel* diagram, which plots physical ocean variables in a spatio-temporal logarithmic frame, to represent zooplankton biomass variability. Nowadays, physical-biological interactions have been extensively reported from *planetary* to *Kolmogorov* scales (Steele, 1978; Mann and Lazier, 1991; Denman and Gargett, 1995). The combination of these wide range of spatial scales results in complex and deterministic plankton patterns, which are reflected in the sea surface chlorophyll distributions as measured from space satellites. Highly

productive regions are localized at western boundaries, sub-polar latitudes, and the Equator (Yoder et al., 1993), where coastal upwelling, water mass subduction, and Trade Winds forcing, respectively, overcome the light-nutrient vertical segregation. These areas are called *eutrophic*, because communities are not limited by nutrients, as opposed to *oligotrophic* zones. The largest part of the open ocean is oligotrophic. Its sea surface chlorophyll concentration (CC) has a geometric mean about two orders of magnitude smaller than that of eutrophic waters, and a variability dominated by submonthly mesoscale variance (Doney et al., 2003). Since CC images carry information about the ocean surface turbulent flow (Nieves et al., 2007), plankton variability in the oligotrophic open ocean may be likely caused by mesoscale phenomena, and vortical structures may be particularly involved. The dynamics and three-dimensional structure of ecosystems in the open ocean remain largely unknown because synoptic and high spatial resolution sampling there is more costly and challenging than in the coastal ocean. In this context, the aim of this thesis is to provide further insight on how ubiquitous mesoscale eddies alter the basis of the food web in oligotrophic environments. To this end, we analyze first which factors shape plankton patterns at mesoscales in order to choose an appropriate physical descriptor (section 1.1). We then review the mechanisms through which vortices generate ecological heterogenity (section 1.2) and identify those which are related to our purpose (section 1.3). Finally, the specific objectives of this thesis are outlined by chapters (section 1.4).

1.1 Plankton patchiness at mesoscales: Ecological footprint of potential vorticity

First synoptic maps of sea surface chlorophyll were obtained in the early 80's (Gordon et al., 1980; Gower et al., 1980). At first glance, these type of maps show high correlation with sea surface temperature at mesoscales, which has led to consider plankton as a passive tracer to a first approximation. However, discrepancies between physics and ecology arise when they are quantified (see review Martin, 2003). Two main facts account for these differences, nutrient pumping at smaller scales and plankton time lag response to perturbations. Submesoscale structures have gained increasing attention the last decade because they enhance vertical velocity w one order of magnitude with respect to mesoscale structures and are responsible for injection of allochthonous nutrients to the photic zone (see review Klein and Lapeyre,

2009), where light irradiance is greater than one per cent of that arriving at the sea surface. Since physical and ecological timescales are similar at the submesoscale, plankton couples to this nutrient upwelling and w collocates with primary production (Lévy et al., 2001) and some photosynthetic indexes (Falkowski, 1983; Cullen and Lewis, 1988). However, exact correlation with w depends on the ecological parameter timescale. Those parameters with timescales greater than that of horizontal advection, such as phytoplankton biomass, show a spatial lag with w (Lima et al., 2002). The importance of inherent ecological timescales in plankton patterns was nicely illustrated by Abraham (1998) using a two-dimensional turbulence numerical model. He observed an increasing patchiness from physics to phytoplankton, and to zooplankton. Therefore mesoscale plankton distributions result from an interplay between horizontal advection, vertical advection, and intrinsic plankton timescales. Whether these distributions are caused by ecological or physical phenomena depends on their relative timescale (Mahadevan and Campbell, 2002). In order to relate both timescales, we seek to describe the fully three-dimensional flow nature with a single timescale.

A very useful physical quantity that relates horizontal and vertical motion is *potential vorticity* (PV). The concept of PV was introduced by Beltrami in 1871, applied to an adiabatic inviscid multi-layered ocean by Rossby in 1936, and extended to baroclinic flows by Ertel in 1942 (check Viúdez, 2001, for cites and relation between PV definitions). According to the latter, specific PV is defined as

$$\Pi \equiv \frac{\boldsymbol{\omega} + f\mathbf{k}}{\rho} \cdot \boldsymbol{\nabla} T_\theta \,, \tag{1.1}$$

where the sum of vorticity $\boldsymbol{\omega} = (\xi, \eta, \zeta)$ relative to a reference frame rotating with Earth's angular velocity and the vertical component of the planetary vorticity f, which is the Coriolis parameter, is the absolute vorticity. Additionally, ρ is the mass density, T_θ the potential temperature, though it could be any scalar fluid property materially conserved (Pedlosky, 1987, chapter 2), and $\boldsymbol{\nabla}$ the three-dimensional gradient operator. The geophysical significance of PV lies on its material invariance, that is,

$$\frac{\mathrm{d}\Pi}{\mathrm{d}t} = 0 \,. \tag{1.2}$$

One way to derive (1.2) comes from the conservation of circulation for frictionless motion considering material conservation of T_θ and mass conservation (Pedlosky, 1987, chapter 2).

Thus (1.2) can be interpreted as the conservation of circulation along material circuits and angular momentum for a given volume, which let us to relate horizontal and vertical motions. When the fluid is barotropic this relation is straightforward since (1.1) becomes

$$\Pi \equiv \frac{\zeta + f}{h}\,, \tag{1.3}$$

where h is the vertical separation between neighboring material isosurfaces (eq. 3.4.9. Pedlosky, 1987). Thus changes in h imply adjustments in ζ in order to conserve PV, which explains the well-known *ballerina* and *ice skater* effects. Instead, when the fluid is baroclinic the tilting of material isosurfaces introduces nontrivial changes in $\boldsymbol{\omega}$. Furthermore, if some balance condition is established in the momentum equations (along with proper boundary conditions), then for a given distribution of PV at a fixed time the velocity vector, pressure, and density three-dimensional fields associated to the *balanced* flow (void of inertia–gravity waves IGWs) can be recovered in a process known as PV inversion (Hoskins et al., 1985; McIntyre and Norton, 2000; Viúdez, 2008a).

PV is relevant to ecological dynamics for several reasons. Firstly, it describes the *balanced* velocity vector field and the vertical displacement of isopycnals $\mathcal{D}$. Secondly, it relates vertical upwelling with horizontal advection, which is crucial to plankton patchiness (Martin et al., 2002). The importance of PV in ecology was first pointed out by Woods (1987) and Strass and Woods (1987). They observed chlorophyll increase in regions of large PV isopycnal gradients, which were thought to be areas of high w. Their hypothesis agrees with experimental (Pallàs-Sanz and Viúdez, 2005) and numerical (Viúdez and Dritschel, 2003, 2004b) works that demonstrate that zones with large horizontal gradients of ζ and PV are related to high values of w. Large PV horizontal gradients involve large horizontal gradients in ρ and therefore in $\mathcal{D}$. Consequently, when these $\mathcal{D}$ gradients are advected, large local rates of $\mathcal{D}$ and w occur. However, vertical advection does not account for the whole plankton big picture aforementioned.

1.2 How do mesoscale vortices alter ecosystems?

Many in-situ observations reveal eddies impact on marine biology. At the basis of the food web, vortices qualitatively affect community structure (Thompson et al., 2007; Huang et al., 2010), physiological processes (Bibby et al., 2008), and ecosystems transport (Batten

and Crawford, 2005). Additionally, they quantitatively alter biogeochemical balances by enhancing new primary productivity (NPP) (Morán et al., 2001). For instance, they are involved in the North Atlantic carbon balance, though their specific contribution is under scientific debate ranging from 50% to less than 10% of NPP (see review Oschlies, 2008). As a result, vortices also perturb higher trophic levels (Mackas et al., 2005; Atwood et al., 2010).

There are different mechanisms by which ocean eddies introduce the above mentioned ecological variability. Next, we analyze their ecological spatial signature in order to relate it with PV when this is possible.

- *Horizontal advection.* Mesoscale two-dimensional turbulence induces a conservative transfer from large to small scales (Abraham, 1998). If we consider that phytoplankton behaves as a passive tracer, then its pattern is determined by vorticity and strain. Inside vortices, vorticity dominates over strain and particles are trapped tracing nearly orbital trajectories. This explains long-term transport of chlorophyll rich waters offshore the Algerian (Arnone and LaViolette, 1986), Alaskan (Batten and Crawford, 2005), and northwest African (Pelegrí et al., 2005) coasts among many others. Outside vortices, strain overcomes vorticity, resulting in chaotic motion (Provenzale, 1999). As a result, eddies stir plankton patches into spirals and filaments (Lehahn et al., 2007) and even wave-like structures (Menkes et al., 2002) at their edges.

- *Eddy pumping.* This term was coined by Falkowski et al. (1991) to denote NPP enhancement due to upwelling of the nutricline into the photic layer caused by the passage of a translating surface cyclone or subsurface anticyclone (McGillicuddy et al., 1999). On the one side, isopycnal uplift is greatest at the eddy center, which explains high values of sea surface chlorophyll at eddy cores (Arístegui et al., 1997; Barton et al., 1998; Mizobata et al., 2002; Siegel et al., 2008; Tew-Kai and Francis, 2009; Siegel et al., 2011). On other side, PV is correlated with the isopycnal vertical displacement (Viúdez and Dritschel, 2003). Consequently, we expect chlorophyll enrichment at maxima absolute PV values.

- *Submesoscale.* Fully-developed vortices are rarely spherical in the isotropic quasi-geostrophic (QG) space. The QG space is the vertically stretched space of dimensions (x, y, cz), where $c \equiv N/f$ is the Prandtl ratio, N the background buoyancy frequency, and f the inertial frequency. Instead, a variety of elliptical geometries are shaped

during their life-time, which lead to vortex rotation, and ultimately to a quadrupolar pattern distribution of vertical velocity w (Viúdez and Dritschel, 2003). Vertical velocity maxima are reached at vortex edges enhancing chlorophyll concentrations at the eddy periphery (Mizobata et al., 2002; Ladd et al., 2005; Siegel et al., 2011). Thus chlorophyll would be better related to PV horizontal gradients than to PV. However, to unveil this w pattern, resolutions smaller than 10 km, which are close to submesoscale sampling, are often required (Lévy et al., 2001).

- *Eddy-eddy interactions.* Vortices interact in a number of ways through bounding, merging, or conforming complex structures (Voropayev and Afanasyev, 1994). Since these interactions modify the flow, they also perturb ecological distributions. For instance, the ubiquitous presence of mushroom-like shapes of sea surface chlorophyll in frontal coastal zones (Sur et al., 1996; Stapleton et al., 2002) are imprints the interaction between two vortices of opposite PV, that is, the vortex dipole. Another example is the merging of anticyclones in the Kuroshio Current, which results in an increase of w which triggers phytoplankton enhancement at vortex edges (Yoshimori and Kishi, 1994).

- *Isopycnal mixing.* As aforemetioned, $\mathcal{D}$ maxima occur at the monopole center, which creates isopycnal gradient of light irradiance. In oligotrophic regimes phytoplankton growth is mainly limited by light and nutrients. Since isopycnal doming modifies the amount of light at which isopycnal confined phytoplankton is exposed, it affects its growth, and indirectly nutrient consumption. Thus isopycnal diffusion may increase the phytoplankton response to light at cyclone cores and anticyclone edges through a down-gradient replenishment flux of nutrients.

- *Vortex-wave interaction.* On the one hand, interactions between vortices and IGWs are ubiquitous in the ocean. Some of these interactions imply inertial to near-inertial wave frequency shift (Perkins, 1976) and trapping of wavepackets within anticyclones (Kunze, 1986). On the other hand, phytoplankton distributions are perturbed by both eddies, and high frequency oscillations (Franks, 1995a; Granata et al., 1995; Gómez et al., 2001; Sangrà et al., 2001). Thus, we expect vortex-wave interaction to affect phytoplankton dynamics.

Several other vortical mechanisms have been proposed to explain plankton patterns. For instance, wind forcing increases primary production either at the vortex edges through *eddy-wind interaction* (Martin et al., 2001; Mahadevan et al., 2008) or anticyclone cores by *deepening of the mixed layer* (Thompson et al., 2007). The contribution of these mechanisms as well as *diapycnal mixing* to phytoplankton patchiness is beyond the scope of this work.

1.3 Relevant physical-ecological interactions in coherent vortices

Vortices life cycle involve three different stages with different dynamics: formation, maturity, and decay (Sangrà et al., 2005). High turbulent areas, such as coastal fronts, are hot-spots of vortex formation and decay. In contrast, the stratified open ocean is mainly dominated by long-lived mature vortices. Fully-developed coherent vortices translate across the ocean conserving their PV. The outer PV isosurface defines the vortex separatrix, which marks vortex limits and acts as an impermeable barrier. Within the separatrix the fluid rotates approximately as a solid body. Outside the separatrix, the horizontal velocity decreases exponentially with radius. Thus vortices can trap waters in their interior and transport ecosystems long distances. If those ecosystems are only affected by horizontal advection, the transporting distance will depend on the sinking rate of nutrients to the aphotic layer. This leads to long-term chlorophyll depletion within vortices unless some nutrient upwelling occurs. In this regard, *eddy pumping* assumes entrainment of new nutrients into the vortex (Martin and Pondaven, 2003), which implies mixing across vortex boundaries and thus restricts the mechanism to developing cyclones and decaying anticyclones (Franks et al., 1986b). This mechanism causes the initial seed of ecological heterogeneity though does not explain how it is maintained during vortex translation. In contrast, the vertical velocity of mesoscale and submesoscale monopoles or complex vortical structures may contribute to ecosystem subsistence in one year living vortices. Additionally, nutrient injection by isopycnal diffusion is likely to occur in the open ocean, where the flow is mainly two-dimensional. Though the contribution of isopycnal mixing in upwelling new nutrients is minimal compared to the mentioned mechanisms (Siegel et al., 1999; Ledwell et al., 2008), it may play some role in upwelling regenerated nutrients. Finally, the way vortex-wave interaction affects ecology remains largely unknown.

1.4 Thesis aims and outline

The main objective of this work is to explore some mechanisms that may explain plankton subsistence within long-lived mature vortices translating across oligotrophic environments. In this context, we aim to assess the role of *potential vorticity* (PV) as an ecological descriptor. To this end, we use a non-hydrostatic numerical model that simulates the volume-preserving three-dimensional flow of a stratified rotating fluid under the Boussinesq and f plane approximations, the $\mathcal{AB}\varpi$-model (Dritschel and Viúdez, 2003). This algorithm is specially appropriate for our purpose because it explicitly conserves PV on isopycnals, which enables conservation of large gradients of quantities, and thus resolves w with high accuracy. Our investigation is structured in four chapters addressing the following specific goals.

In **Chapter 2** we couple a NPZ (Nutrients-Phytoplankton-Zooplankton) ecological model to the $\mathcal{AB}\varpi$-model. It is devoted to find valid ecological solutions to initialize the NPZ model. The suitability of these solutions is tested by analyzing the plankton response to the submesoscale vertical velocity of a baroclinic unstable jet.

In **Chapter 3** we extend the investigation of the previous chapter to mesoscale and submesoscale vortices. We focus in a particular vortex structure, i.e. vortex dipole, since it is the simplest vortical structure with propagation speed. Thus we are able to investigate the effect of vortex translation on ecosystems trapped at vortex cores and also contained in surrounding oligotrophic waters.

In **Chapter 4** we quantify the ecological response to light and nutrients upwelled by small-scale motions in mesoscale vortices. Specifically, we consider a spherical cyclone, in the isotropic QG space, because it allows us to construct a very simple physical-ecological coupled model with smaller computational cost than the $\mathcal{AB}\varpi$-NPZ coupled model. This enables us to explore a vast range of isopycnal diffusion coefficients κ, cyclone intensities, and trophic regimes. The chapter is therefore designed to determine the values of κ that maximize the phytoplankton response to light and nutrient conditions in different vortices.

In **Chapter 5** we address the vortex-wave interaction, though only from a physical point of view. It uses the $\mathcal{AB}\varpi$-model to investigate the interaction between QG spherical monopoles and dipoles embedded in an initial field of both pure gravity and inertial plane waves. The aim of this chapter is to relate the resulting vertical velocity field to PV.

To conclude, a general discussion of the results obtained is given in **Chapter 6** and the main conclusions stated in **Chapter 7**.

Chapter 2

Numerical Simulations of Submesoscale Balanced Vertical Velocity Forcing Unsteady Nutrient-Phytoplankton-Zooplankton Distributions

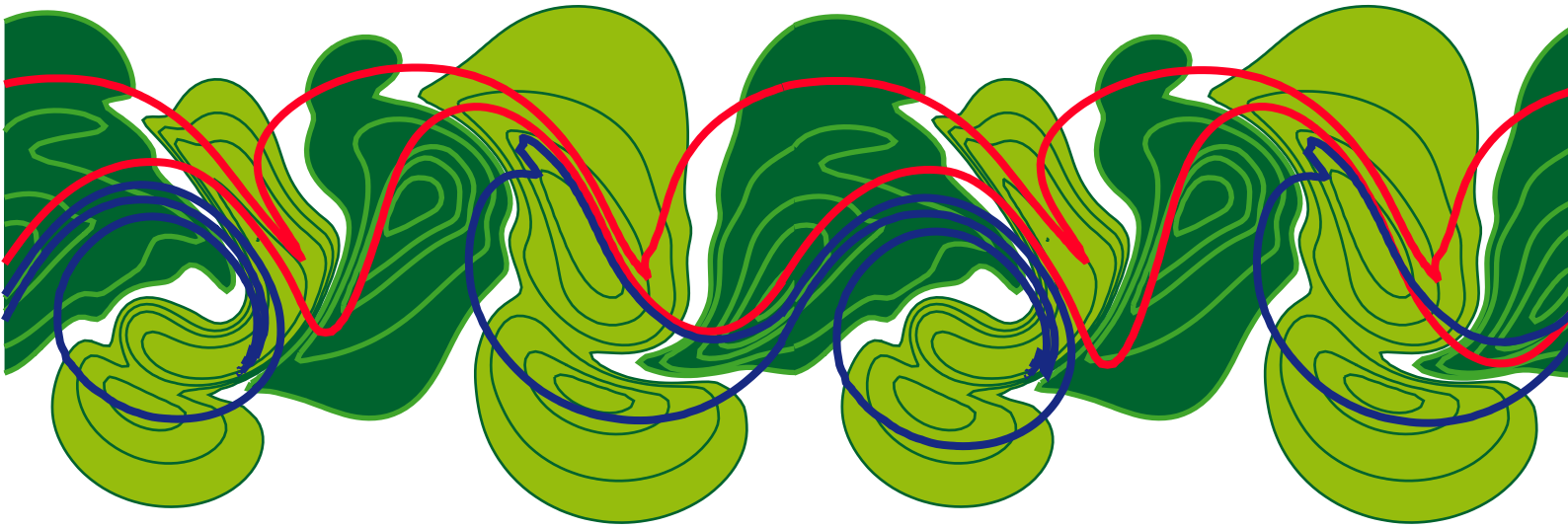

This chapter has been published as:
Viúdez, A., M. Claret, 2009: Numerical Simulations of Submesoscale Balanced Vertical Velocity Forcing Unsteady Nutrient-Phytoplankton-Zooplankton Distributions, *J. Geophys. Res.*,**114, C04023**, doi:10.1029/2008JC005172.

Retxes de sol atravessen blaus marins,
ses algues tornen verdes i brillen ses estrelles,
que ja s'ha fet de nit i es plàncton s'il·lumina
i canten ses sirenes aproximadament per no existir.

Batiscafo Katiuscas, Antònia Font

ABSTRACT

The effect of submesoscale balanced (void of waves) vertical velocity on initially steady nutrient-phytoplankton-zooplankton (*NPZ*) distributions is investigated numerically. First, steady vertical *NPZ* profiles, continuous but not continuously differentiable at several depths, are found as analytical solutions to the *NPZ* equations in the absence of flow. These solutions admit numerical equivalents that are continuously differentiable in the numerical sense, here meaning convergence of the vertical derivative with respect to increasing vertical resolution. These *NPZ* solutions require however large vertical resolutions, with a grid size of few centimeters, to be properly discretisized. The ecological model is next coupled to a non-hydrostatic Boussinesq f-plane physical model which explicitly conserves potential vorticity on isopycnals. Then, the *NPZ* solutions are used as steady initial ecosystem conditions to investigate the role of submesoscale balanced vertical velocity in forcing *NPZ* anomalies in an idealized case of a baroclinic unstable jet. The results show that the baroclinic flow rapidly develops balanced vertical velocity which in turn favors *NPZ* anomalies. A large cancellation between the local change and the horizontal advection occurs in the ecosystem variables. This particularly occurs for zooplankton anomalies which therefore behave as better passive tracers of the horizontal flow than phytoplankton anomalies. However once phytoplankton and zooplankton anomalies develop locally forced by vertical velocity they are horizontally advected away from the upwelling or downwelling regions so that spatial distributions of vertical velocity and ecological fields become eventually uncorrelated.

2.1 Introduction

The dynamics of oceanic planktonic ecosystems is often investigated using nutrient-phytoplankton-zooplankton (NPZ)-type numerical models (Wroblewski, 1977; Franks et al., 1986a; Franks, 2002; Newberger et al., 2003). These models are discrete versions of the continuous partial differential equations for the field variables *NPZ*. In the absence of flow and horizontal gradients this system of equations has a number of one-dimensional (1D) steady analytical solutions which are very useful both to characterize different planktonic regimes and to serve as initial conditions in coupled physical-ecosystem numerical modeling. It may happen, however, that some of these 1D steady solutions be only continuous, but not continuously differentiable functions of the vertical coordinate z along the water column. This potential lack of differentiability makes these *NPZ* solutions inappropriate as initial conditions in three-dimensional (3D) coupled physical-ecosystem models. These 3D coupled models, if formulated as it is usual in the spatial description, require existence of vertical derivatives for the vertical advective terms, present in the material rate of change of the ecosystem quantities, make sense.

In this paper we present a particular example of a motionless, 1D steady *NPZ* solutions which, being continuous but not continuously differentiable at several depths, do however admit numerical equivalents that are continuously differentiable in the numerical sense (here meaning convergence of the vertical derivative with respect to increasing vertical resolution). In the next section the *NPZ* system of equations is briefly introduced. Though more sophisticated ecological models exist a simple one is used here because we seek to keep the number of free parameters as small as possible, while retaining the essential behavior of the ecological fields, particularly the development of *NPZ* anomalies due to the vertical advection of nutrients into the euphotic zone. The NPZ-type models are ecological bulk algorithms subjected to significant errors in the mathematical parametrization of the different ecological processes (see Anderson, 2005; Flynn, 2005; Mitra et al., 2007).

The motionless 1D continuous steady ecological solutions and their numerical continuously differentiable equivalents are obtained in section 2.3. Convergence of this differentiable solution is reached however at vertical resolutions of a few centimeters. As an application example, in section 2.4 the differentiable steady *NPZ* solutions are used as initial conditions in a 3D coupled physical-ecosystem model (with poor vertical resolution) to address the role

of the vertical velocity in a case of oceanic baroclinic instability. Concluding remarks are given in section 2.5.

2.2 NPZ Model

The dependent variables of the NPZ model are the dissolved inorganic nitrogen (N), the phytoplankton (P), and the zooplankton (Z) biomass. These variables are expressed in units of concentration of nitrogen (here always in mmol N m^{-3}), and satisfy the system of equations (Wroblewski, 1977; Newberger et al., 2003)

$$\frac{\mathrm{d}P}{\mathrm{d}t} = \underbrace{\frac{N}{K_0+N}\,L\,P}_{G_P} - \underbrace{R_0(1-e^{-\Lambda_0 P})Z}_{R} - \underbrace{\Xi_0 P}_{M_P}, \tag{2.1}$$

$$\frac{\mathrm{d}Z}{\mathrm{d}t} = \underbrace{(1-\Gamma_0)R}_{G_Z} - \underbrace{\Phi_0 Z}_{M_Z}, \tag{2.2}$$

$$\frac{\mathrm{d}N}{\mathrm{d}t} = -G_P + \Gamma_0 R + M_Z + M_P\,. \tag{2.3}$$

Above, the material rate of change $\mathrm{d}\chi/\mathrm{d}t \equiv \partial\chi/\partial t + \mathbf{u}\cdot\boldsymbol{\nabla}\chi$ is the sum of the local and advective rates of change of χ, $\mathbf{u} = (u, v, w)$ is the 3D velocity, and $\boldsymbol{\nabla}$ is the 3D gradient operator. The P increases due to its production rate (G_P), which depends on both the inorganic dissolved nitrogen uptake and the photosynthesis, and decreases due to the herbivore grazing (R) and the phytoplankton mortality rate (M_P). Constant K_0 is the half-saturation concentration for phytoplankton uptake of nutrients. The Z increases due to the ingestion of phytoplankton (G_Z) and decreases due to the zooplankton specific excretion and mortality rate (M_Z).

The P production (G_P) follows the Michaelis-Menten kinetics and depends on the following photosynthetic rate,

$$L(\mathbf{x},t) \equiv \frac{V_0\,\Psi_0\,I(\mathbf{x},t)}{\sqrt{V_0^2+\Psi_0^2 I^2(\mathbf{x},t)}} \tag{2.4}$$

(Newberger et al., 2003), which depends on the photosynthetically available radiation

$$I(\mathbf{x},t) \equiv I_0 \exp\left\{A_w z - A_p \int_z^0 P(x,y,z',t)\,dz'\right\}, \tag{2.5}$$

where $z \leq 0$. Above, V_0 is the phytoplankton maximum uptake rate, Ψ_0 is the initial slope of the P-I curve, A_w is the extinction coefficient of seawater in the absence of phytoplankton (following the Lambert-Beer law and light variation with day time is not considered), $I_0 \exp\{A_p\, \kappa(\mathbf{x}, t)\}$ is the light attenuation by phytoplankton self-shading, where constant I_0 is the surface photosynthetically available radiation, and A_p is the extinction coefficient per unit concentration of phytoplankton.

Adding (2.1)+(2.2)+(2.3) the total nitrogen $N_T \equiv N + P + Z$ is materially conserved,

$$\frac{\mathrm{d}N_T}{\mathrm{d}t} = 0\,. \tag{2.6}$$

It is convenient therefore to define the system of independent equations as (2.1)-(2.2)-(**??**), instead that the original set (2.1)-(2.2)-(2.3). In the next section two particular solutions of these equations are obtained in the case of steady and horizontally homogeneous ecosystem distributions in the absence of flow.

2.3 Steady Solutions

2.3.1 Analytical Steady Solutions

In order to obtain analytical steady solutions of horizontally homogeneous distributions we set $\mathrm{d}P/\mathrm{d}t = \mathrm{d}Z/dt = 0$ in (2.1) and (2.2), so that spatial functions depend only on z. The water column is divided into three layers. In the upper layer $P \neq 0$ and $Z \neq 0$, in the mid layer $P \neq 0$ and $Z = 0$, and in the lower layer $P = Z = 0$.

In the upper layer ($z \in (z_1, 0]$) the steady P, obtained directly from (2.2) (e.g., Busenberg et al., 1990, eq. 8; Newberger et al., 2003, eq.18) is independent of z

$$P(z) = P_1 = \frac{-1}{\Lambda_0} \ln\left[1 - \frac{\Phi_0}{R_0(1-\Gamma_0)}\right]\,, \quad z \in (z_1, 0]\,. \tag{2.7}$$

With the commonly used parameters for upwelling conditions given in Table 2.1, $P_1 = 8.468\,\mathrm{mmol\,N\,m^{-3}}$. The values and a sensitivity analysis of these parameters are given in (Newberger et al., 2003). The maximum depth z_1 at which this solution is feasible is determined below. From (2.1) and (**??**) the zooplankton $Z(z) = Z_1(z)$ in the upper layer

	description	value	units
A_w	light attenuation	0.067	m^{-1}
A_p	light attenuation by P	0.0095	$\mathrm{m}^2\,\mathrm{mmol\,N}^{-1}$
Ψ_0	initial slope of P-I curve	0.025	$\mathrm{m}^2\,(\mathrm{W\,d})^{-1}$
V_0	P maximum uptake rate	1.5	d^{-1}
I_0	surface available radiation	158	$\mathrm{W\,m}^{-2}$
K_0	half-saturation for P uptake	1	$\mathrm{mmol\,N\,m}^{-3}$
Ξ_0	P specific mortality rate	0.1	d^{-1}
R_0	Z maximum grazing rate	0.52	d^{-1}
Λ_0	Ivlev constant	0.06	$\mathrm{m}^3\,\mathrm{mmol\,N}^{-1}$
Γ_0	fraction of Z grazing egested	0.3	
Φ_0	Z excretion/mortality rate	0.145	d^{-1}

Table 2.1: List of constants (Newberger et al., 2003). P and Z stand for phytoplankton and zooplankton, respectively.

$z \in (z_1, 0]$ is obtained solving the quadratic equation

$$A_0 Z_1^2 + B Z_1 + C = 0\,, \tag{2.8}$$

where the coefficients

$$A_0 \equiv \frac{\Phi_0}{(1-\Gamma_0)P_1}\,, \tag{2.9}$$

$$B(z) \equiv -L(z) - A_0(K_0 + N_T - P_1) + \Xi_0\,, \tag{2.10}$$

$$C(z) \equiv [L(z) - \Xi_0]\,(N_T - P_1) - \Xi_0 K_0\,. \tag{2.11}$$

Thus,

$$Z_1(z) = \frac{-B(z) - \sqrt{B^2(z) - 4A_0\,C(z)}}{2A_0}\,. \tag{2.12}$$

The negative root solution above ensures that $Z(z) < N_T$. To further simplify the problem we consider N_T as constant, independent of z. N_T must be such that the discriminant $B^2(z) - 4A_0\,C(z) \geq 0$.

The maximum depth z_1 of the upper layer is defined as the shallower depth at which $Z(z_1) = 0$. Using (2.1) or (**??**) this condition implies $C(z_1) = 0$, and therefore

$$L_1 \equiv L(z_1) = \Xi_0 \left(1 + \frac{K_0}{N_T - P_1}\right)\,. \tag{2.13}$$

Inverting $L(z_1)$ using (2.4) the depth z_1 defining the lower boundary of the upper layer is

$$z_1 = \frac{1}{2(A_p P_1 + A_w)} \ln\left[\frac{V_0^2 L_1^2}{(V_0^2 - L_1^2)\Psi_0^2 I_0^2}\right] . \tag{2.14}$$

In the mid layer, $z \in (z_2, z_1]$, $Z(z) = Z_2(z) = 0$ and $P(z) = P_2(z) \neq 0$. In this layer, due to (2.3) or (2.1), P_2 satisfies the relation

$$P_2(z) = N_T - \frac{\Xi_0 K_0}{L(z) - \Xi_0} , \tag{2.15}$$

where $L(z)$ is given by (2.4) and (2.5). The solution $P_2(z)$ is found here solving (**??**) numerically. This solution is feasible as long as $P_2(z) \leq N_T$ which, from (**??**), implies that $L(z) > \Xi_0$. Consequently, the maximum depth z_2 of this mid layer is defined as that at which $L(z_2) = \Xi_0$. Inversion of this equation implies that z_2 satisfies the relation

$$\begin{aligned} z_2 - \frac{A_p}{A_w} \int_{z_2}^{z_1} P_2(z')\, dz' = \\ = \frac{1}{A_w} \ln\left(\frac{V_0\, \Xi_0}{\Psi_0\, I_0\, \sqrt{V_0^2 - \Xi_0^2}}\right) - \frac{A_p}{A_w} P_1 z_1 . \end{aligned} \tag{2.16}$$

For its later use it is convenient to define the maximum depth z_3 of this mid layer as that obtained by neglecting the phytoplankton self-shading only in this mid layer,

$$z_3 \equiv \frac{1}{A_w} \ln\left(\frac{V_0\, \Xi_0}{\Psi_0\, I_0\, \sqrt{V_0^2 - \Xi_0^2}}\right) - \frac{A_p}{A_w} P_1 z_1 . \tag{2.17}$$

Clearly, $z_3 < z_2$. Finally, in the lower layer, $z \in [z_{\min}, z_2]$, there is neither P nor Z ($P_3 = Z_3 = 0$), so that the dissolved inorganic nitrogen $N(z) = N_3 = N_T$.

The choice of N_T is particularly important in this *NPZ* solution since it must be such that the resulting distance between z_1 and z_2 be large enough to be properly discretisized using a finite grid size. Based on the behaviour of z_1 and z_3 as functions of N_T (Fig. 2.1), N_T must be close to $P_1 = 8.468\,\mathrm{mmol\,N\,m^{-3}}$. We select $N_T = 8.8\,\mathrm{mmol\,N\,m^{-3}}$. With this choice the values of the transition depths are $z_1 = -15.26\,\mathrm{m}$, $z_2 = -25.13\,\mathrm{m}$, and $z_3 = -36.52\,\mathrm{m}$. The maximum Z, obtained from (**??**) at $z = 0$, becomes $Z_0 = Z(0) = 0.25\,\mathrm{mmol\,N\,m^{-3}}$. The solutions *NPZ* at the three layers are shown in Fig. 2.2.

In the upper layer the amount of Z decreases with depth (from Z_0 to 0) which is compensated (since both P and N_T are constant) by an equally small increase of N. In the mid layer, P decreases from P_1 to 0, and is compensated (since $Z = 0$) by an equally large increase of N.

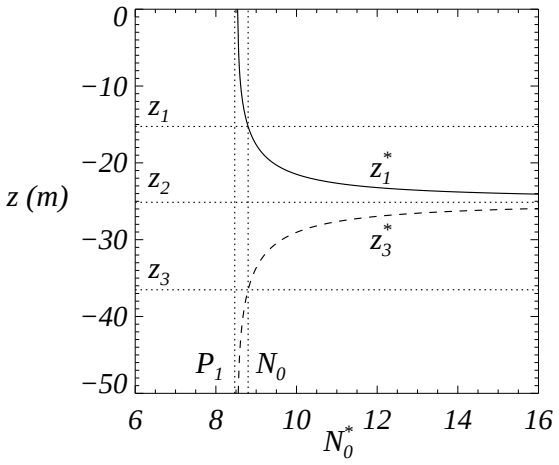

Figure 2.1: Depths z_1^* (**??**) and z_3^* (2.6) as functions of the variable total nitrogen N_0^*. Units are mmol N m^{-3}. Note that $z_1 = z_1^*(N_T)$ and $z_3 = z_3^*(N_T)$.

In this steady solution, and in the upper layer, the large z-dependent $G_P(z)$ is mainly balanced by the large constant M_P (Fig. 2.3). The remanent, smaller part of $G_P(z)$ is balanced by the small z-dependent grazing $R(z)$. In the Z balance, the small growth $G_Z(z)$ of zooplankton is balanced by $M_Z(z)$. In the mid layer $R = 0$, so that $G_P(z)$ and $M_P(z)$ exactly balance.

These steady NPZ solutions are continuous functions of z, but they have been obtained without any requirement on differentiability conditions. It is clear, at least visually from Fig. 2.2, that these functions are not vertically differentiable at $z = z_1$ or $z = z_2$. As a simple proof consider differentiability of $P(z)$ at z_2. The vertical derivative of (**??**) is

$$\begin{aligned} \frac{\partial P_2}{\partial z} &= \frac{\Xi_0 K_0}{L(z) - \Xi_0} \frac{\partial L}{\partial z} = \frac{\Xi_0 K_0}{L(z) - \Xi_0} \frac{V_0^3 \Psi_0}{\sqrt{(V_0^2 + \Psi_0^2 I^2)^3}} \frac{\partial I}{\partial z} \\ &= \frac{\Xi_0 K_0}{L(z) - \Xi_0} \frac{V_0^3 \Psi_0 [A_w + A_p P_2(z)]}{\sqrt{(V_0^2 + \Psi_0^2 I^2)^3}} I(z)\,. \end{aligned} \tag{2.18}$$

As $z \to z_2$, we have $P_2(z) \to 0$ and $L(z) \to \Xi_0$, and therefore $\partial P_2/\partial z \to \infty$ in the mid layer, as observed in Fig. 2.2a. This limit does not match with the vertical derivative of P as $z \to z_2$ in the lower layer, where $\partial P_3/\partial z = 0$. This lack of differentiability (the functions are continuous but not continuously differentiable) implies that these steady solutions are questionable as initial conditions in many coupled physical-ecosystem models. Most of these models are formulated in the spatial (Eulerian) description and require that solutions NPZ be continuously differentiable for the vertical gradients present in the advective derivative on the right hand side of (2.1)-(2.2) make sense. In the next section NPZ solutions, similar to the ones described above but continuously differentiable, are numerically obtained.

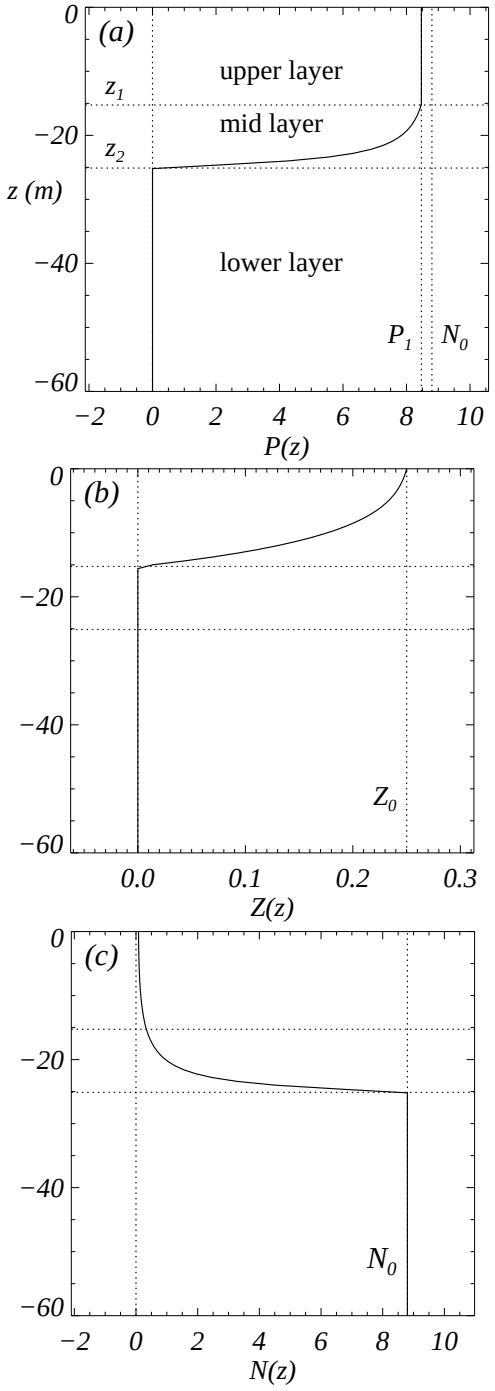

Figure 2.2: Steady vertical profiles of (a) $P(z)$, (b) $Z(z)$, and (c) $N(z)$ in the three layers. The constant concentrations P_1, N_T, and Z_0, as well as the transition depths z_1 and z_2 are indicated. Units are mmol N m^{-3}.

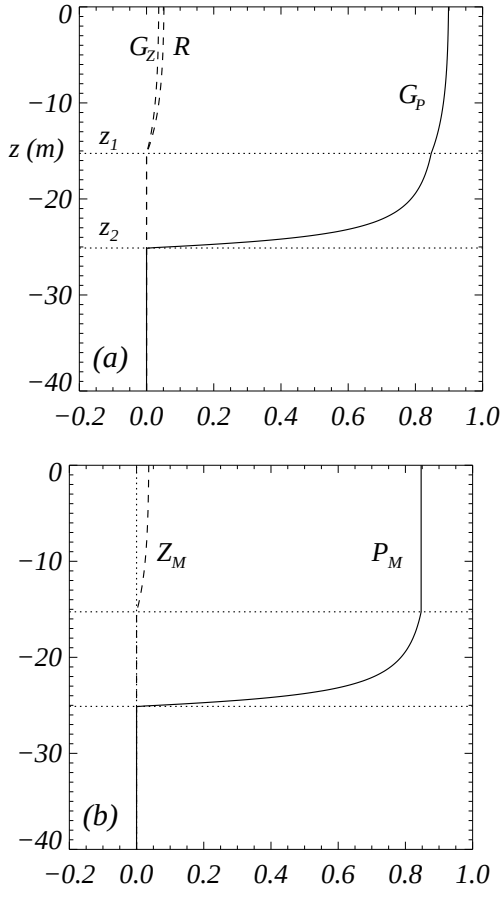

Figure 2.3: Vertical profiles of (a) phytoplankton production $G_P(z)$, grazing $R(z)$, and zooplankton growth $G_Z(z)$; (b) phytoplankton mortality $M_P(z)$ and zooplankton mortality $M_Z(z)$. Units are mmol N m^{-3} d^{-1}.

2.3.2 Numerical Steady Solutions

In order to obtain continuously differentiable steady $P(z)$ and $Z(z)$ solutions, the prognostic equations (2.1)-(2.2) are numerically integrated in time, using as initial conditions smooth profiles $P^{(0)}(z)$ and $Z^{(0)}(z)$, until a steady state is reached. The initial profiles $P^{(0)}(z)$ and $Z^{(0)}(z)$ are identical to the solutions obtained in the previous section (Fig. 2.2a,b) except that in the non homogeneous layers, that is, the mid layer in the case of P and the upper layer in the case of Z, the z-dependent profiles are replaced by transition cosine functions. Since $\partial \cos(z)/\partial z = -\sin(z) = 0$ at $z = \{0, \pi\}$, $P^{(0)}$ and $Z^{(0)}$ have continuous (zero) derivatives at z_1 and z_3, and at 0 and z_1, respectively. Specifically, we define the initial profiles

$$P^{(0)}(z) = \begin{cases} P_1, & z \in (z_1, 0] \\ \frac{1}{2} P_1 \left[1 + \cos \frac{(z-z_1)\pi}{z_1 - z_3}\right], & z \in [z_3, z_1] \\ 0, & z < z_3\,, \end{cases} \tag{2.19}$$

and

$$Z^{(0)}(z) = \begin{cases} \frac{1}{2} Z_1 \left(1 + \cos \frac{z\pi}{z_1}\right), & z \in [z_1, 0] \\ 0\,, & z < z_1\,. \end{cases} \tag{2.20}$$

These initial profiles are shown in Fig. 2.4. Next, $P^{(0)}(z)$ and $Z^{(0)}(z)$ are vertically discretisized and integrated forward using (2.1)-(2.2) with $\mathbf{u} = 0$. Nine different numerical resolutions, ranging from constant grid-size $\delta z = 4\,\mathrm{m}$ ($i = 1$) to $\delta z = 1.5625\,\mathrm{cm}$ ($i = 9$), are implemented (Table 2.2).

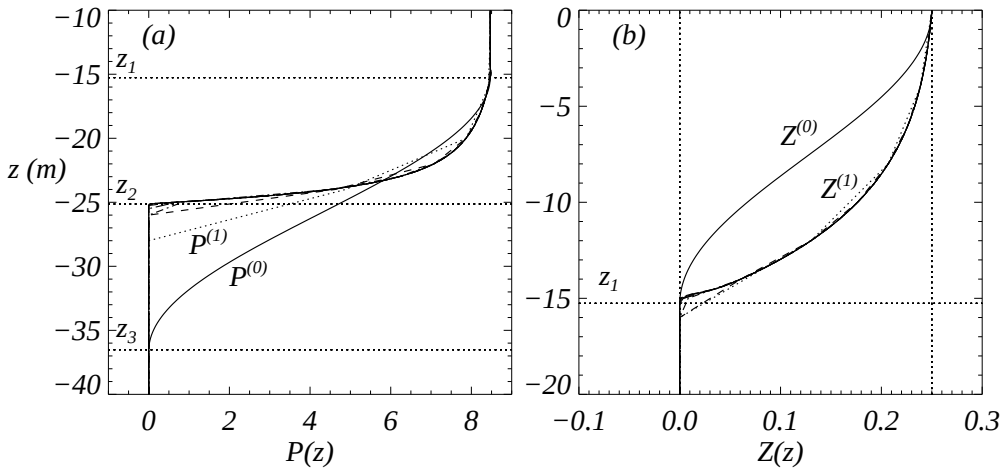

Figure 2.4: (a) $P(z)$, and (b) $Z(z)$. The initial profiles are $P^{(0)}$ and $Z^{(0)}$. The steady solutions for the different numerical resolutions are $P^{(i)}$ and $Z^{(i)}$ ($i = \{1, \ldots, 9\}$). Close up views of $P^{(i)}$ at $z \sim z_2$, and of $Z^{(i)}$ at $z \sim z_1$ are shown in Figs. 2.5a and 2.6a, respectively. Units are mmol N m^{-3}.

label i	grid points $n_i = 25 * i + 1$	resolution (m) $\lvert\mathcal{Z}_{\min}\rvert/(n_i - 1)$
1	26	4
2	51	2
3	101	1
4	201	0.5
5	401	0.25
6	801	0.125
7	1601	0.0625
8	3201	0.03125
9	6401	0.015625

Table 2.2: List of numerical resolutions. Here $\mathcal{Z}_{\min} = -100\,\mathrm{m}$.

Time integration is carried out using an explicit leap-frog scheme, together with a Robert-Asselin time filter to avoid the computational mode (see e.g., Durran, 1998, p. 62). The time integration was 10^4 days, at the end of which the maximum forcing term in the local rate of change of P or Z was of the order of $10^{-7}\,\mathrm{mmol\,N\,m^{-3}\,d^{-1}}$. During the integration time P and Z monotonically converged to the steady solutions $P^{(i)}$ and $Z^{(i)}$ $(i = 1, \ldots, 9)$ shown in Fig. 2.4. After a first look these solutions seem to be very similar to the non continuously differentiable solutions obtained in the previous section. However, a closer view around the layer boundary depths (zooms on $z = z_2$ and $z = z_3$ in Figs. 2.5a and 2.6a, respectively) reveals that for large resolutions $(i \geq 7)$ the solutions $P^{(i)}$ and $Z^{(i)}$ become continuously differentiable functions of z. From the numerical point of view this means that the vertical gradients $\partial P^{(i)}/\partial z$ and $\partial Z^{(i)}/\partial z$, here computed using a simple second order centered scheme, have converged to finite values and no longer depend on the numerical resolution (Figs. 2.5b and 2.6b).

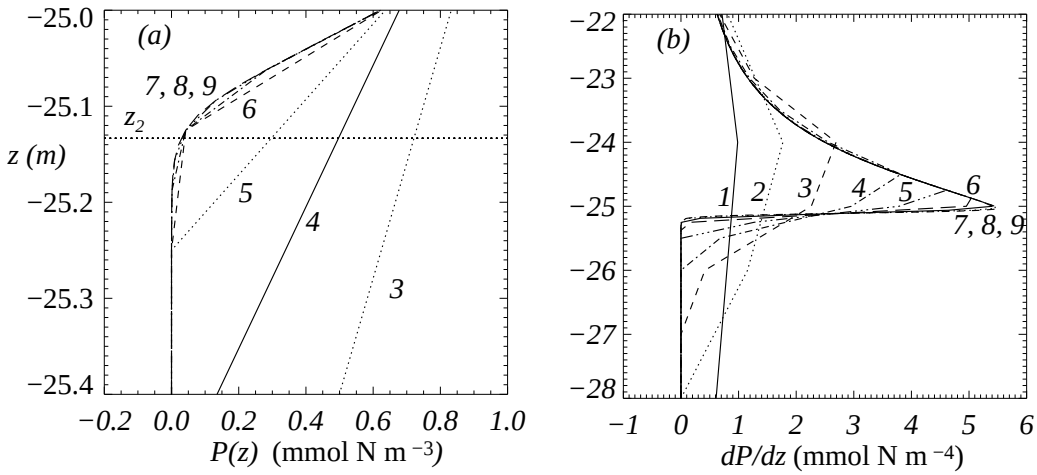

Figure 2.5: A close up view at $z \sim z_2$ of (a) $P^{(i)}(z)$, and (b) $\partial P^{(i)}/\partial z$.

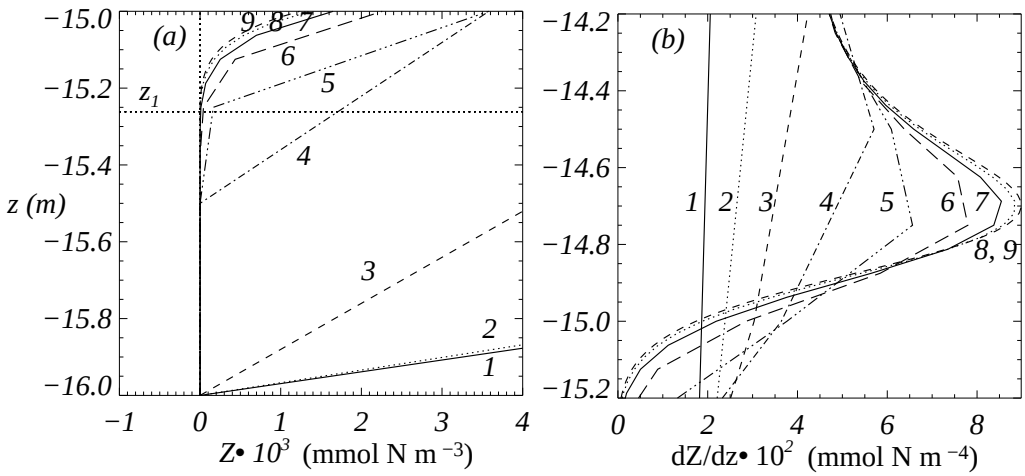

Figure 2.6: A close up view at $z \sim z_1$ of (a) $Z^{(i)}$ ($\times 10^3$), and (b) $\partial Z^{(i)}/\partial z$ ($\times 10^2$).

The results above show that steady and continuously differentiable *NPZ* solutions to equations (2.1)-(2.3) in absence of flow are possible. These steady solutions, despite the fact that are highly idealized with respect to those observed in the real unsteady ocean, can be used as initial conditions in coupled physical-ecosystem numerical models to investigate the role of vertical advection of properties. However, if the discrete numerical models have to faithfully reproduce the continuous *NPZ* system of equations (2.1)-(2.3), vertical resolutions of few centimeters are needed. The next section describes a simple application example of the numerical NPZ model coupled to a three-dimensional dynamical numerical model. The numerical simulations are initialized with the steady ecosystem solutions found in this section, while the initial physical conditions lead to an idealized case of baroclinic instability process. The implications of the vertical resolution used, that due to computational limitations is restricted to 65 cm, are addressed.

2.4 Coupled Physical-Ecosystem Numerical Simulations

2.4.1 The dynamical $\mathcal{AB}\varpi$ model

The physical model (hereinafter referred to as the $\mathcal{AB}\varpi$-model) is non-hydrostatic and simulates the volume-preserving flow of a stratified rotating fluid under the Boussinesq and f-plane approximations (Dritschel and Viúdez, 2003). The initial flow is specified by the potential vorticity (PV) using the PV initialization approach (Viúdez and Dritschel, 2003). This initialization technique largely avoids the initial generation of inertia–gravity waves which otherwise could contaminate the balanced vertical velocity. The theoretical basis of

the numerical model is explained in detail in appendix A and only a brief summary is given next to introduce the indispensable symbol definitions and mathematical expressions.

The Froude number $\mathcal{F} \equiv \omega_h/\mathcal{N}$ and the Rossby number $\mathcal{R} \equiv \zeta/f$, where ω_h and ζ are the horizontal and vertical components of the relative vorticity $\boldsymbol{\omega} \equiv \boldsymbol{\omega}_h + \zeta\mathbf{k}$, and f and $\mathcal{N}$ are the Coriolis and *total* Brunt-Väisälä frequencies, respectively. The isopycnal vertical displacement $\mathcal{D}$ with respect to a reference density configuration $\mathcal{D}(\mathbf{x},t) \equiv z - d(\mathbf{x},t)$ where $d \equiv (\rho - \rho_0)/\varrho_z$ is the depth, or vertical location, that an isopycnal located at $\mathbf{x}$ at time t has in the reference density configuration defined by $\rho_0 + \varrho_z z$, where ρ is the mass density, and $\rho_0 > 0$ and $\varrho_z < 0$ are constant values that do not need to be specified in the Boussinesq approximation. Therefore, static instability occurs when the stratification number $\mathcal{D}_z > 1$, and inertial instability when $\mathcal{R} < -1$.

The $\mathcal{AB}\varpi$-model integrates the dimensionless ageostrophic horizontal vorticity $\mathcal{A}_h = (\mathcal{A},\mathcal{B}) \equiv \tilde{\boldsymbol{\omega}}_h - c^2\boldsymbol{\nabla}_h\mathcal{D}$ using the equation

$$\frac{\mathrm{d}\mathcal{A}_h}{\mathrm{d}t} = -f\mathbf{k}\times\mathcal{A}_h + (1-c^2)\boldsymbol{\nabla}_h w + \tilde{\boldsymbol{\omega}}\cdot\boldsymbol{\nabla}\mathbf{u}_h + c^2\boldsymbol{\nabla}_h\mathbf{u}\cdot\boldsymbol{\nabla}\mathcal{D}\,,$$

where the Prandtl ratio $c \equiv N/f$, the relative vorticity $\boldsymbol{\omega} \equiv \boldsymbol{\nabla}\times\mathbf{u} = (\xi,\eta,\zeta)$, and $\tilde{\chi} \equiv \chi/f$ for any quantity χ.

The third prognostic equation is the explicit conservation of PV *anomaly* ϖ through PV contour advection on isopycnals, $d\varpi/dt = 0$, where

$$\begin{aligned}\varpi &\equiv \Pi - 1 = \frac{\boldsymbol{\omega} + f\mathbf{k}}{f}\cdot\boldsymbol{\nabla}d - 1 = \\ &= (\tilde{\boldsymbol{\omega}} + \mathbf{k})\cdot(\mathbf{k} - \boldsymbol{\nabla}\mathcal{D}) - 1 = \tilde{\zeta} - \frac{\partial\mathcal{D}}{\partial z} - \tilde{\boldsymbol{\omega}}\cdot\boldsymbol{\nabla}\mathcal{D}\,,\end{aligned} \tag{2.21}$$

and $\Pi \equiv (\tilde{\boldsymbol{\omega}} + \mathbf{k})\cdot\boldsymbol{\nabla}d$ is the *total* dimensionless PV.

The state variables are the components of the three-dimensional vector potential $\boldsymbol{\varphi} = (\varphi,\psi,\phi)$ which provide the velocity $\tilde{\mathbf{u}} = -\boldsymbol{\nabla}\times\boldsymbol{\varphi}$ and the vertical displacement $c^2\mathcal{D} = -\boldsymbol{\nabla}\cdot\boldsymbol{\varphi}$. The horizontal components of the vector potential $\boldsymbol{\varphi}_h = (\varphi,\psi)$ are diagnosed every time-step by inversion of $\mathcal{A}_h = \boldsymbol{\nabla}^2\boldsymbol{\varphi}_h$, while the vertical component ϕ is obtained from the inversion of the ϖ definition (2.7) as a function of (φ,ψ,ϕ). This procedure, based on the explicit conservation and inversion of PV, allows long term simulations of large PV gradients as those happening during baroclinic instability processes. Also, owing to the fact that the

divergenceless condition ($\boldsymbol{\nabla} \times \mathbf{u} = 0$) is implicitly satisfied using the vector potential $\boldsymbol{\varphi}$, this algorithm is specially precise in obtaining the vertical velocity field which, though crucial for the development of *NPZ* anomalies, is typically three orders of magnitude smaller than the horizontal velocity in submesoscale balanced flow.

2.4.2 Numerical Parameters

The domain is a triply periodic box of vertical extent $L_Z = 2\pi$ (which defines the unit of space) and horizontal extents $L_X = L_Y = cL_Z$, with $c \equiv N/f = 10$. The number of grid points is $(n_X, n_Y, n_Z) = (128, 128, 128)$, and the number of isopycnals $n_L = 128$. The background Brunt-Väisälä frequency $N = 2\pi$, which defines the background buoyancy period as the unit of time, $T_{bp} \equiv 2\pi/N = 1$. Thus one inertial period $T_{ip} = cT_{bp}$. The time-step $\delta t = 0.01$. In order to relate the non-dimensional quantities of the physical model to the dimensional ones of the NPZ model only two dimensional parameters must be specified, namely the maximum depth $\mathcal{Z}_{\min}$ and the mean latitude θ_0. These two parameters specify the length $\mathcal{L}$ and time $\mathcal{T}$ conversion factors, being $\mathcal{L} \equiv |\mathcal{Z}_{\min}|/\pi \cong 31.83\,\mathrm{m}$, for $\mathcal{Z}_{\min} = -100\,\mathrm{m}$, and $\mathcal{T} \equiv 24 \times 3600/(c\,2\sin\theta_0)\,\mathrm{s} \cong 6109.5\,\mathrm{s}$ for $\theta_0 = 45°\mathrm{N}$. The dimensional quantities in the previous section, including the constants in Table 2.1, are made dimensionless using the appropriate combination of $\mathcal{L}$ and $\mathcal{T}$ factors. The dimension of amount of substance (mmol N) is unchanged since it exclusively belongs to the *NPZ* equations. The relation between the physical and ecosystem models is that the $\mathcal{AB}\varpi$-model provides the three-dimensional velocity $\mathbf{u}$ for the advective terms in the NPZ-model. The $\mathcal{AB}\varpi$-model is still adiabatic, since heating by solar radiation is ignored, and diffusion processes are neglected so that PV is materially conserved.

2.4.3 Numerical Results

We simulate a shallow current containing both positive and negative ϖ. The current is set up by placing two horizontal PV cylinders of opposite sign, slightly perturbed, next to each other (Fig. 2.7). Each PV cylinder has a horizontal and vertical semi-axis of $0.5\,c$ and 0.7, respectively. The minimum and maximum ϖ at the center of the cylinders is $\{\varpi_{\min}, \varpi_{\max}\} = \{-0.75, 0.75\}$. This PV distribution induces a northward current which, during the baroclinic instability process, rolls up into a street of cyclonic and anticyclonic vortices that pair forming

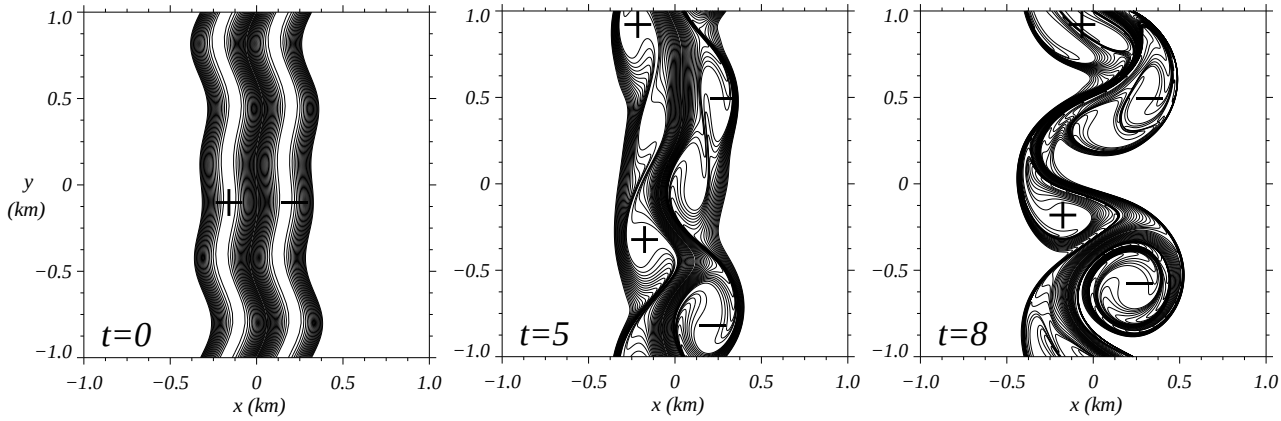

Figure 2.7: PV contours at the surface ($z = 0$). Horizontal extent is $\Delta x = \Delta y = [-\pi, \pi] c\mathcal{L} = [-1, 1]$ km. Time is shown in T_{ip}.

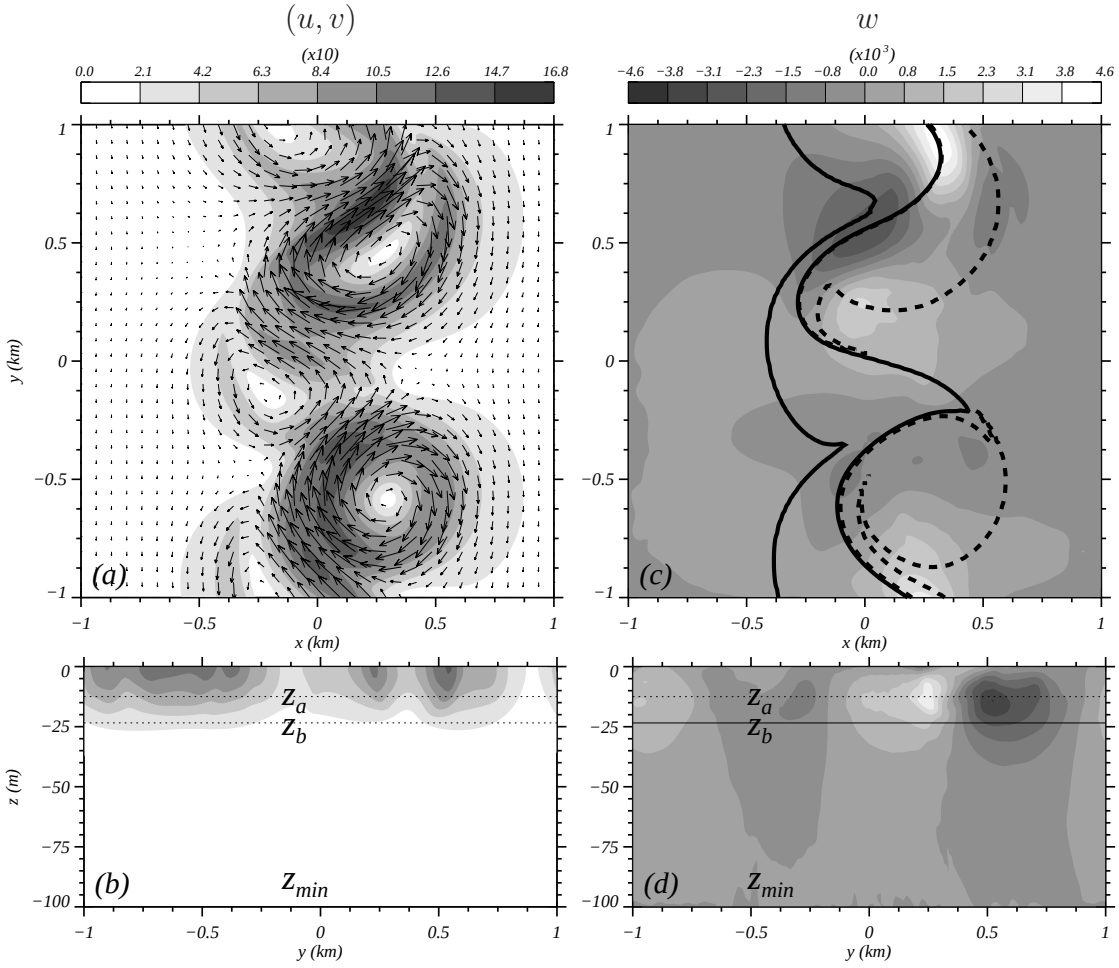

Figure 2.8: (a) Horizontal distribution of $\mathbf{u}_h = (u, v)$ at $z = 0$. Only every 4 vectors is plotted. Contours are speed $u_h \equiv |\mathbf{u}_h|$ ($\max\{u_h\} = 1.7$). (b) $u_h(y, z)$ on vertical section $x = 0$ ($\max\{u_h\} = 1.52$). (c) Horizontal distribution of w at $z_b \simeq -23.4$ m ($w \in [-2.9, 4.5] \times 10^{-3}$). The PV contours $\varpi = \pm 0.05$ at $z = 0$ are included for reference. (d) $w(y, z)$ on vertical section $x = 0$ ($w \in [-3.9, 3.6] \times 10^{-3}$). Time $t = 8\, T_{ip}$, $\mathcal{Z}_{\min} = -100$ m, $z_a = -12.5$ m, and $z_b \simeq -23.4$ m.

vortex dipoles (Figs. 2.7 and 2.8a,b). During this process vertical velocity is generated (Fig. 2.8c,d). We choose a shallow jet, located in the first 50 m (Fig. 2.8b) in order to increase the numerical resolution in the first 100 m, and a small Prandtl ratio $c = 10$ in order to favor vertical velocities.

Vertical velocities reach maxima at $t = 8$ and $t = 9\,T_{ip}$ at the northern side of the northern anticyclone (Fig. 2.8c). At this stage $\mathcal{F}_{\max} = 0.41$ and $\mathcal{R}_{\min} = -0.67$. A vertical section along $x = 0$ (Fig. 2.8d) shows that w maxima occur between $z \simeq -13$ m and $z \simeq -25$ m, and is three orders of magnitude smaller than $|\mathbf{u}_h|$. The vertical velocity is mostly in balance in the sense that inertia–gravity waves, either due to unbalanced initial conditions or to spontaneous generation, have very small amplitude.

As expected, P anomalies $P'(\mathbf{x}, t) \equiv P(\mathbf{x}, t) - P_s(z)$, where $P_s(z)$ is the stationary P profile defined in the previous section, reach maxima at $z \simeq z_2$ while Z anomalies $Z'(\mathbf{x}, t) \equiv Z(\mathbf{x}, t) - Z_s(z)$ reach maxima at $z \simeq z_1$ (Fig. 2.9a). These anomalies have been forced by w since the horizontal advection of the stationary profiles $P_s(z)$ and $Z_s(z)$ is zero. The standard deviation of G_P has two maxima (Fig. 2.9b), the largest one is located at $z \simeq z_2$ and is related to P', while the secondary one, located some meters above at $z \simeq -19$ m, is related to Z' through the term $N/(K_0 + N)$ in (2.1).

Grazing anomalies R' reach maxima at the Z transition depth $z \simeq z_1$ (Fig. 2.9b). R' however remain small, roughly a 25% of G'_P at z_1, so that the phytoplankton balance involves mainly $\mathrm{d}P/\mathrm{d}t$, U, and M_P. Horizontal advection $\mathbf{u}_h \cdot \boldsymbol{\nabla}_h P$ and local change $\partial P/\partial t$ (Fig. 2.9c) are the largest contributions to the material rate of change of P. Vertical advection $w\partial P/\partial z$ is about 50%, while $\mathrm{d}P/\mathrm{d}t$ is only 10% which corresponds to the phytoplankton physiological reaction to light absorption changes due to vertical displacement. There is therefore a large cancellation between $\mathbf{u}_h \cdot \boldsymbol{\nabla}_h P$ and $\partial P/\partial t$ which, together with the smallness of $w\partial P/\partial z$ and $\mathrm{d}P/\mathrm{d}t$, implies that horizontal distributions of P resemble a tracer of the horizontal flow (i.e., $\partial P/\partial t \simeq -\mathbf{u}_h \cdot \boldsymbol{\nabla}_h P$).

A similar fact occurs with the local and advective terms of Z (Fig. 2.9d). Here the difference is that $\mathrm{d}Z/\mathrm{d}t$ is only about a 0.1% of $\partial Z/\partial t$ or $\mathbf{u}_h \cdot \boldsymbol{\nabla}_h Z$. Thus Z' behaves as a tracer of the horizontal flow better than P'.

The horizontal distributions of P' and Z' (Fig. 2.10a,c) are related to w (Fig. 2.8c). Positive anomalies occur in downwelling areas and negative anomalies in upwelling areas. The correlation between w, P', and Z' along the water column can be noticed comparing

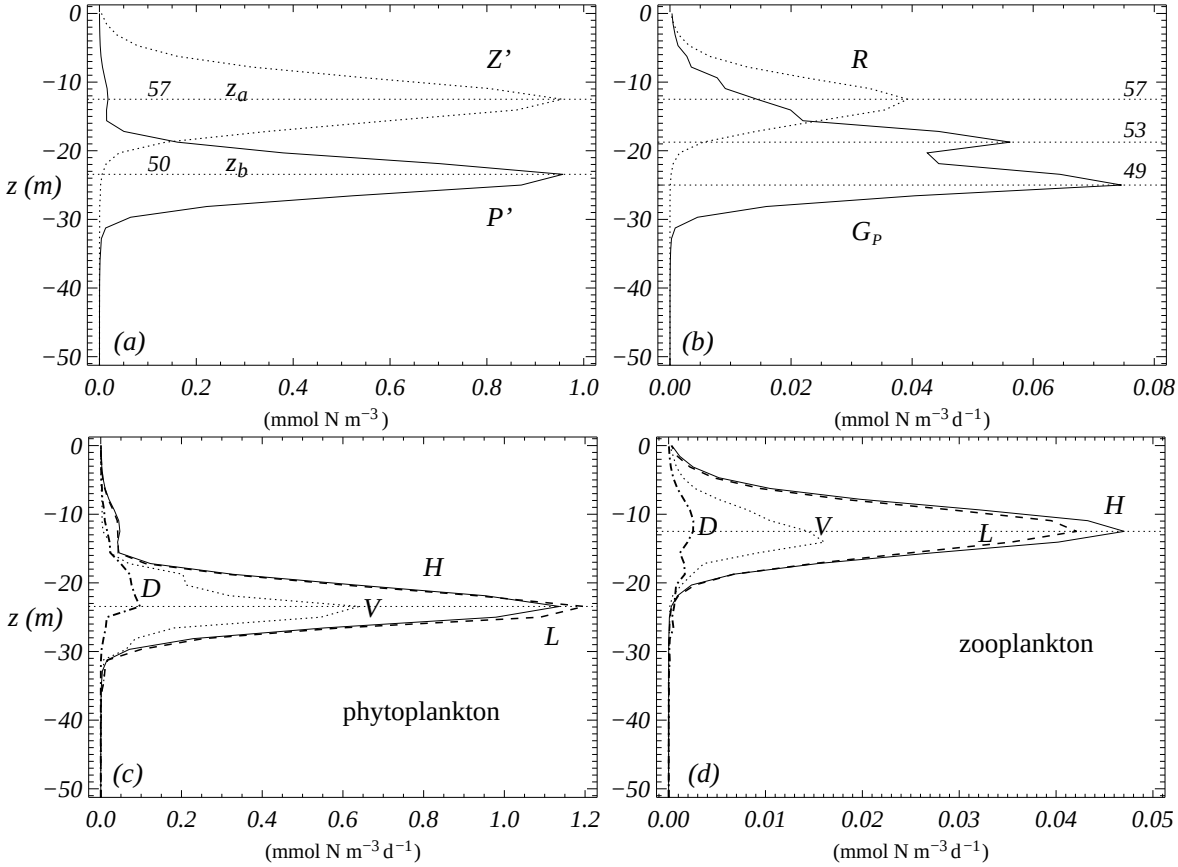

Figure 2.9: Standard deviation profiles $\sigma\{\chi\}(z) \equiv (\langle(\chi - \langle\chi\rangle_h)^2\rangle_h)^{1/2}$, where $\langle\chi\rangle_h$ is the horizontal average, as a function of depth z at $t = 8\,T_{ip}$ of (a) P' and Z' ($\times 50$); (b) P production (G_P) and grazing ($R \times 10$); (c) $\mathbf{u}_h \cdot \boldsymbol{\nabla}_h P$ (H), $w\partial P/\partial z$ (V), $\partial P/\partial t$ (L), and $\mathrm{d}P/\mathrm{d}t$ (D); (d) $\mathbf{u}_h \cdot \boldsymbol{\nabla}_h Z$ (H), $w\partial Z/\partial z$ (V), $\partial Z/\partial t$ (L), and $\mathrm{d}Z/\mathrm{d}t$ ($\times 100$, D). The i_Z indices of the relevant depths are indicated.

the vertical sections of w (Fig. 2.8d), P' and Z' (Fig. 2.10b,d). In the large shear regions Z' has horizontal gradients larger than those of P', which is a consequence of the fact that Z' is materially conserved better than P' as we have commented above.

The existence of two maxima in $\sigma\{G'_P\}(z)$ (Fig. 2.9b) is explained through the spatial distributions shown in Fig. **??**. In upwelling regions $G'_P > 0$ and $G'_P < 0$ above and below z_b, respectively, while the opposite happens in downwelling regions. This behaviour is mainly due to the nonlinear relation between Z and P through the term $(N_T - P - Z)/(K_0 + N_T - P - Z) \times P$ included in U in (2.1) since the product $\sigma\{P'\}\sigma\{Z'\}$ (not shown) reaches a maximum at $z \simeq -19\,\mathrm{m}$. Grazing anomaly R' at the Z transition depth $z \simeq z_a = -12.5\,\mathrm{m}$. (not shown) is obviously spatially correlated with Z' (Fig. 2.10c,d). Grazing however continues having a minor role in the P budget due to the relatively small amount of Z in the upper layer.

The relevant quantities are however $\mathrm{d}P/\mathrm{d}t$ and $\mathrm{d}Z/\mathrm{d}t$ (Fig. 2.11) since they represent

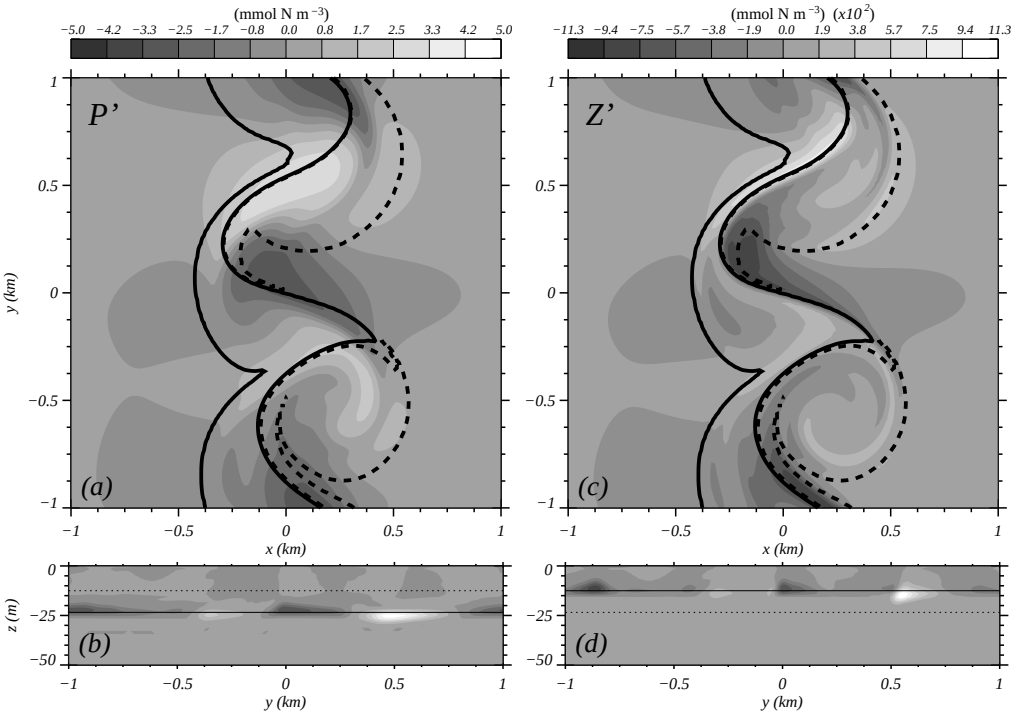

Figure 2.10: (a) $P'(x, y)$ at $z_b \simeq -23.4\,\mathrm{m}$ ($P' \in [-3.3, 3.1]\,\mathrm{mmol\,N\,m^{-3}}$). PV contours $\varpi = \pm 0.05$ at $z = 0$ are included for reference. (b) $P'(y, z)$ on vertical section $x = 0$ ($P' \in [-3.3, 4.8]\,\mathrm{mmol\,N\,m^{-3}}$). (c) $Z'(x, y)$ at $z_a = -12.5\,\mathrm{m}$ ($Z' \in [-9.0, 8.3] \times 10^{-2}\,\mathrm{mmol\,N\,m^{-3}}$). (d) $Z'(y, z)$ on vertical section $x = 0$ ($Z' \in [-8.9, 11.2] \times 10^{-2}\,\mathrm{mmol\,N\,m^{-3}}$). Time $t = 8\,T_{ip}$.

the total P and Z changes (the rhs of (2.1) and (2.2), respectively) forced by w and are independent of the effect of mere advection. Ascending fluid particles experience an increase of their P content while descending particles experience a decrease of P. Note particularly the large P decrease at the northern side of the domain (Fig. 2.11a,b), where $w < 0$ (Fig. 2.8c,d). Positive P budgets occur at depths a bit shallower than negative P budgets, which explains why $\mathrm{d}P/\mathrm{d}t$ is mostly negative at the depth shown in Fig. 2.11a. The material rate of change of Z (Fig. 2.11c,d) and w are also clearly correlated. However $\mathrm{d}Z/\mathrm{d}t$ usually displays a minimum and a maximum along the water column, which is consistent with the two maxima in $\sigma\{\mathrm{d}Z/\mathrm{d}t\}$ (Fig. 2.9d).

The analysis of $\mathrm{d}P/\mathrm{d}t$ and $\mathrm{d}Z/\mathrm{d}t$ into their local and advective changes (Fig. 2.12) shows that, as inferred from their standard deviations (Fig. 2.9c,d), there is a large cancelation between the local change and the horizontal advection of P and Z. The vertical advection is smaller. Consistently also with the P' and Z' distributions (Fig. 2.10) the local change and horizontal advection of Z present patterns more elongated than those of P. This is a

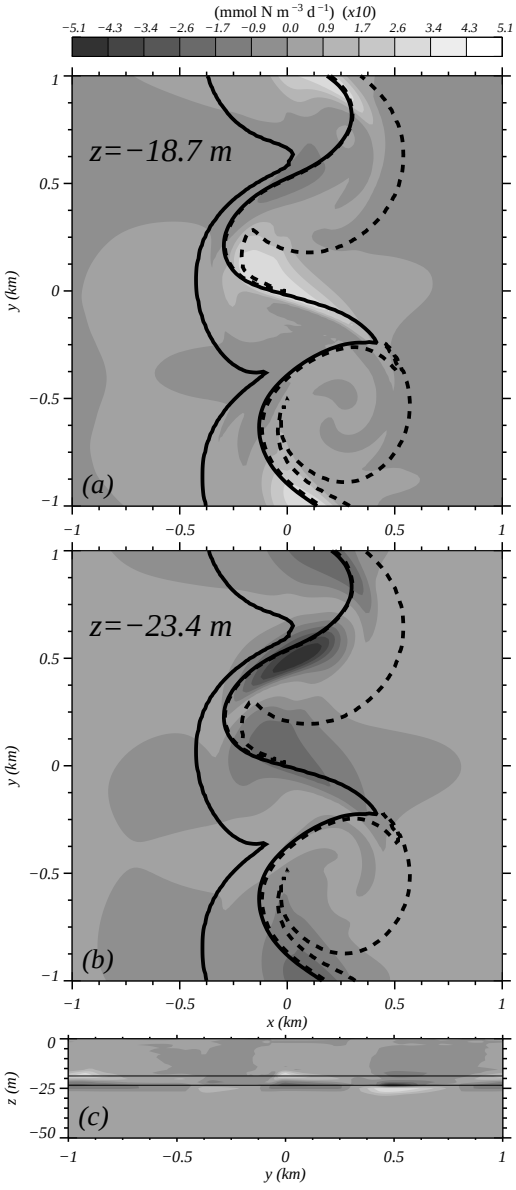

Figure 2.11: P production anomaly $G'_P(x, y)$ on horizontal planes (a) $z = -18.75\,\mathrm{m}$ ($i_z = 53, G'_P \in [-0.12, 0.33]\,\mathrm{mmol\,N\,m^{-3}\,d^{-1}}$). (b) $z = z_b \simeq -23.4\,\mathrm{m}$ ($i_z = 50, G'_P \in [-0.51, 0.035]\,\mathrm{mmol\,N\,m^{-3}\,d^{-1}}$). (c) $G'_P(y, z)$ on vertical section $x = 0$ ($G'_P \in [-0.51, 0.34]\,\mathrm{mmol\,N\,m^{-3}\,d^{-1}}$). Time $t = 8\,T_{ip}$.

consequence of the better material conservation of Z in comparison con P. Large local rates occur in the frontal areas, where both horizontal velocity and horizontal gradients of P and Z are large. The vertical advection of P and Z have however similar patterns. This is so because $\partial P/\partial z \simeq \partial P_s/\partial z > 0$ at $z = z_b$ and $\partial Z/\partial z \simeq \partial Z_s/\partial z > 0$ at $z = z_a$, so that the vertical advection patterns (Fig. 2.12c,f) resemble the w pattern (Fig. 2.8c).

The time evolution of $\sigma\{\mathrm{d}P/\mathrm{d}t\}$, $\sigma\{\mathrm{d}Z/\mathrm{d}t\}$, and $\sigma\{w\}$ (Fig. 2.13) show that the ecosystem time response to w maxima is about $5\,T_{ip}$. The second w maximum at $t \simeq 37\,T_{ip}$ is related to the flow enhancement due to the fusion of two anticyclones. The vertical resolution used in this simulation ($\delta z = 65\,\mathrm{cm}$) is not good enough to fully resolve the large vertical gradients of P and Z at transition depths. Based on Figs. 2.5b and 2.6b, vertical gradients are underestimated by a 50%. Larger vertical resolutions would correctly resolve the vertical advection of P and Z which would cause an important increase in P' and Z' distributions. However, as another consequence of an increased vertical resolution, these larger anomalies would be restricted to thinner ocean layers, so that only quantitative changes are expected in the ecosystem variables.

These numerical results correspond to a non diffusive NPZ ecosystem model coupled to an adiabatic inviscid physical model. These results will not apply when vertical mixing is added to the NPZ model (see Edwards et al., 2000) since in such a case the large vertical *NPZ* gradients found here would turn P_s and Z_s into unsteady solutions. We note that the mere existence of vertical eddy diffusion in a numerical model already requires vertical differentiability. Vertical diffusion is not included here because the NPZ model is kept as simple as possible in order to analyze the vertical velocity forcing of *NPZ* anomalies. Including vertical diffusion will add new free parameters (the vertical diffusivity coefficients) to the already large list of *NPZ* parameters on Table 2.1. Furthermore, the absence of *NPZ* diffusion This is also consistent with the inviscid nature of the PV-conserving dynamical model (only a very small amount of numerical diffusivity is included to avoid grid-size noise).

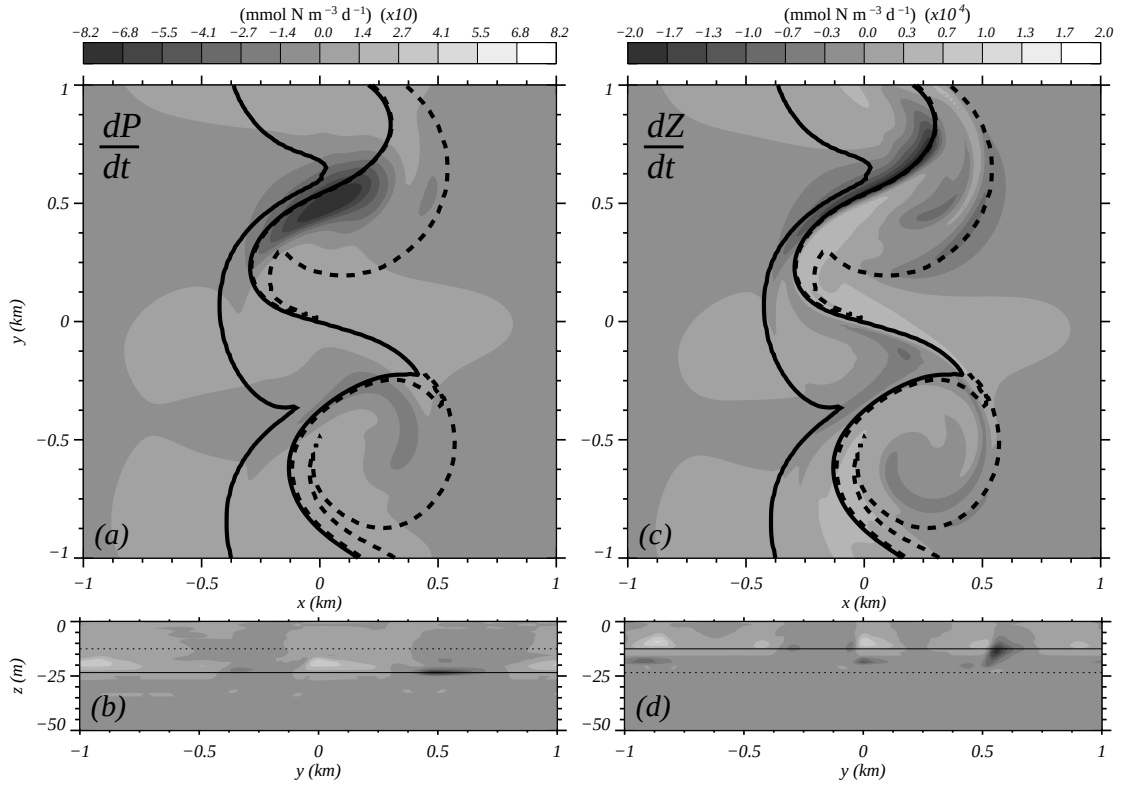

Figure 2.12: (a) $\mathrm{d}P/\mathrm{d}t$ at $z_b \simeq -23.4\,\mathrm{m}$ ($i_z = 50, \mathrm{d}P/\mathrm{d}t \in [-0.82, 0.081]$). (b) $\mathrm{d}P/\mathrm{d}t$ at $x = 0$ ($\mathrm{d}P/\mathrm{d}t \in [-0.82, 0.42]$). (c) $\mathrm{d}Z/\mathrm{d}t$ at $z = -12.5\,\mathrm{m}$ ($i_z = 57, \mathrm{d}Z/\mathrm{d}t \in [-19.8, 5.3] \times 10^{-5}$). (d) $\mathrm{d}Z/\mathrm{d}t$ at $x = 0$ ($\mathrm{d}Z/\mathrm{d}t \in [-19.6, 10.5] \times 10^{-5}$). Time $t = 8\,T_{ip}$.

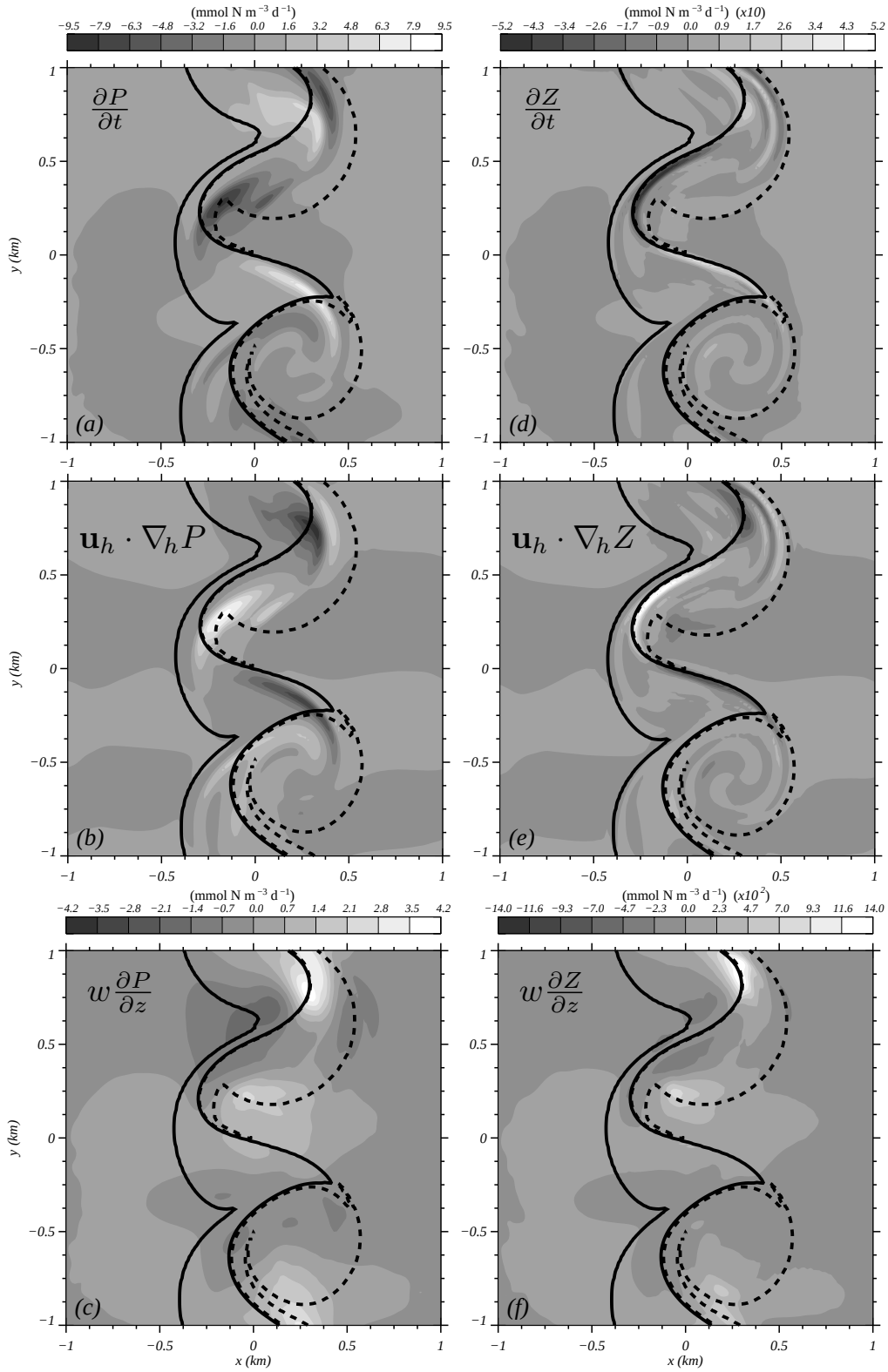

Figure 2.13: (a) $\partial P/\partial t$ at $z \simeq z_b = -23.4\,\mathrm{m}$ ($\partial P/\partial t \in [-8.3, 7.4]$). (b) $\mathbf{u}_h \cdot \boldsymbol{\nabla}_h P$ ($\in [-9.4, 8.3]$). (c) $w\partial P/\partial z$ ($\in [-1.8, 4.2]$). (d) $\partial Z/\partial t$ at $z_a = -12.5\,\mathrm{m}$ ($\partial Z/\partial t \in [-0.51, 0.30]$). (e) $\mathbf{u}_h \cdot \boldsymbol{\nabla}_h Z$ ($\in [-0.32, 0.53]$). (f) $w\partial Z/\partial z$ ($\in [-0.042, 0.14]$). Time $t = 8\,T_{ip}$.

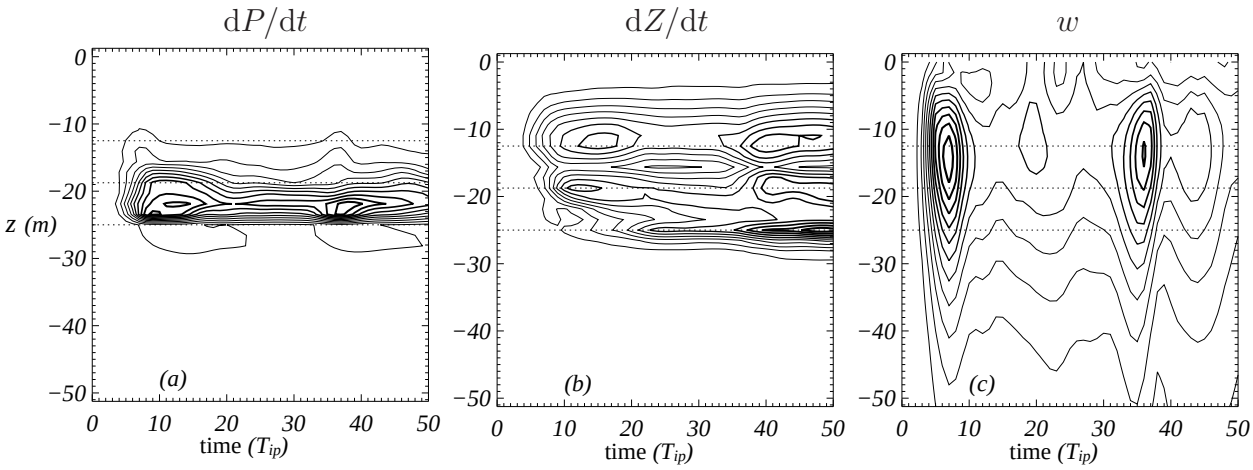

Figure 2.14: (a) $\sigma\{\mathrm{d}P/\mathrm{d}t\}(z,t)$ (max = 0.11, Δ = 0.01). (b) $\sigma\{\mathrm{d}Z/\mathrm{d}t\}(z,t)$ (max = 5×10^{-6}, $\Delta = 5.4\times10^{-5}$). Units are mmol N m^{-3} d^{-1}. (c) $\sigma\{w\}(z,t)$ (max = 1.2×10^{-3}, $\Delta = 10^{-4}$).

2.5 Concluding Remarks

We have first shown that 1D steady and continuously differentiable (in a numerical sense) solutions to the *NPZ* equations are possible. These solutions are potentially useful as initial steady ecosystem conditions to investigate the role of horizontal and vertical advection in 3D coupled physical-ecosystem numerical models. An example of ecological development due to vertical velocity enhancement during a baroclinic instability process has been presented.

This example shows that once phytoplankton and zooplankton anomalies develop locally forced by balanced vertical velocity they are horizontally advected away from the upwelling or downwelling regions so that spatial distributions of vertical velocity and ecological fields become eventually uncorrelated (for experimental evidence of this process see e.g. Ruiz et al., 2001). Thus the biological distributions are more related to PV gradients than to PV itself. This fact, and the submesoscale vertical origin of *NPZ* anomalies, is consistent with (Lévy et al., 2001), who used a primitive equations model with vertical diffusion. However, the experimental work of (Lévy et al., 2005) questions the contribution of submesoscale total advection in the phytoplankton variability over large time scales.

The physical-ecological model used here has several limitations. On the one hand, these *NPZ* solutions require very good vertical resolutions, with a grid size of few centimeters, to be properly discretisized. This imposes a severe handicap to the available random access memory of current computers running 3D coupled physical-ecosystem models. Though from a strict numerical perspective this fact is a serious modeling limitation, from a wider

perspective other handicaps, for instance, errors in the mathematical parametrization of the different *NPZ* processes, are likely to be of larger relevance (see Anderson, 2005; Flynn, 2005; Mitra et al., 2007). It is nevertheless important to know the degree at which ecosystem modeling solutions faithfully reproduce the underlaying ecosystem dynamics and that, even with poor vertical resolution, it is possible to obtain good qualitative results from these models.

On the other hand, our results show that P and Z approximately behave as passive tracers while organisms are in fact active tracers. This is so because the simple initial steady *NPZ* profiles let little interaction between P and Z. In future work we will address these interactions using both more realistic initial *NPZ* profiles and a more complex biological model.

To conclude, these results are a first approximation towards a better understanding of biological processes forced by vertical velocity at the submesoscale. Many questions still remain to be answered in this context. How much does the submesoscale vertical velocity contribute to primary and secondary productivity in comparison to the mesoscale? Does the vertical advection induce different biological patterns in eutrophic and oligotrophic regimes? Is the submesoscale important in the seasonal biological variance?

Chapter 3

Phytoplankton enhancement by oceanic dipoles

Chapter submitted as M.Claret, A.Viúdez, and Y. H. Spitz, 2012: Phytoplankton enhancement by oceanic dipoles.

Al cim d'un promontori que domina les ones de la mar,
quan l'astre rei cap a ponent declina me'n pujo a meditar.
Amb la claror d'aqueixa llàntia encesa contemplo mon no-res;
contemplo el mar i el cel, i llur grandesa m'aixafa com un pes.

Vora la mar, Jacint Verdaguer

ABSTRACT

Phytoplankton distributions associated to oceanic dipoles are investigated using a high-resolution, non-hydrostatic, three-dimensional numerical model coupled to a NPZ (Nutrient-Phytoplankton-Zooplankton) oligotrophic model. Two scenarios are considered, a submesoscale surface and a mesoscale subsurface dipoles, in order to characterize both the effect of vortices in translation and the distant action of potential vorticity (PV) on phytoplankton dynamics. We observe that the dipole separatrix acts as an impermeable barrier dividing two different ecological niches. On the one hand, plankton trapped within vortices reaches a near steady state, which depends on the community entrained at the formation stage of vortices. On the other hand, phytoplankton advection by the dipole introduces ecological heterogeneity outside the separatrix. A balance between vertical advection (VA) and biological forcing generates a subsurface trail of phytoplankton at the wake of the translating dipole. The length of this trail is nearly constant and may be used to estimate the phytoplankton mortality rate for a known dipole speed. When negative gradients of PV exist in the upper ocean, horizontal advection accounts indirectly for a larger phytoplankton increase, though much localized, than that caused by VA. If a subsurface dipole is considered, an ecosystem patch is stirred such that a filament runs along its axis. The filament extent increases with depth and as a result phytoplankton self-shading decreases at the filament front in benefit of light irradiance, and thus of phytoplankton production. Finally, the horizontal extension of the filament is approximated to an analytical expression derived for a dipole of known geometry and intensity.

3.1 Introduction

Plankton is largely heterogeneous mainly at the mesoscale and submesoscale, where physical and ecological processes have similar spatio-temporal scales. Ecological populations are affected by flow phenomena such as fronts, filaments, vortices, inertia–gravity waves, and coastal upwelling. In particular, vortices alter ecosystem dynamics in a number of ways. Eddies inject nutrients in the upper ocean and may affect primary productivity, PP (Oschlies and Garçon, 1998; Martin and Pondaven, 2003). Also, vortices create ecological niches which may increase phytoplankton diversity (Thompson et al., 2007; Huang et al., 2010) and induce mesoscale heterogeneity of higher trophic levels (Read et al., 2002; Atwood et al., 2010).

Vortical structures modify plankton patterns by several mechanisms. Remote sensing observations have displayed off-shore transport of chlorophyll-*a* trapped in vortices (Batten and Crawford, 2005; Thompson et al., 2007; Serra et al., 2010) or the deformation of individual chlorophyll patches into elongated and spiral filaments due to mesoscale dynamics (Lehahn et al., 2007). As a consequence of this vortical structures, horizontal advection by mesoscale flow can trigger plankton patchiness of smaller scales (Abraham, 1998). Though the role of vertical advection of chlorophyll by submesoscale structures is more difficult to unveil, several eddy resolving numerical simulations (Oschlies and Garçon, 1998; Mahadevan and Archer, 2000; Lévy et al., 2001; McGillicuddy and Anderson, 2003) suggest that nutrient injection by eddies is relevant to explain basin or regional PP.

Two main theories of nutrient upwelling have been proposed in single vortices. On the one hand, Falkowski et al. (1991) coined the term *eddy pumping* to refer to the uplift of nutrient isolines by isopycnal doming during cyclogenesis. This process has been characterized at the mesoscale, where phytoplankton enhancement is associated with surface cyclones (McGillicuddy et al., 1999) and subsurface anticyclones (Fernández et al., 2005), and thus should correlate with positive vorticity. On the other hand, vertical velocity at submesoscales can be one order of magnitude greater than at mesoscales (Mahadevan, 2006). As a result, localized upwelling occurs at the edges of vortical structures (Read et al., 2002; Ladd et al., 2005) and can double PP (Lévy et al., 2001). Consequently, phytoplankton would be better correlated with vorticity gradients than with vorticity. Several other processes are likely to transport nutrients to the euphotic zone such as eddy/wind interactions (Martin and Richards, 2001; Ledwell et al., 2008), however their contribution to advective transport

remains under scientific debate.

While oceanic monopole impact on ecological distributions has been widely reported, distributions by dipole (two vortices of opposite vorticity sign) interactions are little known. Here, we investigate how vortex dipoles cause anomalies in the phytoplankton distribution. Dipoles are the simplest coherent vortical structures with linear momentum (e.g., Voropayev and Afanasyev, 1994). This property allows us to investigate in the simplest way the effect of eddy translation on ecological fields. Dipoles, which are ubiquitous in the ocean (Fedorov and Ginzburg, 1986), stir sea-surface chlorophyll patches into mushroom-like shapes (Sur et al., 1996; Stapleton et al., 2002; Lehahn et al., 2007). Moreover, ocean dipoles can generate vertical heterogeneity of resources and sustain plankton diversity Thompson et al. (2007).

The purpose of this research is to provide further insight on plankton 3D distributions associated with vortex dipoles and the mechanisms implied. Specifically, the perturbations caused by vortex translation and the distant action of potential vorticity (PV) on a ecosystem in steady state are addressed considering different dipole configurations. To this end, we couple a physical numerical model that explicitly conserves PV on isopycnals to a simple three-variable ecological model (section 3.2). Our results show that vertical advection generates a phytoplankton trail at the wake of translating cyclones (section 3.3.1). These trails are also induced by subsurface anticyclones within a shallow stationary patch of plankton (section 3.3.2). Nevertheless, in the latter case, a larger increase in phytoplankton is developed inside a filament that runs along the dipole axis as a result of horizontal stirring and vertical shear. Finally, conclusions are given in section 3.4.

3.2 Physical-ecological coupled model and implementation

3.2.1 The dynamical $\mathcal{AB}\varpi$ model

The physical model (hereinafter referred to as the $\mathcal{AB}\varpi$-model) is non-hydrostatic and simulates the volume-preserving flow of a stably stratified rotating fluid under the Boussinesq and f-plane approximations (Dritschel and Viúdez, 2003). Though the flow in our numerical simulations remains largely in hydrostatic balance, the hydrostatic condition is not numerically imposed. The lack of non-hydrostatic processes, like gravity waves, is a consequence of

the particular initial conditions set up here. Different initial conditions could give rise to the development of non-hydrostatic flow in the dipole as the well-known dipole inertia–gravity wavepacket (Viúdez, 2008b). Large scale effects due to Earth's curvature are not considered. The theoretical basis of the numerical model is explained in detail in appendix A and for completeness a brief summary is given here.

The basic equations are the linear momentum and non-hydrostatic balances, and the mass conservation equation, the non-divergence flow condition,

$$\frac{\mathrm{d}\mathbf{u}}{\mathrm{d}t} + f\mathbf{k}\times\mathbf{u} = -\alpha_0\,\boldsymbol{\nabla}p' - \alpha_0 g_0\rho'\mathbf{k}\,, \tag{3.1}$$

$$\frac{\mathrm{d}\rho}{\mathrm{d}t} + \rho\,\boldsymbol{\nabla}\cdot\mathbf{u} = 0\,, \tag{3.2}$$

$$\boldsymbol{\nabla}\cdot\mathbf{u} = 0\,, \tag{3.3}$$

where α_0 is a constant specific volume, g_0 the acceleration due to gravity, and $\mathbf{u}=(u,v,w)$ the velocity vector. Above, the material time derivative $\mathrm{d}\chi/\mathrm{d}t \equiv \partial\chi/\partial t + \mathbf{u}\cdot\boldsymbol{\nabla}\chi$ for any quantity χ, and $\boldsymbol{\nabla}$ is the 3D gradient operator. The mass density ρ is decomposed into a *b*ackground constant density $\rho_0 \equiv 1/\alpha_0$, a constant density stratification ϱ_0, and a density anomaly ρ', so that $\rho(\mathbf{x},t) \equiv \rho_0 + \varrho_0 z + \rho'(\mathbf{x},t)$. Constants $\rho_0 > 0$ and $\varrho_0 < 0$ do not need to be specified in the Boussinesq approximation. The pressure anomaly $p'(\mathbf{x})$ includes the pressure field $p(\mathbf{x})$ associated to the baroclinic flow and a term balancing the hydrostatic pressure of constant stratification, namely $p'(\mathbf{x}) \equiv p(\mathbf{x}) + g_0\,(\rho_0 + \varrho_0 z/2)\,z$. For convenience, we express ρ' in terms of isopycnal vertical displacement $\mathcal{D}$ with respect to a reference density configuration $\mathcal{D}(\mathbf{x},t) \equiv z - d(\mathbf{x},t)$. In this reference configuration isopycnals are flat and defined by $\rho_0 + \varrho_0 z$. Therefore, $d(\mathbf{x},t) \equiv (\rho(\mathbf{x},t) - \rho_0)/\varrho_0$ is the depth, or vertical location, that an isopycnal localized at $\mathbf{x}$ at time t has in the reference density configuration.

The $\mathcal{AB}\varpi$-model integrates the dimensionless ageostrophic horizontal vorticity $\mathcal{A}_h = (\mathcal{A},\mathcal{B}) \equiv \tilde{\boldsymbol{\omega}}_h - c^2\boldsymbol{\nabla}_h\mathcal{D}$, where $\tilde{\boldsymbol{\omega}}_h$ is the horizontal component of the relative vorticity $\boldsymbol{\omega} \equiv \boldsymbol{\omega}_h + \zeta\mathbf{k}$, using the equation

$$\frac{\mathrm{d}\mathcal{A}_h}{\mathrm{d}t} = -f\mathbf{k}\times\mathcal{A}_h + (1-c^2)\boldsymbol{\nabla}_h w + \tilde{\boldsymbol{\omega}}\cdot\boldsymbol{\nabla}\mathbf{u}_h + c^2\boldsymbol{\nabla}_h\mathbf{u}\cdot\boldsymbol{\nabla}\mathcal{D}\,, \tag{3.4}$$

which is derived from (3.1)–(3.3). Above the Prandtl ratio $c \equiv N/f$ is the ratio between *background* Brunt-Väisälä N and Coriolis f frequencies, and the relative vorticity $\boldsymbol{\omega} \equiv$

$\boldsymbol{\nabla} \times \mathbf{u} = (\xi, \eta, \zeta)$. To simplify the notation we denote $\tilde{\chi} \equiv \chi/f$ for any quantity χ. The additional prognostic equation is the explicit conservation of PV *anomaly* ϖ through PV contour advection on isopycnals, $\mathrm{d}\varpi/\mathrm{d}t = 0$, where the PV anomaly

$$\varpi \equiv \Pi - 1 = \frac{\boldsymbol{\omega} + f\mathbf{k}}{f} \cdot \boldsymbol{\nabla} d - 1 = (\tilde{\boldsymbol{\omega}} + \mathbf{k}) \cdot (\mathbf{k} - \boldsymbol{\nabla}\mathcal{D}) - 1 = \tilde{\zeta} - \frac{\partial \mathcal{D}}{\partial z} - \tilde{\boldsymbol{\omega}} \cdot \boldsymbol{\nabla}\mathcal{D}, \quad (3.5)$$

and $\Pi \equiv (\tilde{\boldsymbol{\omega}} + \mathbf{k}) \cdot \boldsymbol{\nabla} d$ is the *total* dimensionless PV.

This numerical model reduces the five unkowns of the basic equations to only three by introducing a 3D vector potential $\boldsymbol{\varphi} = (\varphi, \psi, \phi)$. The vector potential gives $\mathcal{D}$ and $\mathbf{u}$ through $c^2\mathcal{D} = -\boldsymbol{\nabla} \cdot \boldsymbol{\varphi}$ and $\tilde{\mathbf{u}} = -\boldsymbol{\nabla} \times \boldsymbol{\varphi}$, respectively. The horizontal components of $\boldsymbol{\varphi}$ are diagnosed every time-step by inversion of the Poisson equation $\mathcal{A}_h = \nabla^2 \boldsymbol{\varphi}_h$, while the vertical component ϕ is obtained from the inversion of the ϖ definition (**??**) as a function of (φ, ψ, ϕ). This procedure, based on the explicit conservation and inversion of PV, allows long-term simulations of large PV gradients as those happening during baroclinic instability processes. Also, owing to the fact that the non-divergent flow condition ($\boldsymbol{\nabla} \cdot \mathbf{u} = 0$) is implicitly satisfied using the vector potential $\boldsymbol{\varphi}$, this algorithm is highly accurate in obtaining the vertical velocity field. This vertical velocity, though crucial for the development of *NPZ* anomalies, is however typically three orders of magnitude smaller than the horizontal velocity in submesoscale balanced flows.

3.2.2 The ecological model

A simple nitrogen-based model is constructed with three variables, namely phytoplankton (P), zooplankton (Z), and nutrients (N), such that within one compartment all species behave identically or one species with greater ecological fitness dominates the population. We consider this simplification of the food web to describe the plankton response to a vortex dipole forcing while keeping to a minimum the number of ecological parameters.

The dynamics of $P(\mathbf{x}, t)$, $Z(\mathbf{x}, t)$, and $N(\mathbf{x}, t)$ is modeled as a balance of gain and loss rates, due to physiological processes, namely

$$\frac{\partial P}{\partial t} + \mathbf{u}\cdot\boldsymbol{\nabla} P = \underbrace{\frac{N}{K_0+N} L\, P}_{G_P} - \underbrace{R_0(1-e^{-\Lambda_0 P})Z}_{R} - \underbrace{\Xi_0 P}_{M_P}, \tag{3.6}$$

$$\frac{\partial Z}{\partial t} + \mathbf{u}\cdot\boldsymbol{\nabla} Z = \underbrace{(1-\Gamma_0)R}_{G_Z} - \underbrace{\Theta_0 Z^2}_{M_Z}, \tag{3.7}$$

$$\frac{\partial N}{\partial t} + \mathbf{u}\cdot\boldsymbol{\nabla} N = -G_P + \Gamma_0 R + M_P + M_Z. \tag{3.8}$$

The constants above are defined in Table 3.1 and correspond to an oligotrophic environment. Phytoplankton production (G_P) is nutrient and light limited. The nutrient uptake follows a Michaelis-Menten kinetics (Dugdale, 1967) determined by K_0, an indicator of the P affinity for N. Phytoplankton growth (L) has a saturating response to the available radiation (Smith, 1936; Jassby and Platt, 1976) satisfying

$$L(\mathbf{x},t) \equiv \frac{V_0\,\Psi_0\, I(\mathbf{x},t)}{\sqrt{V_0^2 + \Psi_0^2 I^2(\mathbf{x},t)}}\,, \tag{3.9}$$

where the solar radiation is attenuated by both sea water and phytoplankton self-shading according to

$$I(\mathbf{x},t) \equiv I_0 \exp\left\{ A_w z - A_p \int_z^0 P(x,y,z',t)\, dz' \right\}\,, \tag{3.10}$$

where $z \leq 0$. The effect of solar radiation is considered only in the ecological NPZ model,

symbol	description	value	units
A_w	light attenuation by sea water	0.03 (0.023)	m^{-1}
A_p	light attenuation by phytoplankton	9.5×10^{-3}	$\mathrm{m}^2\,\mathrm{mmol\,N}^{-1}$
I_0	surface available radiation	234.11	$\mathrm{W\,m}^{-2}$
Ψ_0	initial slope of the P-I curve	0.025	$\mathrm{m}^2\,\mathrm{W}^{-1}\,\mathrm{d}^{-1}$
V_0	phytoplankton maximum uptake rate	3.6	d^{-1}
K_0	half-saturation for phytoplankton uptake	0.5	$\mathrm{mmol\,N\,m}^{-3}$
Ξ_0	phytoplankton specific mortality rate	0.1	d^{-1}
R_0	zooplankton maximum grazing rate	0.8	d^{-1}
Λ_0	Ivlev constant	0.4	$\mathrm{mmol\,N}^{-1}\,\mathrm{m}^3$
Γ_0	fraction of zooplankton grazing egested	0.25	
Φ_0	zooplankton excretion/mortality rate	0.05	d^{-1}
T_1	maximum total nitrogen concentration	1 (3)	$\mathrm{mmol\,N\,m}^{-3}$
$z_{\min}$	total depth	-150 (-1000)	m

Table 3.1: List of constants. The Z *specific* excretion/mortality rate Θ_0 is computed normalizing Φ_0 by the spatially averaged Z. Values in parenthesis correspond to those used in the subsurface dipole case (section 3.3.2).

since the dynamical $\mathcal{AB}\varpi$ model is adiabatic so that changes in water density due to solar radiation are ignored. Phytoplankton is removed by zooplankton grazing $R(\mathbf{x},t)$, modeled with an Ivlev response (Parsons et al., 1967), and a linear term (M_P) that represents death, exudation, excretion or other processes. A portion $(1-\Gamma_0)$ of the P grazed is converted to Z production (G_Z), which is balanced by a density dependent death rate (M_Z). A quadratic closure term for Z has a double purpose. On the one hand, it eliminates the oscillatory behavior of the NPZ model with $\mathbf{u}=0$ that appears when a linear closure term is instead considered (Edwards and Yool, 2000). On the other hand, it introduces the effect of cannibalism (Pitchford and Brindley, 1998; Ohman et al., 2002), and predation by higher trophic levels (Ohman and Hirche, 2001). Finally, detrital matter ($\Gamma_0 R + M_P + M_Z$) is remineralized and nutrients are again available for P uptake. Therefore, the total nitrogen $N_T \equiv P+Z+N$ is materially conserved,

$$\frac{\mathrm{d}N_T}{\mathrm{d}t} = 0\,. \tag{3.11}$$

The above equation lets us to define the original NPZ equations (3.5)–(3.7) depending on only two variables, P and Z, which satisfy (3.5), (3.6), and (3.10).

The ecological model is coupled to the physical one such that the latter provides the 3D velocity field to advect the variables of the former. Additionally, diffusion processes are neglected so that PV is materially conserved.

3.2.3 Numerical parameters

We work in the quasigeostrophic (QG) space, where vertical dimension is stretched by c. Thus the numerical domain is isotropic with vertical extent $L_Z = 2\pi$ (which defines the unit of space) and horizontal extents $L_X = L_Y = cL_Z$. Triply-periodicity is also imposed but only in the dependent variable $\boldsymbol{\varphi}(\mathbf{x},t)$. For example, though $\mathcal{D}(\mathbf{x},t)$ is triply-periodic the total density field $\rho(\mathbf{x},t)$ is not. The number of grid points is $(n_X,n_Y,n_Z)=(128,128,128)$, and the number of isopycnals $n_L = 128$.

Equations (3.4), (3.5), and (3.6) are integrated forward in time using an explicit leap-frog scheme combined with a Robert-Asselin time filter to avoid the computational mode. Time-step is $\delta t = 7\times10^{-4}$ d in all the cases considered. Finally, a biharmonic hyperdiffusion operator $\mu\nabla_q^4$ for $\mathcal{A}_h$, P, and Z is added to their respective diagnostic equations in order

to dump the amplitude of grid-size scale noise due to spatial discretization on a fixed grid. Above, $\boldsymbol{\nabla}_q \equiv c\boldsymbol{\nabla}_h + \mathbf{k}\,\partial_z$ is the gradient operator in the QG space, and the hyperviscosity coefficient μ is defined by specifying the e-folding time of the largest wave number in spectral space per inertial period, which corresponds to about 0.7 d for a mean latitude of 45°. In the $\mathcal{AB}\varpi$-model $e_f = 100$, while in the NPZ model $e_f = 10$.

3.2.4 Initial conditions

The $\mathcal{AB}\varpi$-model is initialized using the so called PV initialization approach (Viúdez and Dritschel, 2003), which is unique to the PV conserving algorithm used in this numerical model. It consists in a gradual increase of PV in every fluid particle until a prescribed value is reached. This initialization technique largely avoids the generation of inertia–gravity waves due to the initial imbalance between density and velocity fields, which otherwise could contaminate the balanced vertical velocity. In the dipole cases here considered, an initialization time period of about 3.5 d is sufficient to avoid the appearance of the imbalance.

The NPZ model is initialized with steady state solutions in order to isolate the processes that control plankton dynamics when the physical system is perturbed by an oceanic dipole. Stationary stable ecological solutions $\hat{N}(z)$, $\hat{P}(z)$, and $\hat{Z}(z)$ are obtained numerically by time integration of the NPZ model (3.5)–(3.7) in the state of rest ($\mathbf{u} = 0$) with the following initial $\{N_T, P, Z\}$ profiles

$$N_T(z) = \begin{cases} T_1 \cos\left[\left(\frac{z}{z_1} - 1\right)\frac{2\pi}{5}\right], & z \in [z_1, 0], \\ 1, & z \in [z_{\min}, z_1), \end{cases} \tag{3.12}$$

$$(P, Z)(z) = \begin{cases} (P_1, Z_1) \sin\left[\left(\frac{z}{z_2} - 1\right)\frac{\pi}{2}\right], & z \in [z_2, 0], \\ 0, & z \in [z_{\min}, z_2), \end{cases} \tag{3.13}$$

where $T_1 = 1\,\mathrm{mmol\,N\,m^{-3}}$, $P_1 = 0.22\,\mathrm{mmol\,N\,m^{-3}}$, and $Z_1 = 0.1\,\mathrm{mmol\,N\,m^{-3}}$. In contrast, the values of $z_{\min}$, z_1, and z_2 differ whether a surface or a subsurface dipole is considered. Independently of the $\{z_{\min}, z_1, z_2\}$ choice, time integration of (??)-(??) converges to a steady state (Fig. 3.1). The resulting stationary profiles $\{\hat{P}, \hat{Z}, \hat{N}\}$, where $\hat{N}$ is recovered by inversion of (3.10), are used to initialize the ecological model in the $\mathcal{AB}\varpi$-NPZ coupled cases.

Both models are coupled once the PV field is fully initialized at $t = t_i$ since, in the

PV initialization approach, PV is not materially conserved during the initialization period ($t < t_i$). Note that at initial time, $t_0 = 0$, isopycnals are flat and therefore $d(\mathbf{x}, t_0) = z$ since $\mathcal{D}(\mathbf{x}, t_0) = 0$. However, at the end of the initialization period doming of isopycnals implies $\mathcal{D}(\mathbf{x}, t_i) \neq 0$. As a result, two different ecological initial conditions can be further distinguished depending on whether N_T is considered homogenous on isopycnals (constant d) or on horizontal layers (constant z). In this work, we have considered the former initialization when $z_P \cong -61\,\mathrm{m}$ (section 3.3.1) and the latter when $z_P \cong -90\,\mathrm{m}$ (section 3.3.2).

3.3 Numerical simulations

The effects of both vortex translation and the distant PV action on ecological dynamics are investigated considering two oligotrophic scenarios typical of the open ocean. We first focus on how a surface dipole perturbs a stationary ecosystem at the submesoscale (section 3.3.1), where high-resolution remote sensing observations have recently unveiled many vortical structures (Munk et al., 2000). In this case phytoplankton subsurface maximum $\hat{P}_{\max} \equiv \hat{P}(z_P)$ is initially placed underneath the dipole, so that $z_P \simeq -61\,\mathrm{m}$ (Fig. 3.1a), by choosing $(z_1, z_2, k_w) = (-120\,\mathrm{m}, -150\,\mathrm{m}, 0.03\,\mathrm{m}^{-1})$. Secondly, the distant influence of a subsurface dipole on a plankton 3D patch is investigated at the mesoscale (section 3.3.2), the scale at which subsurface long-lived vortices, such as meddies, are widespread in the ocean (Richardson et al., 2000). Since the shallowest dipole edge is at $z \cong -200\,\mathrm{m}$, we have deepened $\hat{P}_{\max}$ to $z_P \simeq -90\,\mathrm{m}$ (Fig. 3.1b) by setting $(z_1, z_2, k_w) = (-290\,\mathrm{m}, -187\,\mathrm{m}, 0.023\,\mathrm{m}^{-1})$.

3.3.1 Submesoscale surface dipole

The submesoscale is here introduced as $c = 50$, and only half of the vertical domain L_Z is considered with $z_{\min} = -150\,\mathrm{m}$. Thus the horizontal domain is 15 km. The vortex dipole consists of a baroclinic cyclone (+) and anticyclone (−) with PV anomalies $\varpi^{\pm}_{\max} = 0.5$ ($\cong 0.35\,\mathrm{d}^{-1}$). The maximum length of the horizontal semi-axes of the ellipsoids of constant PV in both vortices are $a_X \cong 1.9\,\mathrm{km}$ and $a_Y \cong 2.9\,\mathrm{km}$. The length of the vertical semi-axes $a^{\pm}_Z$ are different in the initial configuration with flat isopycnals, being $a^{+}_Z \cong 62\,\mathrm{m}$ and $a^{-}_Z \cong 52.5\,\mathrm{m}$. However, during the initialization time the isopycnals stretch (shrink) in the anticyclone (cyclone), so that at $t_i \cong 3.5\,\mathrm{d}$ the vortices have similar vertical extent and the dipole describes a straight trajectory along the x-axis (Dubosq and Viúdez, 2007). At

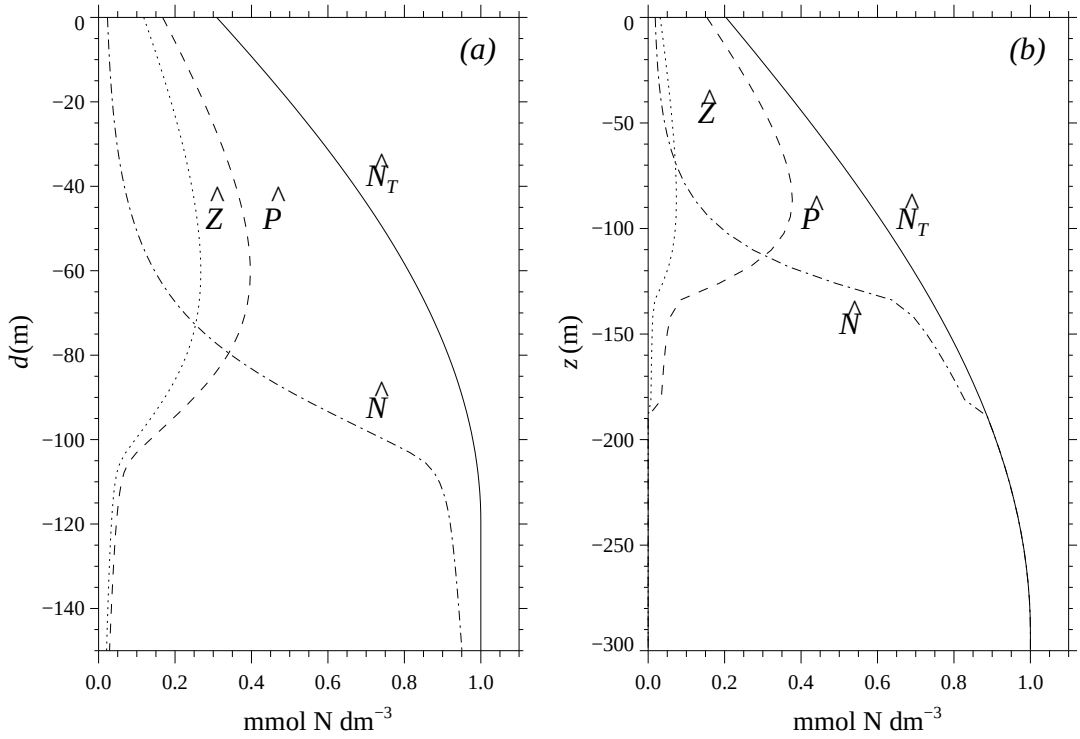

Figure 3.1: Vertical profiles of total nitrogen $N_T(z)$, and its associated stationary and stable profiles of $\{P, Z, N\}$ obtained with the parameters given in Table 3.1 and without physical forcing. In the surface dipole case the profiles corresponding to (a) are initialized homogeneous on isopycnals (d), while in the subsurface dipole scenario those of (b) are homogeneous on horizontal levels (z).

the end of the initialization time $t = t_i$, the horizontal speed contours correspond to those of concentric deformed double tori intersecting an horizontal plane with a maximum speed $|\mathbf{u}|_{\max} = 4.76\,\mathrm{cm\,s^{-1}}$ along the dipole axis (Figs. 3.2a,b). We note that submesoscale dipoles, as long as they remain isolated and do not interact with other submesoscale vortices, have a quadrupolar pattern of w (Fig. 3.2c) similar to mesoscale dipoles (Pallàs-Sanz and Viúdez, 2007). The w maximum absolute value $|w|_{\max} = 71.23\,\mathrm{cm\,d^{-1}}$ is placed at $z = -35\,\mathrm{m}$ ($i_Z = 50$, Fig. 3.2d). As the dipole moves forward, the isopycnals are displaced upwards (downwards) at the front (rear) of the cyclone. The opposite changes occur in the anticyclone. The dipole flow remains always statically and inertially stable since the Rossby number $\mathcal{R} \equiv \omega_h/\mathcal{N}$, where the squared *total* Brunt-Väisälä frequency $\mathcal{N}^2(\mathbf{x}, t) \equiv -g\alpha_0\partial\rho/\partial z = N^2[1-\partial\mathcal{D}/\partial z(\mathbf{x}, t)]$, minimum is $\mathcal{R}_{\min} = -0.43$, and the Froude number $\mathcal{F} \equiv \zeta/f$ maximum $\mathcal{F}_{\max} = 0.19$.

The NPZ model is coupled to the above described dynamical conditions at $t = t_i$. In this case, total nitrogen is set homogeneous on isopycnal levels by projecting the initial profiles

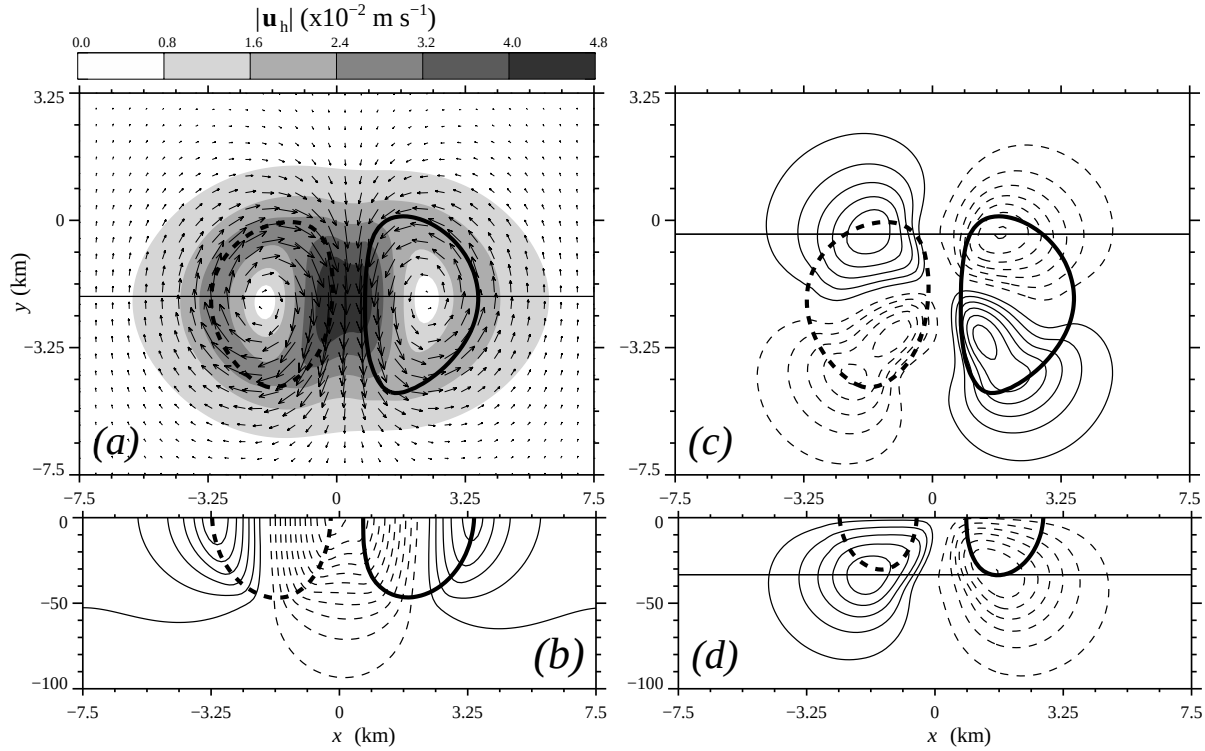

Figure 3.2: (a) Horizontal distribution of $|\mathbf{u}_h|$ at $z = 0$ ($i_Z = 65$). Only every other vector is plotted. A straight solid line is drawn where the vertical distribution of v is shown in (b) at $y \cong -2.6\,\mathrm{km}$ ($i_Y = 43$, $v \in [-4.76, 2.76]\,\mathrm{cm\,s^{-1}}$, contour interval $\delta v \simeq 0.4\,\mathrm{cm\,s^{-1}}$). Horizontal (c) and vertical (d) distributions of w (contour line range is $|w| < 71.23\,\mathrm{cm\,d^{-1}}$ with $\delta w \simeq 1\,\mathrm{cm\,d^{-1}}$) at $z \cong -33\,\mathrm{m}$ ($i_Z = 50$) and at $y \cong -0.82\,\mathrm{km}$ ($i_Y = 58$), respectively. Distributions correspond to the initial time $t_i \cong 3.5\mathrm{d}$. PV contours $\varpi = \pm 0.2$ ($\cong 0.28\,\mathrm{d^{-1}}$) are included for reference. Hereinafter, solid and dashed contours are used for positive values and negative values, respectively. We observe that the dipole translates southwards as a solid body since $\mathbf{u}_h$ has a surface maximum along the dipole axis. In contrast, extreme w bounds are reached at the subsurface.

(Fig. 3.1a) on isopycnals as

$$N_T(\mathbf{x}, t) = \hat{N}_T(d(\mathbf{x}, t))\,. \tag{3.14}$$

Note that this function does not depend explicitly on t because $\hat{N}_T$ is materially conserved. In accordance to this N_T initialization, $\{P, Z, N\}$ variables are also set constant on isopycnals at $t = t_i$ satisfying

$$P(\mathbf{x}, t_i) = \hat{P}(d(\mathbf{x}, t_i))\,, \tag{3.15}$$

with similar relations for $Z(\mathbf{x}, t_i)$ and $N(\mathbf{x}, t_i)$. Thus the initial distributions of these variables depend on their vertical gradient and the isopycnal vertical displacement $\mathcal{D}$. For instance, P shows a quadrupolar pattern at $t = t_i$ (Fig.3.3a) because P_i has a subsurface maximum at $z_P \cong -61\,\mathrm{m}$, and thus a dipolar pattern is observed within each vortex. This also explains

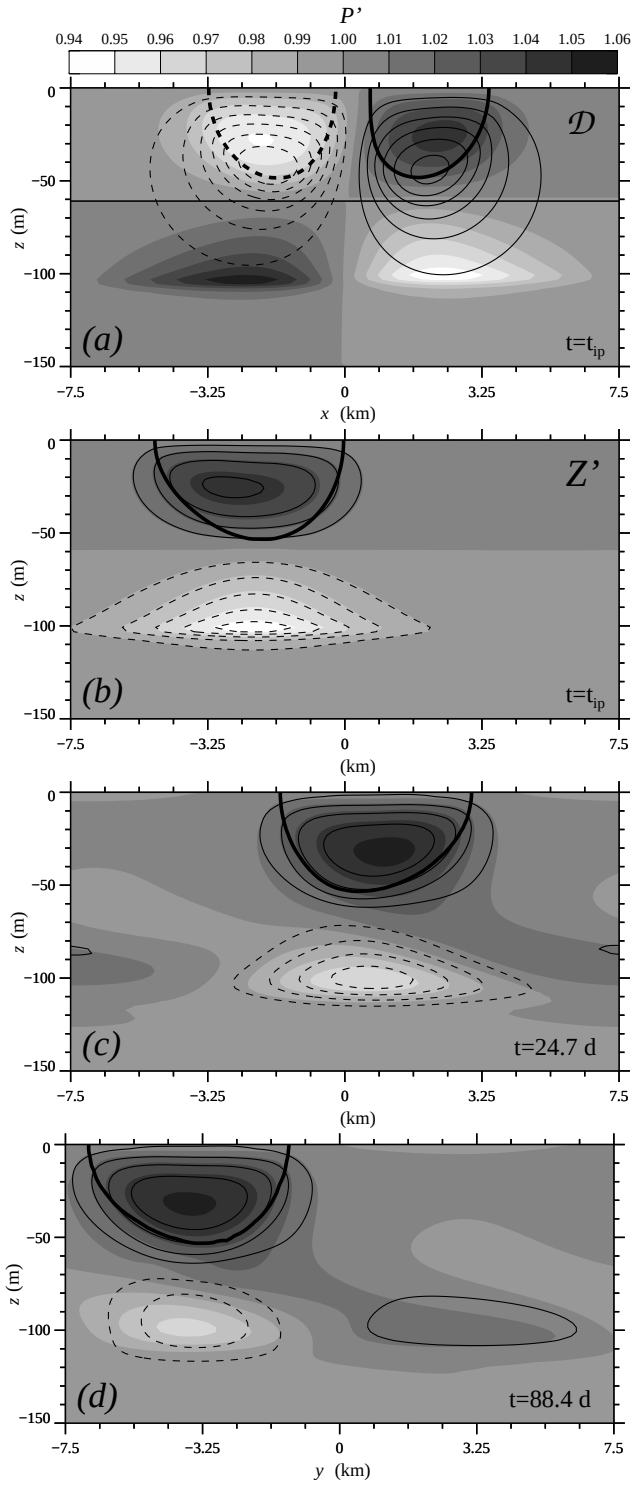

Figure 3.3: (a) Vertical section crossing the vortex centers, at $y \cong -2.6$km, ($i_Y = 43$), of $P'(x,z)$ in grey scale and $\mathcal{D}$ ($|\mathcal{D}| < 4.3\,$m, contour interval $\delta\mathcal{D} \simeq 0.6\,$m) after PV initialization at $t = t_i$. (b, c, d) Vertical sections parallel to the dipole axis of $P'(y,z)$ and $Z'(y,z)$ in contour lines ($|Z'| < 1.06, \delta Z' = 1\%$) at different times and (b) $x \cong 2.1\,$km ($i_X = 83$), (c) $x \cong 2.3\,$km ($i_X = 85$), and (d) $x \cong 3.5\,$km ($i_X = 95$). Phytoplankton subsurface maximum z_P (straight line in (a)) and contours of $\varpi = \pm 0.2$ are indicated for reference. Note that P' increases about 2% at the cyclone wake.

the quadrupolar initial distribution of Z, though of different magnitude (not shown). In contrast, N has a dipolar pattern (not shown) since N_i increases gradually with depth. The initial fields of P, and Z are advected with the 3D velocity at times $t > t_i$, while N is obtained using (3.5), (3.6), and (3.10). In order to quantify the dipole impact on the ecosystem, ecological properties are adimensionalized such that they are normalized by a value outside the dipole where isopycnals are flat, that is, by the stationary solution at the isopycnal depth in the reference density configuration (d). So that, any ecological variable χ_v is characterized through the following enhancement factor,

$$\chi_v'(\mathbf{x},t) \equiv \frac{\chi_v(\mathbf{x},t)}{\hat{\chi}_v(d(\mathbf{x},t))}\,, \tag{3.16}$$

while any ecological rate χ_r is refered to the steady state P production (G_P) as

$$\chi_r'(\mathbf{x},t) \equiv \frac{\chi_r(\mathbf{x},t)}{\hat{D}_P(d(\mathbf{x},t))}\,. \tag{3.17}$$

The P' maximum is located at the center of the cyclone, where isopycnal displacement is the largest, and moves with the translating dipole (Figs. 3.3b–d). It represents about a 6% increase referred to its steady state $\hat{P}(d)$. Zooplankton enhancement Z' is of the same order as P' and its distribution is positively correlated with that of P'. Based on the biological forcing balance (Eq. 3.5), we found that zooplankton grazing is much smaller than the other terms. In light of that, we shall focus on the phytoplankton response only. Two different phytoplankton dynamics are observed depending on a critical depth $z_c \simeq -80.8\,\mathrm{m}$, which corresponds to the maximum depth of the dipole. Above z_c, the physical forcing dominates over the ecological forcing and P behaves mainly as a passive tracer. In contrast, below z_c vertical advection triggers an ecological response of similar magnitude to physical terms and a P' trail develops at the dipole wake.

Above z_c, the dipole separatrix, which is defined by the minimum ϖ isosurface, acts as a dynamical barrier. On the one hand, the horizontal advection of P is greater than its vertical advection (Fig.3.4a). On the other hand, vertical uplift of P to lighter levels triggers a P increase, however it is much smaller than the horizontal advection (not shown). Thus P is translated at the dipole phase speed. Furthermore, P correlates with $\mathcal{D}$ (Fig.3.4b), and ultimately with ϖ through (**??**). This fact suggests that stationary stable ecological solutions are reached within vortices, which are close to their initial conditions at t_i when

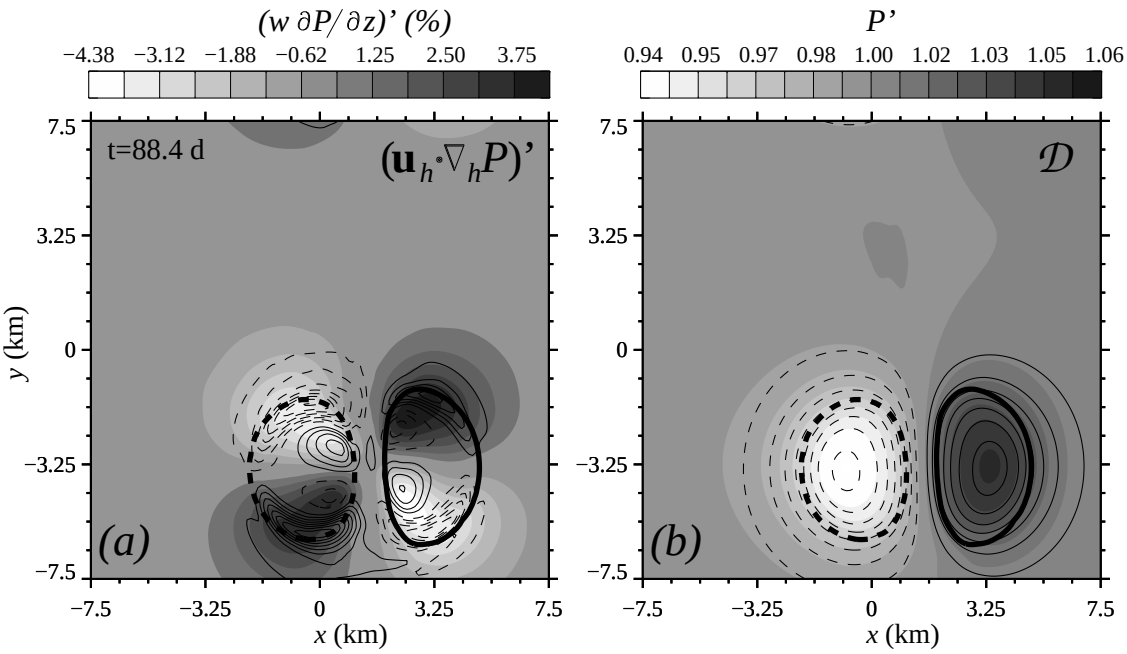

Figure 3.4: Horizontal section at $z \simeq -34.6\,\mathrm{m}$ ($i_Z = 50$) of (a) $(w\,\partial P/\partial z)'$ in grey scale and $(\mathbf{u}_h \cdot \nabla_h P)'$ in contour lines ($|\Delta| < 0.054$, $\delta = 6.25 \times 10^{-3}$), and (b) P' in grey scale and $\mathcal{D}$ in contour lines ($\mathcal{D} \in (-4.15, 3.75)\,\mathrm{m}$, $\delta\mathcal{D} = 0.5\,\mathrm{m}$). PV contours $\varpi^{\pm} = \pm 0.2$ at $z = 0$ (thickest line) are included for reference. After $\delta t = 88\,\mathrm{d}$, P' correlates with $\mathcal{D}$ within vortices as in the initial configuration at time t_i.

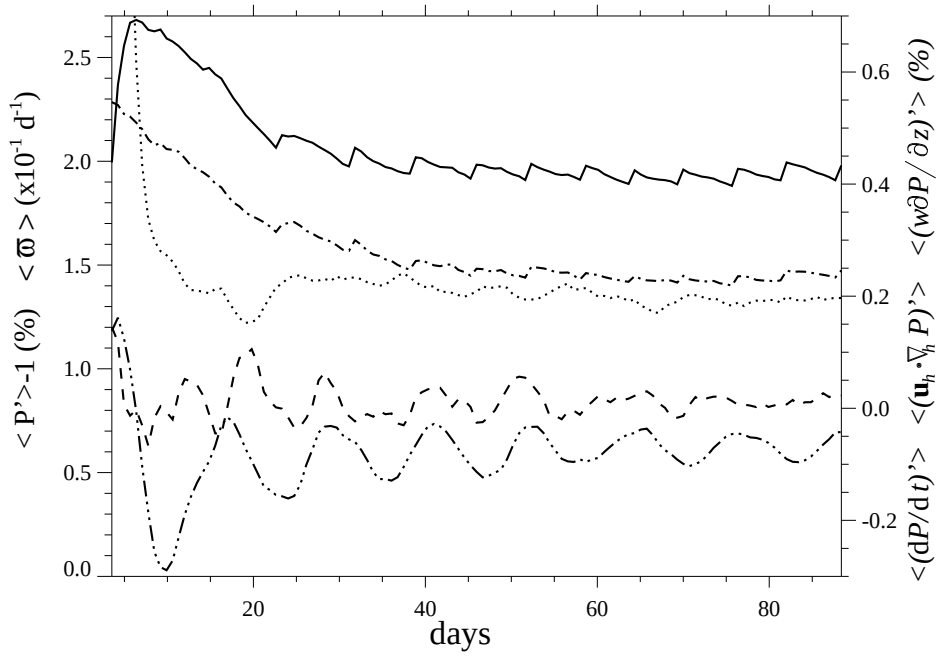

Figure 3.5: Time evolution of $\langle P' \rangle$ (solid line), $\langle \varpi \rangle$ (dash dotted line), $\langle (\mathrm{d}P/\mathrm{d}t)' \rangle$ (dotted line), $\langle (\mathbf{u}_h \cdot \boldsymbol{\nabla}_h P)' \rangle$ (dash triple dotted line) and $\langle (w\,\partial P/\partial z)' \rangle$ (dashed line), averaged over the cyclone volume. After an initial adjustment, $\langle P' \rangle$ reaches a steady state close to the initial configuration.

N_T is initialized homogeneous on isopycnals and so ecological variables.

In order to unveil this steady state, any property χ is integrated on the cyclone volume as

$$\langle\chi\rangle(t) = \frac{1}{n}\int_{\Omega} \chi(\mathbf{x},t)\,\mathrm{d}\mathcal{V}, \tag{3.18}$$

where the spatial domain Ω comprises those grid points n with $\varpi > 0$. As expected, after an initial adjustment of about $\delta t \cong 20\,\mathrm{d}$, $\langle P'\rangle$ remains nearly constant oscillating around a time averaged value of 1.9% (Fig. 3.5). The oscillation in $\langle P'\rangle$ has a period $T \simeq 5.6\,\mathrm{d}$ different from that of advective terms. Actually, $\langle P'\rangle$ is in phase with $\langle\varpi\rangle$, which oscillates due to vortex Rossby waves (VRWs) (Rodríguez-Marroyo and Viúdez, 2009). VRWs cause a periodic azimuthal oscillation of the dipole geometry, relative to its time averaged configuration, with a period of 8 inertial periods, so that close to T for a midlatitude, and thus also alter P distributions.

A distinct plankton dynamics occurs below the dipole at $z < z_c$. In this case, P' increases at the cyclone wake as a combination of physical and biological processes, which have similar magnitude. Firstly, $(w\partial P/\partial z)'$ is negatively correlated with $P'-1$ at the dipole rear ($t = 7\,\mathrm{d}$, Fig. 3.6a). This suggests that P' increases (decreases) due to subduction of shallower depths richer (poorer) in P' at the anticyclone (cyclone) wake. As dipole translates, the fluid parcels that experience these P' changes decelerate relative to vortices and reach a state of rest at later times. However, P' does not inmediately converge to its stationary initial condition ($P' = 1$) since the ecosystem responds with some inertia to a perturbation. As a result, changes in P' retain some memory of their causing mechanism and thus P' correlates in this case with the time integrated vertical advection $\int(w\,\partial P/\partial z)'\,\mathrm{d}t$ (Fig. 3.6b, $t = 10.6\,\mathrm{d}$). Later on, after $\delta t \cong 15.5\,\mathrm{d}$ of the increase in P', biological forcing $(\mathrm{d}P/\mathrm{d}t)'$ reaches the order of magnitude of $(w\partial P/\partial z)'$ (Fig. 3.6c). Since ecological and advective terms are opposite, we conclude that P' is induced at the dipole wake due to a balance both and thus it becomes correlated with the time integrated local rate $\int(\partial P/\partial t)'\,\mathrm{d}t$ (Fig. 3.6d, $t = 24.7\,\mathrm{d}$). The long term evolution of this P' trail is quantified by volume integration of properties using (3.11). In this case, the spatial domain Ω is enclosed within isosurface $P' = 1.002$ at the dipole wake. We observe that $\langle P'\rangle$ reaches a nearly stationary stable state after an initial adjustment of $\delta t \cong 35\,\mathrm{d}$, however $\langle(\mathrm{d}P/\mathrm{d}t)'\rangle \equiv \langle(\partial P/\partial t)'\rangle + \langle(\mathbf{u}\cdot\boldsymbol{\nabla}P)'\rangle + \langle(w\partial P/\partial z)'\rangle \neq 0$ (Fig. 3.7).

In order to unveil what we are missing in the abovementioned balance, we take a Lagrangian approach. To this end, particles that experience a smaller P' increase than that

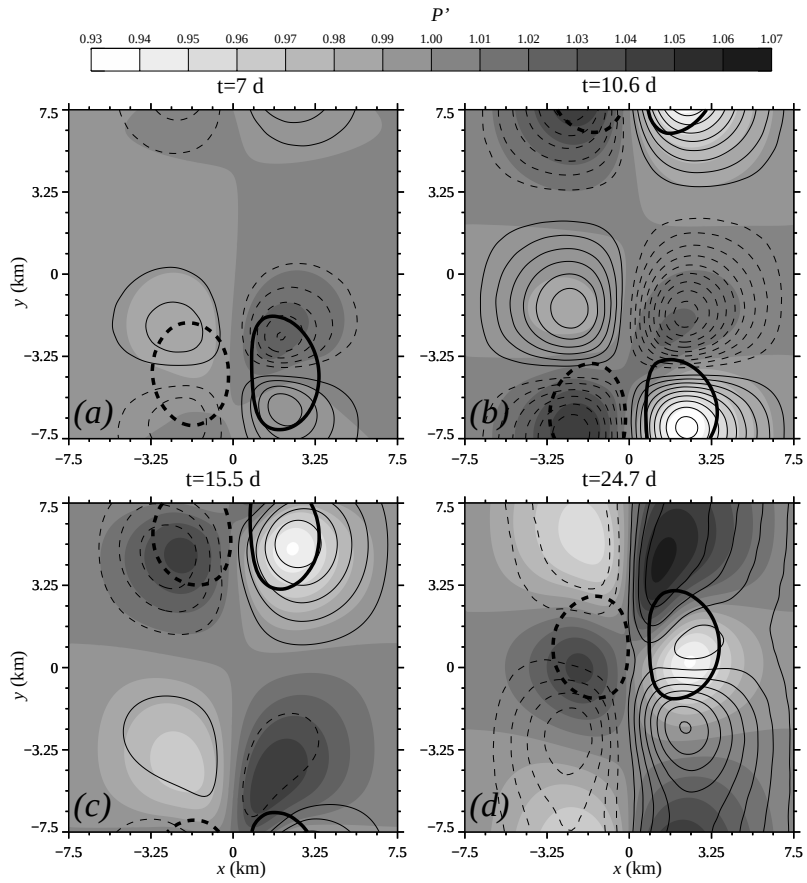

Figure 3.6: Horizontal sections of P' in grey-scale and contour lines of (a) $(w\,\partial P/\partial z)'$ with maximum absolute value $|\Delta|_{\max} \cong 0.016$ and contour interval $\delta \cong 3 \times 10^{-3}$, (b) $\int (w\,\partial P/\partial z)'\,\mathrm{d}t$ with $|\Delta|_{\max} \cong 0.24$ and $\delta = 0.025$, (c) $(\mathrm{d}P/\mathrm{d}t)'$ with $|\Delta|_{\max} = 0.019$ and $\delta \cong 3 \times 10^{-3}$, and (d) $\int (\partial P/\partial t)'\,\mathrm{d}t$ with $|\Delta|_{\max} = 0.32$ and $\delta \cong 0.04$. Section layers are $z \simeq -71.5\,\mathrm{m}$ ($i_Z = 34$) in (a) and $z \simeq -85.4\,\mathrm{m}$ ($i_Z = 28$) in (b–d). Finally, PV contours $\varpi = 0.2$ are included for reference. Note that the P' increase results from a balance between vertical advection and biological forcing.

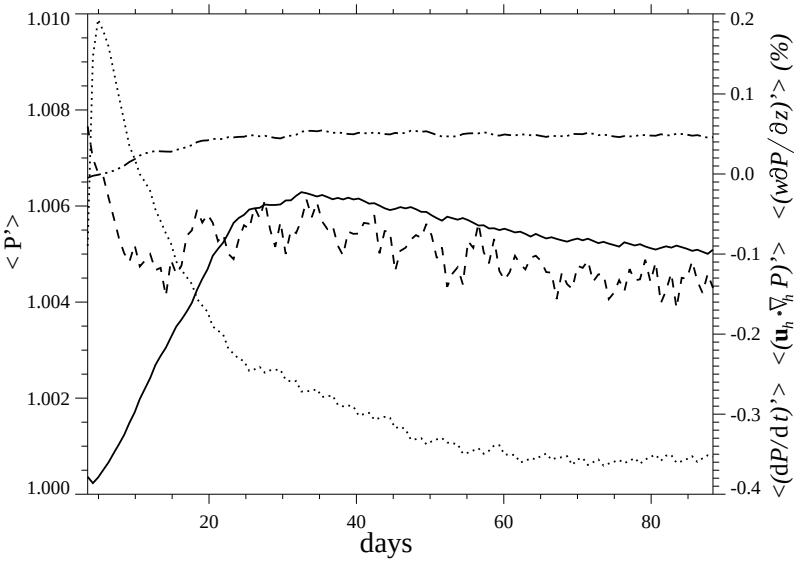

Figure 3.7: Time evolution of $\langle P' \rangle$ (solid line), $\langle (\mathrm{d}P/\mathrm{d}t)' \rangle$ (dotted line), $\langle (w\,\partial P/\partial z)' \rangle$ (dashed line), and $\langle (\mathbf{u}_h \cdot \boldsymbol{\nabla}_h P)' \rangle$ (dash dotted line) averaged within isosurface $P' = 1.002$ below the deepest PV edge of the dipole. Note that $\langle P' \rangle$ reaches a nearly steady state, though ecological terms do not balance out.

observed within the dipole, that is, $1 < P' < 1.02$, are identified. This particle set is initially placed at the cyclone front and circulates anticlockwise to its rear, happening to locate at the P' trail developed as dipole translates (Fig. 3.8). Thus we focus on whether the ecological changes experienced by this particle set may explain why P' increases at the cyclone wake. At this point, we distinguish a subset of *black* particles ($\mathcal{B}$) from another of *white* particles ($\mathcal{W}$). This separation is done to improve clarity since the latter subset reaches a state close to rest after the physical perturbation. Next a given ecological property χ is averaged on the number m of fluid particles X belonging to each subset as

$$\overline{\chi}(t) = \frac{1}{m} \sum_{j=1}^{m} \chi(X_j, t)\,. \tag{3.19}$$

In both particle subsets, the P' increase is preceded by an uplift of particles to lighter levels, $(w\partial P/\partial z)' > 0$, as they move from the dipole front to its rear (Fig. 3.9). The P responds to this perturbation with a time lag of about $\delta t \cong 1.4\,\mathrm{d}$, which implies a spatial decorrelation between the P' increase and its causing mechanism. This explains the near stationary behaviour of the P' trail at the cyclone wake, though advective and ecological terms do not exactly balance out when averaged within this trail (Fig. 3.7). Finally, particles reach a state of rest evolving to their stationary stable ecological initial condition. This is made evident in $\mathcal{W}$-particles, since $\mathcal{B}$-particles are continuosly perturbed by the dipole.

To conclude, the dipole separatrix, which is defined by the outermost ϖ isosurface, divides two different ecological dynamics. Within vortices P reaches a near steady state close to the initial ecological configuration. Note that this steadiness is feasible since the ecosystem is fully recycling, that is, $\mathrm{d}N_T/\mathrm{d}t = 0$. Outside the dipole, a trail of P develops at the cyclone wake. As particles circulate anticlockwise from the cyclone front to its rear, they are uplifted to lighter levels and inmediately subducted to their isopycnal depth in the reference density configuration where isopycnals are flat. However, the P responds to this vertical advection with some time lag and P increases at the dipole wake. This P increase translates slower than the dipole phase speed, and as a result a P trail is developed. The extension of this trail is nearly constant and mainly determined by $\mathrm{d}P/\mathrm{d}t$. Considering $\mathrm{d}P/\mathrm{d}t = -2.2\,\mathrm{mmol\,N\,m^{-3}\,d^{-1}}$ and a dipole horizontal speed $U_d \cong 0.64\,\mathrm{cm\,s^{-1}}$, a wake length $L_w = 6.4\,\mathrm{km}$ is predicted for $P' = 2 \times 10^{-3}\,\mathrm{mmol\,N\,m^{-3}}$ ($P' = 1.02$) isosurface, that is, of the same order of magnitude than the observed $L_w = 4.8\,\mathrm{km}$. In contrast, P is impoverished

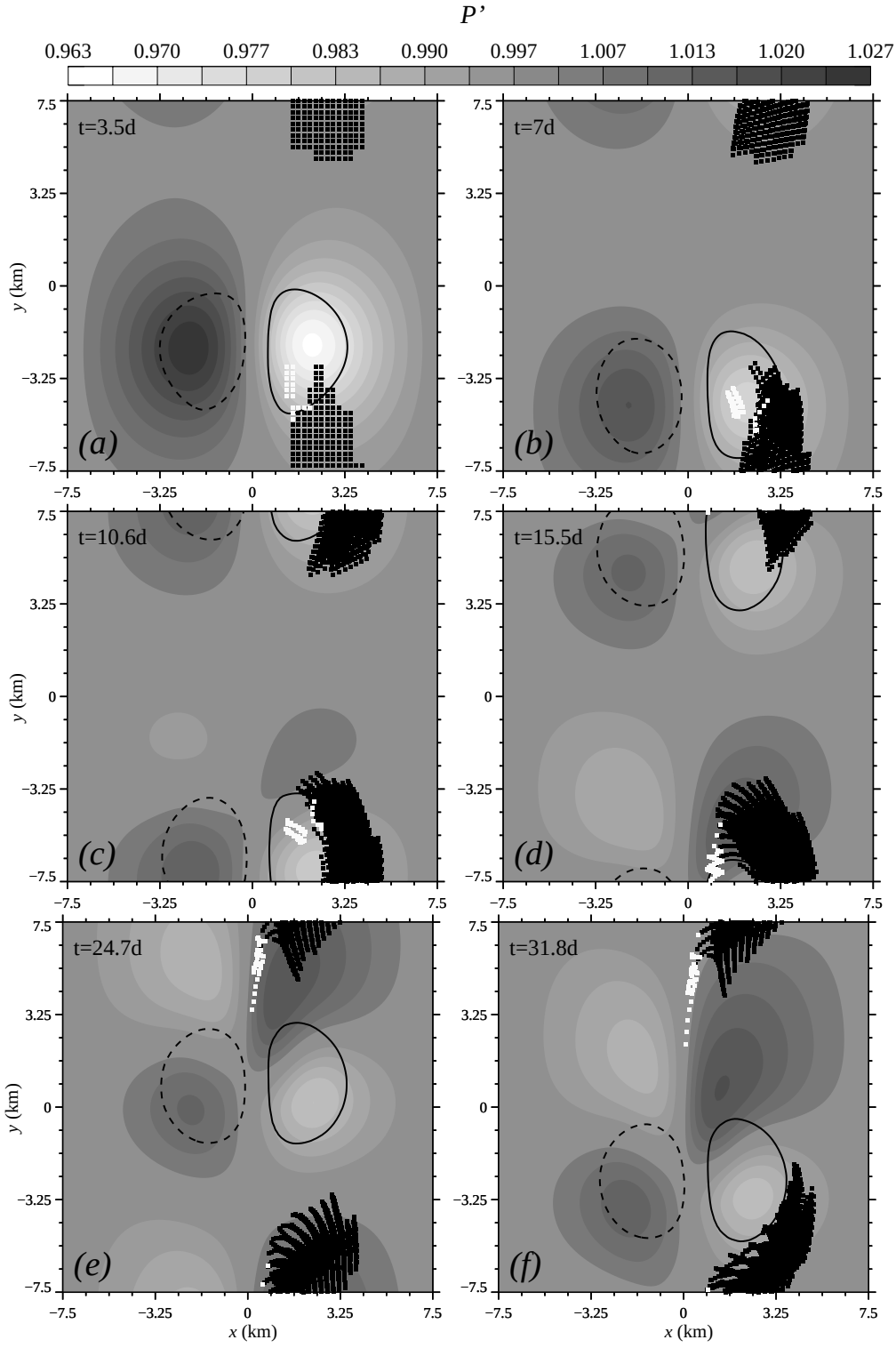

Figure 3.8: Temporal evolution of the location of fluid particles that experience an increase in P' similar to that of the P' trail, that is, $1 < P' < 1.02$, in different times. Black ($\mathcal{B}$) and white ($\mathcal{W}$) subsets of particles are denoted with the corresponding colour. Additionally, the distribution of P' at $z \simeq -65\,\mathrm{m}$, ($i_Z = 28$) is shown in shaded contours. PV contours $\varpi = 0.2$ are included for reference. Note that the particles selected are placed at the cyclone wake when the P' trail develops.

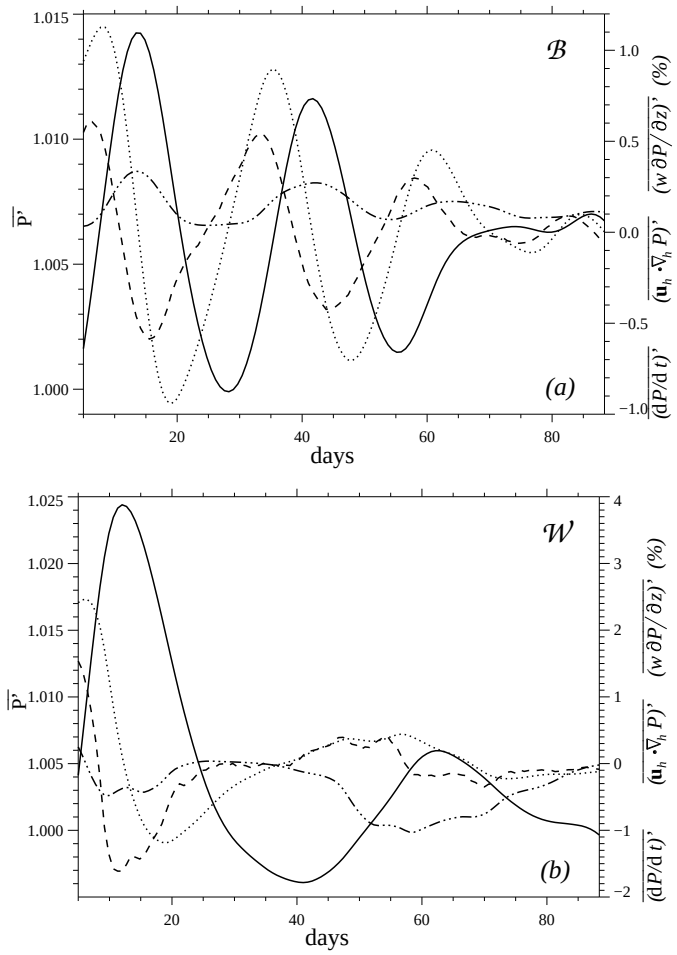

Figure 3.9: Time evolution of $\overline{P'}(t)$ (solid line), $\overline{(\mathrm{d}P/\mathrm{d}t)'}(t)$ (dotted line), $\overline{(\mathbf{u}_h\cdot\boldsymbol{\nabla}_h P)'}(t)$ (dash triple dotted line), and $\overline{(w\,\partial P/\partial z)'}(t)$ (dashed line). The locations of particles X_j that belong to black $\mathcal{B}$ (a) and white $\mathcal{W}$ (b) subsets are shown in Fig. 3.8. Combining both figures, note that the P' increase and its generation mechanism, that is, vertical advection, are spatially uncoupled.

at the anticyclone wake since particles are first subducted and uplifted afterwards by the anticyclone passage. In contrast, P increases at its fronts because fluid particles rich in P are subducted (Fig.3.6a). However, in this case P behaves as a passive tracer.

3.3.2 Mesoscale subsurface dipole

In this section, the influence of a mesoscale subsurface dipole on a stationary plankton patch, initially horizontally homogeneous and vertically heterogeneous, is investigated. To this end, the mesoscale is introduced with a Prandtl ratio $c = 100$ and the entire vertical extent $L_Z = 2\pi$ is dimensionalized considering $z_{\min} = -1000\,\mathrm{m}$, thus $L_X = L_Y = 100\,\mathrm{km}$.

Vortices are centered at $z = -500\,\mathrm{m}$ with horizontal semi-axes $a_X^{\pm} \cong 12.7\,\mathrm{km}$ and $a_Y^{\pm} \cong 15.9\,\mathrm{km}$. The cyclone has $\varpi^+ = 1$ ($\cong 1.4\,\mathrm{d}^{-1}$) and vertical semi-axis $a_Z^+ = 0.95$ ($\cong 223\,\mathrm{m}$), while the anticyclone counterpart has $\varpi^- = -0.95$ ($\cong -1.34\,\mathrm{d}^{-1}$) and $a_Z^- \cong 175\,\mathrm{m}$. As a result, the dipole translates southwards with speed $U_d \cong 0.73\,\mathrm{cm\,s}^{-1}$. Horizontal speed at the location where P is maximum $z_P = -86\,\mathrm{m}$ is two orders of magnitude smaller than in the previous section (Fig. 3.10a), due to the fact that z_P is 197 m distant from the top edge of the dipole (Fig. 3.10b). However, vertical velocity is only reduced by one order of magnitude in the upper layer. In contrast to the former case, w has the opposite sign since the upper half

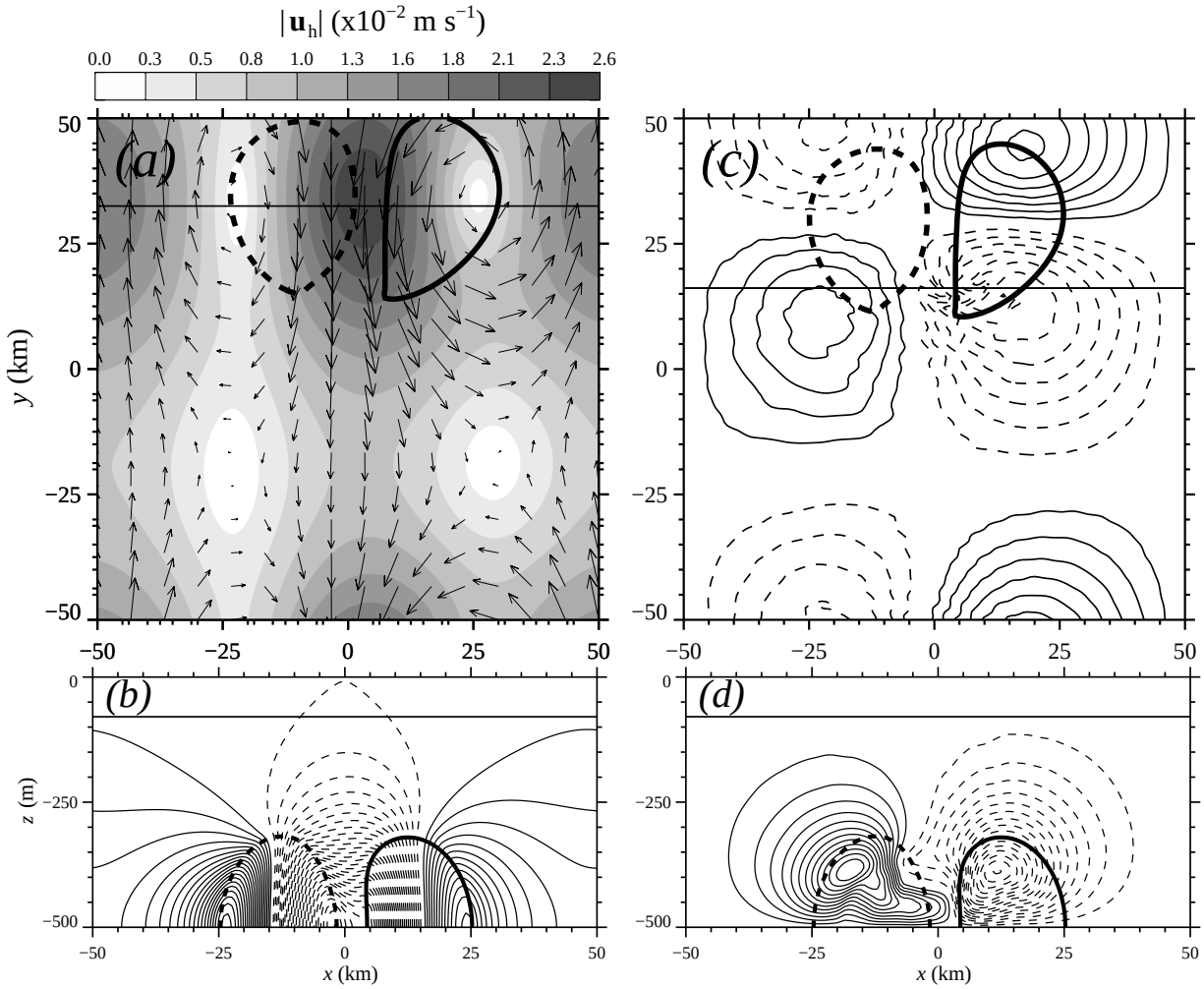

Figure 3.10: (a) Horizontal velocity $\mathbf{u}_h$ and its magnitude in shaded contours at $P_{\max}$ depth z_P. Only every four vectors is plotted. Straight thin line indicates the position $y \simeq 77.3\,\mathrm{km}$ ($i_Y = 99$) of the vertical section of v ($v \in (-6, 4) \times 10^{-2}\,\mathrm{m\,s}^{-1}, \delta v \cong 0.02\,\mathrm{m\,s}^{-1}$) shown below (b). (c)-(d) Distributions of w ($|w| < 8\,\mathrm{m\,d}^{-1}, \delta w = 0.05\,\mathrm{m\,d}^{-1}$) at z_P ($i_Z = 117$) in (c), and at $y \simeq 65.62\,\mathrm{km}$ ($i_Y = 84$) in (d). Time is $t = t_i$. PV contours $\varpi = \pm 0.2$ are shown for reference. As in the previous case, the dipole translates southwards but the w quadrupolar pattern is opposite. This is so because upper isopycnals are uplifted within the anticyclone while downlifted in the cyclone, in contrast to the surface dipole scenario.

of the cyclone (anticyclone) induces a downlift (uplift) of isopycnals (Figs. 3.10c,d). Though PV anomalies ϖ are large, the flow remains always statically and inertially stable.

The ecological model is coupled at $t = t_i$ with a patch of N_T that extends from $y_1 \cong 4.7\,\mathrm{km}$ to $y_2 = 50\,\mathrm{km}$. Inside this patch, N_T is homogeneous on horizontal levels but vertically heteregeneous according to (**??**), where $z_2 = -290\,\mathrm{m}$, that is

$$N_T(\mathbf{x}, t_i) = \hat{N}_T(z). \tag{3.20}$$

The initial distributions of $\{N, P, Z\}$ correspond to the stationary conditions associated to (**??**) with $z_1 = -187\,\mathrm{m}$, which are obtained as described in section 3.2.4 (Fig. 3.1b). These distributions depend on the availability of N_T, which is restricted to the patch domain in contrast to the other case. Thus we first analyze the straining of the N_T patch by the subsurface dipole in order to address afterwards to the ecological dynamics within it. The deformation of N_T is mainly determined by horizontal advection. Thus we can characterize the N_T transport by defining two vertical layers divided by the shallowest location of the dipole separatrix z_S as it acts as an impermeable barrier. On the one hand, in layer $L_U = (z_S, 0]$ the N_T patch is stirred such that a filament penetrates southwards along the dipole axis (Fig.3.11a), where $|\mathbf{u}|_h$ is maximum. On the other hand, in layer $L_B = [-500\,\mathrm{m}, z_S]$ N_T is entrained inside the dipole and translated at its constant phase speed U_d (Fig.3.11b). That is, described in the dipole frame of reference, the N_T front at z_S is at rest (Fig. 3.12a). Above z_S, the N_T edge is retarded relative to the dipole at a speed that decreases exponentially with depth, while below this edge gradually adquires the separatrix curvature. In order to characterize the dynamics of this frontal edge, initially located at y_1, we use the QG approximation.

In the linear QG approximation the geostrophic velocity v^g along the dipole axis is computed as the sum $v^g = 2v_e^g$ of the velocity generated by each vortex $\tilde{v}_e^g(r, z)$, where $\tilde{v}_e^g(r, z)$ is the exterior azimuthal solution obtained by Thorpe and Bishop (1994, see also Holton, 2004, p. 162), namely

$$\tilde{v}_e^g(r, z) \equiv \frac{v_e^g(r, z)}{f} = \frac{\varpi_0}{3} R_0^3 \frac{r}{R^3(r, z)}\,, \tag{3.21}$$

where ϖ_0 is the constant PV density of a spheric vortex (in the QG space) of radius R_0, r is the horizontal distance of the N_T edge to the vortex center, and $R^2(r, z) \equiv r^2 + z^2 > R_0^2$.

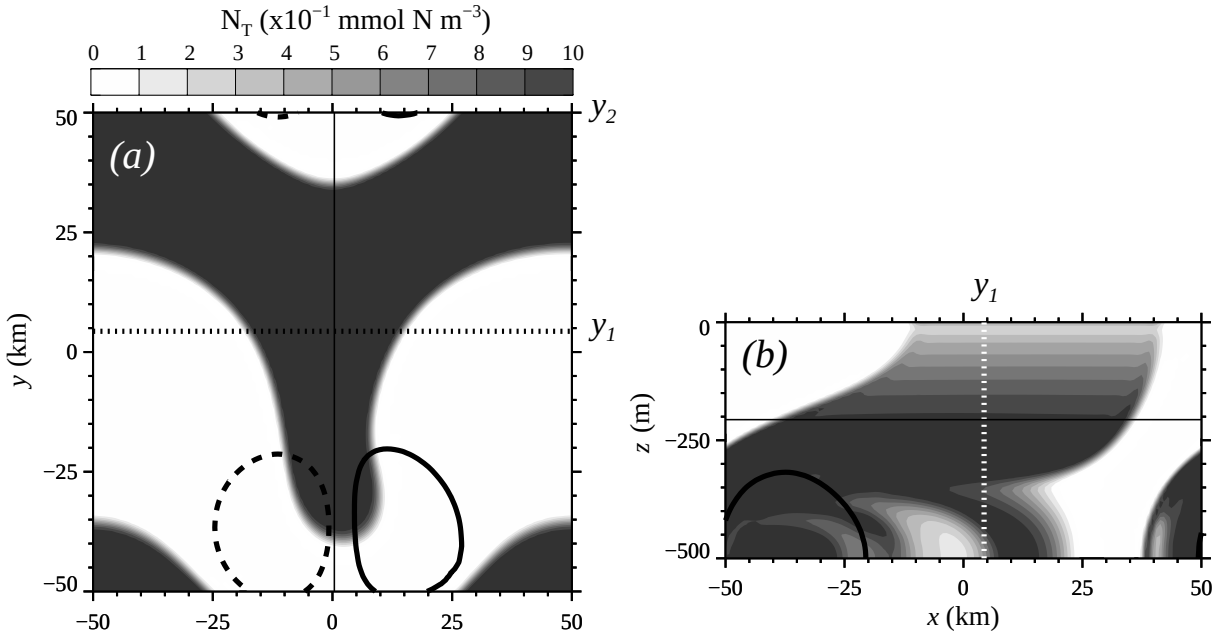

Figure 3.11: (a) Horizontal distribution of N_T at $t = 10.6\,\mathrm{d}$ where separatrix depth is shallowest z_S ($i_Z = 102$). Vertical section of N_T along the dipole axis ($x = 0$, $i_X = 65$, thin line) is shown in (b). PV contours $\varpi = \pm 0.2$ are included for reference. Dotted straight lines indicate the initial limits of the N_T patch. Note that dipole stirring causes the ecosystem patch to penetrate southwards along the dipole axis.

This theoretical dipole configuration is set so that v^g at the dipole center is close to that obtained numerically. To this end, we use the interior azimuthal solution (Viúdez, 2008a, eq. 4.17), that is,

$$\tilde{v}_i\,(r,z) = \frac{1}{2}\left(\sqrt{1+4C}-1\right) r\,, \tag{3.22}$$

where $C \cong \varpi_0/3$ depends linearly on ϖ_0 in the QG approximation. Thus, assuming a dipole composed by a pair of spheric vortices of radius $R_0 \cong 9.1\,\mathrm{km}$, which are horizontally separated by $1.6\,\mathrm{km}$, and PV density $\varpi_0 = 0.97 (\cong 1.37\,\mathrm{d}^{-1})$, $v^g \cong 52.1\,\mathrm{cm\,s}^{-1}$ is obtained at the dipole center using (3.13), which is comparable to v obtained along the dipole axis of the simulated non-constant PV case. This parametrization is next used to obtain the time evolution of the N_T front placed initially at y_1, which corresponds to an initial distance $r_i \cong 24.7\,\mathrm{km}$ from the dipole center.

The horizontal position of the N_T edge $r(z,t)$, relative to vortex centers, is expressed as a function of $v^g_e(r,z)$, according to Viúdez (2008b, eq. 11). The time interval $\delta t \equiv t(r,z) - t_i(r_i,z)$ taken by the N_T front to move from r_i to $r = \sqrt{r_X^2 + r_Y^2}$ at a given depth, where $r_X = R_0 + 0.05$ and $r_Y \in [-\pi, 0]$ are the zonal and meridional distances to the dipole

center, respectively, is

$$\begin{aligned} \delta t &= \int_{r_i}^{r} \frac{\mathrm{d}r'}{v_e^g(r',z)} \\ &= \frac{\gamma_0}{3}\left[R^3(r,z) - R_i^3(r_i,z)\right] + \gamma_0\, z^2[R(r,z) - R_i(r_i,z)] \\ &+ \gamma_0 z^3 \ln\left|\frac{[R(r,z)-z][R_i(r_i,z)+z]}{[R(r,z)+z][R_i(r_i,z)-z]}\right|, \end{aligned} \tag{3.23}$$

where constant $\gamma_0 = 3/(2N\varpi_0 R_0^3)$. Since all the terms above are strictly increasing continuous functions of r, $r(z, t_i + \delta t)$ is easily obtained by numerical inversion. This approximation predicts a maximum separatrix depth z_A close to the observed z_S (Fig.3.12b). Above z_A the predicted N_T front translation is about half the observed one, a discrepancy that may be explained by the absence of non-linear terms in the QG PV dynamics. Below z_A, the front line gradually converges to the separatrix curvature with a maximum displacement at $z = -500\,\mathrm{m}$ close to twice the vortices radius. Though the differences observed, equation (3.15) may be used to obtain a first estimate of the length of the patch filamentation at any depth for a given dipole geometry and intensity.

Finally, the ecological dynamics inside this N_T patch is investigated. To this end, ecological properties are quantified through the enhancement factors (**??**) and (**??**), which are referred to a location outside the dipole where isopycnals are flat. In this case, the ecosystem moves with a spatial and temporal dependent speed since the photic depth is shallower than that of the dipole separatrix, that is, $z = -240\,\mathrm{m} < z_S$. As in the previous section, we focus only on P dynamics since grazing is much smaller than the P growth. We observe that two different mechanisms cause a P increase of different order of magnitude. On the one hand, a P' maximum increase of about 7% develops at the wake of the anticyclone, since this vortex type has isopycnals uplifted in the photic zone. As discussed in the previous section, this increase is generated by vertical advection (Fig. 3.13a) and diminishes afterwards by biological forcing (Fig. 3.13b). Note that the observed P increase is independent of whether N_T is initialized homogeneous on horizontal layers or isopycnals, and thus of the ecological initial conditions. On the other hand, positive P' increases up to a $42\%\hat{P}$ at the filament front. Since the patch translation speed has negative vertical shear, deep P layers translate further southwards than shallow ones. As a result, P self-shading decreases at the filament front in benefit of P net growth $(\mathrm{d}P/\mathrm{d}t)'$ (Fig. 3.13c).

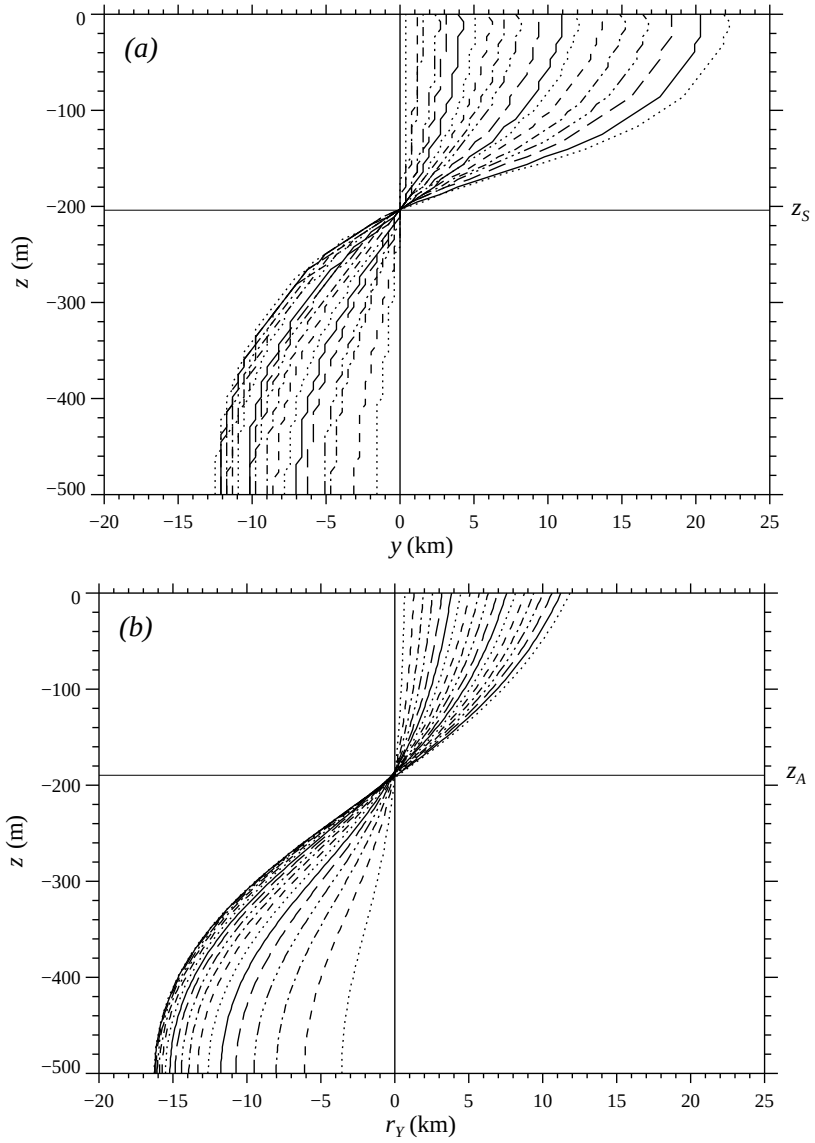

Figure 3.12: Position of the N_T frontal edge along dipole axis, $x = 0$, centered at y_1 and relative to the dipole. Numerical results (a) are approximated analitically (b) using the exterior geostrophic velocity $\tilde{v}_e^g(r,t)$ of the QG approximation, equation (3.12), where r_Y is the distance between the front edge and the dipole center. In both cases, the vertically straight N_T front tilts gradually with time around the minimum separatrix depth z_S. Each line corresponds to consecutive times ranging from $t \in (t_i, 15.9)\,\mathrm{d}$ with $\delta t \cong 0.7\,\mathrm{d}$.

In order to quantify the contribution of both mechanisms to the P increase, ecological properties are integrated on the patch volume above the photic depth using (3.11). At initial times, $\langle P' \rangle$ rapidly increases up to 7% due to vertical advection (Fig. 3.13a), though $(w\partial P/\partial z)'$ nearly balances out since w has a symmetric distribution within the patch (Fig. 3.14). At times $t > 12\,\mathrm{d}$, the patch has been decelerated relative to the dipole and thus P vertical advection decreases while patch filamentation increases. The elongation of this filament enlarges with depth causing P self-shading to diminish at its front in benefit

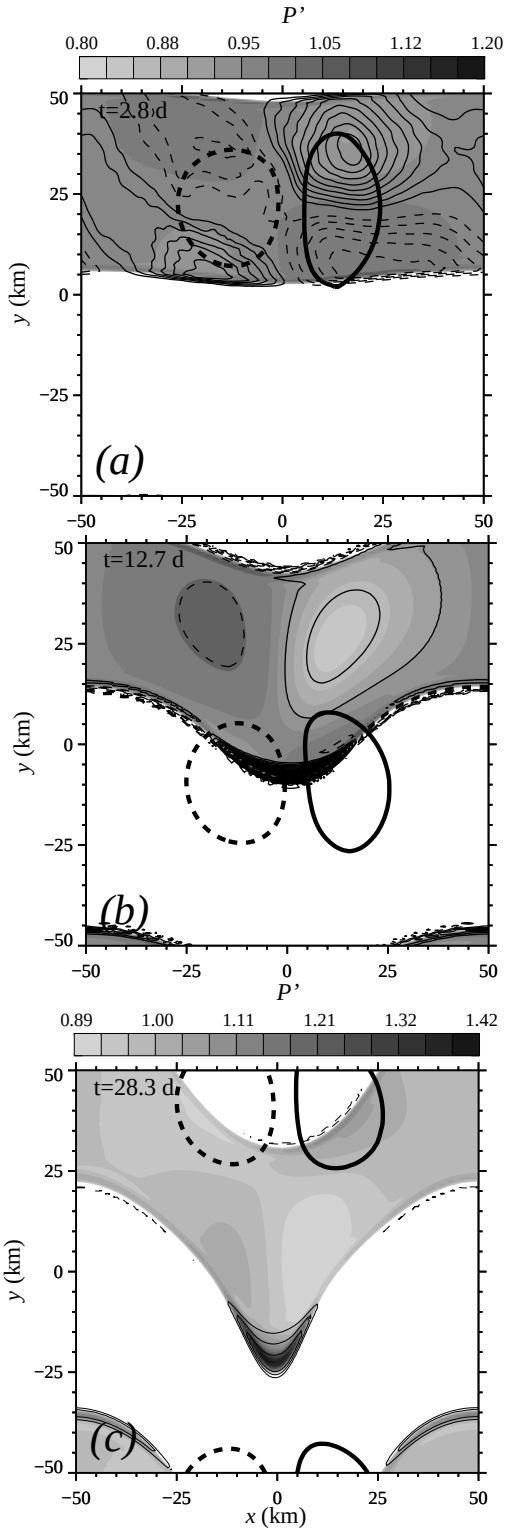

Figure 3.13: Horizontal distributions at $z = -125\,\mathrm{m}$ ($i_Z = 112$) and at the indicated times of P' (grey scale) and (a) $(w\,\partial P/\partial z)'$ (contour lines range is $(-0.28, 0.48)$ with $\delta = 0.05$), and (b)-(c) $(\mathrm{d}P/\mathrm{d}t)'$ (contour line range is $\in (-0.14, 0.4)$ with $\delta = 0.02$ in b and $\delta = 0.1$ in c). PV contours $\varpi = 0.2$ are included for reference. Two mechanisms are responsible for P' increase, and biological forcing at the filament front.

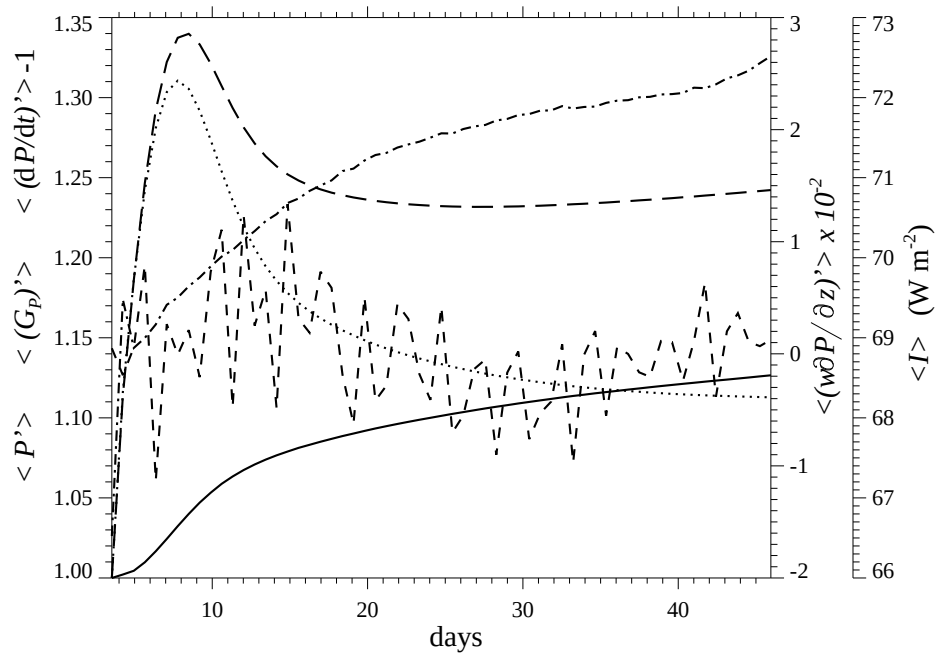

Figure 3.14: Time evolution of $\langle P' \rangle$ (solid line), $\langle (\mathrm{d}P/\mathrm{d}t)' \rangle$ (dotted line), $\langle G'_P \rangle$ (long dashed line), $\langle (w\,\partial P/\partial z)' \rangle$ (short dashed line), and $\langle I' \rangle$ (dash-dotted line) averaged on the patch above the photic depth $z = -240\,\mathrm{m}$ ($i_Z = 97$). The observed $\langle P' \rangle$ increase is caused by two mechanisms. At initial times, vertical advection accounts for an enhancement of about 6%. Later on, a decrease in P self-shading in benefit of solar radiation increases G_P, which doubles $\langle P' \rangle$ at $t = 45\,\mathrm{d}$.

of solar radiation I. As a consequence, G_P converges to a value around 1.23, which forces the ecosystem to be unsteady ($\langle \mathrm{d}P/\mathrm{d}t \rangle > 0$) and ultimately doubles $\langle P' \rangle$ within the following $t = 45\,\mathrm{d}$.

3.4 Concluding remarks

Three-dimensional plankton distributions were related to potential vorticity (PV) using a numerical physical-biological coupled model that explicitly conserved PV on isopycnals. In particular we investigated how vortex translation and the distant PV action perturbed an oligotrophic system in steady state. The former fact was addressed by considering a mature dipole embedded in the ecosystem, while the latter by initializing a subsurface dipole and a surface ecosystem patch.

We stated that dipole separatrix, which was defined by PV edges, acted as an impermeable barrier, creating two different ecological niches. Firstly, phytoplankton and zooplankton trapped within vortices converged to an equilibrium state, which was sustained by regener-

ated production. This may explain the subsistence of communities within long-lived vortices moving across the open ocean (Mackas et al., 2005; Whitney et al., 2005). The steady state observed depended on both the isopycnal vertical displacement, and thus on PV, and the ecological initial configuration. This was in agreement with previous numerical and experimental works which concluded that vortex geometry changes (Lévy, 2003) and biogeochemical properties of source waters (Thompson et al., 2007), respectively, alter phytoplankton distributions. One caveat worth noting is that we assumed a fully-recycling ecosystem and slow mixing processes and sedimentation are likely to occur as vortices translate. The way these facts alter the ecological steadiness within vortices is left for future research.

Secondly, plankton heterogeneity at the dipole outer was generated by vertical and horizontal advection, which were of the same order of magnitude as biological forcing. Plankton enhancement through vertical advection occurred at the wake of the dipole. As the dipole translated, fluid particles were displaced from the vortices front to their rear around PV edges. Therefore, they were upwelled to better lit depths when moving anticlockwise and clockwise in surface and subsurface dipoles, respectively. Phytoplankton response to this forcing had a time lag of about $\delta t = 1.4\,\mathrm{d}$ causing a spatial uncoupling between the increase in phytoplankton and its causing mechanism. As a result, fluid particles with enhanced phytoplankton biomass accumulated at the vortices wake and since they moved slower than the dipole phase speed, a trail of phytoplankton was observed behind it. The extent of this trail was proportional to the phytoplankton material rate of change $\mathrm{d}P/\mathrm{d}t$. So that, for a given length of the phytoplankton trail and dipole speed, $\mathrm{d}P/\mathrm{d}t$ could be inferred. The formation of a phytoplankton trail behind vortices was first conceptualized by Olaizola et al. (1993). In this work, we took a step further by conceiving two upwelling mechanisms ocurring simultaneously in a single vortex. A permanent upwelling of trapped waters within the vortex separatrix and a transient upwelling along the vortical periphery (Flierl and McGillicuddy, 2002). Both upwellings may explain the chlorophyll trail developed below a shallow chlorophyll peak (Ning et al., 2004, Fig. 9d) at the wake of a pair of vortices of opposite sea level anomaly (Chang et al., 2010, Fig. 10).

We also evidenced that horizontal advection was indirectly responsible for a phytoplankton increase when negative vertical gradients of PV existed. Since horizontal speed $|\mathbf{u}|_h$ was maximum along the dipole axis and increased with depth, a filament of phytoplankton runned along the direction of the dipole trajectory, the extent of which was maximum at

depth. The horizontal extension of this filament was qualitatively in agreement with the analytical relation between the front displacement and vortex PV derived using a simple theoretical quasigeostrophic dipole model composed of spheric vortices of fixed radius and depth. Therefore, the filament elongation was approximated for a PV structure of known geometry and intensity. As a result of the negative $|\mathbf{u}|_{\mathbf{h}}$ shear, phytoplankton increased at the filament front due to a decrease in self-shading in benefit of light irradiance. Though the light change was small, it accounted for significant enhancements of phytoplankton as was reported within an anticyclone over which waters with higher transparency flooded (Baird et al., 2011). Thus, mesoscale subsurface dipoles are responsible of off-shore transport of surface chlorophyll filaments Serra et al. (2010) and also of phytoplankton enhancement. The mechanism described may explain the subsistence of subsurface communities as filaments penetrate into the open ocean, which otherwise would decay through mortality and sinking. Finally, sharp phytoplankton fronts such as the one described here are often associated to well-defined density fronts (Jones et al., 1991), which induce upwelling along the filament edges (Moisan and Hofmann, 1996). The simultaneous contribution of a change in the light regime and localized upwelling to the community subsistence in coastal filaments is left for further investigation.

Chapter 4

Plankton resonant response to light and nutrients in mesoscale vortices

Chapter submitted as M. Claret, A. Viúdez, and Y. H. Spitz, 2012: Plankton resonant response to light and nutrients in mesoscale vortices.

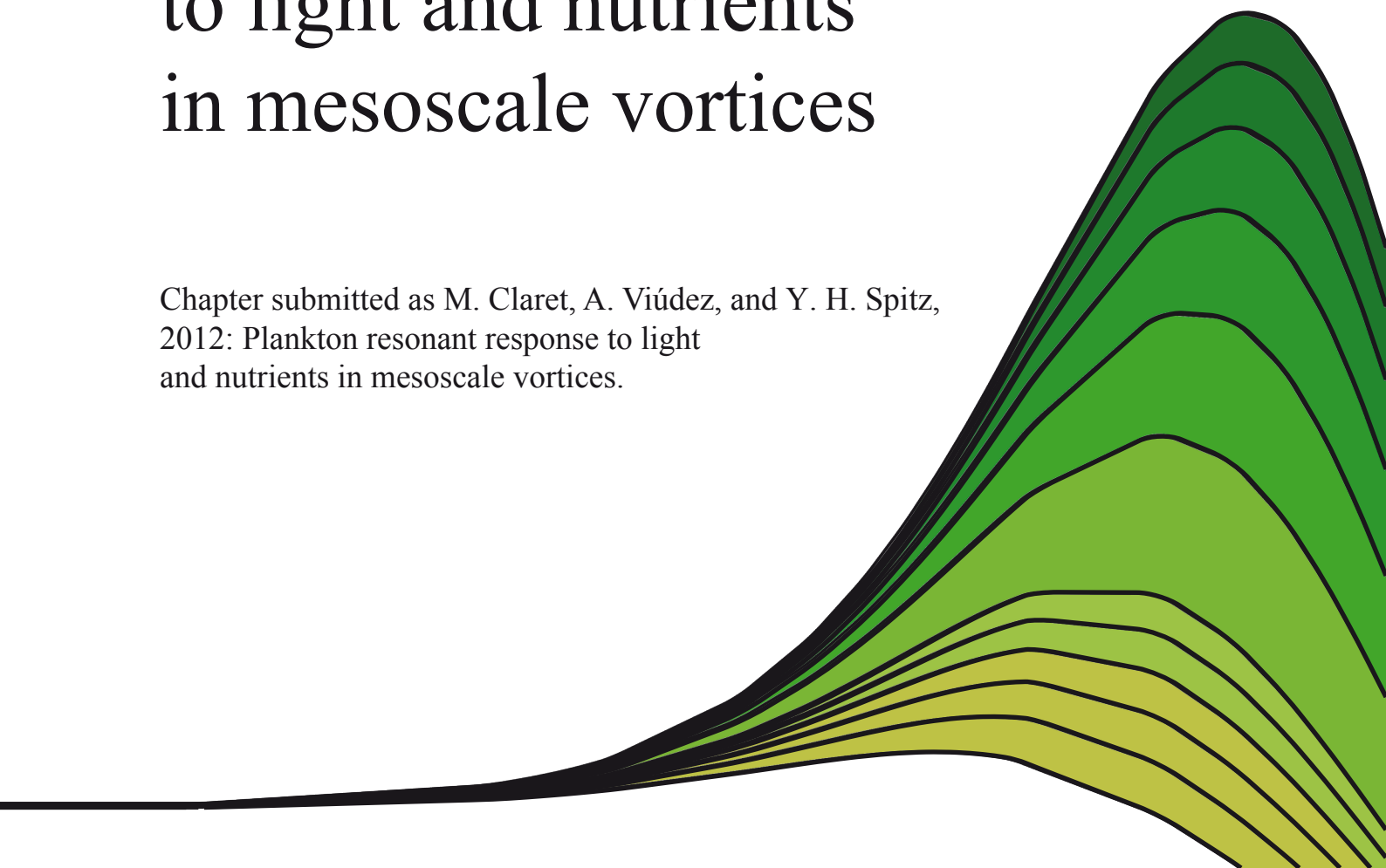

Només viu qui pregunta.

Pòrtic, Miquel Martí i Pol

ABSTRACT

The response of a fully-recycling ecosystem to light and nutrients variability within mesoscale cyclones is investigated. A simple physical-ecological coupled numerical model is used to study the horizontal and steady flow of ellipsoidal vortices. Ecological variables have only vertical spatial dependence through phytoplankton growth. This enables us to introduce mesoscale forcing in terms of vertical displacement of isopycnals in a NPZ (Nutrients-Phytoplankton-Zooplankton) model. Small-scale motions is parametrized as a Fickian-type diffusion along isopycnals. We observe that stationary stable ecological solutions are possible within mesoscale vortices with non-zero P and Z profiles. The dependence of these solutions on small-scale motion, vortex intensity, and trophic regime is explored. Firstly, small-scale motions increase the spatially integrated P biomass at a characteristic diffusion coefficient $\mathcal{K}^*$, at which resonance between phytoplankton and diffusive timescales occurs. Two mechanisms are involved in this P increase, namely nutrients uplift to better lit levels, and Z grazing pressure decrease. Secondly, vortex intensity exerts a double effect on the ecosystem. On one side, it enhances the irradiance affecting isopycnals, which induces a positive linear response in P. On the other side, it increases the diffusive fluxes. As a result, $\mathcal{K}^*$ is unaffected by vortex intensity, that is, P enhancements caused by isopycnal doming and small-scale motions are approximately additive. Finally, the trophic regime determines the magnitude of the ecosystem response. The increase in P biomass caused by small-scale motion is significant only in mesotrophic regimes, and it remains independent of the trophic condition when the vortex intensity varies.

4.1 Introduction

Mesoscale vortices are ubiquitous in the ocean and exert a strong influence on plankton dynamics. Pelagic organisms are embedded within the fluid and thus they are affected by its dynamics. Characteristic mesoscale horizontal and vertical velocities are of the order of $0.1\,\mathrm{m\,s^{-1}}$ and $10^{-5}\ \mathrm{m\,s^{-1}}$, respectively (Gill, 1984). Vertical processes inject nutrients to the photic zone, which extends where one per cent of the light irradiance arrives, increasing ocean primary production. Many mechanisms involving vortex structures contribute to upwell nutrients in the upper ocean. To mention a few, the isopycnal uplift associated to surface cyclones in formation and anticyclones in decay entrains the nutricline into the photic layer in a process known as *eddy pumping* (Falkowski et al., 1991; McGillicuddy et al., 1999). *Eddy-wind interactions* cause divergence at anticyclone cores (Martin et al., 2001; Ledwell et al., 2008). Moreover, nutrients are pumped likewise at vortex edges through perturbations in the vorticity field typical of *submesoscale* dynamics (see review by Klein and Lapeyre, 2009).

Once ecological heterogeneity develops, it may undergo filamentation by mesoscale stirring (Lehahn et al., 2007) or get confined within coherent vortices. Long-lived vortices are able to transport coastal ecosystems long distances (Arnone and LaViolette, 1986; Batten and Crawford, 2005). If horizontal advection is the only ecological perturbing cause, then vortices would become chlorophyll depleted after some weeks due to nitrogen sinking into the aphotic layer. Instead, vortices remain chlorophyll rich at their cores as they translate accross the open ocean (Kahru et al., 2007; Siegel et al., 2008). Several physical mechanisms may contribute to this long-term phytoplankton subsistence within mature vortices, such as eddy-wind interactions, isopycnal and diapycnal diffusion, or vertical mixing. Additionally, the ecosystem community composition may change in order to optimize nutrients. In this regard, several works reported a shift with vortex aging from bloom communities, typical of nutrients rich eutrophic waters of coastal origin, to postbloom communities, characteristic of nutrients poor oligotrophic waters of the open ocean (Thompson et al., 2007; Brown et al., 2008). In particular, Bibby et al. (2008) observed a subsurface deep chlorophyll maximum at a constant density surface in eddies of different development stage. In that case, the transition from bloom to postbloom condition was driven by both the photosynthetic rate and nutrient availability. Though this phytoplankton response was mainly observed during

cyclogenesis, some of their results suggest further biological activity within coherent mature cyclones.

Time evolution of the three-dimensional plankton structure remains largely unknown in the open ocean, where high spatio-temporal resolution surveys are more challenging and costly than nearby coasts. The aim of this paper is to give some insight on the long-term phytoplankton subsistence within mature mesoscale vortices in oligotrophic environments. To this end, we assume a steady-state axisymmetric vortex monopole, where the flow is along isopycnals (the velocity $\mathbf{u}$ is perpendicular to the density gradient $\boldsymbol{\nabla}\rho$, so that density advection $\mathbf{u} \cdot \boldsymbol{\nabla}\rho = 0$). This assumption is based on the relevant contribution of nutrients advection on isopycnals to open ocean irrigation, such as occurs in the North Atlantic (see review Pelegrí et al., 2006), and the isopycnal confinement of phytoplankton (Navarro et al., 2006; Niewiadomska et al., 2008; Frajka-Williams et al., 2009). Consistently with this isopycnal point of view, two main mechanisms may enhance phytoplankton at the vortex eye. The irradiance received by an isopycnal belonging to surface cyclones and subsurface anticyclones is greatest at their core. In this case, we address the following question: can the light regime associated with these vortices lead to a phytoplankton biomass enhancement at their center? If so, phytoplankton growth and nutrient consumption would be maximum at that location, which would create isopycnal gradients of nutrients. As a result, small-scale motions could drive a replenishment down-gradient flux of nutrients along isopycnals. The contribution of isopycnal mixing upwelling new nutrients has been found unrelevant compared to other processes (Ledwell et al., 2008; Siegel et al., 1999). However, since we intend to quantify the contribution of diffusion in upwelling regenerated nutrients, we consider our second question: may isopycnal mixing maximize the phytoplankton response to light?

We address the two aforementioned questions from a numerical point of view taking into account vortex intensity, trophic condition, and isopycnal diffusion in the ecological dynamics. We consider along isopycnal flow in a fully-developed mesoscale surface cyclone (section 4.2.1). Since long-living vortices are sealed to injection of new nutrients, productivity is largely supported by local regeneration of nutrients. Thus a NPZ (nutrients, phytoplankton, and zooplankton) model consistent with an oligotrophic/mesotrophic condition (section 4.2.2) is considered. The physical-ecological coupled model (section 4.2.3) is next initialized with stationary profiles obtained for the fluid at rest (section 4.3). Our results show that ecological steady state solutions sustained by the light regime in vortices of variable intensity

are possible within a given range of total nitrogen (section 4.4.1). When isopycnal diffusion is included, the phytoplankton response is maximized through a resonance mechanism between physical and ecological timescales (sections 4.4.2 and 4.4.3). Finally, some implications of these results are discussed in the concluding remarks (section 4.5).

4.2 Physical-ecological coupled model

The flow dynamics results from a single mesoscale baroclinic cyclone and small-scale motions. For simplification, the vortex is spherical in the quasi-geostrophic (QG) space, which is the vertically stretched space of dimensions (x, y, cz), where $c \equiv N/f$ is the Prandtl ratio, N the background Brunt-Väisälä frequency, and f the Coriolis frequency. As a result, the mesoscale motion is horizontal and steady along isopycnals. In this scenario, plankton ecology only depends on the depth of isopycnals if we consider, as a first approximation, that nitrogen is homogeneous on isopycnals in stratified waters. For this reason, we derive the governing mesoscale flow equations in terms of vertical displacement of isopycnals (section 4.2.1). A simple nitrogen based ecological model (section 4.2.2) is next coupled to the physical dynamics. The mesoscale forcing is introduced in terms of vertical displacements of isopycnals, while small-scale motions are parametrized as an isotropic Fickian diffusion in the ecological dynamics (section 4.2.3).

4.2.1 The mesoscale balanced flow

We consider the isochoric (volume-preserving) flow of a stable stratified fluid, under the Boussinesq approximation. The reference frame is fixed at the surface of a sphere rotating with angular velocity $f/2$ relative to an inertial frame, and the vertical axis is normal to geopotential surfaces. We assume the f-plane approximation, as is typical in mesoscale dynamics, which neglects locally the sphericity of the Earth and assumes plane gravity potential surfaces. The fluid motion associated to a spheric baroclinic vortex is steady and horizontal satisfying the gradient and hydrostatic balances of momentum, and the non-divergence condition,

$$\mathbf{u}\cdot\boldsymbol{\nabla}\mathbf{u}_h + f\,\hat{\mathbf{k}}\times\mathbf{u}_h = -\alpha_0\boldsymbol{\nabla}_h p'\,, \tag{4.1}$$

$$0 = -\alpha_0\frac{\partial p'}{\partial z} - \alpha_0 g\rho'\,, \tag{4.2}$$

$$\boldsymbol{\nabla}\cdot\mathbf{u}_h = 0\,, \tag{4.3}$$

where α_0 is a constant specific volume, and g the acceleration due to gravity. Above $\hat{\mathbf{k}}$ is the vertical unit vector, $\boldsymbol{\nabla}_h$ the horizontal gradient operator, and the 3D gradient $\boldsymbol{\nabla} \equiv \boldsymbol{\nabla}_h + \hat{\mathbf{k}}\,\partial/\partial z$. The pressure anomaly $p'(\mathbf{x})$ includes the pressure field $p(\mathbf{x})$ associated to the baroclinic vortex and a term balancing the hydrostatic pressure of a constant stratification, namely

$$p'(\mathbf{x}) \equiv p(\mathbf{x}) + g(\rho_0 + \frac{1}{2}\varrho_0 z)z. \tag{4.4}$$

The remaining unknowns are the horizontal velocity $\mathbf{u}_h(\mathbf{x})$ and the mass density anomaly $\rho'(\mathbf{x})$. For convenience, we will express the above equations in terms of isopycnal vertical displacement $\mathcal{D}$ using cylindrical coordinates (r, z).

The mass density field ρ is first decomposed into the background mass density ρ_0, a linear stratification $\varrho_0 z$, and the mass density anomaly ρ' generated by the vortex, that is,

$$\rho(r, z) \equiv \rho_0 + \varrho_0 z + \rho'(r, z), \tag{4.5}$$

where $r = \sqrt{x^2 + y^2}$ is the distance to the vortex center and the vertical coordinate $z \leq 0$. The ρ field is replaced with the isopycnal depth d according to

$$d(r, z) \equiv (\,\rho(r, z) - \rho_0\,)/\varrho_0. \tag{4.6}$$

Thus $d(r, z)$ corresponds to the depth that an isopycnal located at (r, z) has in a reference density configuration where isopycnals are flat. The vertical displacement $\mathcal{D}$ experienced by this isopycnal with respect to its reference density state is defined as

$$\mathcal{D}(r, z) \equiv z - d(r, z). \tag{4.7}$$

Therefore, the mass density anomaly is related to the isopycnal vertical displacement through $\mathcal{D} = -\rho'/\varrho_0$. Note that static stability occurs when $\partial\mathcal{D}/\partial z > 1$. Quantities d and $\mathcal{D}$ play

a significant role in this work because isopycnal coordinates will be used later to model the ecological dynamics. The basic equations (4.1)–(4.3) can be now expressed as the momentum balance along r and the hydrostatic equilibrium

$$\frac{\nu^2}{r} + f\nu = \alpha_0 \frac{\partial p'}{\partial r}\,, \tag{4.8}$$

$$0 = \alpha_0 \frac{\partial p'}{\partial z} + N^2 \mathcal{D}\,, \tag{4.9}$$

where ν is the azimuthal velocity, and $N^2 \equiv -\alpha_0 g \varrho_0$.

A relevant quantity in the definition of an oceanic vortex is potential vorticity (PV) density since it is materially conserved in inviscid adiabatic processes. The dimensionless anomaly of the PV density satifies

$$\varpi \equiv \left(\frac{\boldsymbol{\omega} + f\,\hat{\mathbf{k}}}{f}\right) \cdot \boldsymbol{\nabla} d = \frac{\zeta}{f} - \frac{\partial \mathcal{D}}{\partial z} - \frac{\boldsymbol{\omega}}{f} \cdot \boldsymbol{\nabla} \mathcal{D}\,, \tag{4.10}$$

where the relative vorticity $\boldsymbol{\omega} \equiv \xi\,\hat{\mathbf{r}} + \zeta\,\hat{\mathbf{k}} = -\partial\nu/\partial z\,\hat{\mathbf{r}} + (\nu/r + \partial\nu/\partial r)\,\hat{\mathbf{k}}$. Using equations (4.8)-(4.9)-(4.10), ϖ can be expressed as a function of p'. Thus, $\nu(r,z)$ and $\mathcal{D}(r,z)$ can be recovered from a prescribed spatial distribution of $\varpi(\mathbf{x})$, via PV inversion. However, the PV inversion of a baroclinic vortex with horizontal gradients of PV is a nontrivial problem.

We approach this issue by adjusting a polynomial distribution of $\mathcal{D}$ to a numerical one that fully satifies the non-linear equations (4.8)-(4.9). To this end, ϖ is inverted numerically in Cartesian coordinates using the PV Contour Advective Semi-Lagrangian (CASL) algorithm (appendix A) which solves the general case of arbitrary PV vortex geometry. Particularly, we consider a baroclinic Kirchhoff spheric vortex in the QG space of vertical length $L_Z = \pi$ and radial extent $L_R = cL_Z$. The ϖ vortex is defined by circular contours of PV, which are materially conserved on isopycnals. The distribution reaches its maximum $\varpi_{\max}$ at the vortex center and decreases radially along isopycnals as a power of 1/3. The radius of the minimum PV contour specifies the horizontal vortex semi-axis $r_H = 1.5c$, and the vortex vertical extent is $r_Z = 1.5$. On the vertical, the maximum isopycnal vertical displacement $\mathcal{D}_{\max}$ is reached at the vortex center at $z_D \simeq -0.92$ (Fig. 4.2), independently of $\varpi_{\max}$. Above this depth, vertical gradients of $\mathcal{D}$ are larger than below. This vertical asymmetry is introduced in the polynomial distribution as $z(z+\pi)^2$. The cubic vertical dependence

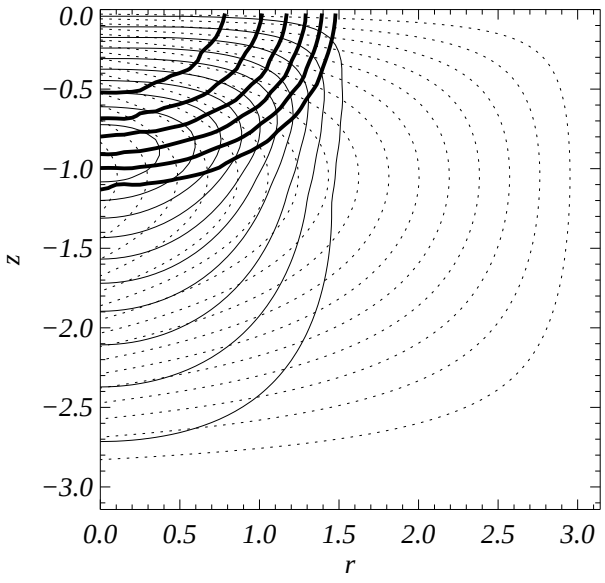

Figure 4.1: Vertical distribution of $\mathcal{D}(r,z)$ (dashed line) corresponding to the polynomial function (**??**) is compared with that obtained using the CASL algorithm (solid line) for a cyclone with $\mathcal{D}_{\max} = 0.39$. PV contours with maximum $\varpi = 1.8$ and $\delta\varpi = 0.3$ (thickest line) are included for reference. (b) Vertical distribution of $\overline{\mathcal{D}}(s,d)$ corresponding to $\mathcal{D}_{\max} = 0.39$ (upper case, $\lambda_0 = 0.027$, solid line), and $\mathcal{D}_{\max} = 0.16$ ($\lambda_0 = 0.011$, dashed line). Contour interval $\delta\mathcal{D} = 0.025$.

places $\mathcal{D}_{\max}$ at $z = -\pi/3 \simeq z_D$. On the horizontal, $\mathcal{D}$ decreases exponentially with the radius, similarly to the PV distribution. However, a radial linear dependence of type $\pi - r$ is only considered in the polynomial expression of $\mathcal{D}$. This simplification allows a closed-form solution for the isopycnal radius, which facilitates the physical-ecological coupling (explained in section 4.2.3). The resulting polynomial expression for $\mathcal{D}(r,z)$ is

$$\mathcal{D}(r,z) = -\lambda_0\, z(z+\pi)^2(\pi - r)\,, \tag{4.11}$$

where λ_0 is a dimensionless scaling factor. This parameter adjusts the magnitude of our analytical solution for $\mathcal{D}$ to the numerical one $\hat{\mathcal{D}}$ through the relation $\lambda_0 = 27/(4\pi^4)\,\hat{\mathcal{D}}_{\max}$.

4.2.2 The NPZ model

The ecological model consists of three dependent variables, namely, phytoplankton (P), zooplankton (Z), and dissolved nutrients (N). Each variable represents a functional group and they are related through physiological processes. Functional groups are composed either by one dominant species or several species with similar physiological characteristics. This simplification of the food web minimizes the error associated to unconstrained free parameters, while maintains the ecological dynamics of our interest. The addition of complexity to the ecological model is found convenient when reproducing specific data sets (Friedrichs et al., 2006), rather than when used in a heuristic way as in this work.

We consider first an oligotrophic environment typical of the open ocean (Lawson et al., 1996). In this case, the light-nutrients segregation implies an acute scarcity of resources, and species compete by optimizing their nutrient assimilation. This ecological system is fully-recycling and satisfies the set of equations

$$\frac{\mathrm{d}P}{\mathrm{d}t} = \underbrace{\frac{N}{K_0+N}\,L\,P}_{G_P} - \underbrace{R_0(1-e^{-\Lambda_0 P})Z}_{R} - \underbrace{\Xi_0 P}_{M_P}, \tag{4.12}$$

$$\frac{\mathrm{d}Z}{\mathrm{d}t} = \underbrace{(1-\Gamma_0)R}_{G_Z} - \underbrace{\Theta_0 Z^2}_{M_Z}, \tag{4.13}$$

$$\frac{\mathrm{d}N}{\mathrm{d}t} = -G_P + \Gamma_0 R + M_P + M_Z\,, \tag{4.14}$$

where $\mathrm{d}(\,)/\mathrm{d}t$ is the material time derivative. Phytoplankton production (G_P) is nitrogen and light limited. The nutrient uptake follows a Michaelis-Menten kinetics (Dugdale, 1967) governed by K_0, an indicator of the P affinity for N. The photosynthetic rate L has also a saturating response (Smith, 1936; Jassby and Platt, 1976) according to

$$L(r,z,t) \equiv \frac{V_0\,\Psi_0\,I(r,z,t)}{\sqrt{V_0^2+\Psi_0^2 I^2(r,z,t)}}\,, \tag{4.15}$$

where the available radiation

$$I(r,z,t) \equiv I_0 \exp\left\{A_w z - A_p \int_z^0 P(r,z',t)\,dz'\right\} \tag{4.16}$$

is the surface solar radiation attenuated by both sea water and P self-shading. Phytoplankton is removed by zooplankton grazing R, which has an Ivlev response (Parsons et al., 1967), and by a linear term (M_P) including death and exudation. Only a fraction $(1-\Gamma_0)$ of the P grazed is converted into Z production G_Z, while the remainder is transferred to the N compartment. In contrast to P, Z has a quadratic closure term for two purposes. Firstly, it gives stability to the model (Edwards and Yool, 2000), and secondly, it introduces implicitly the effect of intratrophic cannibalism (Ohman et al., 2002; Pitchford and Brindley, 1998) and predation by higher trophic levels (Ohman and Hirche, 2001). Finally, detrital matter ($\Gamma_0 R + M_P + M_Z$) is remineralized making nutrients again available for P uptake.

4.2.3 Physical ecological coupling

Ecological steady-state solutions are found here numerically by considering material conservation of total nitrogen N_T. The small-scale and sub-grid ecological dynamics are parametrized through Fickian diffusion. We focus next on the spatial heterogeneity introduced at the mesoscale, which depends on three main factors. Firstly, P growth is affected by the vertical light regime, which is determined by the isopycnal depth. Secondly, the diffusive flux depends on the isopycnals slope. And thirdly, N_T is homogeneous on isopycnals but we assume a negative diapycnal gradient of N_T. Consequently, the perturbation in the ecosystem caused by the mesoscale forcing can be characterized through the spatial distribution of isopycnals, which is given by $\mathcal{D}(r,z)$.

We focus next on expressing the NPZ equations in terms of $\mathcal{D}(r,z)$. In order to simplify the derivatives along isopycnals we switch from cylindrical (r,z) to isopycnal (s,d) coordinates. An expression for the isopycnal radius $s(r,z)$ is obtained by combination of (4.7) and the line element definition $\mathrm{d}s^2 \equiv \mathrm{d}r^2 + \mathrm{d}z^2$, that is,

$$s(r,z) = \int_0^r \sqrt{1 + \left(\frac{\partial \mathcal{D}}{\partial r'}(r',z)\right)^2}\,\mathrm{d}r' \,. \tag{4.17}$$

Considering (**??**), the above integral has the following exact solution

$$s(r,z) = \begin{cases} \sqrt{1+\beta^2}\, r, & \gamma = 0\,, \\ -\frac{1}{\gamma}\left(\tau + \frac{\beta}{2}\ln\left|\frac{\tau-\beta}{\tau+\beta}\right|\right) + \mathcal{C}(z), & \gamma \neq 0\,, \end{cases} \tag{4.18}$$

where

$$\beta(z) \equiv \lambda_0\, z(z+\pi)^2\,, \tag{4.19}$$

$$\gamma(z) \equiv 3\,\lambda_0\,(z+\pi)(z+\pi/3)\,, \tag{4.20}$$

$$\tau(r,z) \equiv \sqrt{(1+\gamma(z)(\pi-r))^2 + \beta(z)^2}\,, \tag{4.21}$$

and $\mathcal{C}(z)$ is obtained from the boundary condition $s(r=0,z)=0$. The vertical displacement of isopycnals $\overline{\mathcal{D}}(s,d)$ as a function of s and d, that is $\overline{\mathcal{D}}(s(r,z),d(r,z)) \equiv \mathcal{D}(r,z)$, is found using a numerical iterative procedure.

Finally, parametrizing the small-scale isopycnal mixing as a Fickian diffusion, the concluding NPZ equations to solve are

$$G_P - R - M_P + \kappa \frac{\partial^2 P}{\partial s^2} = 0\,, \tag{4.22}$$

$$G_Z - M_Z + \kappa \frac{\partial^2 Z}{\partial s^2} = 0\,, \tag{4.23}$$

$$-G_P + \Gamma_0 R + M_P + M_Z + \kappa \frac{\partial^2 N}{\partial s^2} = 0\,, \tag{4.24}$$

where κ is the isopycnal mixing coefficient, and the spatial dependence of the available radiation is computed using $\overline{z}(s,d) = d + \overline{\mathcal{D}}(s,d)$. Above, and hereinafter, unless otherwise specified, all the dependent variables are assumed to be function of the independent variables (s,d), e. g. , $P = P(s,d)$, etc. Note that the material rate of change of the the total nitrogen $N_T \equiv P + Z + N$ balances its isopycnal diffusion

$$\frac{\mathrm{d}N_T}{\mathrm{d}t} = \kappa \frac{\partial^2 N_T}{\partial s^2}\,. \tag{4.25}$$

Equations (4.16)–(4.18) are used in the next section to obtain stationary ecosystem solutions with the fluid at rest.

4.3 Initial conditions

4.3.1 Numerical parameters

4.3.1.1 Spatio-temporal domain

The unit of space in the QG domain is defined by the vertical extent $L_Z = \pi$. Thus the radial extent $L_R = cL_Z$. The number of grid points is $(n_R, n_Z) = (64, 128)$, and the number of isopycnals $n_L = 128$. Variables can be adimensionalized by specifying two dimensional parameters. Firstly, the maximum depth $\mathcal{Z}_{\min} \equiv -150\,\mathrm{m}$ determines the length conversion factor according to $\mathcal{L} \equiv |\mathcal{Z}_{\min}|/L_Z$. Secondly, the maximum photosynthetic rate $L_{\max}$, corresponding to that at the sea surface $L_{\max} = \alpha_0 I_0 V_0/\sqrt{V_0^2 + (\alpha_0 I_0)^2} \cong 3\ \mathrm{d}^{-1}$ with constant sea surface irradiance I_0, gives the time conversion factor as $\mathcal{T} \equiv L_{\max}^{-1}$. Consequently, ecological variables are expressed in terms of mmol N. Dimensional physical values can therefore be

recovered by multiplying the adimensional values by the spatio-temporal conversion factors $\mathcal{L}$ and $\mathcal{T}$ elevated to the appropiate powers to match physical dimensions. For exemple, the dimensional equivalent of a P production $G_P = 700\,\mathrm{mmol\,N}$ is $700/(\mathcal{L}^3 \times \mathcal{T}) = 0.02$ $\mathrm{mmol\,N\,m^{-3}\,d^{-1}}$.

4.3.1.2 Parameter λ_0

The intensity of cyclones is modeled through the magnitude of the vertical displacement of isopycnals $\mathcal{D}$, and thus through the dimensionless scaling factor λ_0. We have considered spherical cyclones from $\varpi = 0.75$ to $\varpi = 2$, which is at the limit of their stability. This range corresponds to $\mathcal{D}_{\max} \in [0.16, 0.39]$, using the CASL algorithm aforementioned (section 4.2.1), and thus to $\lambda_0 \in [0.11, 0.27]$. An arbitrary $\delta\lambda_0 = 1.7 \times 10^{-3}$ is chosen. Note that λ_0 does not alter the pattern of $\mathcal{D}(r, z)$ but that of $\overline{\mathcal{D}}(s, d)$. As $\mathcal{D}_{\max}$ increases, the corresponding isopycnal level deepens (Fig. 4.3).

4.3.1.3 Isopycnal diffusion coefficient κ

Suggestive eddy diffusivities are extracted from the North Atlantic Tracer Release Experiment (Ledwell et al., 1998; Polzin and Ferrari, 2004). Scale-dependent measurements of lateral dispersion were performed at 300 m and estimated κ for scales ranging 1–30 km at about 2 $\mathrm{m^2\,s^{-1}}$. Subinertial vortical structures had a major contribution to the mentioned

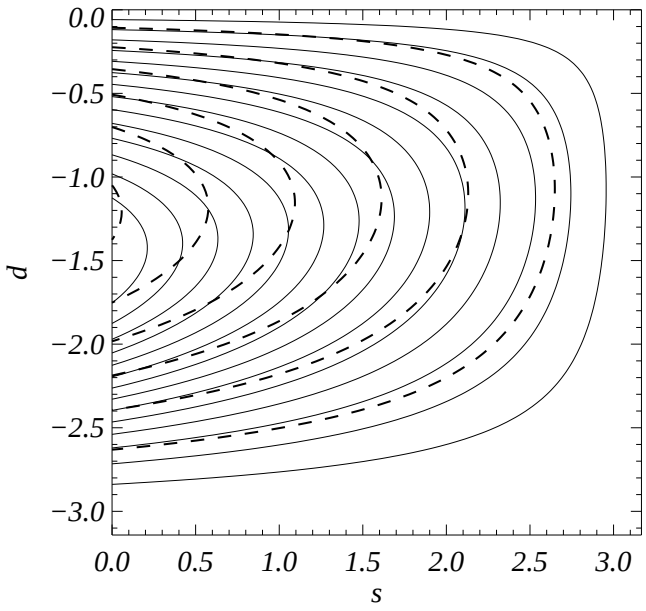

Figure 4.2: Vertical distribution of $\overline{\mathcal{D}}(s, d)$ corresponding to $\mathcal{D}_{\max} = 0.39$ (upper case, $\lambda_0 = 0.027$, solid line), and $\mathcal{D}_{\max} = 0.16$ ($\lambda_0 = 0.011$, dashed line). Contour interval $\delta\mathcal{D} = 0.025$.

isopycnal coefficient with $\kappa \in (0.5, 2.5)$ $\mathrm{m^2\,s^{-1}}$, followed by mesoscale-submesoscale interactions ($\kappa \simeq 0.1$ $\mathrm{m^2\,s^{-1}}$), ultimately developing into inertia–gravity waves ($\kappa \simeq 0.01$ $\mathrm{m^2\,s^{-1}}$) (Polzin and Ferrari, 2004).

The estimates above are based on mesureaments of an inert tracer. However, the dispersion rate of κ of a reactive tracer, such as plankton, depends on its reactive timescale (Pasquero, 2005). Furthermore, spectral slopes between inert or active tracers and chlorophyll diverge at a critical lengthscale 2–7 km, where the flow and ecological timescales have the same order of magnitude (see review Martin, 2003). Many theories may account for this divergence such as the scale of the tracer supply (Bracco et al., 2009), and thin layers (Franks, 2005). As a result of the uncertainity about bounding an isopycnal difussion coefficient for ecological variables, we constrain κ within the widest plausible range $\kappa \in [0.01, 10]$ $\mathrm{m^2\,s^{-1}}$.

According to the above mentioned scaling, the isopycnal diffusion coefficient is adimensionalized such that

$$\mathcal{K} \equiv \frac{\kappa \mathcal{T}}{(\mathcal{L}c)^2}\,. \tag{4.26}$$

Note the squared dependence on c due to the fact that the QG space is vertically streched. It must be kept in mind also that the parameter c specifies QG mesoscale vortices as well as submesoscale or small scale vortices.

4.3.1.4 Trophic regime

The nutrients availability of the system is modified through the maximum of total nitrogen T_1. We have considered a range of T_1 from $1\mathcal{L}^3$, which is representative of an oligotrophic condition, to $8\mathcal{L}^3$, with increments $\delta T_1 = 1\mathcal{L}^3$ mmol N (see Fig. 4.4 for associated vertical profiles).

4.3.2 Stationary ecosystem with the fluid at rest

A first step in solving the time evolution of the ecosystem is to define the appropriate initial conditions for the NPZ dynamics. Stable steady-state solutions of the coupled model are obtained by time integration of (4.16)–(4.18), which converge to an equilibrium state when using an initial solution close enough to that state. To this end, we first seek for ecological steady state profiles with the fluid at rest, that is, outside the vortex. In this case, isopycnals

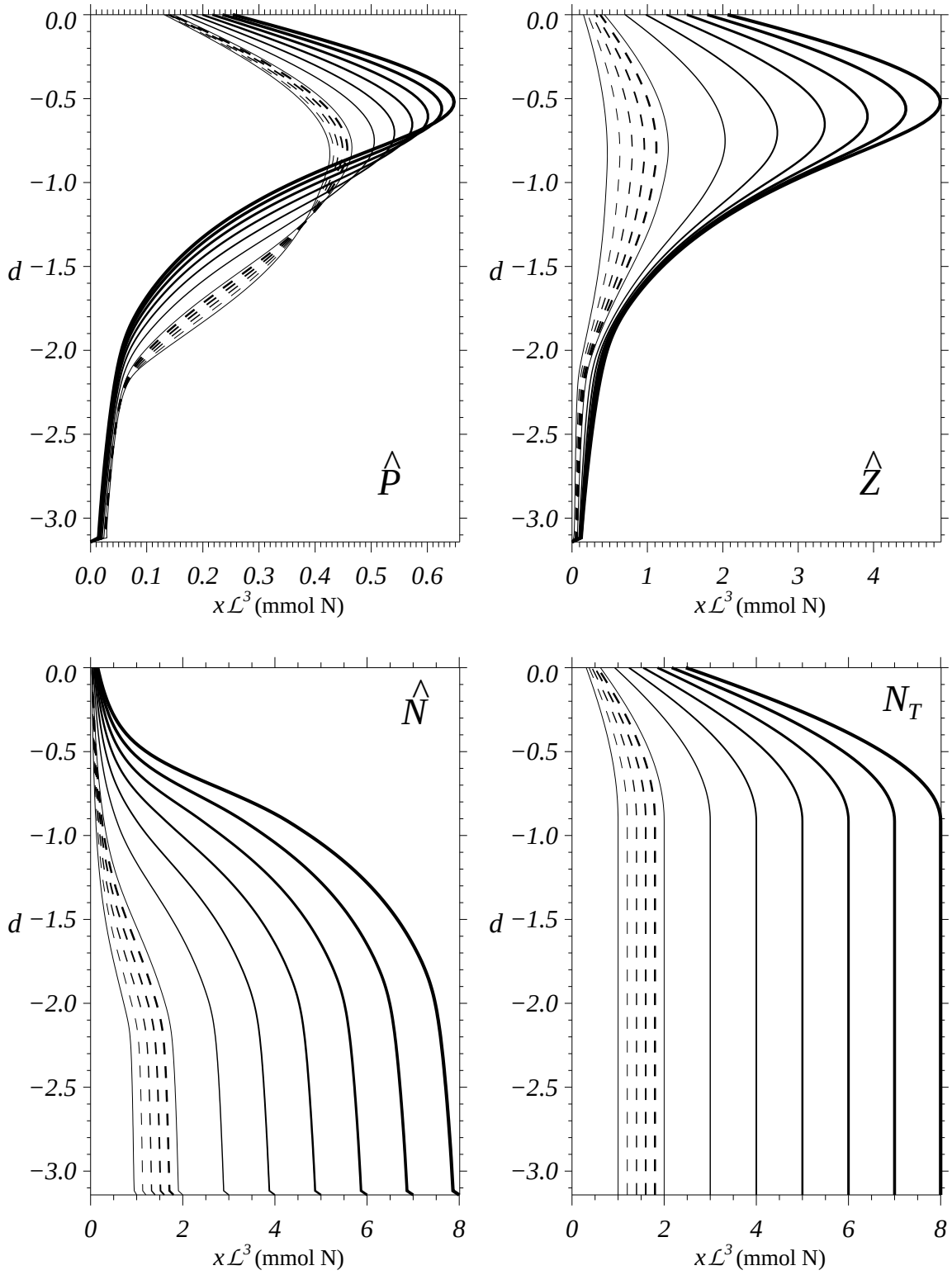

Figure 4.3: Steady-state profiles $\hat{P}$, $\hat{Z}$, and $\hat{N}$ for a given profile of N_T with the fluid at rest. Ecological variables are adimensionalized and expressed in terms of mmol N. Hereinafter, progressive line thickness indicates an increase in N_T maximum $\delta T_1 = 1\,\mathcal{L}^3$ mmol N (solid lines) and $\delta T_1 = 0.2\,\mathcal{L}^3$ mmol N (dashed lines).

are flat ($\mathcal{D} = 0$), so that light availability is horizontally homogeneous and the ecosystem has only vertical variability. The vertical dependence of $\{NPZ\}$ is obtained by time integration of (4.16)–(4.18), with $\mathcal{K} = 0$ and using the oligotrophic non-dimensional parametrization (Table 4.1) of Lawson et al. (1996) and the following initial profiles

$$N_T(d) = \begin{cases} T_1 \cos\left[\left(1 - \frac{d}{d_1}\right)\frac{2\pi}{5}\right], & d \in [d_1, 0], \\ 1, & d \in [-\pi, d_1), \end{cases} \tag{4.27}$$

$$(P_i, Z_i)(d) = S_1 \left(1 - \frac{d}{d_{\min}}\right), \tag{4.28}$$

where $T_1 \in (1, 8)\,\mathcal{L}^3\,\mathrm{mmol\,N}$, $S_1 = 0.1\,\mathcal{L}^3\,\mathrm{mmol\,N}$, $d_1 \cong -0.91$ (isopycnal index, $i_L = 91$), and $d_{\min} = \mathcal{Z}_{\min}$. Time integration is performed using an explicit leap-frog scheme, together with a Robert-Asselin time filter to avoid the computational mode. The initial profiles smoothly converge to steady-state solutions (Fig. 4.4), which are hereinafter referred to as $\{N_T, \hat{P}, \hat{Z}\}$. Phytoplankton and zooplankton have similar vertical distributions (Fig. 4.4), though the latter is slightly larger than the former, with a subsurface maximum at $d \cong -0.86$ ($i_L = 92$). The obtained $\{N_T, \hat{P}, \hat{Z}\}$ distributions have a double purpose. On the one hand, they are used as a first guess in the coupled model with given distribution of $\overline{\mathcal{D}}(s, d)$ by projecting them on isopycnals. On the other hand, they define the boundary condition at $s_{\max}$, that is, outside the vortex where isopycnals are flat.

4.4 Results

In this section we investigate the phytoplankton response to light and nutrients. To this end, different cases are explored considering the isopycnal vertical displacement $\mathcal{D}$, the non-dimensional diffusion coefficient $\mathcal{K}$, and the maximum of total nitrogen T_1 (see section 4.3.1 for parameters range). The distribution of $\mathcal{D}$ modifies the phytoplankton light regime of a given isopycnal, while diffusion tends to homogenize ecological variables along isopycnals. The factor T_1 defines the trophic regime of the system. The ecosystem dynamics without diffusion is first analyzed considering vortices of variable isopycnal vertical displacement embedded in various trophic regimes (section 4.4.1). Next, diffusion is considered in these

symbol	description	value	units
A_w	light attenuation by sea water	0.03	m^{-1}
A_p	light attenuation by phytoplankton	9.5×10^{-3}	$\mathrm{m}^2\,\mathrm{mmol\,N}^{-1}$
I_0	surface available radiation	234.11	$\mathrm{W\,m}^{-2}$
Ψ_0	initial slope of the P-I curve	0.025	$\mathrm{m}^2\,\mathrm{W}^{-1}\,\mathrm{d}^{-1}$
V_0	phytoplankton maximum uptake rate	3.6	d^{-1}
K_0	half-saturation for phytoplankton uptake	0.5	$\mathrm{mmol\,N\,m}^{-3}$
Ξ_0	phytoplankton specific mortality rate	0.1	d^{-1}
R_0	zooplankton maximum grazing rate	0.8	d^{-1}
Λ_0	Ivlev constant	0.4	$\mathrm{mmol\,N}^{-1}\,\mathrm{m}^3$
Γ_0	fraction of zooplankton grazing egested	0.25	
Θ_0	zooplankton excretion/mortality rate	0.05	d^{-1}

Table 4.1: List of ecological constants corresponding to an oligotrophic environment as extracted from Lawson et al. (1996). The Z *specific* excretion/mortality rate Φ_0 is computed normalizing Θ_0 by the spatially averaged Z. All constants are made adimensional in the physical-ecological coupled model.

different trophic conditions (section 4.4.2) and vortex types (section 4.4.3). One general result is that ecological stationary profiles numerically stable are reached in all considered cases.

4.4.1 Isopycnal vertical displacement and trophic regime

Isopycnal doming deepens the isolines of N,P,and Z towards the vortex center (Fig. 4.5) because the irradiance received by an isopycnal increases when it shallows. Thus P increases in detritment of N, and so does the grazer community. In addition, when T_1 increases from $1\mathcal{L}^3$ mmol N to $8\mathcal{L}^3$ mmol N, the maximum of P is doubled (Figs. 4.5a,b), while that of Z is enhanced by one order of magnitude (Figs. 4.5c,d). In fact, this is not an original contribution since phytoplankton growth is limited by light and nutrients. Our aim is to quantify this limitation when the light regime is modulated by cyclones. To this end, we define the anomaly of any variable $\chi(s, d, \mathcal{K}, \mathcal{D}_{\max}, T_1)$ with respect to a reference state where isopycnals are flat (dotted lines in Fig. 4.5) as

$$\chi'(s, d, \mathcal{K}_0, 0.39, T_1) \equiv \chi(s, d, \mathcal{K}_0, 0.39, T_1) - \chi(s, d, \mathcal{K}_0, 0, T_1)\,, \tag{4.29}$$

where $\mathcal{K}_0 = 0$. The largest isopycnal vertical displacement, and thus irradiance change, occurs at the vortex center at isopycnal $d_I = -1$ (Fig. 4.3). Accordingly, in the $T_1 = 8\mathcal{L}^3$ mmol N case, the maximum of P' is located close to d_I, but it turns out to be much deeper

($d \cong -1.9$) when $T_1 = 1\,\mathcal{L}^3$ mmol N (Figs. 4.6a,b). This paradox is addressed by subsequently splitting the anomalies of the physiological processes. Anomalies of phytoplankton growth G_P and grazing R are positively coupled as are P' and Z' in both trophic conditions. However, they are one order of magnitude larger in the $T_1 = 8\,\mathcal{L}^3$ mmol N case than the lowest T_1 case (Figs. 4.6c,d). The production of P depends upon the light but also upon nutrients. While the former attenuates with depth, the latter increases. When $T_1 = 1\,\mathcal{L}^3$ mmol N, the distribution of P' resembles that of the nutrient uptake. In contrast, when $T_1 = 8\,\mathcal{L}^3$ mmol N the pattern of P' correlates better with the photosynthetic rate L (Figs. 4.6e,f). Thus we have characterized two different ecological dynamics depending on the light regime and the trophic condition.

We have focused so far on one vortex type and on two trophic regimes. In order to

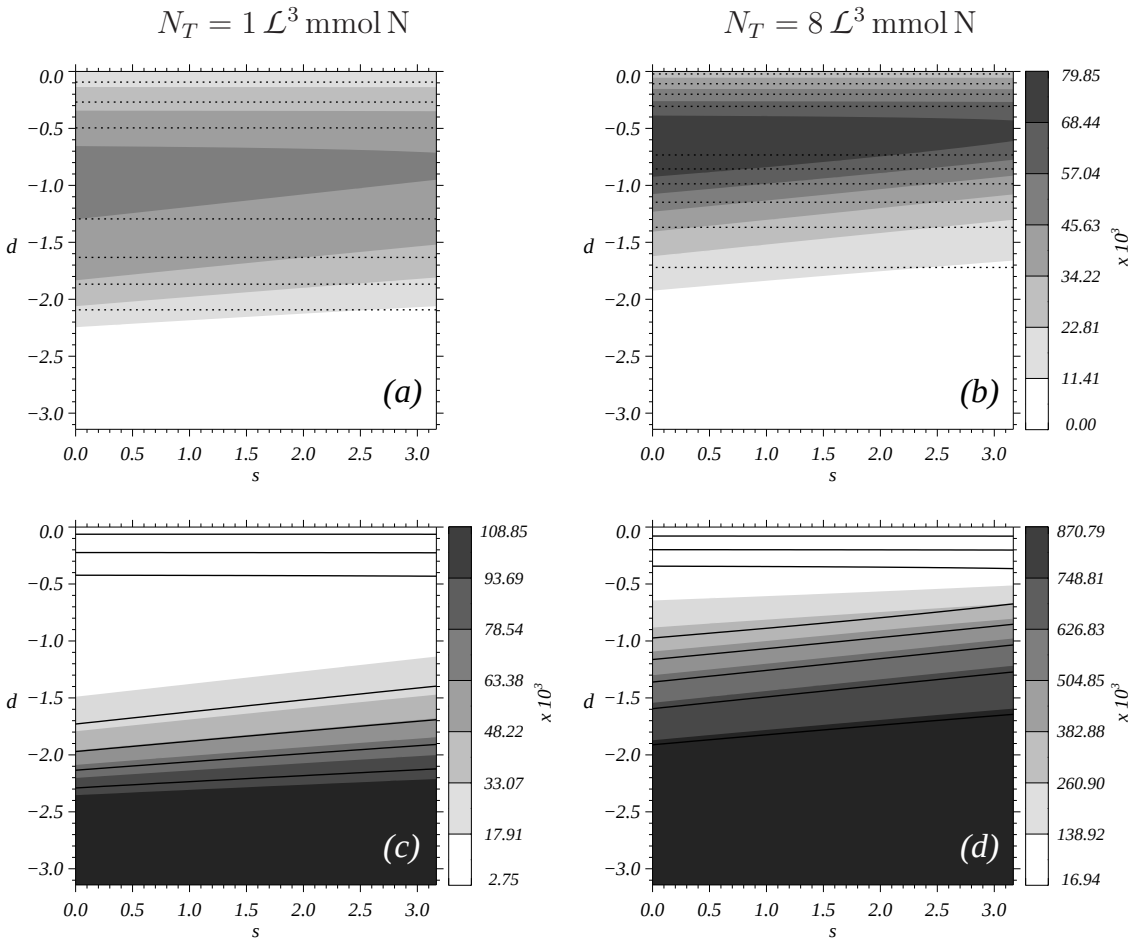

Figure 4.4: Vertical distributions with $\mathcal{K} = 0$ and $\mathcal{D}_{\max} = 0.39$ of (a,b) $P(s,d)$ in shaded contours and $\hat{P}(d)$ (dotted line, max $\cong 70.5 \times 10^3$ mmol N, $\delta \simeq 10^5$ mmol N); and (c,d) $N(s,d)$ and $Z(s,d)$ (solid line, $Z_{\max} \cong 52.79\,(592.57) \times 10^3$ mmol N, $\delta Z \simeq 10^4\,(10^5)$ mmol N in c (d)). Left panels correspond to N_T maximum $T_1 = 1\,\mathcal{L}^3$ mmol N, while right panels to $T_1 = 8\,\mathcal{L}^3$ mmol N.

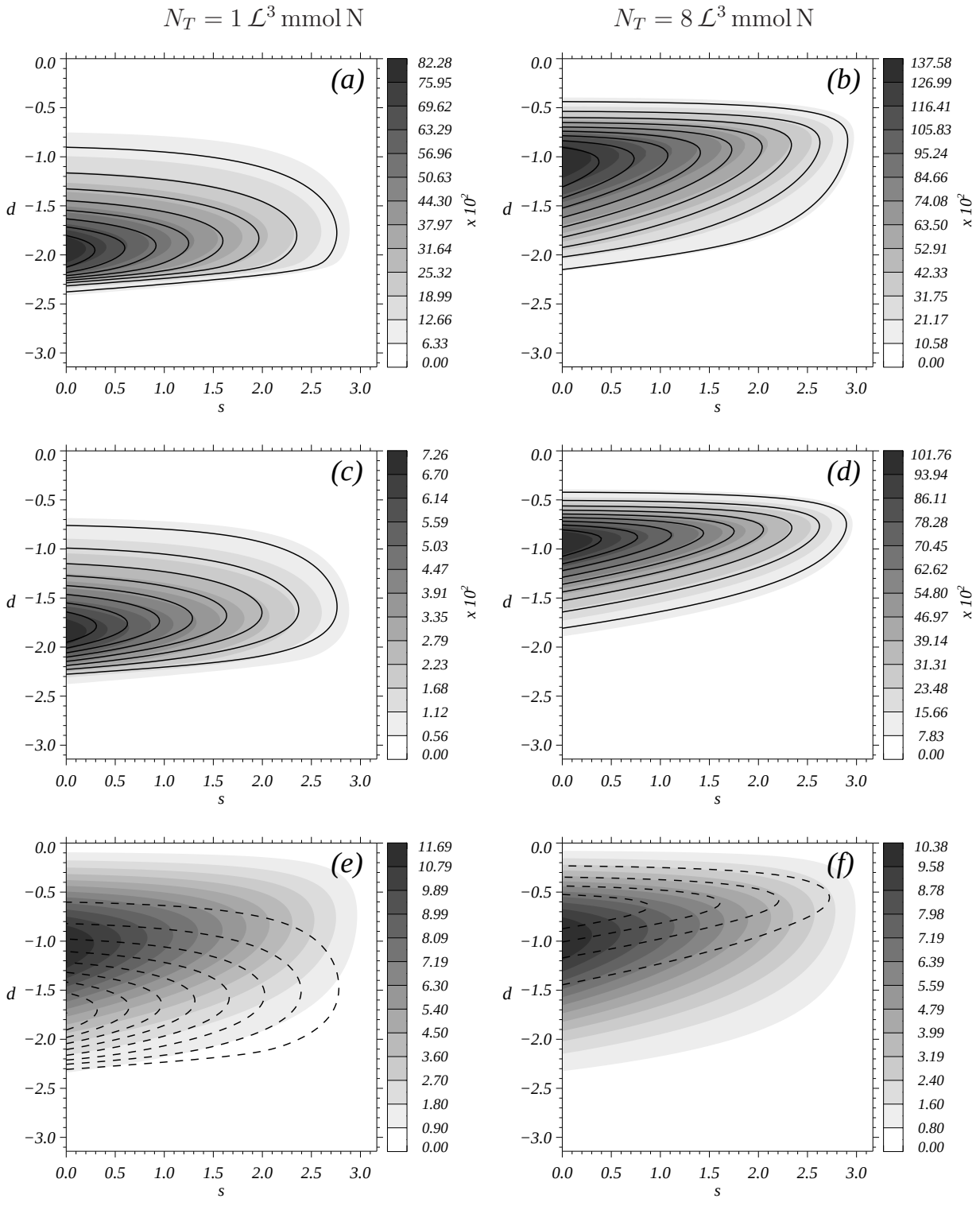

Figure 4.5: (a,b) Vertical distributions of $P'(s,d)$, in grey scale, and $Z'(s,d)$, contour lines, for (a) $Z'_{\max} \cong 8995$ mmol N ($\delta Z' \simeq 10^3$ mmol N), and (b) $Z'_{\max} \cong 97569$ mmol N ($\delta Z' \simeq 10^4$ mmol N). (c,d) Vertical distributions of $G'_P(s,d)$, in grey scale, and $R'(s,d)$, contour lines, for (c) $R'_{\max} \cong 467$ mmol N ($\delta R'_{\max} \simeq 50$ mmol N), and (d) $R'_{\max} \cong 9741$ mmol N ($\delta R'_{\max} \simeq 10^3$ mmol N). (e,f) Vertical distributions of $G'(s,d)$, in grey scale, and $N/(K_0+N)|'(s,d)$, contour lines, max $\cong 9.39 \times 10^{-2}$ ($\delta \simeq 10^{-2}$).

unveil whether values of $\mathcal{D}_{\max}$ and T_1 can cause a switch on the ecosystem dynamics, we characterize the phytoplankton response through the following enhancement factors

$$\tilde{\chi}(\mathcal{K}_0, \mathcal{D}_{\max}, T_1) \equiv \frac{\chi_\Omega(\mathcal{K}, \mathcal{D}_{\max}, T_1)}{\chi_\Omega(\mathcal{K}, 0, T_1)}, \tag{4.30}$$

$$\breve{\chi}(\mathcal{K}_0, \mathcal{D}_{\max}, T_1) \equiv \frac{\chi_\Omega(\mathcal{K}, \mathcal{D}_{\max}, T_1)}{\chi_\Omega(\mathcal{K}, \mathcal{D}_{\max}, 1\,\mathcal{L}^3\,\mathrm{mmol\,N})}, \tag{4.31}$$

where χ_Ω is the spatially integrated χ over the radial section Ω, that is,

$$\chi_\Omega(\mathcal{K}, \mathcal{D}_{\max}, T_1) \equiv \int_\Omega \chi(s, d, \mathcal{K}, \mathcal{D}_{\max}, T_1)\,\mathrm{d}\mathcal{S}. \tag{4.32}$$

The former parameter ($\tilde{\chi}$) gives the increase factor of χ_Ω with respect to the vortex case with minimum $\mathcal{D}_{\max}$ for a given trophic regime. In contrast, the latter ($\breve{\chi}$) is the increase factor compared to the case with minimum T_1 for a fixed vortex type. On the one hand, we observe that $\tilde{P}$ and $\tilde{Z}$ increase linearly with $\mathcal{D}_{\max}$ and thus with light (Figs. 4.7a,b). On the other hand, $\breve{P}$ and $\breve{Z}$ show a saturating response with $\mathcal{D}_{\max}$ (Figs. 4.7c,d). In addition, the increase of Z with T_1 is nearly independent of $\mathcal{D}_{\max}$ and may represent about a seven-fold increase with respect to that of P. Consequently, the ecosystem is more sensitive to N_T than to $\mathcal{D}_{\max}$ and seems to evolve to a top-down control as T_1 increases.

4.4.2 Diffusion and trophic regime

We have stated in the previous section that the light regime may increase the spatially integrated P and Z up to 14% and 13%, respectively, depending on the trophic regime. We investigate next whether diffusion may account for further increase. To this end, we focus on the vortex case with maximum $\mathcal{D}_{\max}$ since it determines the largest P_Ω and Z_Ω increase without diffusion, and explore a range of $\mathcal{K}$ for different trophic regimes (varying T_1). Each case is here characterized through an enhancement factor referred to the case without diffusion, that is,

$$\acute{\chi}(\mathcal{K}, \mathcal{D}_{\max}, T_1) \equiv \frac{\chi_\Omega(\mathcal{K}, \mathcal{D}_{\max}, T_1)}{\chi_\Omega(\mathcal{K}_0, \mathcal{D}_{\max}, T_1)}. \tag{4.33}$$

In this section we consider $\acute{\chi}\,(\mathcal{K}, \mathcal{D}_{\max} = 0.39, T_1)$, though other vortex types are investigated in the upcoming section. We observe that diffusion maximizes P_Ω at given values of $\mathcal{K}$,

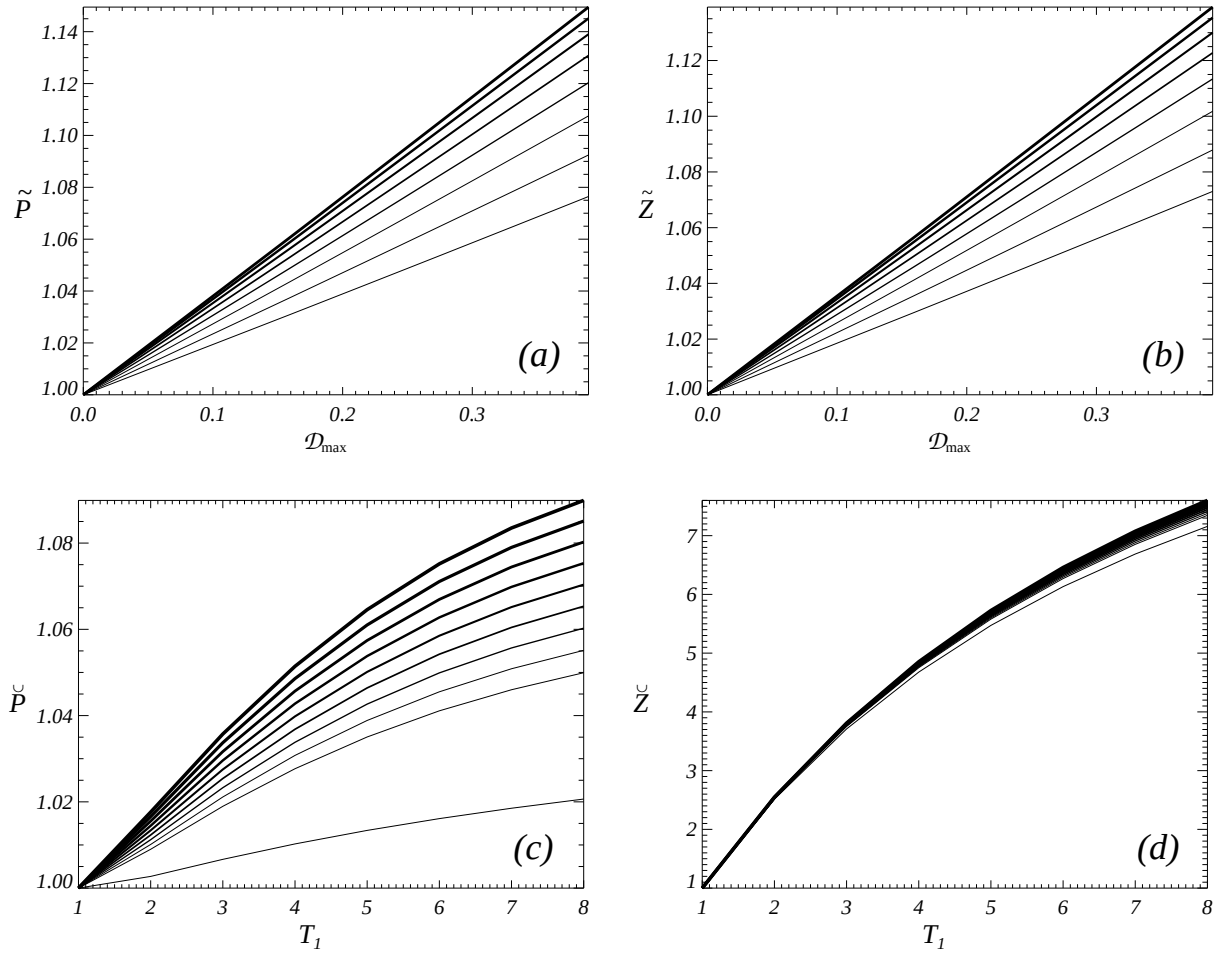

Figure 4.6: Distributions of (a) $\tilde{P}(\mathcal{D}_{\max})$ and (b) $\tilde{Z}(\mathcal{D}_{\max})$ for different N_T profiles. Progressive line thickness denotes an increase $\delta T_1 = 1\,\mathcal{L}^3$ mmol N. Distributions of (c) $\breve{P}(\mathcal{D}_{\max})$ and (d) $\breve{Z}(\mathcal{D}_{\max})$ for different vortex types. Progressive line thickness indicates an increase $\delta\mathcal{D}_{\max} \cong 0.025$.

which are referred to $\mathcal{K}^*$, for different trophic scenarios. For an oligotrophic condition ($T_1 = 1\,\mathcal{L}^3$ mmol N), the $\acute{P}$ maximum is achieved at $\mathcal{K}^* = 0.06$ and barely represents an 1% increase (Fig. **??**a). The value of $\mathcal{K}^*$ increases with T_1, reaching 0.3 at $T_1 = 8L^3$. When $\mathcal{K}^* \in (0.2, 0.3)$, $\acute{P}$ is the largest and accounts for a 5%–15% enhancement. In contrast, Z_Ω decreases with diffusion in all trophic regimes (Fig. **??**b). In order to put into general context the mentioned values, we consider the lower limit of the mesoscale ($c = 35$). In this case, $\mathcal{K}^* = 0.06$ and $\mathcal{K}^* = 0.3$ correspond to $\kappa = 5.8$ m^{2}s^{-1} and $\kappa = 30$ m^{2}s^{-1}, respectively. The former value of κ is in agreement with small-scale motions (section 4.3.1.3), while the latter with mesoscale flow. Thus we would expect that non-axisymmetric vortices would cause a similar overall increase in P when $T_1 > 1\,\mathcal{L}^3$ mmol N, which is in agreement with Pasquero (2005).

The enhancement of P_Ω occurs when physical and ecological time frequencies are in resonance. This mechanism has been described in stochastic systems with intrinsic spatio-temporal variability (noise), which are perturbed by an external periodic force when some threshold value is reached (Gammaitoni et al., 1998). In fact, resonant behaviours have been reported in plankton models considering either an intrinsic variability caused by light (Huisman et al., 1999; Ghosal and Mandre, 2003) or by an horizontal gradient of nutrients (Pasquero, 2005; McKiver and Neufeld, 2011). Thus the observed phytoplankton resonance response when both light and nutrients are spatially heterogeneous is predictable. However, in our case phytoplankton and diffusive time-scales are not comparable. This is so because the phytoplankton growth timescale is fixed in all considered cases. If we consider instead the spatially averaged P growth, that is $\tilde{\mathcal{T}} \equiv \langle GN/(K_0+N)\rangle$, and redefine the non-dimensional diffusion coefficient accordingly,

$$\tilde{\mathcal{K}} \equiv \frac{\kappa \tilde{\mathcal{T}}}{(\mathcal{L}c)^2}\,, \tag{4.34}$$

then the resonance behaviour occurs when ecological and diffusive timescales have about the same order of magnitude (Fig.**??**c). We take a step forward here by analyzing the three-dimensional nature of plankton dynamics at the resonant diffusion coefficient ($\mathcal{K}^*$). To this end, we quantify the departure of χ from its steady-state without diffusion through the following anomaly evaluated at $\mathcal{D}_{\max} = 0.39$

$$\chi''(s, d, \mathcal{K}^*, \mathcal{D}_{\max}, T_1) \equiv \chi(s, d, \mathcal{K}^*, \mathcal{D}_{\max}, T_1) - \chi(s, d, \mathcal{K}_0, \mathcal{D}_{\max}, T_1)\,, \tag{4.35}$$

considering the extreme trophic conditions. In both cases, diffusion enhances P at vortex midsection, while causes a maximum decrease in Z at vortex core (Figs. 4.8a,b). Firstly, the observed increase in P results from a balance between phytoplankton production G_P and diffusion. The order of magnitude of G''_P and $\mathcal{K}^*\partial^2 P/\partial s^2$ are similar, however G''_P has greater radial extension, which explains why the maximum of P'' is displaced from the vortex center (Figs. 4.8c,d). The distribution of G''_P results from a non-linear interaction between light and nutrients. Isopycnal diffusion causes a downgradient influx of N that uplifts N to better lit depths (not shown). The influx of N has similar order of magnitude than that of P but of opposite sign. This is so because the diffusive flux of Z is much smaller than that of P, since is more homogenized on isopycnals than P, and N_T is materially conserved. As a result, P'' correlates with $G''_P + \mathcal{K}^*\partial^2 P/\partial s^2$ (Figs.4.8e,f). Secondly, Z does not couple to

the P increase and its diffusive rate is larger than its growth rate (not shown), which implies a decrease in the grazing pressure. However, when nutrients availability is high, the along isopycnal outflux of Z is unsufficient to disrupt the P-Z coupling due to isopycnal doming. This explains why P'' correlates with R'' when $T_1 = 8\,\mathcal{L}^3\,\mathrm{mmol\,N}$.

Therefore, diffusion maximizes P biomass within vortices at a characteristic resonant diffusion coefficient. Two main mechanisms account for this increase. On the one side, diffusion uplifts nutrients to better lit levels through an influx along isopycnals that counterbalances the P diffusive outflux. On other side, Z does not couple to this P increase and shows a higher homogenization on isopycnals than P. As a result, the Z grazing pressure on P disminishes, uncoupling completely the distributions of P and Z in oligotrophic systems.

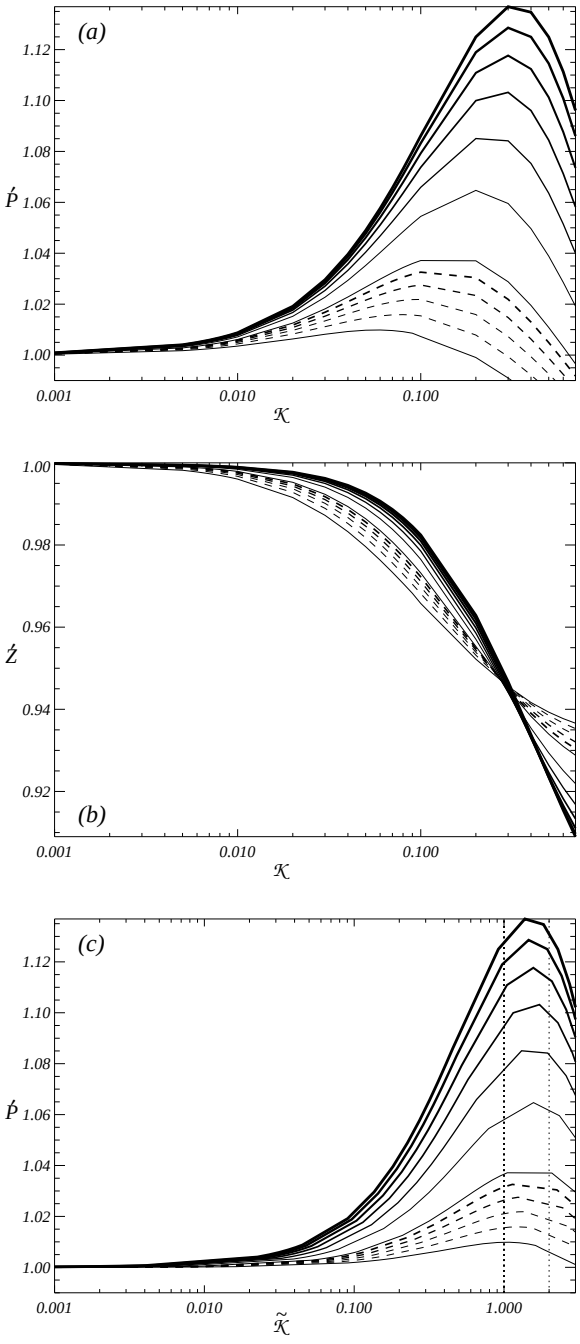

Figure 4.7: Distributions of (a) $\acute{P}(\mathcal{K})$, (b) $\acute{Z}(\mathcal{K})$, and (c) $\acute{P}(\tilde{\mathcal{K}})$ for different trophic conditions. Solid lines indicate an increase $\delta T_1 = 1\,\mathcal{L}^3\,\mathrm{mmol\,N}$, while dashed lines indicate an increase $\delta T_1 = 0.2\,\mathcal{L}^3\,\mathrm{mmol\,N}$.

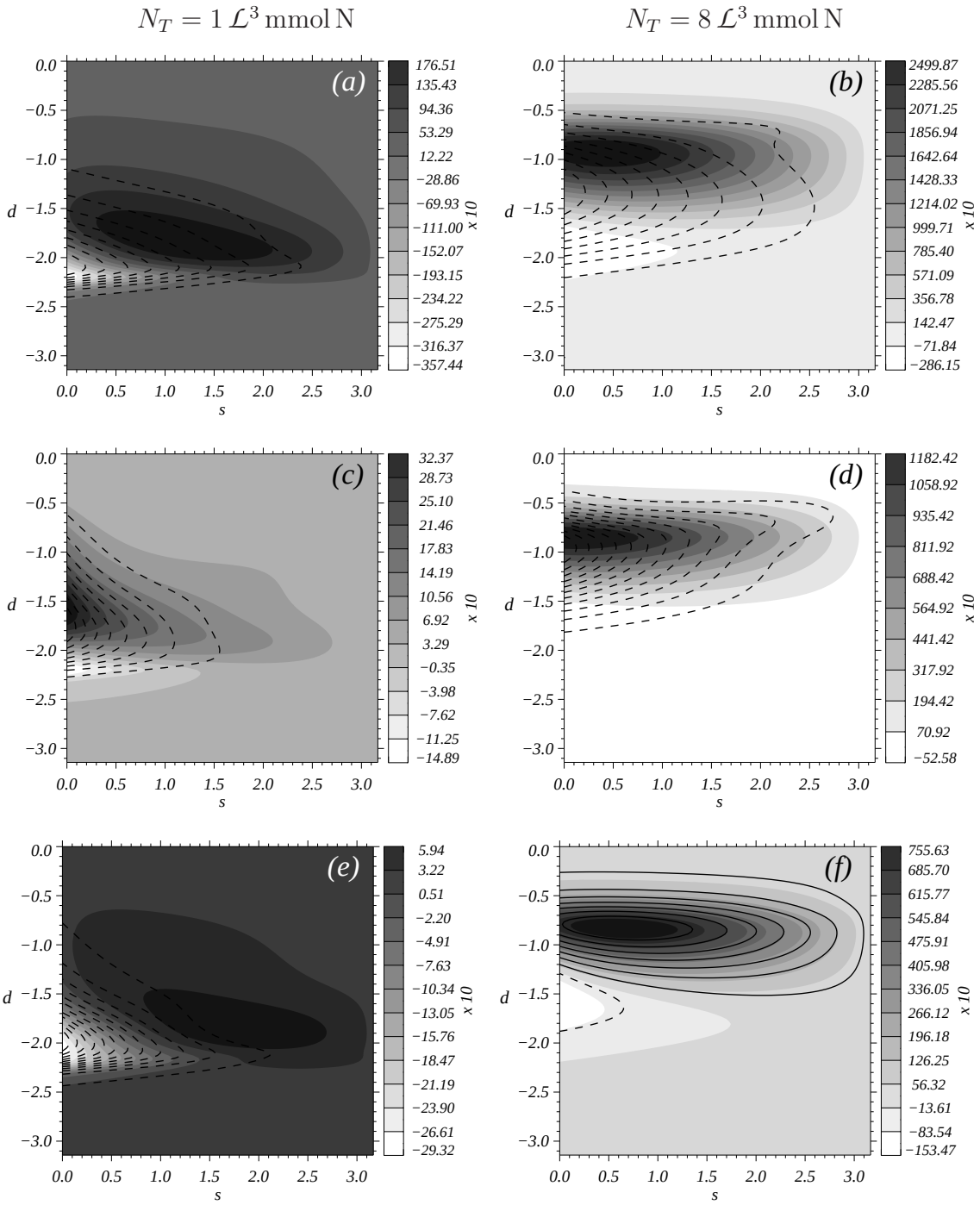

Figure 4.8: (a,b) Vertical distributions of $P'(s,d)$, in grey scale, and $Z'(s,d)$, contour lines, for (a) $Z'_{\min} = 8789$ mmol N ($\delta Z' \simeq 10^3$ mmol N), and (b) $Z'_{\min} = -90049$ mmol N ($\delta Z' \simeq 10^4$ mmol N). (c,d) Vertical distributions of $G'_P(s,d)$, in grey scale, and $(\mathcal{K}^* \, \partial^2 P/\partial s^2)(s,d)$, contour lines, for (c) min $= -433$ mmol N ($\delta \simeq 50$ mmol N), and (d) min $= -5909$ mmol N ($\delta \simeq 500$ mmol N). (e,f) Vertical distributions of $(G'_P + \mathcal{K}^* \, \partial^2 P/\partial s^2)(s,d)$, in grey scale, and $R'(s,d)$, contour lines, for (e) $R' \in (-233, 13)$ mmol N ($\delta R'_{\max} \simeq 20$ mmol N), and (f) $R' \in (-1634, 6793)$ mmol N ($\delta R'_{\max} \simeq 10^3$ mmol N).

4.4.3 Isopycnal vertical displacement and diffusion

We analyze next whether the characteristic resonant diffusion coefficient depends on the isopycnal vertical displacement. To this end, we fix the trophic condition to an arbitrary value $T_1 = 1.4\,\mathcal{L}^3\,\mathrm{mmol\,N}$ within the range $1 < T_1 < 2\,\mathcal{L}^3\,\mathrm{mmol\,N}$, where $\mathcal{K}^*$ shows the highest sensitivity (Fig. **??**a).

The maximum P response to diffusion occurs when $\mathcal{K}$ is $\mathcal{O}(0.1)$. Thus we explore a range of $\mathcal{K}$ comprised within $(0, 0.4)$ considering a subset of vortices with $\mathcal{D}_{\max} \in (0.16, 0.39)$. Each case is characterized by the enhancement factor with respect to the state without diffusion, that is, $\acute{P}(\mathcal{K}, \mathcal{D}_{\max}, 1.4\,\mathcal{L}^3\,\mathrm{mmol\,N})$. We observe that $\mathcal{D}_{\max}$ affects the magnitude of $\acute{P}$ maximum but not the value of $\mathcal{K}$ (Fig. 4.9a). Firstly, as stated in the first section, P increases linearly with $\mathcal{D}_{\max}$ and accordingly a linear increase is also expected in $\acute{P}$. Secondly, $\mathcal{K}^*$ shifts from 0.08 to 0.1 at $\mathcal{D}_{\max} = 0.16$ and $\mathcal{D}_{\max} = 0.4$, respectively. The resonant behaviour is reached when P and diffusive timescales are comparable. So that, the factors determining the location of $\acute{P}$ maximum in the $(\mathcal{K}, \mathcal{D}_{\max})$ space should be related to the P diffusive rate and the increase in the P growth rate caused by diffusion. In this regard, $\acute{P}$ maximum is reached when

$$\eta \equiv \frac{\mathcal{K}\partial^2 P/\partial s^2|_\Omega}{(G''_P - M''_P)|_\Omega} \cong 1.08\,, \tag{4.36}$$

which corresponds to the characteristic non-dimensional diffusion coefficient $\tilde{\mathcal{K}}$ at which $\acute{P}$ is maximum for this trophic condition. Isopycnal doming increases diffusion, since it steepens isopycnals slopes, and also phytoplankton growth, because it enhances the irradiance received by the uplifted phytoplankton. As a result, $\mathcal{K}^*$ is nearly unaffected by $\mathcal{D}_{\max}$. However, phytoplankton growth and diffusion do not account totally for $\acute{P}$ (Fig. 4.9b). We observed that diffusion uncouples P and Z, and thus decreases the grazing pressure on P. Consequently, when Z grazing is included, the resulting balance correlates with $\acute{P}$ (not shown).

4.5 Concluding remarks

We constructed a simple numerical model to investigate the dynamics of a fully-recycling ecosystem within mesoscale vortices. Particularly, we focused on surface cyclones and subsurface anticyclones since their isopycnals are domed in the upper layer. The novelty of

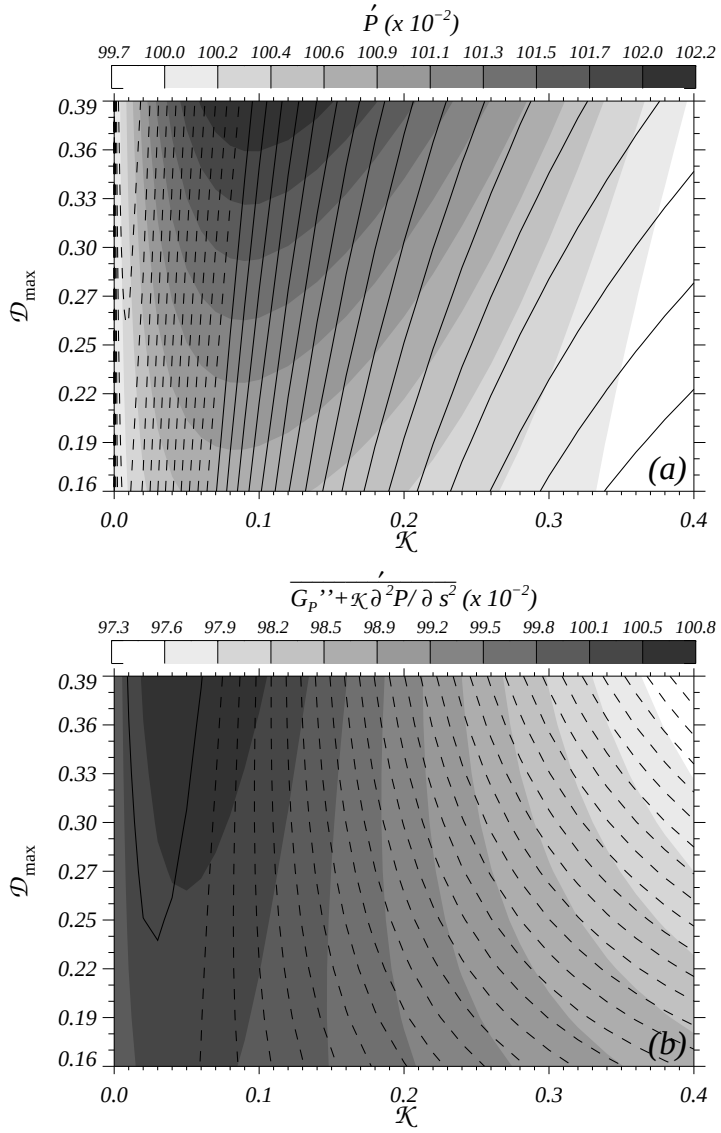

Figure 4.9: Distributions of (a) $\acute{P}\,(\mathcal{K}, \mathcal{D}_{\max})$ and $\eta' = \eta - 1.08$ (contour line, $\eta' \in (-0.4, 0.6)$, $\delta\eta' \cong 0.035$), (b) $\overline{G_P'' + \mathcal{K}\partial^2 P/\partial s^2}\,(\mathcal{K}, \mathcal{D}_{\max})$ and $\acute{R}''\,(\mathcal{K}, \mathcal{D}_{\max})$ (contour line, $\in (-4, 0.2) \times 10^{-2}$, $\delta \cong 1.5 \times 10^{-3}$). The trophic condition is $T_1 = 1.4\,\mathcal{L}^3\,\mathrm{mmol\,N}$.

this model was that the mesoscale forcing was introduced in terms of vertical displacement of isopycnals in the NPZ (Nutrients-Phytoplankton-Zooplankton). Using this physical-ecological coupled model, the impact of the trophic regime, vortex intensity, and small-scale motions, parametrized as a Fickian-type isopycnal diffusion, on the ecosystem was explored. In all considered cases, stationary ecological solutions numerically stable, with coexistence of phytoplankton (P) and zooplankton (Z), were obtained.

The trophic regime, determined by the maximum of total nitrogen, characterized two different ecological dynamics. In the oligotrophic regime case, P and Z anomalies (with respect to a reference state where isopycnals are flat as outside the vortex) had similar magnitude.

These anomalies were localized at the vortex bottom edge, where the nutrients (N) flux was the largest. When a mesotrophic regime was instead initialized, Z anomalies were one order of magnitude larger than those of P. Both anomalies had their maximum localized at the isopycnal with the largest vertical displacement, and thus the one experiencing the largest change in irradiance.

Small-scale motions, parametrized as a Fickian-type diffusion along isopycnals, increased the spatially integrated P biomass up to 1% or 15% depending on the trophic condition. This increase occurred at a characteristic diffusion coefficient ($\mathcal{K}^*$) due to a resonance mechanism between diffusive and phytoplankton timescales. That is, when the ratio between diffusive and phytoplankton growth rates was close to one. Two main mechanisms were involved in this P increase. Firstly, diffusion uplifted N to better lit levels through a N influx that counterbalances the P outflux. Secondly, Z uncoupled to its prey increase because the growth rate of P was larger than that of Z. As a result, the Z outflux was larger than that of P and the grazing pressure diminished in benefit of the latter. The largest contribution of diffusion in maximizing P was observed in mesotrophic regimes. However, large $\mathcal{K}^*$ values were required and some caution should be taken when interpreting them. Considering $\mathcal{K}^* = 0.3$ and the upper bound of the small-scale motion parametrization ($\kappa = 10\,\mathrm{mmol\,N\,m^3}$), results in a Prandtl ratio $c \cong 20$, which is comprised within the submesoscale. Since our basic equations were inappropiate to model submesoscale viscid dynamics, we constrain instead c to the lowest mesoscale bound ($c = 35$). In this case, $\kappa \cong 30\,\mathrm{m^2\,s^{-1}}$, which approaches to the parametrization of mesoscale motions (Martin et al., 2001; Ledwell et al., 2008). This suggests that resonance between plankton growth and advective rates occurs within non-axisymmetric vortices, which has been already reported by Pasquero (2005).

Finally, the vortex intensity, modeled through the maximum isopycnal vertical displacement, exerted an antagonistic effect on the ecosystem. On the one side, it induced a positive linear P response since P and N were uplifted to better lit depths. Isopycnal doming accounted for an increase about 8% or 15% of the P biomass corresponding to a scenario with flat isopycnals depending on the trophic condition. On other side, it also increased diffusive fluxes since steepened the isopycnal slopes. As a result, $\mathcal{K}^*$ was nearly independent of the isopycnal vertical displacement. This suggests that the P enhancement factor may be approximated by additive contributions of isopycnal doming and diffusion at $\mathcal{K}^*$.

Chapter 5

Vertical velocity in the interaction between inertia-gravity waves and submesoscale baroclinic structures

This chapter has been published as:
Claret, M., and A. Viúdez, 2010: Vertical velocity in the interaction between inertia-gravity waves and submesoscale baroclinic structures. *J. Geophys. Res.*, **115, C12060**, doi:10.1029/2009JC005921.

A la vida o al cor quelcom li prenen les ones que se'n van;
si no tinc res, les ones que ara vénen dieu-me què voldran?

Vora la mar, Jacint Verdaguer

ABSTRACT

The interaction between submesoscale baroclinic vortical structures and large amplitude inertia–gravity waves (IGWs), with emphasis on the vertical velocity, is numerically investigated using a high-resolution three-dimensional non-hydrostatic model. A rich variety of vortex-wave interactions are possible depending on the potential vorticity (PV) content and length scale of the submesoscale monopoles or dipoles, and on the amplitude and wavenumber of the IGWs. On the one hand the large amplitude IGWs cause horizontal and vertical advection of the vortices, which conserve their stability though their geometry is largely modified by the wave motion. On the other hand the horizontal vortical motion Doppler shifts the local frequency of the IGWs. The vortical angular velocity and vortex density stratification lead to a wave dispersion relation involving the *effective* Coriolis frequency (Coriolis frequency plus the vortical angular velocity) and the *total* Brunt-Väisälä frequency. This inhomogeneous change in the local wave frequency causes the IGWs depart from their initial plane geometry. In the particular case of inertial waves, the non-linear vortex-wave interaction generates spiral IGWs, having vertical velocities one order of magnitude larger than the submesoscale vortical flow in the absence of waves.

5.1 Introduction

Recent numerical works have reproduced the fully three-dimensional nature of submesoscale flows (e. g., Capet et al., 2008), where vertical velocity can reach values one order of magnitude greater than those at the mesoscale (Mahadevan, 2006). Submesoscale structures have been reported both in the upper ocean (Rudnick and Luyten, 1996; Shay et al., 2003; Capet et al., 2008) and deep ocean (McWilliams, 1985; Testor and Gascard, 2003; Steffen and D'Asaro, 2004; Kasajima et al., 2006). On the other hand, inertia–gravity waves (IGWs) are also ubiquitous in the ocean (Garrett and Munk, 1979; Miropol'sky, 2001; Pedlosky, 2003), and consequently interaction between submesoscale flows and IGWs is a frequent phenomenon. Here we address this interaction, focusing on the vertical velocity, in the special case where vortical and wave flows have similar amplitudes.

The submesoscale refers to flows with horizontal scales L of order 1, and Rossby $\mathcal{R}$ and Froude $\mathcal{F}$ numbers also of order 1. It plays an important role in the ocean because it facilitates the energy transfer from the mesoscale to smaller scales (Molemaker et al., 2005), and the vertical flux of momentum, buoyancy, potential vorticity (PV), and biogeochemical properties (Lévy et al., 2001; Thomas et al., 2008). In the deep ocean, long-lived submesoscale vortices are also responsible for both deep convection (Gascard et al., 2002), and horizontal transport, as they are advected away from their origin by mean currents (Testor and Gascard, 2003).

In the particular case of near-inertial oscillations, anisotropy of the wave field caused by the mesoscale geostrophic motions has been extensively reported (Mooers, 1975a,b; Perkins, 1976; Weller, 1982; Kunze, 1984; van Meurs, 1998; Niwa and Hibiya, 1999). Several vortex-wave interactions have been proposed to explain this wave heterogeneity, like wave trapping of IGWs inside vortices (Kunze, 1985), wave capture (Bühler and McIntyre, 2005), dispersion of near-inertial energy by geostrophic eddies (Young and Jelloul, 1997; van Meurs, 1998), inertial pumping (Rubenstein and Roberts, 1986), or resonance mechanisms (Niwa and Hibiya, 1999; Danioux and Klein, 2008b). Here we address both the vortex-wave mechanisms that explain the wave frequency shift by submesoscale vortices and the PV structures that remain coherent after being advected by large amplitude IGWs. Our results extend the works mentioned above by using a non-hydrostatic numerical model, which considers the fully nonlinear three-dimensional momentum equations and resolves the vertical velocity

with high accuracy, to simulate baroclinic assymmetric PV flows of length scales *similar* to those of the pre-existent wave field.

The first vortex-wave interaction we introduce implies vortical motion affecting plane IGWs. This occurs both through the wave frequency Doppler-shift ($\mathbf{K}_h \cdot \mathbf{u}_{bh}$), where $\mathbf{K}_h$ is the horizontal wavenumber and $\mathbf{u}_{bh}$ the horizontal vortical (balanced) velocity, and through the vortical angular velocity and vortex density stratification anomaly, which lead to *effective* Coriolis and Brunt-Väisälä frequencies in the dispersion relationship of Kunze (1985). The second interaction is the advection of the vortical flow by large amplitude IGWs. In this case, the vortex geometry is largely deformed giving rise to new circulation generated in the process towards geostrophic adjustment. Finally, nonlinear vortex-waves interactions trigger a spiral IGW when a pure inertial wave is present in a vortex flow. In this case horizontal gradients of the vertical vorticity ζ generate gradients in the *effective* Coriolis frequency, through the $\zeta/2$ shift (Mooers, 1975a; Kunze, 1985; Rubenstein and Roberts, 1986) originating divergence of the wave field from which vertical velocity develops.

In this work we use a triply periodic non-hydrostatic numerical model under the Boussinesq and f-plane approximations (section 5.2) to examine the interaction between submesoscale baroclinic vortex structures with Rossby number $\mathcal{R} \lesssim 1$ and pre-existent IGW fields. We particularly focus on the generation of spiral patterns of vertical velocity. The flow has constant *background* Prandtl ratio $N/f = 10$, where N and f are constant background Brunt-Väisälä and Coriolis frequencies, respectively. We consider two types of vortical structures and waves, namely the monopolar vortex (cyclonic and anticyclonic) and the vortex dipole, and two types of waves, namely pure inertial and gravity plane waves (section 5.3). Next we investigate the flow of a monopole embedded in initially plane inertial and gravity wave fields (sections 5.4.1 and 5.4.2). The vortex, although no longer homogeneous nor steady, remains always stable despite the substantial advection by the large IGWs. Interactions between a submesoscale dipole, the simplest vortical structure having linear momentum, and large amplitude IGWs of different wavenumbers are addressed in section 5.5. The baroclinic dipole remains coherent despite the presence of large amplitude wave fields. The balanced and unbalanced components of the flow are extracted from the *total* flow and are separately analyzed. Finally, conclusions are given in section 5.6.

5.2 Numerical Model And Parameters

5.2.1 $\mathcal{AB}\varpi$-model

The non-hydrostatic numerical model (hereinafter referred to as the $\mathcal{AB}\varpi$-model) simulates the isochoric (volume-preserving) flow of a stratified rotating fluid under the Boussinesq and f-plane approximations (Dritschel and Viúdez, 2003). Here the flow is initialized with 1) a localized vortical flow specified by the potential vorticity PV using the PV initialization approach (Viúdez and Dritschel, 2003), and 2) a plane IGW background field (described in section 5.3.1). The theoretical basis of the numerical model is explained in detail in the references above, succinctly here in appendix A and only a brief definition of the physical quantities is given next.

The Froude number $\mathcal{F} \equiv \omega_h/\mathcal{N}$ and the Rossby number $\mathcal{R} \equiv \zeta/f$, where ω_h and ζ are the horizontal and vertical components of the relative vorticity $\boldsymbol{\omega} \equiv \boldsymbol{\omega}_h + \zeta\mathbf{k}$, and $\mathcal{N}$ is the *total* Brunt-Väisälä frequency. The vertical displacement of isopycnals is defined as $\mathcal{D}(\boldsymbol{x},t) \equiv z - d(\boldsymbol{x},t)$, where $d \equiv (\rho-\rho_0)/\varrho_z$ is the depth that an isopycnal located at $\boldsymbol{x}$ at time t has in the reference density configuration defined by $\rho_0 + \varrho_z z$. Above $\rho(\boldsymbol{x},t)$ is the mass density, and $\rho_0 > 0$ and $\varrho_z < 0$ are constant values that do not need to be specified in the Boussinesq approximation. The squared *total* Brunt-Väisälä frequency is therefore

$$\mathcal{N}^2(\mathbf{x},t) = N^2\left(1 - \frac{\partial\mathcal{D}}{\partial z}(\mathbf{x},t)\right). \tag{5.1}$$

Static instability occurs when the stratification number $\mathcal{D}_z \equiv \partial\mathcal{D}/\partial z > 1$, and inertial instability when $\mathcal{R} < -1$.

The $\mathcal{AB}\varpi$-model integrates the dimensionless ageostrophic horizontal vorticity $\mathcal{A}_h = (\mathcal{A},\mathcal{B}) \equiv \tilde{\boldsymbol{\omega}}_h - c^2\boldsymbol{\nabla}_h\mathcal{D}$,

$$\frac{d\mathcal{A}_h}{dt} = -f\mathbf{k}\times\mathcal{A}_h + (1-c^2)\boldsymbol{\nabla}_h w + \tilde{\boldsymbol{\omega}}\cdot\boldsymbol{\nabla}\mathbf{u}_h + c^2\boldsymbol{\nabla}_h\mathbf{u}\cdot\boldsymbol{\nabla}\mathcal{D}\,, \tag{5.2}$$

where $N^2 \equiv -g\varrho_z/\rho_0$, the Prandtl ratio $c \equiv N/f$, the relative vorticity $\boldsymbol{\omega} \equiv \boldsymbol{\nabla}\times\mathbf{u}$, the velocity $\mathbf{u} = \mathbf{u}_h + w\mathbf{k}$, $\boldsymbol{\nabla}$ is the gradient operator, subscript h denotes the horizontal component, and $\tilde{\chi} \equiv \chi/f$, for any quantity χ. The material derivative $d\chi/dt \equiv \partial\chi/\partial t + \mathbf{u}\cdot\boldsymbol{\nabla}\chi$. The third prognostic equation is the explicit conservation of PV *anomaly* ϖ through

PV contour advection on isopycnal surfaces

$$\frac{d\varpi}{dt} = 0\,, \tag{5.3}$$

where

$$\varpi \equiv \Pi - 1 = \frac{\boldsymbol{\omega} + f\mathbf{k}}{f} \cdot \boldsymbol{\nabla} d - 1 = (\tilde{\boldsymbol{\omega}} + \mathbf{k}) \cdot (\mathbf{k} - \boldsymbol{\nabla}\mathcal{D}) - 1 = \tilde{\zeta} - \frac{\partial \mathcal{D}}{\partial z} - \tilde{\boldsymbol{\omega}} \cdot \boldsymbol{\nabla}\mathcal{D}\,, \tag{5.4}$$

and Π is the *total* PV.

The state variables are the components of the three-dimensional vector potential $\boldsymbol{\varphi} = (\varphi, \psi, \phi)$ which provide the velocity $\tilde{\mathbf{u}} = -\boldsymbol{\nabla} \times \boldsymbol{\varphi}$ and the vertical displacement of isopycnals $\mathcal{D} = -c^{-2}\boldsymbol{\nabla} \cdot \boldsymbol{\varphi}$. The horizontal components of the vector potential $\boldsymbol{\varphi}_h = (\varphi, \psi)$ are diagnosed every time-step by inversion of $\mathcal{A}_h = \nabla^2 \boldsymbol{\varphi}_h$, while the vertical component ϕ is obtained from the inversion of the ϖ definition (5.4) as a function of (φ, ψ, ϕ).

5.2.2 Numerical Parameters

The model domain is a triply periodic box of vertical extent $L_Z = 2\pi$ (which defines the unit of space) and horizontal extents $L_X = L_Y = cL_Z$, where $c = 10$. The number of grid points $(n_X, n_Y, n_Z) = (128, 128, 128)$, and isopycnal surfaces $n_l = 128$. The background Brunt-Väisälä frequency $N = 2\pi$, which defines the background buoyancy period as the unit of time, $T_{bp} \equiv 2\pi/N = 1$. One inertial period $T_{ip} = cT_{bp}$.

All variables are non-dimensional. To recover the physical dimensions of any quantity given the dimensional domain depth H and mean latitude θ_0, we need to multiply the dimensionless numerical value by the spatial and time scale conversion factors $S_z = H/\pi$ and $S_t = 1\,\text{day} \,/\, 2c\sin\theta_0$, respectively, elevated to the appropriate powers to match the physical dimensions. The time-step δt ranges from $\delta t = 0.1$ for slow inertial waves to $\delta t = 10^{-4}$ for large amplitude and fast gravity waves.

5.3 Initialization

5.3.1 Wave Initialization

The initial IGW field is set at $t = 0$ from the complex plane wave solutions for the potential components $\hat{\boldsymbol{\varphi}}_i$ in terms of the complex vertical displacement $\hat{\mathcal{D}}_i$, namely

$$\hat{\boldsymbol{\varphi}}_i = (\hat{\varphi}_i, \hat{\psi}_i, \hat{\phi}_i) = \frac{1}{K_h^2}[\tilde{\omega}_l\,(-l + \mathrm{i}k\tilde{\omega}_l)\,, \tilde{\omega}_l\,(k + \mathrm{i}l\tilde{\omega}_l)\,, \mathrm{i}m(1-c^2)]\,\hat{\mathcal{D}}_i\,. \tag{5.5}$$

Above the complex fields $\hat{\chi} = \hat{\chi}_0\, e^{\mathrm{i}\theta}$ for any variable χ, where θ is the wave phase, the three-dimensional wavenumber $\mathbf{K} = (k, l, m) \equiv \boldsymbol{\nabla}\theta$, $K_h \equiv |\mathbf{K}_h|$, and the *local* frequency $\omega_l \equiv -\partial\theta/\partial t$ satisfies the dispersion relation $\omega_l^2 = (N^2K_h^2 + f^2m^2)/K^2$, with $K \equiv |\mathbf{K}|$. These plane IGWs have zero PV *anomaly* ($\varpi\{\hat{\boldsymbol{\varphi}}_i\} = 0$) and imply

$$\begin{aligned} \hat{\mathbf{u}}_i &= (\hat{u}_i, \hat{v}_i, \hat{w}_i) = \frac{m}{k_h^2}\,(\mathrm{i}\omega_l\mathbf{K}_h + f\mathbf{k}\times\mathbf{K}_h)\hat{\mathcal{D}}_i - \mathrm{i}\omega_l\hat{\mathcal{D}}_i\,\mathbf{k}\,, \\ \hat{\zeta}_i &= \mathrm{i}fm\hat{\mathcal{D}}_i\,, \qquad\qquad \hat{\mathcal{D}}_{iz} = \mathrm{i}m\hat{\mathcal{D}}_i\,, \end{aligned} \tag{5.6}$$

so that static stability ($\mathcal{D}_z < 1$) and inertial stability ($\mathcal{R} < -1$) require $m|\hat{\mathcal{D}}| < 1$, which is always satisfied in our initial conditions.

The wave potentials $\hat{\boldsymbol{\varphi}}_i$ for a pure gravity wave initialization are obtained from (5.5) by setting $m = 0$, so that $\omega_l = N$, $\hat{u}_i = \hat{v}_i = 0$, and

$$\hat{\boldsymbol{\varphi}}_i = (\hat{\varphi}_i, \hat{\psi}_i, \hat{\phi}_i) = \frac{c}{K_h^2}\,(-l + \mathrm{i}kc, k + \mathrm{i}lc, 0)\,\hat{\mathcal{D}}_i\,. \tag{5.7}$$

For pure inertial waves $\omega_l = f$ and $\hat{\mathcal{D}}_i = \hat{w}_i = k = l = 0$, so that (5.5) is not valid. In this case $\hat{\boldsymbol{\varphi}}_i$ is expressed instead in terms of $\hat{u}_i$ as

$$\hat{\boldsymbol{\varphi}}_i = (\hat{\varphi}_i, \hat{\psi}_i, \hat{\phi}_i) = \frac{1}{fm}(1, -\mathrm{i}, 0)\hat{u}_i\,, \tag{5.8}$$

and the value $\hat{u}_0$ is specified by the initial conditions.

5.3.2 Vortex Initialization

The vortex initialization procedure is required to avoid the initial generation of IGWs during the geostrophic adjustment. This is specially important for w which, having an amplitude several orders of magnitude smaller than $|\mathbf{u}_h|$, would be largely interfered by horizontal imbalanced motions. The initialization procedure (Viúdez and Dritschel, 2003) is based on the slow, progressive growth of the PV *anomaly* field $\varpi(\mathbf{X}, t)$ in every *fluid particle* $\mathbf{X}$, that is, in a Lagrangian way during a time interval from $t = 0$ (when $\varpi(\mathbf{X}, 0) = 0$) to $t = t_i$ (when $\varpi(\mathbf{X}, t_i) = \varpi_0(\mathbf{X})$ is the prescribed PV *anomaly*). The initialization is done in the presence of IGWs over a time period of $t_i = 5\,T_{ip}$, which has been found to be sufficient to avoid significant excitation of IGWs. In the case of initialization with large amplitude plane gravity waves there is no need for a smooth initialization of the vortical motion since the w of the IGWs already present is several orders of magnitude larger than the w of the waves due to the initial imbalance. In these cases shorter initialization periods are chosen, ranging from $t_i = 0.2\,T_{ip}$ to $t_i = 0.5\,T_{ip}$.

5.4 Vortex-Wave Interaction

The interaction between a submesoscale monopole (cyclone and anticyclone) and large amplitude IGWs (a pure inertial and gravity wave) is first investigated in order to understand how this interaction occurs in more complex vortical structures like the vortex dipole. The dipolar vortex is of special interest because is the simplest vortical structure with net linear momentum. A list of the vortices parameters (ϖ minima or maxima and maximum length of the semiaxes of the ellipsoids of constant PV of the vortices a_X, a_Y, and a_Z), wave properties ($\mathbf{u}_{ih}$ and $\mathcal{D}_i$), and flow numbers ($\mathcal{D}_z$ maxima, $\mathcal{R}$ minima, and $\mathcal{F}$ maxima) of the simulations is given in Table 5.1. In all cases the flow remains statically and inertially stable.

In this section we analyze the interaction between waves and baroclinic *axisymmetric* monopoles, which have $w = 0$ at $t = 0$, of *similar* length and velocity amplitude. As a result of this interaction, the vortex geometry is largely modified by inertial (section 5.4.1) or gravity (section 5.4.2) wave flows.

Table 5.1: List of parameters

.

Case	# vortices	$\varpi_{\min/\max}$	a_X/c	a_Y/c	a_Z	(ck, cl, m)	$\lvert\mathbf{u}_{ih}\rvert$	$\mathcal{D}_i$	$\lvert\mathcal{D}_z\rvert_{\max}$	$\mathcal{R}_{\min}$	$\mathcal{F}_{\max}$
C1	1	$+0.75$	1.5	1.5	1.5	$(0, 0, 6)$	1		0.3	-0.53	1.37
C2	1	-0.5	1	1	1	$(0, 0, 6)$	0.1		0.19	-0.42	1.17
C3	1	-0.75	1.5	1.5	1.5	$(8, 0, 0)$		10^{-2}	0.2	-0.63	0.27
C4	1	$+0.75$	1.5	1.5	1.5	$(8, 0, 0)$		10^{-2}	0.19	-0.05	0.15
C5	2	$+0.75$	0.6	0.4	0.4				0.36	-0.63	0.35
C6		-0.75	0.6	0.4	0.27	$(0, 0, 4)$	0.75		0.6	-0.87	1.6
C7						$(-6, 0, 0)$		0.2	0.35	-0.68	0.45
C8	2	$+0.75$	1.2	0.8	0.8	$(8, 0, 0)$					0.40
C9		-0.75	1.2	0.8	0.54	$(-8, 0, 0)$		10^{-2}	0.39	-0.65	0.37
C10						$(0, 8, 0)$					0.37

5.4.1 Vortex And Inertial Waves Interaction

We consider here the interaction between a vortex and an inertial wave field of *similar* velocity amplitude. An initially *axisymmetric* cyclone with $\varpi_{\max} = 0.75$ and horizontal a_h and vertical a_Z radii $a_h/c = a_Z = 1.5$ (case C1) is initialized, as described in section 5.3.2, during $t_i = 5\,T_{ip}$ in a field of inertial waves (section 5.3.1) of horizontal velocity amplitude $|\mathbf{u}_{ih}| = 1$ and vertical wave number $m = 6$ (wavelength $\lambda_Z = 2\pi/m \simeq 1$).

The inertial wave causes horizontal advection of the vortex, which is horizontally displaced completing a cycle every inertial period (Fig. 5.1). Because λ_Z and a_Z are similar, the vertical shear of the wave distorts the vortex which no longer remains spherical in the QG space (Fig. 5.1). The $|\mathbf{u}_h|$ of the waves is similar to the $|\mathbf{u}_h|$ of the vortical flow altogether reaching *total* $|\mathbf{u}_h|_{\max} = 1.80$ at $t = 8.5\,T_{ip}$. This implies that the spatially homogeneous but time rotating inertial wave flow is also largely distorted by the spatially inhomogeneous (circular) but steady vortical flow. As a result the total flow is neither spatially homogeneous nor steady (Fig. 5.2).

The initially straight inertial wave phase lines are curved by the vortex also in the vertical plane. This effect is explained by the modification of the local wave frequency ω_l in the vortex-wave interaction region. Splitting the total velocity $\mathbf{u}$ into a wave component $\mathbf{u}_i$ plus a vortical (balanced) component $\mathbf{u}_{bh}(\mathbf{x}_h, z) = \Omega(z)\ \mathbf{k} \times \mathbf{x}_h$ (subscripts i and b, respectively) of a rigid rotation with angular velocity $\Omega(z)$ in the basic flow equations (A.4)–(A.7), the wave dynamics satisfies at $x \cong y \cong 0$ the equations

$$\begin{aligned} \frac{\partial \mathbf{u}_i}{\partial t} + f_e \mathbf{k} \times \mathbf{u}_i &= -\alpha_0 \boldsymbol{\nabla} p_i - N^2 \mathcal{D}_i \mathbf{k}\,, \\ \frac{\partial \mathcal{D}_i}{\partial t} + w_i \frac{\partial \mathcal{D}_b}{\partial z} &= w_i\,, \\ \boldsymbol{\nabla} \cdot \mathbf{u}_i &= 0\,, \end{aligned} \tag{5.9}$$

where $f_e\,(z) \equiv f + \Omega(z)$ is the *effective* Coriolis frequency.

The new dispersion relation is obtained substituting the plane wave fields $\tilde{\chi}(\mathbf{x}, t) = \tilde{\chi}_0\ e^{\mathrm{i}(\mathbf{K}\cdot\mathbf{x} - \omega_l t)}$ into (**??**), yielding

$$\omega_l^2 = \frac{\mathcal{N}^2 K_h^2 + f_e^2 m^2}{K^2}, \tag{5.10}$$

where ω_l is the local frequency, and $\mathcal{N}^2 \equiv -\alpha_0 g \partial\rho/\partial z = N^2(1 - \partial\mathcal{D}/\partial z)$ the *total* Brunt-

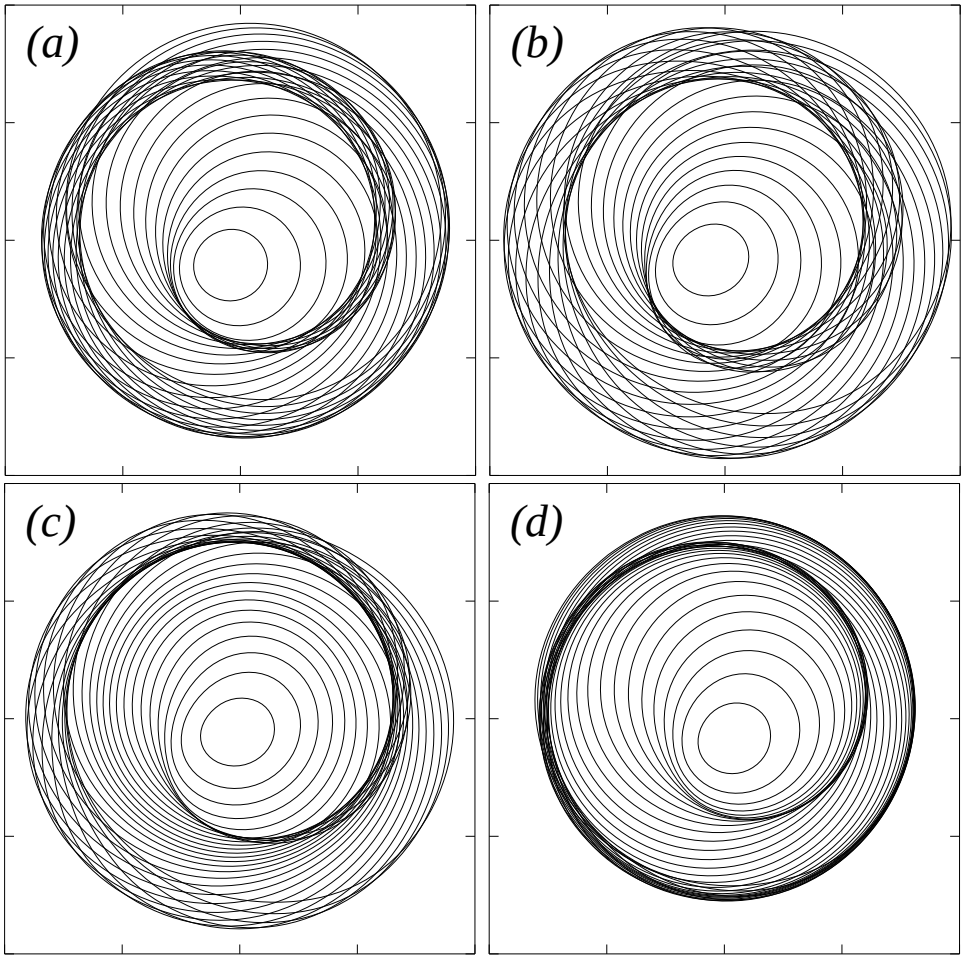

Figure 5.1: Time sequence of the outer PV contour in every isopycnal of the lower half of the vortex, from the middle isopycnal $i_l = 65$ (contours with larger radius) to $i_l = 46$, the deepest isopycnal with $\varpi \neq 0$ (contours with shorter radius). Time is (a) $t = 5\,T_{ip}$, (b) $t = 5.25\,T_{ip}$, (c) $t = 5.5\,T_{ip}$, and (d) $t = 5.75\,T_{ip}$. The horizontal extent is $\delta x = \delta y = 1.5c$.

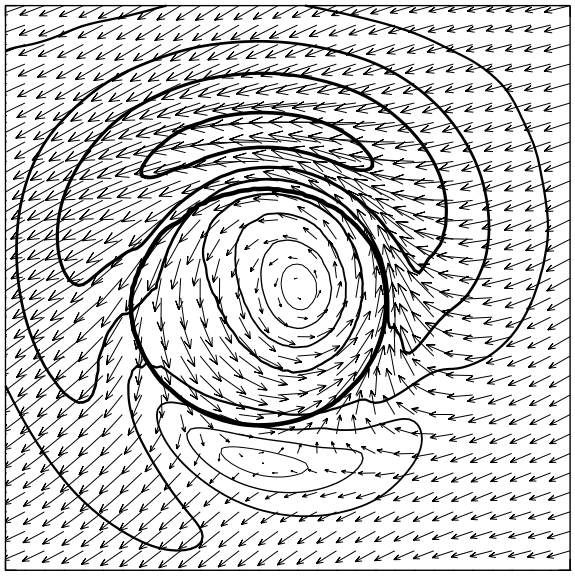

Figure 5.2: Horizontal velocity $\mathbf{u}_h$ ($|\mathbf{u}_h|_{\max} = 1.49$, $\delta|\mathbf{u}_h| = 0.25$) at $t = 5.5\,T_{ip}$ and $i_Z = 65$ ($z = 0$). PV contour $\varpi = 0.22$ at $z = 0$ (thick contour) is included. Domain extent is $\delta x = \delta y = 5.8c$. Only each every four vectors is represented.

Väisälä frequency.

In the cyclone case (C1) an *effective* wave frequency $\omega_l \cong 0.13$ is predicted from (**??**). This is confirmed by numerical results which show that the wave frequency peak evolves from inertial $\omega_l = 0.1$ to near-inertial frequency $\omega_l = 0.12 \pm 0.01$ (Fig. 5.3). So that the local frequency shift $\zeta/2$ (Mooers, 1975a; Kunze, 1985; Rubenstein and Roberts, 1986) is also caused by baroclinic PV structures that remain no longer *axisymmetric* after the vortex-wave interaction.

In order to analyze how the balanced flow affects the wave motion and viceversa, we have extracted the balanced flow from the *total* flow. The *balanced* vector potential $\boldsymbol{\varphi}_b = (\varphi_b, \psi_b, \phi_b)$ is here diagnosed using the Optimal PV Balance (OPVB) approach (Viúdez and Dritschel, 2004a), and the balanced quantities are derived therefrom. From a given PV field *anomaly* $\varpi(x, y, z)$, the OPVB approach diagnoses a flow having only those IGWs that have been spontaneously generated during the process of acquiring its own PV (that is, during a time interval set equal to the initialization time $t_i = 5\,T_{ip}$). The OPVB flow does not contain most of the IGWs, which remain, almost entirely, in the *unbalanced* vector potential $\boldsymbol{\varphi}_i \equiv \boldsymbol{\varphi} - \boldsymbol{\varphi}_b$. The unbalanced velocity and vertical displacement of isopycnals, are obtained directly from $\boldsymbol{\varphi}_i$ through the usual relations $\mathbf{u}_i = -f\boldsymbol{\nabla} \times \boldsymbol{\varphi}_i$ and $\mathcal{D}_i = -\epsilon^2 \boldsymbol{\nabla} \cdot \boldsymbol{\varphi}_i$. An alternative way to obtain the interaction between the inertial waves and the vortical flow in this case is using the near-inertial oscillation (NIO) equation of Young and Jelloul (1997), which is valid for small Rossby numbers. We note that their geostrophic streamfunction Ψ

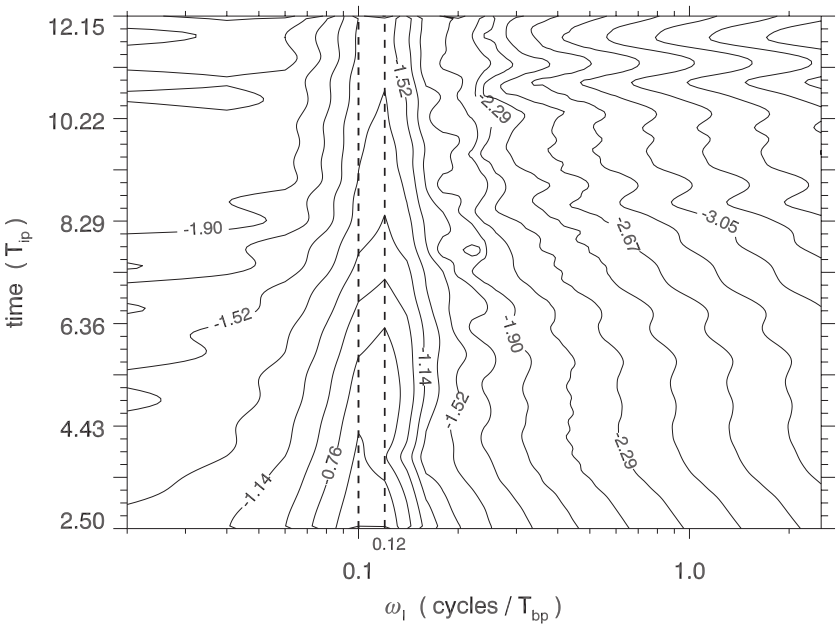

Figure 5.3: Clockwise rotatory spectrogram of $u + iv$. The spectrogram comprises 194 spectra from $t = 0$ to $t = 14.25\,T_{ip}$ using a window of $5\,T_{ip}$ and a time lag of $\delta t = 0.5\,T_{bp}$. The distribution shows the Fourier transform magnitude of the components $\sqrt{\hat{u}^2(\omega_F) + \hat{v}^2(\omega_F)}$ for the Fourier frequencies $\omega_F < 0$. The initial inertial peak evolved to near-inertial, $\omega_l = 0.12 \pm 0.01$.

is similar to our vertical potential ϕ. However, we use here the OPVB because is valid for largely ageostrophic flows.

The wave frequency shift mentioned before is noticeable because the vertical wave phase velocity at the vortex center ($\sigma_Z = (f + \Omega)/m$) is larger than outside the vortex ($\sigma_Z = f/m$). Therefore, phase lines of $\mathbf{u}_i$ at $x \cong y \cong 0$ accelerate inside the vortex (Figs. 5.4a,b). As a result, the originally straight phase lines of $\mathbf{u}_{ih}$ are broken by the cyclone, and the vertical distribution of the speed anomaly of the unbalanced horizontal velocity is distorted (Fig. 5.4c), reaching negative values at the vortex center.

As we have seen, the initial inertial wave field is strongly modified by the vortex, but at the same time the vortex is also deformed by the wave velocity, which causes the PV contours to depart from the spherical geometry, modifying the vertical distribution of $\mathcal{D}$ (Fig. 5.5a). Since $\mathcal{D}$ is related to the geostrophic velocity shear $\mathbf{u}^g_{hz} \equiv \partial \mathbf{u}^g_h / \partial z$ by the thermal-wind relation

$$\mathbf{u}^g_{hz} = -\frac{N^2}{f} \mathbf{k} \times \boldsymbol{\nabla}_h \mathcal{D}\,, \tag{5.11}$$

the $|\mathbf{u}^g_h|$ contours (Fig. 5.5b) depart from the circular geometry typical of a vortex in the absence of a wave field. This is also confirmed when extracting the balanced flow from the *total* flow (Fig. 5.5c).

An important result of the vortex-wave interaction is the generation of w in the form of spiral waves (Fig. 5.6). Since the motion of the isolated spherical vortex on the one hand, and the motion of the isolated inertial waves on the other hand, are purely horizontal, the development of w in the vortex-wave system is a clear result of *non-linear* vortex-wave interaction.

The maximum w amplitude reaches $|w|_{\max} = 5 \times 10^{-2}$, that is 5% of the horizontal inertial wave speed, from $t = 5\,T_{ip}$ to $t = 6\,T_{ip}$ (Figs. 5.6a,b). This spiral w pattern seems to be related to wave motion rather than to balanced motion since the QG vertical velocity w^q obtained by solving the QG omega equation (Hoskins et al., 1978)

$$c^2 \boldsymbol{\nabla}^2_h w^q + \frac{\partial^2 w^q}{\partial z^2} = 2 \boldsymbol{\nabla}_h \cdot \mathbf{Q}^g_h, \tag{5.12}$$

where $\mathbf{Q}^g_h \equiv c^2 \boldsymbol{\nabla}_h \mathbf{u}^g_h \cdot \boldsymbol{\nabla}_h \mathcal{D}$ is the geostrophic $\mathbf{Q}$-vector and $\mathbf{u}^g_h$ is the geostrophic velocity. Though having a spiral pattern as well, is about one order of magnitude smaller than the total w (not shown). The unbalanced origin of the *total* w is confirmed by splitting it into w_b and w_i using the OPVB approach. The vertical distribution of w (Fig. 5.6b) follows the

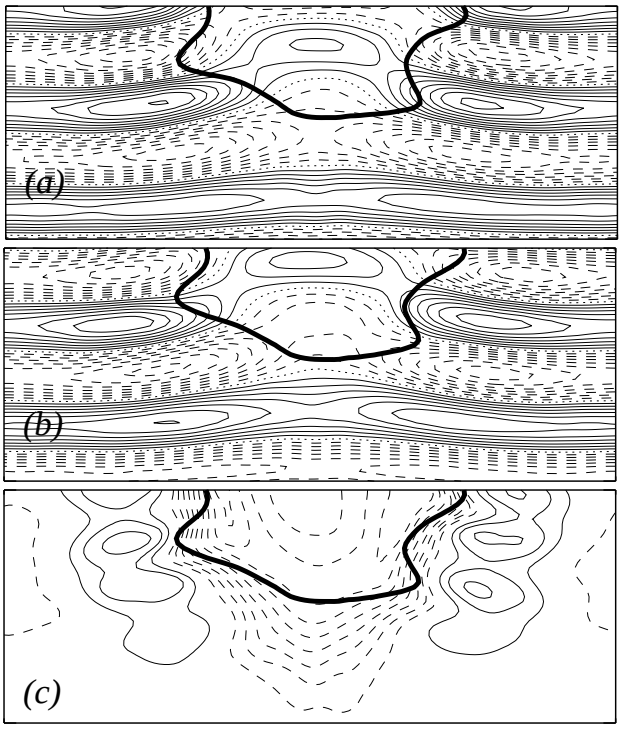

Figure 5.4: Vertical distributions in the x-z plane $i_Y = 65$ ($y = 0$) at $t = 5\,T_{ip}$ of (a) u_i ($u_i \in [-1.3, 1.28]$, $\delta u_i = 0.15$), (b) v_i ($v_i \in [-1.17, 1.19]$, $\delta v_i = 0.15$), and (c) the speed anomaly of the unbalanced horizontal velocity $U_i' = |\mathbf{u}_i| - 1$ ($U_i' \in [-0.82, 0.31]$, $\delta U_i' = 0.09$). Domain extend is $x \in [-\pi, \pi]c$, $z \in [-3/4\pi, 0]$. The PV contour $\varpi = 0.2$ (thick line) is included for reference. Hereinafter, solid and dashed lines indicate positive and negative values, respectively.

Figure 5.5: Vertical distributions in the x-z plane at $i_Y = 65$ ($y = 0$) and $t = 5\,T_{ip}$ of the (a) isopycnal displacement $\mathcal{D}$ ($\mathcal{D} \in [-0.06, 0.17]$, $\delta\mathcal{D} = 0.017$), (b) horizontal geostrophic speed anomaly $U^{g\prime} = |U_h^g| - 1$ ($U^{g\prime} \in [-0.15, 0.82]$, $\delta U^{g\prime} = 0.07$). and (c) balanced v ($v_b \in [-1.55, 1.18]$, $\delta v_b = 0.15$). Domain extent is $x \in [-\pi, \pi]c$, $z \in [-\pi, 0]$. The PV contour $\varpi = 0.2$ is included.

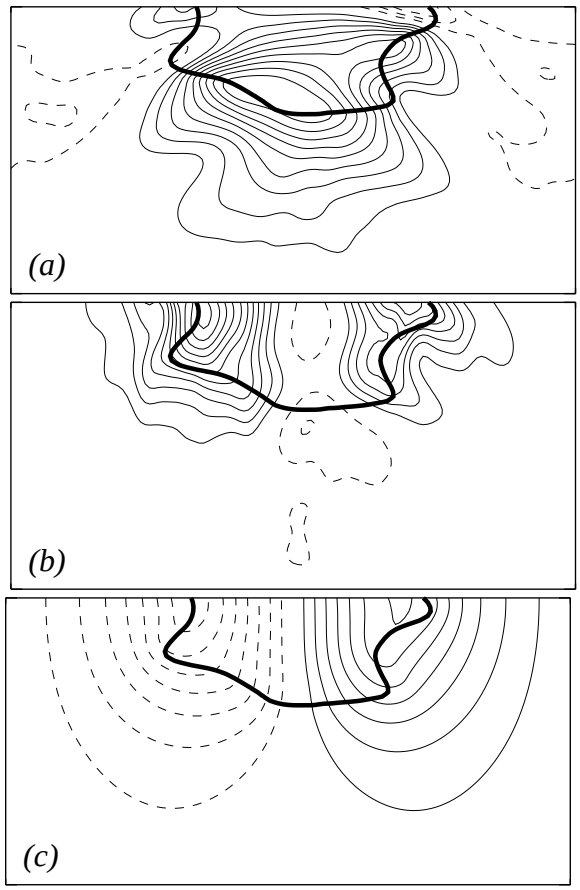

pattern of w_i and both have the same order of magnitude, which is two times larger than that of w_b (Fig. 5.6c). The motion of the spiral IGWs is that of a right-handed helix (the height increasing with increasing phase, Fig. 5.7), rotating anticyclonically so that the phases propagate upwards. The wave packet propagates downward and horizontally leaving the vortical region in a few inertial periods (not shown).

This spiral IGW has a local frequency ranging from f to f_e at initial times and extending to $2f$ and $3f$ frequencies afterwards (Fig. 5.8). Near-inertial w is generated by divergence of the $\mathbf{u}_i$ field, which becomes horizontally inhomogeneous because ζ shifts the frequency of pure inertial waves. When separating unbalanced from balanced flows we observe that ζ_i and ζ_b have the same order of magnitude after $t > t_i$. On the one hand, ζ_i is in phase with w (not shown), as predicted from (5.6). However pure inertial waves have $\zeta_i = 0$ at $t = 0$. On the other hand, we observe that w correlates with $|\boldsymbol{\nabla}\zeta_b|$ maxima after $t > t_i$ and in deeper layers, where horizontal advection is minimum (Fig. 5.9a). As a result, w_i develops at vortex edges (note that $\mathcal{F} > 1$, $\mathcal{F}_{\max} = 1.37$, occurs once the spiral wave has been already generated). Since the vortex geometry is largely horizontally advected by an initially pure inertial wave, $|\boldsymbol{\nabla}\zeta_b|$ isosurfaces become spiralized with depth (Fig. 5.9b) generating an helical IGW. Thus, while the frequency of the *total* w is directly related to ζ, its 3D structure is explained by $|\boldsymbol{\nabla}\zeta_b|$, in accordance with the stated correlation between w and the eddy relative vorticity (Danioux and Klein, 2008a). Finally, superinertial w observed at later times is due to resonance mechanisms, in agreement with the results of Niwa and Hibiya (1999) and Danioux and Klein (2008b), that occur when PV structures and IGWs have similar length scales.

Analogous results were obtained with an *axisymmetric* anticyclone (case C2), having $\varpi_{\min} = -0.5$ and semi-axes $a_h/c = a_Z = 1$, initialized with an inertial wave field of $|\mathbf{u}_{ih}| = 0.1$ and $m = 6$ (wavelength $\lambda_Z \cong 1$). In this case the vortex has $\Omega < 0$ and the local frequency $\omega_l \cong 0.79 < f$. Consequently, σ_Z at the vortex center is smaller than that far away from it, which is the opposite effect to that described in the cyclonic case, and wave phase lines accumulate at eddy edges (Fig. 5.10a). The *total* w also shows a right handed helical structure (not shown), consistent with the anticyclonic rotation with time of the inertial wave velocity, which propagates horizontally and downwards at initial times but it is trapped at the eddy bottom later on (Figs. 5.10b–d). This spiral IGW has a subinertial frequency $\omega_l \simeq 0.08 \pm 0.01$ (Fig. 5.12) and therefore close to the predicted f_e.

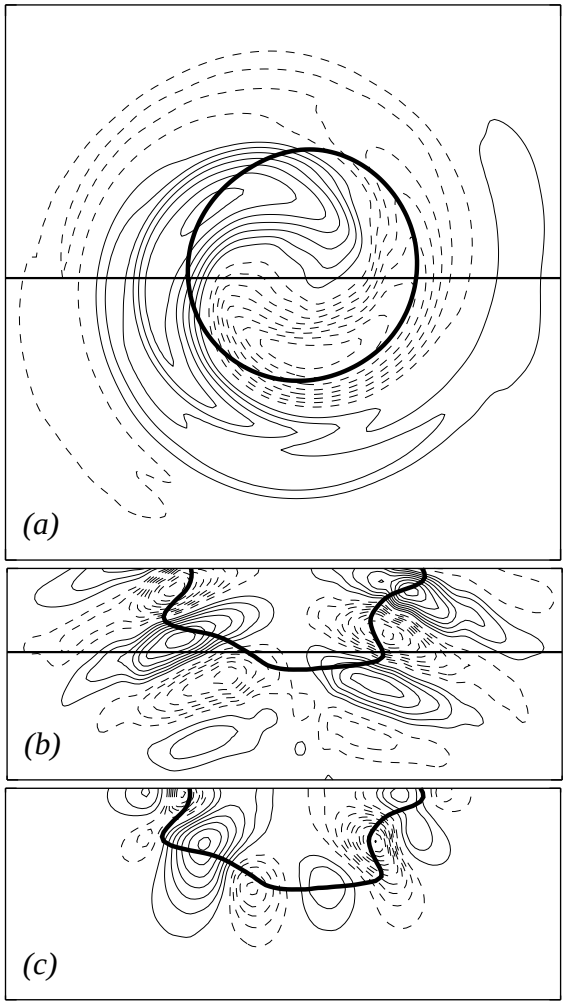

Figure 5.6: Distributions of *total* vertical velocity w ($w \in [-4.81, 4.23]\times 10^{-2}$, $\delta w = 5\times 10^{-3}$) at $t = 5\,T_{ip}$ (a) in the x-y plane at $i_Z = 45$ ($z = -0.98$) and (b) in the x-z plane at $i_Y = 65$ ($y = 0$). (c) Vertical distribution at the same time of w_b ($w_b \in [-5.52, 3.6] \times 10^{-4}$, $\delta w_b = 5 \times 10^{-5}$). Domain extend is $x, y \in [-\pi, \pi]c$, $z \in [-3/4\pi, 0]$. PV contour $\varpi = 0.2$ (thick line) is included. Straight lines mark the horizontal (a) and vertical (b,c) sections plotted.

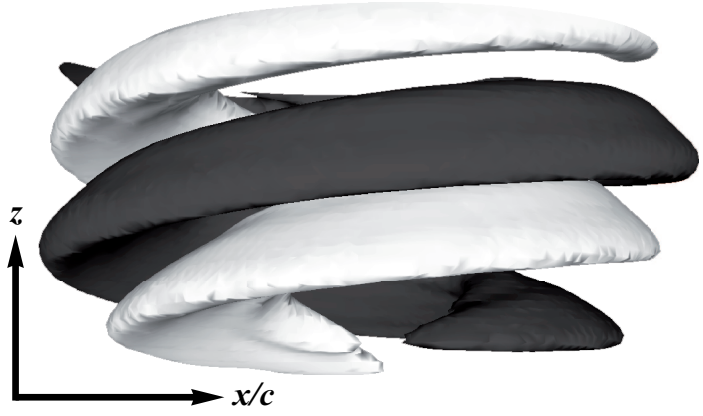

Figure 5.7: Isosurfaces of *total* vertical velocity w ($w = \pm 0.02$) at $t = 5\,T_{ip}$. The view is from the south.

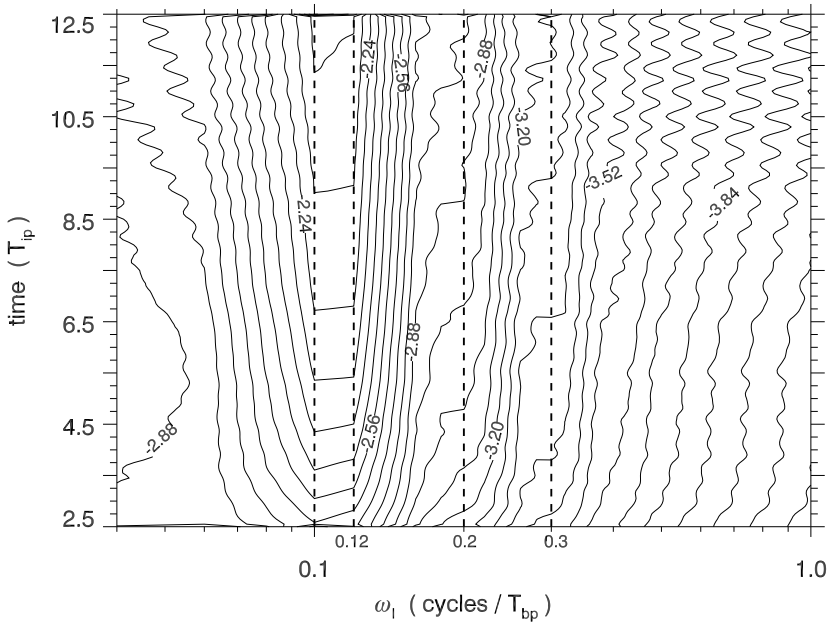

Figure 5.8: Domain averaged spectrogram $w(\omega, t_k) \equiv \frac{1}{n}\sum_{j=1}^{n} \hat{w}(\mathbf{x}_j, \omega; t_k)$ from $t = 0$ to $t = 15\,T_{ip}$, where $\hat{w}(\mathbf{x}_j, \omega; t_k)$ is the Fourier transform of the time series $w(\mathbf{x}_j, t)$ with $t \in [t_k - \Delta_t/2, t_k + \Delta_t/2]$. The spatial average comprises $n = 8^3$ time series equally distributed in the 3D domain. The spectrogram window is $\Delta_t = 5T_{ip}$ and the time lag $\delta_t = 0.5\,T_{bp}$. The vertical dashed lines mark the frequencies f, $f + \zeta/2 \cong 0.12$, $2f$, and $3f$.

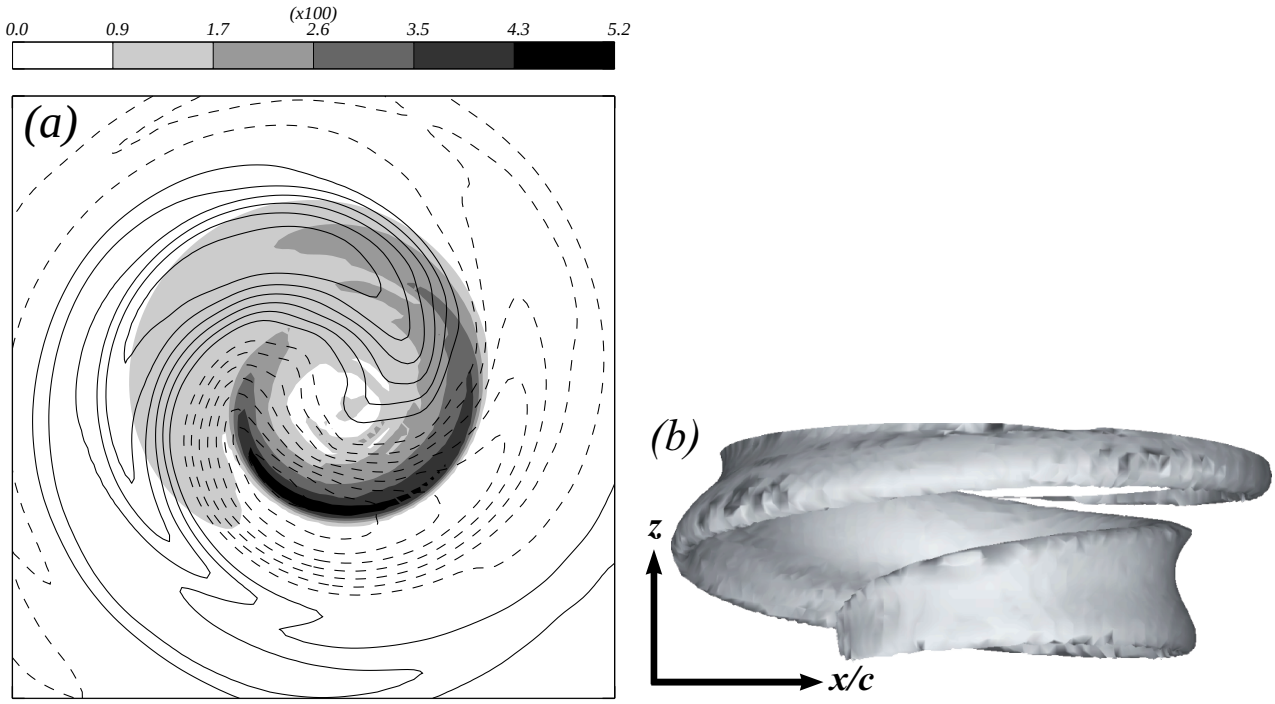

Figure 5.9: (a) As in figure 5.6 but at $i_Z = 43$ ($z = -1.03$) ($w \in [-4.18, 3.48] \times 10^{-2}$, $\delta w = 5 \times 10^{-3}$). Shaded contours are $|\boldsymbol{\nabla}_h \zeta_b|$ (max $= 5.1 \times 10^{-2}$, $\Delta = 8.7 \times 10^{-3}$). Domain extend is $x, y \in [-3/4\pi, 3/4\pi]$. (b) Isosurface $|\boldsymbol{\nabla}_h \zeta_b| = 0.04$ at the same time $t = 5\,T_{ip}$. The view is from the south.

Though we do not consider in detail the long term vortex-wave interaction we note that, starting at $t = 8.25\,T_{ip}$ and during the next $16\,T_{ip}$, the inertial waves may cause the vortex become unstable in the sense that the vortex losses PV by PV filamentation (not shown). This PV filamentation increases the horizontal PV gradients remaining in the vortex and as a result, later on at $t = 13.43\,T_{ip}$, the flow becomes inertially unstable ($\mathcal{R} < -1$). This long term instability is left for future research.

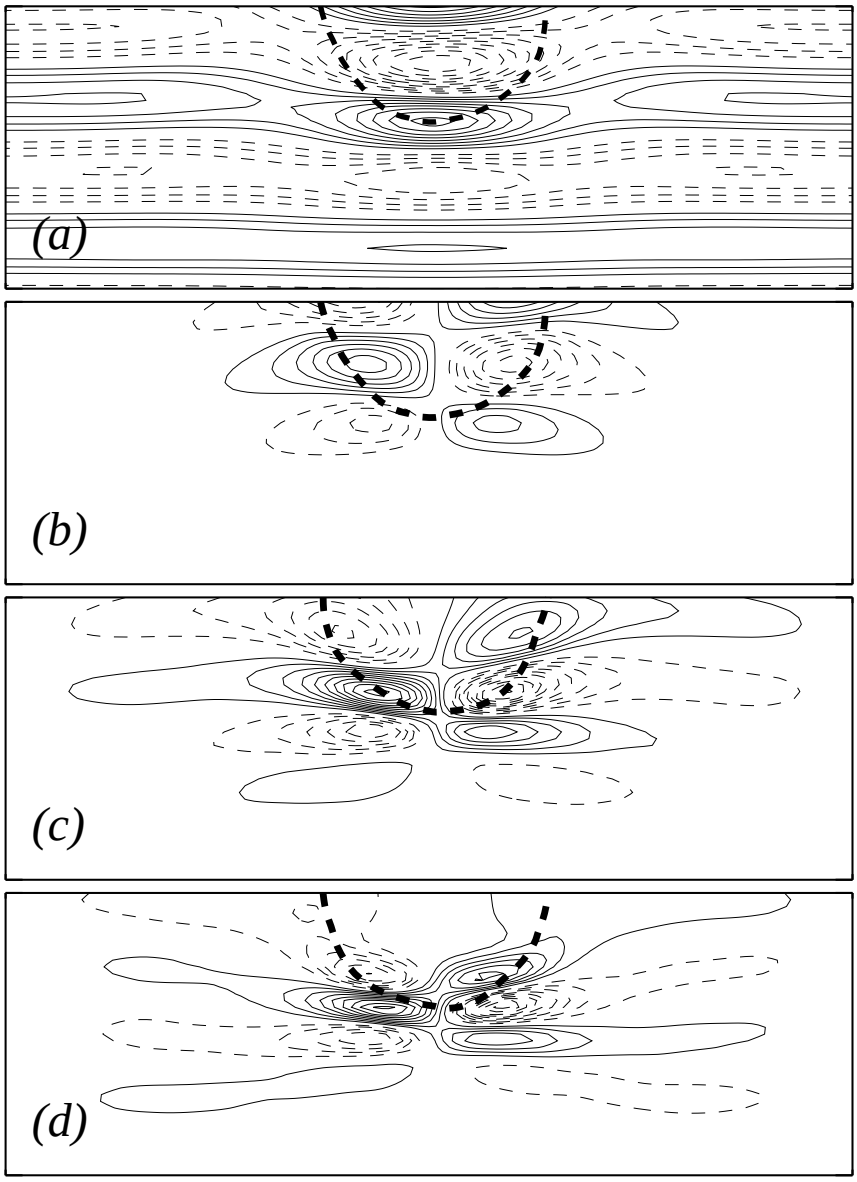

Figure 5.10: Vertical distributions at $i_Y = 65$ ($y = 0$) of (a) $v_i(x,z)$ ($v_i \in [-0.24, 0.2]$, $\delta v_i = 0.025$) at $t = 5\,T_{ip}$ and of *total* $w(x,z)$ ($w \in [-8.5, 8.7] \times 10^{-3}$, $\delta w = 8.3 \times 10^{-4}$) at (b) $t = 5\,T_{ip}$, (c) $t = 5\,T_{ip}$, and (d) $t = 15\,T_{ip}$. PV contour $\varpi = -0.2$ is included (solid thick line). The domain extend is $x \in [-\pi, \pi]c$, $z \in [-2/3\pi, 0]$.

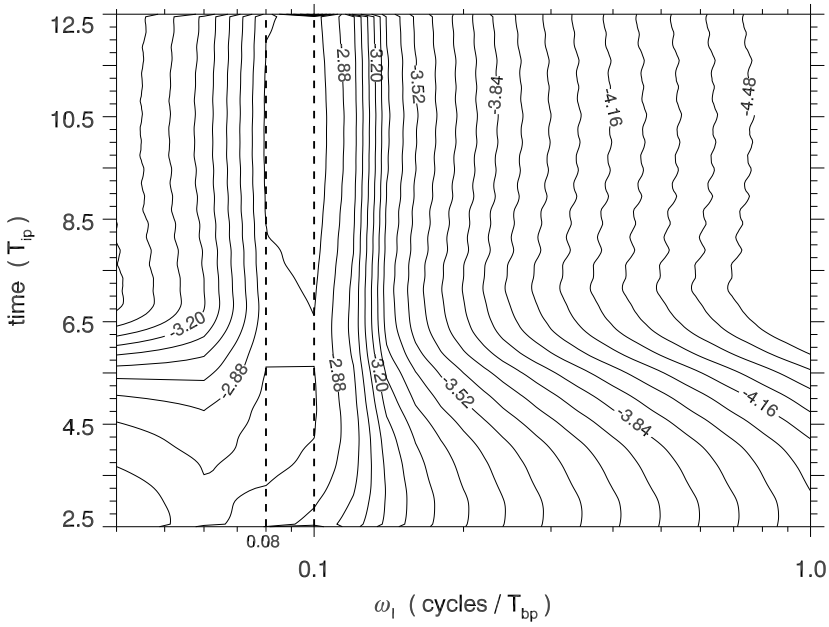

Figure 5.11: Domain averaged spectrogram $w(\omega, t_k)$ as in Fig. 5.8. Spatial average comprises $n = 9^2$ horizontal points equally distributed over 17 vertical levels. In this case vertical dashed lines mark frequencies f and $f - \zeta/2 \cong 0.08$.

5.4.2 Vortex And Gravity Waves Interaction

In this section a spherical (in the QG space) anticyclone, having $\varpi_{\min} = -0.75$ and semi-axes $a_h/c = a_Z = 1.5$ in the initial configuration, is initialized (Fig. 5.13a) embedded in a gravity wave field with $k = 8/c$ (wavelength $\lambda_X/c = 2\pi/(ck) \cong 0.78$) and $\mathcal{D}_i = 10^{-2}$ (case C3, Fig. 5.13b). Thus, the wave spatial scale is smaller, though of the same order, than the vortical flow scale. Note that the vortical $\mathcal{D}$ (due to the otherwise balanced vortex) is zero at $z = 0$. The maximum amplitude of $\mathcal{D}$ caused by the vortical motion is $|\mathcal{D}_b|_{\max} = 0.20$ at the end of the initialization period (Fig. 5.13c), which is about 20 times larger than $\mathcal{D}_i$. However, the amplitude of the vertical wave motion is $w_i = 0.06$, which is 10 times larger than the typical mesoscale QG vertical velocity w^q (that is, w^q is about 10^{-3} times the horizontal vortical speed).

The most noticeable result is the deformation of the initially straight phase lines of w of the gravity waves (Fig. 5.14). This occurs because the oscillating fluid particles are horizontally advected by the vortex giving a new local (absolute) wave frequency ω_l which is the Doppler shifted particle (intrinsic) wave frequency ω_p by the vortex motion, according to

$$\omega_l = \omega_p + \mathbf{K}_h \cdot \mathbf{u}_{bh} \,. \tag{5.13}$$

Since $|\mathcal{D}_z|_{\max} = 0.2$, we have $\mathcal{N} \cong N$, and thus ω_p is approximately homogeneous. Consequently, ω_l is affected mainly by the Doppler shift $\mathbf{K}_h \cdot \mathbf{u}_{bh}$. The anticyclonic vortical motion $\mathbf{u}_{bh} = u_b\,\mathbf{i} + v_b\,\mathbf{j}$ has $u_b > 0$ ($u_b < 0$) at $y > 0$ ($y < 0$), implying a positive (negative)

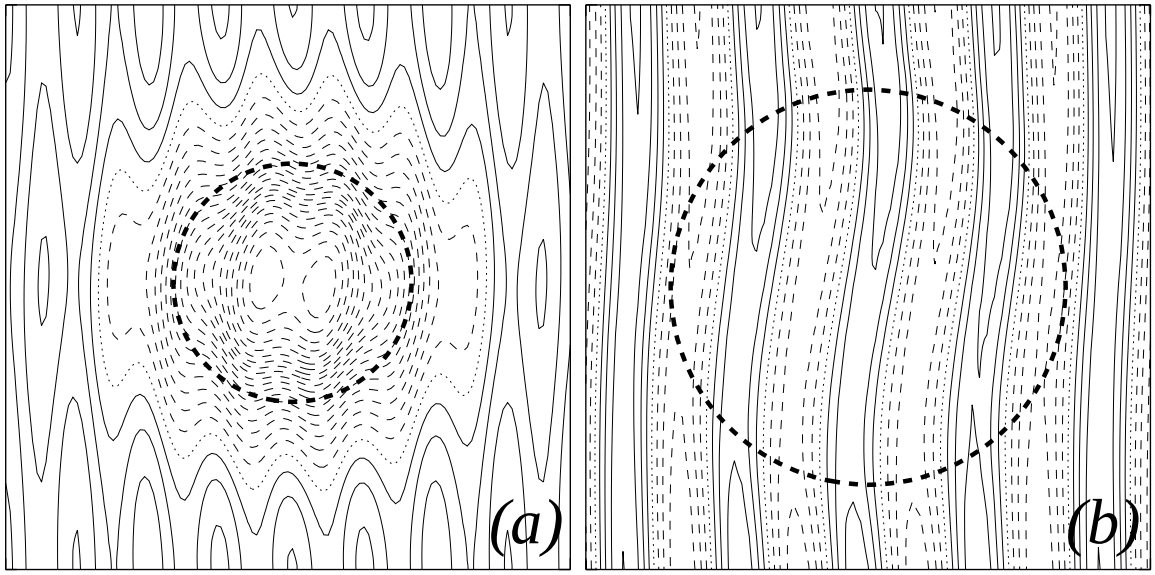

Figure 5.12: Distributions at $t = 4\,T_{bp}$ of the vertical displacement $\mathcal{D}$ at (a) $i_Z = 40$ ($z = -1.2$, $\mathcal{D} \in [-18, 4.2] \times 10^{-2}$, $\delta\mathcal{D} = 1 \times 10^{-2}$), and (b) $i_Z = 65$ ($z = 0$, $\mathcal{D} \in [-1, 1] \times 10^{-2}$, $\delta\mathcal{D} = 2.5 \times 10^{-3}$). The PV contour $\varpi = -0.2$ at $z = 0$ is included. The domain extent is $\delta x = \delta y = 2\pi c$ in (a), and $\delta x = \delta y = 3.62c$ in (b).

frequency Doppler shift. Hence ω_l increases (decreases) in the northern (southern) region of the vortex, so that the initially straight phase lines acquire an anticyclonic pattern.

The deformation of wave phase lines caused by the vortex is not confined to the vortical region but is transferred through all the water column (Fig. 5.14). As a first approximation we assume that the vortical vertical motion can be neglected, so that $\boldsymbol{\nabla}_h \cdot \mathbf{u}_{bh} = 0$, since $\mathbf{u}_{ih} = \mathbf{0}$ for gravity waves, and the non-divergence condition yields $\partial w/\partial z = 0$. Therefore the horizontal phase velocity $\sigma_h \equiv (-\partial w/\partial t)/|\nabla_h w|$ is constant along the water column, $\partial\sigma_h/\partial z = 0$.

Similar results were obtained for a cyclone with $\varpi_{\max} = 0.75$ and semi-axes $a_h/c = a_Z = 1.5$ in a gravity wave field identical to the case above (case C4, not shown). In this case the initial configuration has $|\mathcal{D}|_{\max} = 0.18$, that is, 18 times larger than $\mathcal{D}_i$. Contrary to the anticyclonic case the initially straight phase lines acquire a cyclonic pattern because now ω_l decreases (increases) in the northern (southern) side of the vortex due to the Doppler shift frequency (**??**).

5.5 Dipole-Wave Interaction

We address here the interaction between a vortex dipole, which, unlike the monopolar vortex, possesses a net linear momentum, and large amplitude IGWs. With that purpose we first

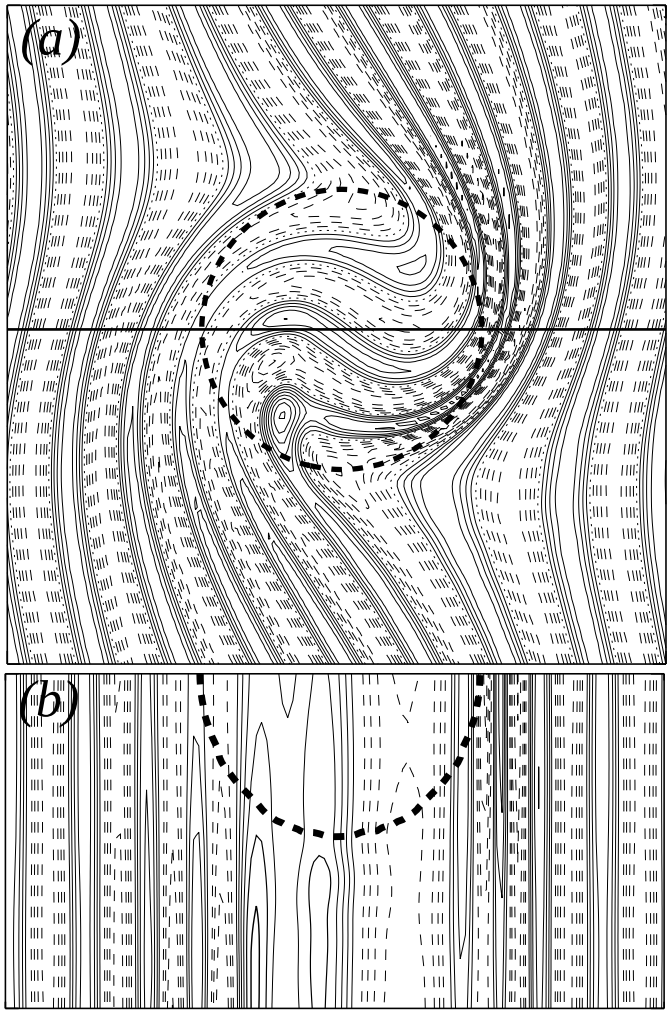

Figure 5.13: Distributions of w ($w \in [-6.8, 8.5] \times 10^{-2}$, $\delta w = 0.13$) at $t = 26.8\, T_{bp}$ (a) in the x-y plane at $i_Z = 65$ ($z = 0$) and (b) in the x-z plane at $i_Y = 65$ ($y = 0$). PV contours $\varpi = -0.2$ at (a) $z = 0$ and (b) $y = 0$ are shown (dashed thick line). Domain extent is $x, y \in [-\pi, \pi]c$, and $z \in [-\pi, 0]$.

describe the flow characteristics of the dipole (section 5.5.1) initialized when pure inertial wave (section 5.5.2) or gravity wave (section 5.5.3) fields are included.

5.5.1 The dipole

A submesoscale baroclinic dipole is here initialized, in the absence of waves, as two ellipsoidal PV distributions with $\varpi_{\max} = 0.75$ and $\varpi_{\min} = -0.75$, horizontal semi-axes $a_X^{\pm} = 0.6c$ and $a_Y^{\pm} = 0.4c$, and vertical semi-axes $a_Z^{+} = 0.4$ and $a_Z^{-} = 0.27$ for the cyclone (+) and the anticyclone (−), respectively (case C5, Fig. 5.15a). The initial asymmetry in the prescribed $a_Z^{\pm}$ is due to the fact that these vortices are defined in the initial (reference) configuration which has flat isopycnals. During the initialization time the isopycnals stretch (shrink) in the anticyclone (cyclone), so that at the end of the initialization period ($t_i = 5\, T_{ip}$) the

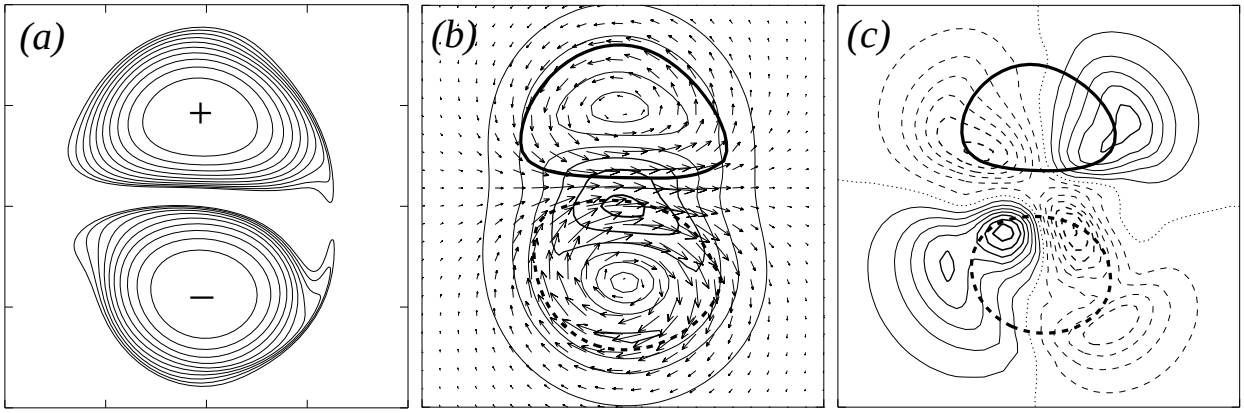

Figure 5.14: Horizontal distributions at $t = 5\,T_{ip}$ of (a) PV contours on the middle isopycnal ($z = 0$, PV jump $\delta\varpi = 7.5 \times 10^{-2}$), (b) the horizontal velocity at $i_Z = 65$ ($z = 0$, $|\mathbf{u}_h|_{\max} = 0.78$, $\delta|\mathbf{u}_h| = 0.12$, only every other vector is plotted), and (c) the vertical velocity at $i_Z = 61$ ($z = -0.15$, $w \in [-7.1, 7.5] \times 10^{-4}$, $\delta w = 10^{-4}$). PV contours $\varpi^{\pm} = \pm 0.2$ are included in (b) and (c) at their corresponding depths. Domain extent is $\delta x = \delta y = 2.26c$.

vortices have a similar vertical extent in the physical space and the dipole describes a straight trajectory (Dubosq and Viúdez, 2007). The horizontal velocity, which is slightly larger in the anticyclone than in the cyclone, reaches maxima $|\mathbf{u}_h|_{\max} = 0.78$ at the dipole center (Fig. 5.15b). The vertical velocity (Fig. 5.15c) is three orders of magnitude smaller than $|\mathbf{u}_h|$, and has the typical quadrupolar pattern of mesoscale QG dipoles (Pallàs-Sanz and Viúdez, 2007).

5.5.2 Dipole And Inertial Waves Interaction

The baroclinic dipole described above is initialized, according to section 5.3.2, embedded in an inertial plane wave field (section 5.3.1) with $m = 4$ (wavelength $\lambda_Z = 2\pi/m \cong 1.57$) and speed $|\mathbf{u}_{ih}| = 0.75$, case C6. Thus, λ_Z is about twice the vortex vertical extent $2a_Z \cong 0.7$. Nevertheless, despite the large wave amplitude, the dipole remains coherent as a stable structure during many inertial periods.

As a result of the dipole-wave interaction the *total* $|\mathbf{u}_h|$ reaches $|\mathbf{u}_h|_{\max} = 1.5$, which approximately corresponds to the sum of the wave ($|\mathbf{u}_{ih}|_{\max} = 0.75$) and dipole ($|\mathbf{u}_{bh}|_{\max} = 0.78$) speeds separately considered. Since the inertial wave field has homogeneous speed, the extreme values of $|\mathbf{u}_h|_{\max}$ occur along the dipole axis, being maxima or minima depending on the phase of the waves (Fig. 5.16a). Initially straight u and v phase lines (see vertical sections in Figs. 5.16b,c) are displaced up (down) in the cyclone (anticyclone). This feature is

consistent with the explanation given in section 5.4.1 for the interaction between a monopolar vortex and inertial waves.

In this interaction the vortex geometry is less deformed by the wave flow than in the monopole-wave case (Fig. 5.4) because $a_Z < \lambda_Z$. Consequently, when applying the aforementioned OPVB method (section 5.4.1), the pattern of the balanced horizontal $\mathbf{u}_{bh}$ and vertical velocity w_b are little distorted by the wave field, despite the large wave velocity, and adjust to the typical horizontal and vertical velocity patterns of the dipole in the absence of waves (Figs. 5.17a,b). The amplitude of w_b is however about twice that of w in the case of the dipole without waves (Fig. 5.15c).

In contrast, dipole-wave interaction clearly occurs in $\mathbf{u}_i$ (Figs. 5.17c,d), with $|\mathbf{u}_{ih}|$ changing by 13.5% at $z = 0$ in the vortices and with the largest phase change happening in the anticyclone (Fig. 5.17c). At the depth of maximum w ($z = -0.15$) w_i is very large (Fig. 5.17d), of about one order of magnitude larger than w_b (Fig. 5.17b), that is about 20

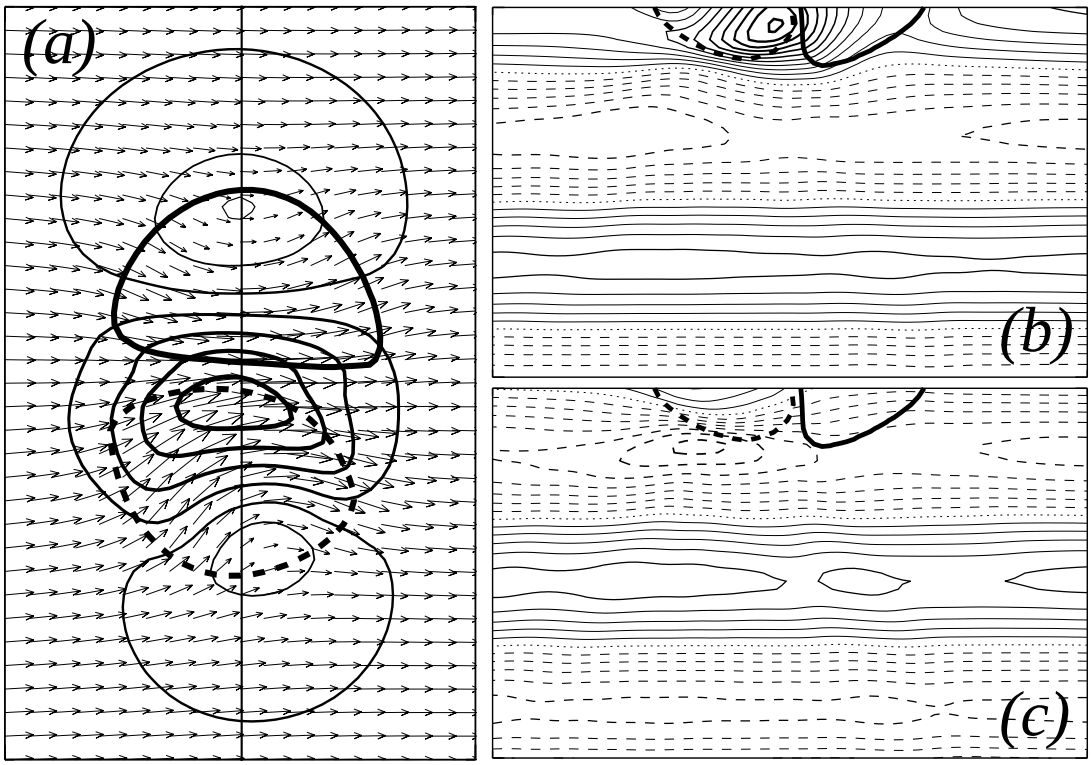

Figure 5.15: (a) Horizontal distributions of $\mathbf{u}_h$ and $|\mathbf{u}_h|$ at $i_Z = 65$ ($z = 0$, $|\mathbf{u}_h|_{\max} = 1.5$, $\delta|\mathbf{u}_h| = 0.17$). The PV contours $\varpi^{\pm} = \pm 0.2$ are included. Domain extent is $[\delta x, \delta y] = [2, \pi]c$. Vertical distribution in the y-z plane at $i_X = 27$ ($x = 1.82$) of (b) u ($u \in [-0.85, 1.59]$, $\delta u = 0.14$) and (c) v ($v \in [-1.06, 0.79]$, $\delta v = 0.14$). Domain extent is $y \in [-1.91, 1.91]c$, $z \in [-2.25, 0]$. Time $t = 5\,T_{ip}$. PV contours $\varpi^{\pm} = \pm 0.1$ are included for reference. The aspect ratio $L_X/L_Z = L_Y/L_Z = c$ is preserved in the figures.

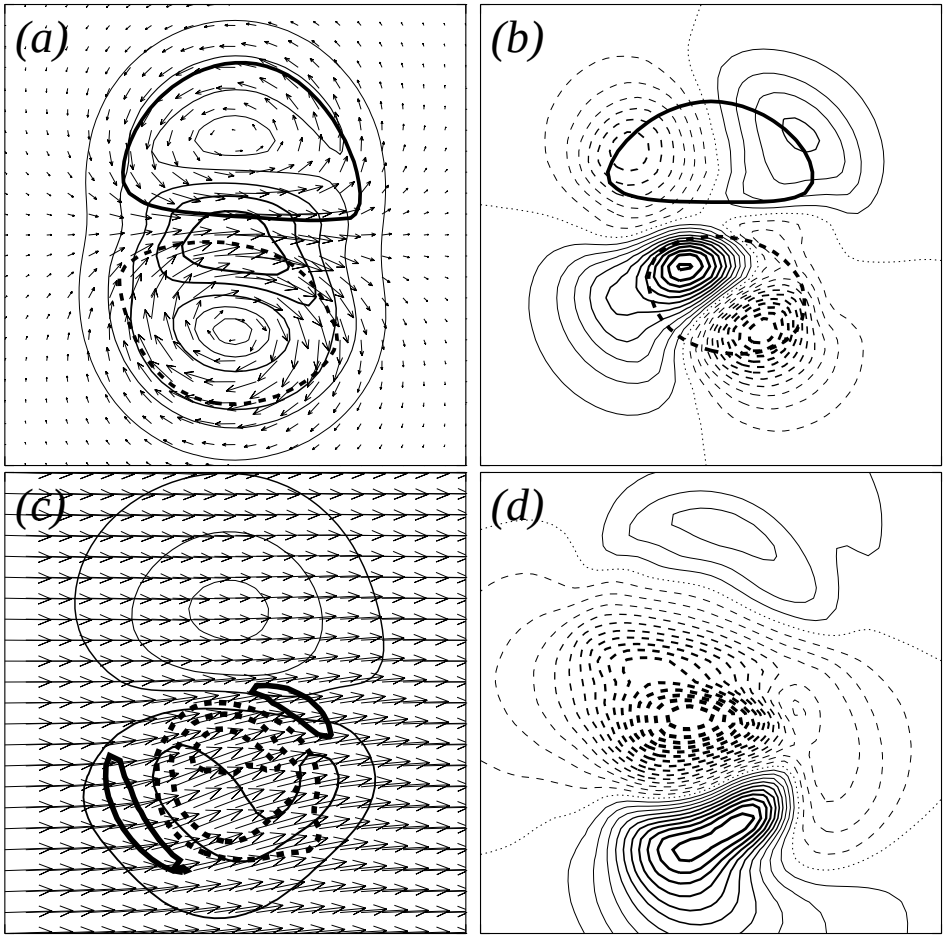

Figure 5.16: Horizontal distributions at $t = 5\,T_{ip}$ of (a) $\mathbf{u}_{bh}$ and $|\mathbf{u}_{bh}|$ ($|\mathbf{u}_{bh}|_{\max} = 0.76$, $\delta|\mathbf{u}_{bh}| = 0.12$, $\varpi^{\pm} = \pm 0.2$), (b) w_b ($w_b \in [-17, 16] \times 10^{-4}$, $\delta w_b = 1.4 \times 10^{-4}$, $\varpi^{\pm} = \pm 0.2$), (c) $\mathbf{u}_{ih}$ and $|\mathbf{u}_{ih}|$ ($|\mathbf{u}_{ih}|_{\max} = 0.84$, $\delta|\mathbf{u}_{ih}| = 6.2 \times 10^{-2}$, $\varpi = [-9, 3] \times 10^{-2}$, PV jump $\delta\varpi \cong \pm 0.03$), and (d) w_i ($w_i \in [-32, 21] \times 10^{-3}$, $\delta w_i = 2 \times 10^{-3}$). (a) and (c) are represented at $i_Z = 65$ ($z = 0$), and (b) and (d) at $i_Z = 61$ ($z = -0.15$), where there is a maxima of total vertical velocity. Domain extent is $\delta x = \delta y = 2.26c$.

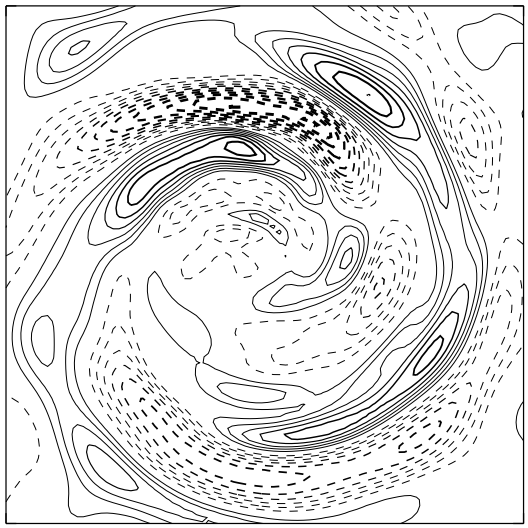

Figure 5.17: Horizontal distribution of w_i at $i_Z = 20$ ($z = -2.21$) and $t = 5\,T_{ip}$ ($w_i \in [-44, 32] \times 10^{-3}$, $\delta w_i = 4 \times 10^{-4}$). Domain extent is $\delta x = \delta y = 4.32c$.

times larger than the w of the dipole in absence of waves. Thus, the interaction between the vortices and the inertial waves enhances the vertical velocity. The horizontal pattern of w_i at $z = -0.15$ (Fig. 5.17d) corresponds to the upper distribution of the interaction between two near-inertial waves triggered in the monopoles after $t > t_i$ (Fig. 5.7, section 5.4.1). The resulting IGW has downward wave packet propagation and a spiral pattern can be noticed in horizontal distributions of w_i at deeper layers ($z = -2.21$, Fig. 5.18). Since the 3D structure of the *total* w is the result of a wave-wave interaction that lies beyond the scope of this work, it is left for future research.

The total energy $E_T(\mathbf{x}, t)$ is decomposed as

$$E_T = E_{Tb} + E_{Ti} + E_{Tint}\,, \tag{5.14}$$

where $E_{Tb} \equiv \mathbf{u}_b^2 + N^2\mathcal{D}_b^2$, $E_{Ti} \equiv \mathbf{u}_i^2 + N^2\mathcal{D}_i^2$, and $E_{Tint} \equiv \mathbf{u}_b \cdot \mathbf{u}_i + N^2\mathcal{D}_b\mathcal{D}_i$ are the total energies of the balanced flow, unbalanced flow, and interaction, respectively. E_{Ti} is one order of magnitude greater than E_{Tb} and E_{Tint} because IGWs are ubiquitous on the domain. Therefore, E_T correlates well with E_{Ti} (Fig. 5.19). The decrease of the spatial average $\langle E_T\rangle(t)$ is about two orders of magnitude smaller than the time mean $\overline{\langle E_T\rangle}$ and is due to the small numerical dissipation.

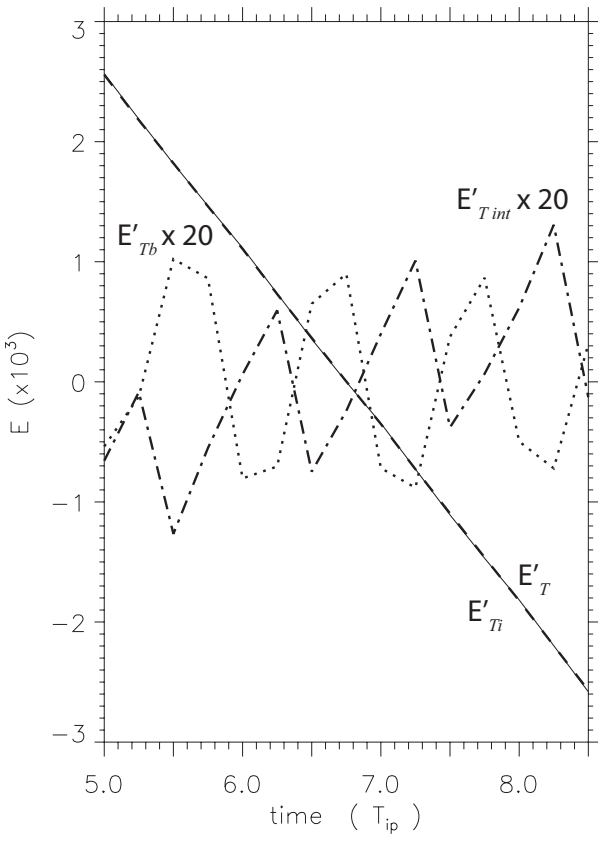

Figure 5.18: Time evolution of anomalies of the total energy E'_T, total energy of the balanced flow E'_{Tb}, total energy of the unbalanced flow E'_{Ti}, and the total energy of the interaction term E'_{Tint}. Anomalies are defined as $E'\chi \equiv \langle E_\chi\rangle - \overline{\langle E_\chi\rangle}$, where $\overline{\langle E_\chi\rangle}$ is the time average of the spatial 3D domain average $\langle E_\chi\rangle$. The time averages and the standard deviations are $\overline{\langle E_T\rangle} = 0.55 \pm 0.16 \times 10^{-2}$, $\overline{\langle E_{Tb}\rangle} = (9.2 \pm 0.37) \times 10^{-4}$, $\overline{\langle E_{Ti}\rangle} = 0.55 \pm 0.16 \times 10^{-2}$, and $\overline{\langle E_{Tint}\rangle} = (2.8 \pm 0.35) \times 10^{-4}$. The decrease of E'_T and E'_{Ti} are due to numerical diffusion.

We note that the unbalanced flow has a small amount of PV (Fig. 5.17c). This *unbalanced* PV, defined as usual from (5.4) using $\mathbf{u}_i$ and $\mathcal{D}_i$, may be used to quantify the interaction between the balanced and unbalanced flows. The unbalanced flow $\boldsymbol{\varphi}_i$, obtained diagnostically from the *total* flow every time t, is not a *true* flow in the sense that $\mathbf{u}_i$ and $\mathcal{D}_i$ do not necessarily have to fulfill the dynamical equations (A.4)–(A.7). Therefore the unbalance pair ($\mathbf{u}_i$ and $\mathcal{D}_i$) may have a non-zero PV (which is a non-linear quantity). The problem arising from the conservation or non conservation of PV in the unbalanced flow is a fictitious one, since the unbalanced and balanced flows, separately, do not generally satisfy the dynamical equations.

5.5.3 Dipole And Gravity Waves Interaction

We analyze here the interaction between a baroclinic dipole identical to case C5 (section 5.5.1) and a gravity wave with $k = -6/c$ ($\lambda_X/c = 2\pi/(ck) \cong 1$) and $\mathcal{D}_i = 0.2$ (case C7). This implies that the dipole and the wave field have similar spatial scales and propagate in opposite directions. In this case $\mathcal{D}_i = |\mathcal{D}_b|_{\max} = 0.2$, that is, the PV vertical advection by the wave flow is larger than in the case of a monopolar vortex and a gravity wave discussed in section 5.4.2.

The large wave motion causes vertical PV vortex advection which largely deforms the PV distribution on horizontal layers (Figs. 5.20a–c). Since ϖ in the vortices decreases as

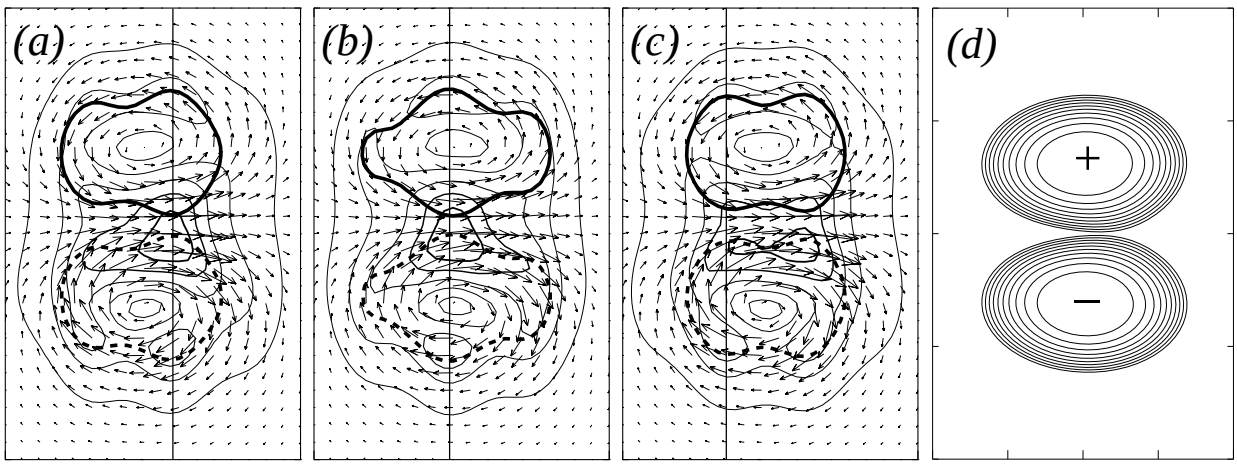

Figure 5.19: (a–c) Horizontal distributions of $\mathbf{u}_h$ and $|\mathbf{u}_h|$ at $i_Z = 65$ ($z = 0$) and at (a) $t = 2\,T_{bp}$, (b) $t = 2.2\,T_{bp}$, and (c) $t = 2.4\,T_{bp}$ ($|\mathbf{u}_h|_{\max} = 0.75$, $\delta|\mathbf{u}_h| = 0.125$). The PV contours with $\varpi = \pm 0.2$ are included. The straight solid line indicates the wave crest position. (d) PV contours on the middle isopycnal ($i_l = 65$, PV jump $\delta\varpi = 7.5 \times 10^{-2}$) at $t = 2.4\,T_{bp}$. Domain extent is $[\delta x, \delta y] = [1.77, 2.65]c$.

the distance from the vortex core increases, the vertical advection of PV by the waves is noticeable in Figs. 5.20a–c as a wave in the PV isolines at $z = 0$ moving westward (the crest is indicated with a solid line in Figs. 5.20a–c). This PV deformation makes the $|\mathbf{u}_h|$ pattern substantially differ from that typical of a dipole in absence of gravity waves (Fig. 5.15b). Interestingly, the dipole remains almost unchanged in the isopycnal space, where PV is always conserved, which proves the stability of vortex dipoles under IGWs perturbations. (Fig. 5.20d).

To address the Doppler-shift frequency in the dipole flow, we improve the numerical resolution by using a dipole with semi-axes twice those given above, that is, $a_X^{\pm} = 1.2c$, $a_Y^{\pm} = 0.8c$, $a_Z^{+} = 0.8$, and $a_Z^{-} = 0.54$. Three cases of plane gravity waves with $\mathcal{D}_i = 0.01$ are considered, namely, $(k, l) = (8/c, 0)$, $(k, l) = (-8/c, 0)$, and $(k, l) = (0, 8/c)$. Owing to the fact that w_i is three orders of magnitude larger than w_b, the vortical w_b quadrupolar pattern is barely noticeable. Thus, the *total* w pattern closely corresponds to the w_i pattern. In all cases the deformation of the wave phase lines evolve into cyclonic or anticyclonic patterns whether a cyclone or an anticyclone, respectively, is involved (see Fig. 5.21). This is consistent with the monopolar vortex case explained in section 5.4.2.

However, some differences can be appreciated when a dipole is considered. In the first case (C8, $(k, l) = (8/c, 0)$), u_b is the velocity component relevant in the Doppler-shift relation (**??**) along the dipole axis. After an unsteady regime, k remains approximately stationary relative to the dipole reference frame (though the wave phase θ continues moving eastward), and therefore the x-derivative of (**??**) implies that

$$\frac{\partial k}{\partial x} = -\frac{k}{u_b - U_d}\frac{\partial u_b}{\partial x} \cong -\frac{k}{u_b}\frac{\partial u_b}{\partial x}, \tag{5.15}$$

where $U_d = 0.02 \ll u_{b\,\max}$ is the x-component of the horizontal dipole velocity. Thus, according to (**??**), the wavelength λ_X increases (decreases) at the entrance (exit) of the dipole axis, where $\partial u_b/\partial x > 0$ ($\partial u_b/\partial x < 0$), as observed in Fig. 5.21a. In the second case (case C9, $k = -8/c$ and $l = 0$), the wave phase line pattern does not differ significantly from that in the first case (Fig. 5.21a) and is not shown. In the last case (case C10, $k = 0$ and $l = 8/c$), the relevant velocity component in the Doppler-shift is v_b. According to (**??**) ω_l increases where $v_b > 0$ (northeastern and southwestern regions) and decreases where $v_b < 0$ (southeastern and northwestern regions) as can be inferred from Fig. 5.21b.

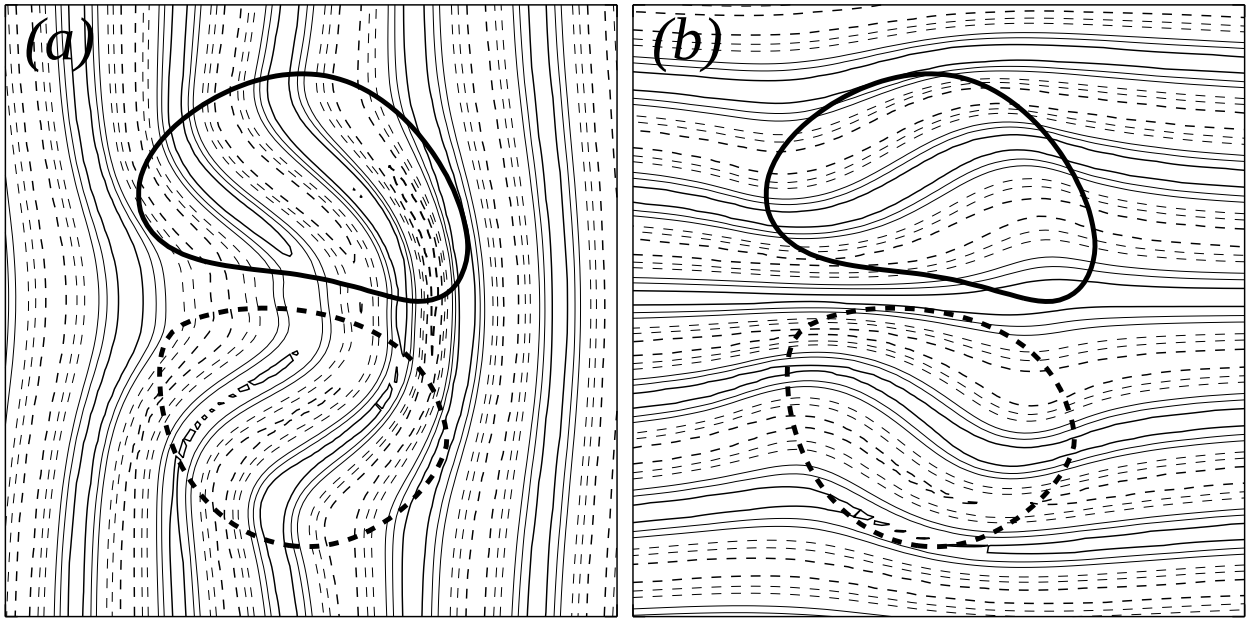

Figure 5.20: Horizontal distributions of w at $i_Z = 65$ ($z = 0$) and at $t = 2.08\,T_{ip}$ with different wavenumbers (a) $(k, l) = (8/c, 0)$ ($w \in [-8.2, 7.3] \times 10^{-2}$, $\delta w = 18 \times 10^{-2}$), and (b) $(k, l) = (0, 8/c)$ ($w \in [-7.5, 7.5] \times 10^{-2}$, $\delta w = 18 \times 10^{-2}$). Domain extent is $\delta x = \delta y = 4.32c$.

5.6 Concluding Remarks

In this work we have numerically investigated the interaction between idealized baroclinic vortical structures and pre-existent plane inertia–gravity waves with similar horizontal velocity or isopycnal vertical displacement amplitudes at the submesoscale. There is a large number of different possible interactions depending on the initial parameters of the vortical structures and IGWs, and we have not attempted to exhaust the very large parameter space. Two main mechanisms are usually involved in this vortex-wave interaction. The first mechanism is the advection of PV by the waves, which makes the vortical structure unsteady and forces it to be permanently in a state of geostrophic adjustment, at the same time that it modifies the upper and lower limits of the IGW frequency wave band. The second mechanism is the advection of waves by the vortices, which changes the local wave frequency through the Doppler-shift frequency relation. These mechanisms operate on submesoscale vortical structures with Rossby numbers close to, but smaller than 1, which remain always stable despite the large amplitude waves.

A remarkable result is the enhancement of the *total* vertical velocity by an order of magnitude when inertial waves are present in vortical flows. This is a clear example of a

non-linear vortex-wave interaction, which results in the generation of right-handed helical waves.Therefore, the wave frequency ranges at initial times from the Coriolis frquency f to an effective frequency f_e and aftewards reaches also suprainertial frequencies due to resonance mechanisms.

Finally, we have considered only interactions between two kinds of submesoscale vortical structures (monopolar and dipole vortices) and two kinds of plane waves (inertial and gravity waves) and many other interactions remain still unexplored. Some examples are the interaction between *localized* wave packets of IGWs and submesoscale vortical structures, and the long term vortex instability of these vortical flows in presence of an inertia–gravity wave field. We also leave for further research the catalytic behaviour of vortical structures triggering IGWs.

Chapter 6

Discussion

This thesis aims to characterize plankton patterns associated to unstable jets and long-lived vortices at mesoscales and submesoscales. Specifically, the effects of horizontal advection, vertical advection, and ecological isopycnal mixing are numerically investigated. Additionally, the flow resulting from a particular kind of vortex-wave interaction is also analyzed due to its likely role at introducing plankton heterogeneity. We summarize here the main results raised in the context of the thesis purpose.

6.1 Ecological initialization

First of all we addressed the non-trivial problem of ecological initialization using a three-variable NPZ (Nutrients-Phytoplankton-Zooplankton) ecological model (chapter 2). We sought vertical profiles in stable equilibrium with the fluid at rest because the purpose of this work was to quantify the ecological response to physical disturbances. To this end, analytical steady solutions with a constant profile of total nitrogen N_T were found. We observed that these profiles are non continuously differentiable, which implies an error source when computing vertical gradients in the advection term of the Eulerian physical-ecological coupled equations. To overcome this error, we found numerical solutions through time integration of a continuously differentiable vertical profile, which converged to a stable stationary state. In contrast to their analytical counterparts, these numerical solutions are continuously differentiable but require vertical resolutions of a few cm, which are computationally unfeasible. However, the numerical error introduced when using larger resolutions is smaller than those associated to uncertainties in ecological parametrization. Thus, numerically stable steady-state vertical profiles are suitable to initialize one dimensional NPZ models, but how are they implemented into three-dimensions? Is N_T homogeneous on horizontal or isopycnal levels? Is

N_T patchy or continuously distributed in the domain? We observed that these initial conditions led to different plankton distributions (chapter 3). Thus care must be taken in choosing proper initial conditions pertinent to the objectives of the specific physical-ecological coupled reasearch.

6.2 Horizontal and vertical advection

The role of horizontal and vertical advection on plankton dynamics was investigated through different three-dimensional initializations of N_T. When N_T was assumed homogeneous on horizontal levels we were able to unveil the plankton heterogeneity caused by vertical advection. Instead, when N_T was homogeneous on isopycnals of fully-developed vortices, an initial seed of horizontal heterogeneity was created. Thus we were able to compare the effects of vertical and horizontal advection on this initial heterogeneity. We considered first the former initialization to quantify the ecological impact of submesoscale vertical velocities associated to a baroclinic unstable jet (chapter 2). We observed that phytoplankton anomalies develop by vertical advection. However, these anomalies are uncorrelated from vertical velocity because phytoplankton responds to the upwelling slower than the timescale of horizontal advection. Based on that, we next considered a submesoscale surface vortex dipole where N_T was initialized constant on isopycnals (chapter 3). This scenario could be conceived as a consequence of an *eddy pumping* event and led us to investigate its long term evolution. We observed two different plankton dynamics spatially divided by the vortex separatrix, and thus by outer PV isosurfaces. Within vortices plankton distribution is dominated by horizontal processes. The generation of plankton anomalies due to vertical advection was insignificant compared to preexisting plankton anomalies, which were trapped inside vortices and thus translated at dipole phase speed. In contrast, outside vortices plankton heterogeneity was introduced by vertical advection, though plankton biomass was dispersed from upwelling regions, analogously to the jet case. As a result, a trail of phytoplankton developed at the cyclone wake. When frontal fluid particles moved anticlockwise to the vortex rear they were uplifted. Since phytoplankton response to the perturbation had some time lag, biomass increased at the cyclone wake. Once there, it decayed at constant mortality rate. This mortality rate was approximated to the parametric value considering a constant trail extent and dipole speed. Firstly, the dominance of horizontal over vertical advection on plankton dynamics when horizontal gradients of plankton exist was in agreement with Lévy

(2003). Secondly, spatial uncorrelation between vertical velocities and the plankton increase caused by them had been already stated at mesoscales and submesoscales (Lévy et al., 2001; Lima et al., 2002). In this work, we took a step further by representing an scenario where both processes occurred, and suggested that potential vorticity contours may act as a spatial divider between them.

The above mentioned results gave us insight on the dynamics of a plankton patch perturbed by a subsurface mesoscale dipole (chapter 3). We observed that the distant action of PV deformed this patch in such a way that a filament runned along the dipole axis, where horizontal speed was maximum. Since this speed increased exponentially with depth, so did the filament elongation. An analytical approximation to this filament extent was derived using a quasi-geostrophic model with vortices of given radius and constant PV. As a result of the negative vertical shear, a given phytoplankton layer was advanced from the layer above, phytoplankton self-shading decreased at its front, and plankton anomalies developed. Horizontal advection has been often considered incapable of introducing heterogeneities unless they already exist (see review Martin, 2003), as in the previous dipole case. We developed further this concept, showing an indirect way through which vertical shear of horizontal speed creates phytoplankton heterogeneity.

6.3 Ecological isopycnal mixing

We have observed that ecosystems get trapped at the interior enclosed by the vortex separatrix. This initial seed of heterogeneity is often introduced by isopycnal doming when vortex formation, such as occurs in *eddy pumping*. Since its long-term evolution remains largely unknown we investigated whether it reaches a steady-state considering three factors: isopycnal vertical displacement $\mathcal{D}$, trophic condition, and isopycnal diffusion (chapter 4).

In order to explore a wide range of the above mentioned factors, an isopycnic physical-ecological coupled model, less complex than the $\mathcal{AB}\varpi$-NPZ model, was first constructed. We considered a spherical mesoscale vortex in the QG space, where the flow is in gradient balance, and thus, is steady and horizontal. As a result, ecological dynamics is only vertically dependent, which let us to introduce the mesoscale vortex forcing into the NPZ model in terms of $\mathcal{D}$. To this end, an analytical expression for $\mathcal{D}$ was found by approximating a polynomial function to a known $\mathcal{D}$ distribution. Finally, this physical-ecological coupled model was initialized using stationary vertical profiles numerically stable with the fluid at

rest (section 6.1).

We observed that these profiles always converged to a steady-state with coexistence of phytoplankton and zooplankton. When isopycnal mixing was not considered, phytoplankton biomass increased linearly with $\mathcal{D}$, due to an enhancement of light irradiance, and logarithmically with total nitrogen, suggesting a saturating response with nutrients. Though these results are restricted to QG spherical vortices, phytoplankton biomass reached also a nearly steady-state in the submesoscale dipole case (Chapter 3). Thus these results may give us some insight in more complex cases that consider three-dimensional fluid motion. Another caveat worth noting is that we assumed a fully-recycling system, while in fact nitrogen is lost across vortex boundaries due to phytoplankton sedimentation. Sinking rates of phytoplankton range from $0.5\,\mathrm{m\,d^{-1}}$ to $10\,\mathrm{m\,d^{-1}}$ in laboratory experiments (Smayda, 1970). This explains why vortices become nutrient depleted after a few months.

When isopycnal mixing was considered, phytoplankton biomass was maximized at a characteristic isopycnal diffusion coefficient $\mathcal{K}^*$ due to a resonance mechanism between diffusive and plankton timescales. Two main effects were involved. Isopycnal doming induced phytoplankton growth, and thus nutrient consumption. This created isopycnal gradients of phytoplankton and zooplankton opposite to those of nutrients, which resulted in an outward diffusive flux of the formers and an inward of the latter. As a result, phytoplankton biomass increased directly through an upward flux of nutrients, and indirectly through a grazing decrease, which was a consequence of a diffusion of zooplankton faster than that of phytoplankton.

Phytoplankton resonant response to nutrients and light has already been stated when including horizontal (Pasquero, 2005; McKiver and Neufeld, 2011) and vertical (Huisman et al., 1999; Ghosal and Mandre, 2003) diffusions, individually. A step further was taken here by exploring a range of nutrient conditions and vortex types considering both diffusions. We observed that the trophic regime determined the magnitude of the phytoplankton response, being meaningful in mesotrophic conditions, in which the largest $\mathcal{K}^*$ was obtained. Conversely, $\mathcal{K}^*$ was nearly unaffected by isopycnal doming. In this case, the phytoplankton growth caused by isopycnal uplift to better lit levels was balanced by an enhancement of phytoplankton outward flux.

We have state therefore that isopycnal mixing upwells nutrients to better lit levels, but can it balance the long-term nutrient depletion within vortices? To answer this question, we

can compare the timescales of the vertical component of the isopycnal diffusion coefficient with a constant plankton sinking rate. The observed nondimensional resonant isopycnal diffusion coefficient ranged from 0.06 to 0.3, for oligotrophic to mesotrophic conditions, respectively. Considering the isopycnal level with the greatest slope, this interval corresponds to a vertical diffusion coefficient $\mathcal{K}_z \in [0.35, 1.8] \times 10^{-2}$. Estimates of phytoplankton sinking rates are about $w_P = -0.65\,\mathrm{m\,d^{-1}}$ (Spitz et al., 2003). This value has been calibrated for a coastal ecosystem and is chosen as an upper bound of sinking rates in oligotrophic environments, where phytoplankton sedimentates slower than in coastal systems. Appropiately adimensionalizing w_P into $\mathcal{W}_P$ we obtain a $|\mathcal{K}_z/\mathcal{W}_P|$-ratio comprised within $[0.78, 4]$. Thus isopycnal mixing could account for long-term plankton subsistence in mesotrophic conditions. The validation of this gross approximation with the simple physical-ecological model constructed is left for future research.

6.4 The role of PV in vortex-wave interactions

In general terms, we have stated that plankton distributions are related with PV when horizontal processes are dominant, which occurs if plankton heterogeneities already exist. Within vortices plankton and PV distributions are in phase since both propagate at vortex translation speed. Outside vortices, the distant action of PV deforms plankton patches in a non-linear way. In contrast, plankton is correlated to horizontal gradients of PV when vertical processes are relevant. However, this correlation is only observed at initial times since ecological anomalies are fastly transported by horizontal advection far from the upwelling location. Additionally, isopycnal mixing accounted for an increase in phytoplankton biomass close to the vortex center. Specifically, this occurs where isopycnal vertical displacement reached its maximum, and thus where vertical gradients of PV are the largest. In order to get an insight on how vortex-wave interaction may alter plankton dynamics we investigated the relation between PV and the flow resulting from a particular type of interaction (chapter 5).

We considered spherical vortex monopoles, in the QG space, and vortex dipoles embedded in an initial pure inertial and gravity wavefield. When inertial waves were involved, a near-inertial right-handed helical wave was developed through a non-linear vortex-wave interaction. Firstly, vortices shifts the inertial frequency to an *effective* frequency $f_e = f + \zeta/2$ (Mooers, 1975a; Kunze, 1985; Rubenstein and Roberts, 1986), where ζ is the vertical component of the relative vorticity. Since the initial configuration of ζ was spatially dependent,

horizontal gradients of f_e were generated. Secondly, waves forced the vortical structure to be in permanent geostrophic adjustment through PV horizontal advection. As a result, PV contours remained no longer *axysimmetric* and *unbalanced* vertical velocities develop, which correlated with horizontal gradients of PV. When fast gravity waves were involved, the wave advection by vortices caused a Doppler shift of the local wavefrequency ω_l. Thus the largest ω_l shifts were observed where horizontal speeds were maximum, and hence where horizontal gradients of PV were large.

Inertia–gravity waves (IGWs) have timescales from minutes to hours, often smaller than the phytoplankton growth timescale, which ranges from half a day to a couple of days. However, a combination of horizontal and vertical advection may allow plankton coupling to IGWs (Franks, 1995b). In fact, some in-situ observations manifest the role of IGWs creating heterogeneities (Franks, 1995a; Granata et al., 1995). The impact of the observed near-inertial spiral wave on plankton dynamics is left for future research.

Overall, the present work contributes to characterize the three-dimensional plankton structure associated to mesoscale and submesoscale vortices through PV. It is thought as a process investigation rather than an attempt to simulate any particular ecosystem. Our results are the consequence of some initial numerical assumptions, which have been designed to widen the comprehension plankton dynamics in the stratified and oligotrophic open ocean.

Chapter 7

Conclusions

1. Ecological steady-state vertical profiles numerically stable were found suitable to initialize physical-ecological coupled models in the Eulerian description.

2. Initialization of the above mentioned profiles, homogeneous on horizontal or isopycnal levels in the whole domain or in spatial patches, led to different plankton distributions. Thus, three-dimensional initial conditions should be carefully chosen based on the proposed research objectives.

3. Vortex separatrix divided two different plankton dynamics. Inside the separatrix, plankton distribution was dominated by horizontal advection and was in phase with potential vorticity (PV) since both translated at vortex phase speed. In contrast, outside the separatrix, plankton vertical and horizontal advections were of the same order of magnitude than the ecological forcing. Vertical advection generated plankton anomalies, which were immediately transported far away from the upwelling location by horizontal advection. As a result, plankton was initially correlated with vertical velocity, and hence with horizontal gradients of PV.

4. A phytoplankton trail was developed at the wake of a translating surface cyclone due to horizontal advection, vertical advection, and phytoplankton intrinsic timescale. The horizontal length of this trail was nearly stationary and depended linearly on the vortex propagation speed and phytoplankton mortality rate.

5. A baroclinic subsurface vortex dipole deformed surface ecosystem patches such that a filament ran along its axis. The elongation of this filament increased with depth because the vertical shear of the horizontal speed was negative. As a consequence, phytoplankton self-shading decreased at the filament front and phytoplankton biomass increased.

Thus horizontal advection may be an indirect source of plankton heterogeneity through modulation of the light regime.

6. A very simple isopycnic physical-ecological model was constructed for baroclinic mesoscale vortex monopoles, spherical in the quasi-geostrophic (QG) vertically stretched space, and small-scale motions. The mesoscale forcing was introduced into the ecological model in terms of vertical displacement of isopycnals, while small-scale forcing was parametrized as a Fickian-type diffusion.

7. Stationary phytoplankton and zooplankton distributions numerically stable were possible considering mesoscale vortices of variable intensity in different trophic conditions and a wide range of isopycnal diffusion coefficients.

8. A characteristic isopycnal diffusion coefficient increased phytoplankton biomass through a resonant mechanism between physical and ecological timescales. This increase was meaningful in mesotrophic conditions. In this case, the maximum of phytoplankton was located at the depth where the isopycnal vertical displacement was the largest, nearby the largest vertical gradients of PV. We suggested that isopycnal diffusion may contribute to long-term plankton subsistence within coherent vortices.

9. The advection of PV by large amplitude inertia–gravity waves made vortex structures unstable, forcing them to be in a process of permanent geostrophic adjustment. Additionally, PV advection modified the upper and lower bounds of the inertia–gravity wave frequency range. The advection of waves by vortices caused a Doppler shift in the local wave frequency.

10. A non-linear interaction between spherical (in the QG space) vortices and initially pure inertial waves generated a near-inertial right handed helical wave which enhanced total vertical velocity by an order of magnitude.

Appendix A

Theoretical basis of the $\mathcal{AB}\varpi$ model

We consider the isochoric (volume-preserving) motion of a stable stratified fluid in a reference frame rotating with constant angular velocity $f/2$ around the vertical z-axis with respect to an inertial frame. The density anomaly ρ' is defined as

$$\rho'(\mathbf{x},t) \equiv \rho(\mathbf{x},t) - \varrho_z\, z - \rho_0\,, \tag{A.1}$$

where ρ is the mass density, and $\rho_0 > 0$ and $\varrho_z < 0$ are density and density stratification constants. We introduce the pressure anomaly p' as the pressure p (including the centripetal potential) minus the hydrostatic pressure due to a constant vertical density stratification

$$p'(\mathbf{x},t) \equiv p(\mathbf{x},t) + g\left(\rho_0 + \frac{1}{2}\varrho_z z\right) z\,, \tag{A.2}$$

where g is the acceleration due to gravity. The Boussinesq approximation in the vertical component of the momentum equation is

$$-\frac{1}{\rho}\left(\frac{\partial p}{\partial z} + g\rho\right) \cong -\alpha_0\left(\frac{\partial p}{\partial z} + g\rho\right) = -\alpha_0\frac{\partial p'}{\partial z} - \alpha_0 g\rho'\,, \tag{A.3}$$

where $\alpha_0 \equiv \rho_0^{-1}$ is a constant specific volume. Vector components here always refer to Cartesian components. The basic equations are the nonhydrostatic, balance of linear momentum in a rotating frame under the f-plane and Boussinesq approximations, the mass conservation equation, and the isochoric condition,

$$\frac{d\mathbf{u}_h}{dt} + f\mathbf{k}\times\mathbf{u}_h = -\alpha_0\,\boldsymbol{\nabla}_h p'\,, \tag{A.4}$$

$$\frac{dw}{dt} = -\alpha_0\,\frac{\partial p'}{\partial z} - \alpha_0 g\rho'\,, \tag{A.5}$$

$$\frac{d\rho}{dt} + \rho\,\boldsymbol{\nabla}\cdot\mathbf{u} = 0\,, \tag{A.6}$$

$$\boldsymbol{\nabla}\cdot\mathbf{u} = 0\,. \tag{A.7}$$

The initial unknowns are the three-dimensional velocity field $\mathbf{u} = (u, v, w)$, the pressure anomaly p', and the density anomaly ρ'.

The incompressibility condition $d\rho/dt = d(d)/dt = 0$ is expressed in terms of $\mathcal{D}$ as

$$\frac{d\mathcal{D}}{dt} = w\,. \tag{A.8}$$

The vertical displacement of isopycnals $\mathcal{D}$ is related to ρ by

$$N^2(\mathcal{D}(\mathbf{x},t) - z) = g\left(\frac{\rho(\mathbf{x},t)}{\rho_0} - 1\right), \tag{A.9}$$

where $N^2 \equiv -\alpha_0\, g \varrho_z$ is the square of the constant background Brunt-Väisälä frequency.

For any quantity χ let $\tilde{\chi} \equiv \chi/f$. The geostrophic velocity shear is defined through the *thermal wind* expression

$$\frac{\partial \tilde{\mathbf{u}}^g}{\partial z} \equiv -c^2 \mathbf{k} \times \boldsymbol{\nabla}_h \mathcal{D} = c^2 \left(\frac{\partial \mathcal{D}}{\partial y}, -\frac{\partial \mathcal{D}}{\partial x}\right), \tag{A.10}$$

where $c = \epsilon^{-1} \equiv N/f$. The relative *pseudovorticity* is the vorticity of the horizontal velocity, defined in Cartesian components as

$$\boldsymbol{\zeta} \equiv \boldsymbol{\nabla} \times \mathbf{u}_h = \left(-\frac{\partial v}{\partial z}, \frac{\partial u}{\partial z}, \frac{\partial v}{\partial x} - \frac{\partial u}{\partial y}\right). \tag{A.11}$$

The horizontal gradient of $\mathcal{D}$ (times c^2) may be interpreted as the dimensionless horizontal geostrophic pseudovorticity

$$\tilde{\boldsymbol{\zeta}}^g_h = \left(-\frac{\partial \tilde{v}^g}{\partial z}, \frac{\partial \tilde{u}^g}{\partial z}\right) = \tilde{\boldsymbol{\omega}}^g_h = c^2 \boldsymbol{\nabla}_h \mathcal{D}\,. \tag{A.12}$$

Since $\boldsymbol{\zeta}$ is solenoidal ($\boldsymbol{\nabla} \cdot \boldsymbol{\zeta} = 0$) the horizontal divergence of $\tilde{\boldsymbol{\zeta}}^g_h$ is equal to (minus) the differential geostrophic vertical vorticity,

$$-\boldsymbol{\nabla}_h \cdot \tilde{\boldsymbol{\zeta}}^g_h = \frac{\partial}{\partial z}\left(\frac{\partial \tilde{v}^g}{\partial x} - \frac{\partial \tilde{u}^g}{\partial y}\right) = \frac{\partial \tilde{\zeta}^g}{\partial z} = \tilde{\zeta}^g_z = -c^2 \nabla_h^2 \mathcal{D}\,. \tag{A.13}$$

Using (A.8) it follows that the rate of change of $\boldsymbol{\nabla}\mathcal{D}$ is

$$\frac{d}{dt}\boldsymbol{\nabla}\mathcal{D} = \boldsymbol{\nabla} w - \boldsymbol{\nabla}\mathbf{u} \cdot \boldsymbol{\nabla}\mathcal{D}\,. \tag{A.14}$$

The horizontal component of the above equation expresses the rate of change of $\tilde{\boldsymbol{\zeta}}^g_h$. It is used below to obtain the rate of change of the dimensionless horizontal ageostrophic vorticity $\tilde{\boldsymbol{\omega}}'_h \equiv \tilde{\boldsymbol{\omega}}_h - \tilde{\boldsymbol{\omega}}^g_h = \tilde{\boldsymbol{\omega}}_h - c^2 \boldsymbol{\nabla}_h \mathcal{D}$, where the relative vorticity $\boldsymbol{\omega} \equiv \boldsymbol{\nabla} \times \mathbf{u}$.

The vorticity equation consistent with (A.7) is

$$\frac{d\tilde{\boldsymbol{\omega}}}{dt} = \tilde{\boldsymbol{\omega}} \cdot \boldsymbol{\nabla}\mathbf{u} + \frac{\partial \mathbf{u}}{\partial z} + fc^2\mathbf{k} \times \boldsymbol{\nabla}_h\mathcal{D}\,, \tag{A.15}$$

and is used next to express the material rate of change of $\tilde{\boldsymbol{\omega}}'_h$.

The three-dimensional vector potential $\boldsymbol{\varphi} = (\varphi, \psi, \phi)$ and its Laplacian $\boldsymbol{\mathcal{A}}$ is introduced by the definitions

$$\boldsymbol{\mathcal{A}} = (\mathcal{A}, \mathcal{B}, \mathcal{C}) \equiv \boldsymbol{\nabla}^2\boldsymbol{\varphi} = (\nabla^2\varphi, \nabla^2\psi, \nabla^2\phi) \equiv \tilde{\boldsymbol{\omega}} - c^2\boldsymbol{\nabla}\mathcal{D}\,. \tag{A.16}$$

From the divergence of (A.14), and using the vector identity

$$\boldsymbol{\nabla}^2\boldsymbol{\varphi} = \boldsymbol{\nabla}(\boldsymbol{\nabla} \cdot \boldsymbol{\varphi}) - \boldsymbol{\nabla} \times \boldsymbol{\nabla} \times \boldsymbol{\varphi}\,, \tag{A.17}$$

we obtain

$$c^2\mathcal{D} = -\boldsymbol{\nabla} \cdot \boldsymbol{\varphi}, \quad \tilde{\mathbf{u}} = -\boldsymbol{\nabla} \times \boldsymbol{\varphi}\,. \tag{A18a,b}$$

Thus, $c^2\mathcal{D}$ is the *source* of $-\boldsymbol{\varphi}$, and $-\boldsymbol{\varphi}$ is the velocity potential of $\tilde{\mathbf{u}}$. Consequently, $c^2\mathcal{D}$ may be interpreted as the source of the velocity potential of $\tilde{\mathbf{u}}$. Because of (A.12), the *horizontal* vector $\boldsymbol{\mathcal{A}}_h = (\mathcal{A}, \mathcal{B})$ is the dimensionless horizontal ageostrophic vorticity

$$\boldsymbol{\mathcal{A}}_h = \boldsymbol{\nabla}^2\boldsymbol{\varphi}_h = \tilde{\boldsymbol{\omega}}_h - \tilde{\boldsymbol{\omega}}^g_h = \tilde{\boldsymbol{\omega}}'_h\,. \tag{A.19}$$

Combining (??) with (??) the rate of change of $\boldsymbol{\mathcal{A}}$ is

$$\frac{d\boldsymbol{\mathcal{A}}}{dt} = -f\mathbf{k} \times \boldsymbol{\mathcal{A}}_h + (1 - c^2)\boldsymbol{\nabla}w + \tilde{\boldsymbol{\omega}} \cdot \boldsymbol{\nabla}\mathbf{u} + c^2\boldsymbol{\nabla}\mathbf{u} \cdot \boldsymbol{\nabla}\mathcal{D}\,. \tag{A.20}$$

The horizontal component of (??) is (5.2).

The prognostic fields are therefore $\boldsymbol{\mathcal{A}}_h$ and ϖ (which is explicitly conserved). The horizontal potential $\boldsymbol{\varphi}_h$ is diagnosed solving $\boldsymbol{\mathcal{A}}_h = \nabla^2\boldsymbol{\varphi}_h$. The vertical potential ϕ is recovered from $\boldsymbol{\varphi}_h$ and ϖ as follows. The dimensionless potential vorticity (PV) anomaly $\varpi \equiv \Pi - 1$ may be written in terms of $\boldsymbol{\varphi}$

$$\varpi = \mathcal{L}_q\{\phi\} + \mathcal{M}\{\boldsymbol{\varphi}\}\,, \tag{A.21}$$

where the linear operator $\mathcal{L}_q = \nabla^2_h + \epsilon^2\partial_{zz}$ is the QG Laplacian operator, and

$$\mathcal{M}\{\boldsymbol{\varphi}\} \equiv -(1 - \epsilon^2)\boldsymbol{\nabla}_h \cdot \boldsymbol{\varphi}_{hz} + \epsilon^2[\boldsymbol{\nabla}^2\boldsymbol{\varphi} - \boldsymbol{\nabla}(\boldsymbol{\nabla} \cdot \boldsymbol{\varphi})] \cdot \boldsymbol{\nabla}(\boldsymbol{\nabla} \cdot \boldsymbol{\varphi})\,. \tag{A.22}$$

The PV equation (A.15) is inverted (Dritschel and Viúdez, 2003) to obtain the vertical

potential ϕ.

The numerical procedure used to solve the nonlinear equation (A.15) is based on iteration. We collect the linear, constant-coefficient terms of ϕ on the left hand side, and consider all remaining terms (computed using a previous guess for ϕ) as a source on the right hand side. The result is an equation of the form $\mathcal{L}_q\{\phi^{(i+1)}\} = S\{\varphi, \psi, \phi^{(i)}\}$ where the source $S\{\varphi, \psi, \phi^{(i)}\} \equiv \varpi - \mathcal{M}\{\varphi, \psi, \phi^{(i)}\}$. Given $S\{\varphi, \psi, \phi^{(i)}\}$, this equation is inverted in spectral space to find a new approximation $\phi^{(i+1)}$, that is $\phi^{(i+1)} = \mathcal{L}_q^{-1}\{S\{\varphi, \psi, \phi^{(i)}\}\}$. If $\phi^{(i+1)}$ is such that $\max\{|\phi^{(i+1)}(\mathbf{x}_j) - \phi^{(i)}(\mathbf{x}_j)|, j = 1 \dots n_X \times n_Y \times n_Z\} < \varepsilon$, where the tolerance $\varepsilon = 10^{-9}$, then the new solution $\phi^{(i+1)}$ is accepted. Otherwise, S is recomputed using the new $\phi^{(i+1)}$, the horizontal potentials (φ, ψ) remain unchanged, and the procedure is repeated $(i \to i + 1)$. This process converges in a few iterations as long as the flow is statically and inertially stable.

Finally, the numerical implementation of (**??**) requires the addition of a bi-harmonic hyperdiffusion term on the rhs and the use of a spectral filter in the spatial derivatives in order to reduce numerical instabilities raised from discretization and aliasing. The hyperdiffusion term is $\mu\mathcal{L}_q^4\mathcal{A}_h$, where μ is the constant hyperviscosity coefficient and the operator $\mathcal{L}_q^4 \equiv \nabla_h^4 + \epsilon^4\partial_{zzzz}$. The spectral filter $F(k) \equiv \exp(-c_0(k/k_{\max})^{10})$, where k is the wavenumber and c_0 is chosen so that $F(k_{\max}) = 10^{-14}$.

Appendix B

Resumen en castellano

Capítulo 1. Introducción

Los ecosistemas marinos son altamente reactivos a la física del océano. Los organismos pelágicos están inmersos en el fluido y por tanto están explícitamente afectados por su dinámica. Debido a que la mayoría de estos individuos no tienen motilidad, derivan por el extenso océano. El nombre de estos errantes proviene de su equivalente griego, *plancton*. El plancton está formado por dos grupos microscópicos, los autótrofos y los heterótrofos. A los primeros se les denomina *fitoplancton*, donde *fito* hace referencia a su proximidad con las *plantas* por la realización de la fotosíntesis. Los segundos son el plancton *animal*, el *zooplancton*, debido a que se alimentan de fitoplancton y zooplancton más pequeño. El fitoplancton es de gran importancia porque constituye la base de la cadena trófica en el océano. Su crecimiento está afectado por el movimiento del fluido ya que los factores limitantes de este crecimiento, luz y nutrientes, están segregados verticalmente en el océano. Por un lado, la capa iluminada es análoga a la punta de un iceberg, constituye la fracción superior de un

océano que es en promedio veinte veces más profundo. Por otro lado, los nutrientes sedimentan en el oscuro océano profundo lenta e incesantemente. Debido a esto, las velocidades verticales en el océano afectan implícitamente los ecosistemas fertilizando la capa iluminada.

La caracterización de patrones ecológicos asociados a determinadas estructuras físicas ha sido objeto de numerosos trabajos. En esta línea, Haury et al. (1978) elaboró la primera analogía ecológica al diagrama de *Stommel*, el cual representa variables oceánicas físicas en función del espacio y del tiempo, para representar la variabilidad de la biomasa de zooplancton. Hoy en día, interacciones físico-biológicas han sido ampliamente documentadas desde escalas *planetarias* hasta escalas de *Kolmogorov* (Steele, 1978; Mann and Lazier, 1991; Denman and Gargett, 1995). La combinación de este amplio rango de escalas espaciales da lugar a patrones complejos y deterministas, los cuales se reflejan en las distribuciones de clorofila superficial tal y como miden los satélites espaciales. Regiones altamente productivas se localizan en márgenes occidentales, latitudes subpolares, y en el Ecuador (Yoder et al., 1993), donde afloramientos costeros, subducción de masa de agua, y los vientos alisios, vencen la segregación vertical de luz y nutrientes. Dichas zonas se denominan *eutróficas*, porque las comunidades no están limitadas por nutrientes, en contraposición a las zonas *oligotróficas*. La mayor parte del océano es oligotrófico. Su concentración de clorofila superficial del mar (CC) tiene una media geométrica alrededor de dos órdenes de magnitud menor que las aguas eutróficas, y su variabilidad está dominada por la varianza submensual y de mesoescala (Doney et al., 2003). Como las imágenes de CC contienen información sobre

el flujo turbulento del océano (Nieves et al., 2007), la variabilidad del plancton en en mar abierto este probablemente generada por fenómenos de mesoescala, y las estructuras verticales en particular pueden estan implicadas. La dinámica y la estructura tridimensional de los ecosistemas en mar abierto son aún bastantes desconocidas porque el muestreo sinóptico con alta resolución espacial es más costoso que en la costa. En esta línea, el objetivo de esta tesis es profundizar sobre cómo los remolinos de mesoescala, los cuales se localizan por doquier, perturban la base de la cadena trófica en regímenes oligotróficos. Para ello, analizamos primero qué factores determinan los patrones planctónicos en mesoescalas para escoger un descriptor físico apropiado (sección 1.1). Luego revisamos los mecanismos generadores de heterogeneidad ecológica (sección 1.2) e identificamos aquellos relacionados con nuestro objetivo (sección 1.3). Finalmente, resumimos los objetivos específicos de cada capítulo (sección 1.4).

1.1. Patrones planctónicos de mesoescala: La huella ecológica de la vorticidad potencial

Los primeros mapas sinópticos de clorofila superficial del mar se obtuvieron a primeros de los ochenta (Gordon et al., 1980; Gower et al., 1980). A primera vista, este tipo de mapas muestran una alta correlación con la temperatura superficial del mar en mesoescalas, por lo que el plancton ha sido frecuentemente considerado como un trazador pasivo. No obstante,

cuando se cuantifican patrones de distribución surgen diferencias entre física y ecología (ver revisión de Martin, 2003). Estas diferencias se explican mediante dos factores principales, el bombeo de nutrientes a escalas pequeñas y un desfase en la respuesta temporal del plancton a las perturbaciones. Las estructuras de submesoescala han sido foco de atención la última década porque incrementan la velocidad vertical w un orden de magnitud respecto a las estructuras mesoescalares y causan la inyección de nutrientes alóctonos en la capa fótica (ver revisión de Klein and Lapeyre, 2009), donde la irradiancia por luz es mayor que el 1% de la irradiancia superficial del mar. Como las escalas temporales físicas y ecológicas son similares en la submesoescala, el plancton se acopla a este afloramiento de nutrientes y se correlaciona con la producción primaria (Lévy et al., 2001) y algunos índices fotosintéticos (Falkowski, 1983; Cullen and Lewis, 1988). No obstante, la correlación con w depende de la escala temporal del parámetro ecológico. Aquellos parámetros con escalas temporales mayores que los de la advección horizontal, como la biomasa de fitoplancton, muestran un desfase espacial con w (Lima et al., 2002). La importancia de una escala temporal inherente a la ecología en los patrones planctónicos fue elegantemente demostrada por Abraham (1998) utilizando un modelo numérico bidimensional de turbulencia. Él constató una mayor dispersión de zooplancton comparado con el fitoplancton, y de éste respecto a la física. Por lo tanto, las distribuciones mesoescalares de plancton resultan de la interacción entre advección horizontal, advección vertical, y escalas temporales intrínsecas al plancton. Si estas

distribuciones están causadas por fenómenos físicos o ecológicos depende de la relación entre sus escalas temporales (Mahadevan and Campbell, 2002). Con el fin de relacionar ambas escalas temporales, buscamos describir la completa naturaleza tridimensional del flujo con una única escala temporal.

Una magnitud física muy útil que relaciona el movimiento horizontal con el vertical es la *vorticidad potencial* (VP). El concepto de VP fue introducido por Beltrami en 1871, aplicado a un océano adiabático y no viscoso constituido de múltiples capas por Rossby en 1936, y extendido a flujos baroclinos por Ertel en 1942 (ver Viúdez, 2001, para referencias y relación entre definiciones de PV). Según éste último, la VP específica se define como

$$\Pi \equiv \frac{\boldsymbol{\omega} + f\mathbf{k}}{\rho} \cdot \boldsymbol{\nabla} T_\theta \,, \tag{A.1}$$

donde la suma de la vorticidad $\boldsymbol{\omega} = (\xi, \eta, \zeta)$ relativa a un sistema de referencia que rota con la velocidad angular de la Tierra y la componente vertical de la vorticidad planetaria f, es decir el parámetro de Coriolis, es la vorticidad absoluta. Además, ρ es la densidad de masa, T_θ la temperatura potencial, aunque podría ser cualquier propiedad escalar del fluido que se conserve materialmente (Pedlosky, 1987, capítulo 2), y $\boldsymbol{\nabla}$ el operador gradiente tridimensional. La importancia geofísica de la VP yace en su invariancia material, es decir,

$$\frac{\mathrm{d}\Pi}{\mathrm{d}t} = 0 \,. \tag{A.2}$$

Una forma de derivar (A.2) proviene de la conservación de circulación para un movimiento sin fricción asumiendo conservación material de T_θ y conservación de masa (Pedlosky, 1987, capítulo 2). Por lo tanto (A.2) se puede interpretar como la conservación de circulación a lo largo de circuitos materiales y momento angular para un volumen fijo, lo cual nos permite relacionar movimientos verticales y horizontales. Cuando un fluido es barotrópico la relación es directa porque (A.1) se convierte en

$$\Pi \equiv \frac{\zeta + f}{h}\,, \tag{A.3}$$

donde h es la separación vertical entre isosuperficies materiales adyacentes (ec. 3.4.9. Pedlosky, 1987). Por consiguiente, cambios en h implican ajustes en ζ para conservar la VP, explicando los conocidos efectos de la *bailarina* o el *patinador sobre hielo*. En cambio, cuando el fluido es baroclínico, la inclinación de las isosuperficies materiales introduce cambios no triviales en $\boldsymbol{\omega}$. Es más, si se puede establecer alguna condición de balance (junto con adecuadas condiciones de contorno), entonces para una determinada distribución de VP dado un tiempo fijo se pueden recuperar los campos tridimensionales del vector velocidad, la presión y la densidad asociados al flujo *en balance* (ausente de ondas inercio–gravitatorias, OIGs) en un proceso conocido como la inversión de la VP (Hoskins et al., 1985; McIntyre and Norton, 2000; Viúdez, 2008a).

La VP es relevante para la dinámica ecológica por varias razones. En primer lugar,

porque describe el campo del vector de velocidad *en balance* y el desplazamiento vertical de las isopicnas $\mathcal{D}$. En segundo lugar, porque relaciona el afloramiento vertical con la advección horizontal, factor determinante en la dispersión del plancton (Martin et al., 2002). La importancia de la VP en ecología fue señalada primero por Woods (1987) y Strass and Woods (1987). Éstos observaron un incremento de la clorofila en zonas con grandes gradientes isopicnos, las cuales se pensó que eran áreas con elevada w. Su hipótesis concuerda con trabajos in-situ (Pallàs-Sanz and Viúdez, 2005) y numéricos (Viúdez and Dritschel, 2003, 2004b) que demuestran que las zonas con grandes gradientes de ζ y VP se asocian con elevados valores de w. Grandes gradientes horizontales de VP implican grandes gradientes horizontales de ρ y por tanto de $\mathcal{D}$. En consecuencia, cuando estos gradientes de $\mathcal{D}$ son advectados, suceden grandes cambios locales en $\mathcal{D}$ y w. No obstante, la advección vertical no es el único mecanismo implicado en las distribuciones de plancton como hemos mencionado anteriormente.

1.2. ¿Cómo los vórtices de mesoescala alteran los ecosistemas?

Muchas observaciones in-situ evidencian el impacto de los remolinos en la biología marina. En la base de la red trófica, los vórtices afectan cualitativamente la estructura de la comunidad (Thompson et al., 2007; Huang et al., 2010), los procesos fisiológicos (Bibby et al., 2008), y el transporte de ecosistemas (Batten and Crawford, 2005). Además, ellos alteran cuantitativamente los balances biogeoquímicos por medio del incremento de la productividad

primaria nueva (PPN, Morán et al., 2001). Por ejemplo, éstos están implicados en el balance de carbono del Atlántico Norte, aunque su contribución específica es sujeto de debate científico variando entre el 50% y el 10% de la PPN (ver revisión de Oschlies, 2008). Como resultado, los vórtices también perturban niveles tróficos superiores (Mackas et al., 2005; Atwood et al., 2010).

Existen diferentes mecanismos a través de los cuales los remolinos introducen la mencionada variabilidad ecológica. A continuación, analizamos su signatura ecológica con el fin de relacionarla con la VP cuando sea posible.

- *Advección horizontal.* La turbulencia bidimensional de mesoescala induce una transferencia conservativa de grandes a pequeñas escalas (Abraham, 1998). Considerando el fitoplancton como un trazador pasivo como primera aproximación, entonces su distribución viene determinada por la vorticidad y la tensión. En el interior de los vórtices, la vorticidad domina sobre el *strain* y las partículas describen trayectorias orbitales. En el exterior, la tensión domina sobre la vorticidad, dando lugar a un movimiento caótico (Provenzale, 1999). Como resultado, las manchas de fitoplancton se deforman en espirales y filamentos (Lehahn et al., 2007) e incluso estructuras ondulatorias (Menkes et al., 2002) en los bordes de los remolinos. Es más, éstos también transportan aguas ricas en clorofila lejos de la costas de Algeria (Arnone and LaViolette, 1986), de Alaska (Batten and Crawford, 2005), o del nordeste africano (Pelegrí et al., 2005)

entre muchas otras.

- *Bombeo de eddy.* Este término fue acuñado por Falkowski et al. (1991) para designar el incremento en la PPN debido al afloramiento de la nutriclina en la capa fótica causado durante el paso de un ciclón superficial o un anticiclón subsuperficial en translación (McGillicuddy et al., 1999). Por un lado, el levantamiento de las isopicnas es máximo en el centro de los remolinos, hecho que explica altos valores de clorofila superficial del mar al núcleo de éstos (Siegel et al., 2008; Tew-Kai and Francis, 2009; Siegel et al., 2011). Por otro lado, la VP está correlacionada con el desplazamiento vertical de las isopicnas (Viúdez and Dritschel, 2003). En consecuencia, esperamos un enriquecimiento de clorofila donde los valores absolutos de VP son máximos.

- *Submesoescala.* Los vórtices completamente desarrollados son raramente esféricos en el espacio isotrópico cuasi-geostrófico (QG). En el espacio QG la extensión vertical se ha estirado de tal forma que sus dimensiones son (x, y, cz), donde $c \equiv N/f$ es el ratio de Prandlt, N la frecuencia de flotabilidad de fondo, y f la frecuencia inercial. Sin embargo, estos vórtices presentan una variedad de geometrías elípticas durante su vida, causando que el vórtice rote en torno a su eje, y genere una distribución cuadrupolar de la velocidad vertical w (Viúdez and Dritschel, 2003). La w máxima se alcanza en el borde de los vórtices incrementando las concentraciones de clorofila en la periferia de los remolinos (Siegel et al., 2011). Por tanto, la clorofila se relaciona mejor

con gradientes horizontales de VP que con la VP. Sin embargo, para obtener estos patrones de w, a menudo se requieren resoluciones más pequeñas que 10 km (Lévy et al., 2001), próximas al muestreo de submesoescala.

- *Interacciones entre remolinos.* Los vórtices interactúan de muchas formas mediante rebote, fusión, o formando estructuras complejas (Voropayev and Afanasyev, 1994). Debido a que estas interacciones modifican el flujo, también perturban las distribuciones ecológicas. Por ejemplo, la ubicua presencia de estructuras en forma de seta de la clorofila superficial del mar en frentes costeros (Sur et al., 1996; Stapleton et al., 2002) son huellas de la interacción entre dos vórtices de VP opuesta, es decir, un vórtice dipolar. Otro ejemplo es la fusión de anticiclones en la Corriente de Kuroshio, la cual resulta en un incremento de w que causa un aumento del fitoplancton en los bordes del vórtice (Yoshimori and Kishi, 1994).

- *Mezcla isopicna.* Como hemos mencionado anteriormente, los máximos en $\mathcal{D}$ ocurren en el centro de monopolos, generando un gradiente isopicno de irradiancia de luz. En regímenes oligotróficos, el crecimiento del fitoplancton está principalmente limitado por luz y nutrientes. Como la curvatura de las isopicnas modifica la cantidad de luz a la cual se expone el fitoplancton confinado en isopicnas, afecta el crecimiento de éste, e indirectamente a la consumición de nutrientes. Por tanto, la difusión isopicna puede incrementar la respuesta del fitoplancton a la luz en el centro de ciclones y en los bordes

de anticiclones por medio de un flujo de repuesto de nutrientes en contra del gradiente.

- *Interacción vórtice-onda.* Por un lado, las interacciones entre vórtices y OIGs es ubicua en el océano. Algunas de estas interacciones implican un cambio de la frecuencia de onda de inercial a casi-inercial (Perkins, 1976) y el hecho que los anticiclones atrapen paquetes de OIGs (Kunze, 1986). Por otro lado, las distribuciones de fitoplancton son alteradas tanto por vórtices como OIGs (Franks, 1995a; Granata et al., 1995; Gómez et al., 2001; Sangrà et al., 2001). Por lo tanto, esperamos que la interacción vórtice-onda afecte la dinámica planctónica.

Otros mecanismos vorticales han sido propuestos para explicar las distribuciones planctónicas, aunque se escapan del objetivo de este trabajo. En esta línea, el forzamiento por viento también incrementa la producción primaria tanto en los márgenes de vórtices mediante *interacciones vórtice-viento* (Martin et al., 2001; Mahadevan et al., 2008) como en el centro de anticiclones por *hundimiento de la capa de mezcla* (Thompson et al., 2007). Por último, *la mezcla diapicna* tiene una contribución pequeña en el afloramiento de nutrientes comparado con los mecanismos anteriormente mencionados (Siegel et al., 1999; Ledwell et al., 2008).

1.3. Interacciones físico-biológicas relevantes en vórtices coherentes

El ciclo de vida de un vórtice comprende diferentes etapas con diferentes dinámicas: formación, madurez, y decaimiento (Sangrà et al., 2005). Áreas altamente turbulentas, como

los frentes costeros, son zonas de formación y decadencia de vórtices. En contraposición, el estratificado mar abierto está principalmente dominado por vórtices maduros de larga vida. Los vórtices coherentes completamente desarrollados se trasladan a través del océano conservando su VP. La isosuperficie de VP más externa define la separatriz del vórtice, la cual delimita el vórtice y actúa como una barrera impermeable. Dentro de la separatriz el fluido rota aproximadamente como un cuerpo sólido. Fuera de la separatriz, la velocidad horizontal decrece exponencialmente con el radio. Por tanto los vórtices pueden atrapar aguas en su interior y transportar ecosistemas a largas distancias. Si estos ecosistemas sólo están dominados por advección horizontal, la distancia de transporte dependerá de la tasa de sedimentación de nutrientes hacía la capa afótica. Hecho que conlleva a un agotamiento de clorofila a largo término dentro de los vórtices, a menos que exista algún tipo de afloramiento de nutrientes. En este respecto, *el bombeo de eddy* asume un transporte de nutrientes alóctonos en el interior del vórtice (Martin and Pondaven, 2003), que implica mezcla a través de los márgenes del vórtice y por tanto restringe el mecanismo a ciclones en formación y anticiclones en decaimiento (Franks et al., 1986b). Este mecanismo genera heterogeneidad ecológica pero no explica como ésta se mantiene durante el vórtice en translación. En contraposición, la velocidad vertical en monopolos o estructuras vorticales complejas de mesoescala y submesoescala puede contribuir a la subsistencia del ecosistema en vórtices de un año de vida. Además, la inyección de nutrientes por difusión isopicna es probable que ocurra en mar abierto, donde el flujo es principalmente bidimensional. Aunque

la contribución de la mezcla isopicna en el afloramiento de nutrientes alóctonos es pequeña comparada con la de los mecanismos anteriormente mencionados (Siegel et al., 1999; Ledwell et al., 2008), puede ser significante en el afloramiento de nutrientes regenerados. Por último, la manera como la interacción vórtice-onda afecta la ecología es aún bastante desconocida.

1.4. Objetivos de la tesis y estructura

El principal objetivo de este trabajo es explorar algunos mecanismos que pueden explicar la subsistencia del plancton dentro de vórtices maduros de larga vida que se trasladan a través de ambientes oligotróficos. En esta línea, pretendemos estimar el papel de la *vorticidad potencial* (VP) como un descriptor ecológico. Para ello, utilizamos un modelo numérico no hidrostático que simula el flujo tridimensional con conservación de volumen de un fluido estratificado y en rotación utilizando las aproximaciones de plano f y de Boussinesq, el modelo $\mathcal{AB}\varpi$ (Dritschel and Viúdez, 2003). Este algoritmo es especialmente apropiado para nuestro objetivo porque conserva explícitamente la VP en isopicnas, hecho que permite la conservación de elevados de gradientes de magnitudes, y por tanto resuelve la w con gran precisión. Nuestro investigación se estructura en cuatro capítulos que tratan los siguientes objetivos específicos.

En el **Capítulo 2** acoplamos un modelo ecológico NPZ (Nutrientes-Fitoplancton-Zooplancton) al modelo $\mathcal{AB}\varpi$. Está dedicado a encontrar soluciones ecológicas válidas para inicializar el modelo NPZ. La idoneidad de estas soluciones es probada analizando la re-

spuesta planctónica a velocidades verticales de submesoescala asociadas a una corriente en chorro con una estabilidad baroclina.

En el **Capítulo 3** extendemos la investigación del capítulo anterior a vórtices de mesoescala y submesoescala. Nos centramos en una estructura vortical particular, el vórtice dipolar, debido a que se trata de la estructura vortical más simple con velocidad de propagación. Por tanto, podemos investigar cómo la traslación del vórtice afecta a ecosistemas atrapados dentro de los vórtices y aquellos contenidos en aguas oligotróficas adyacentes.

En el **Capítulo 4** cuantificamos la respuesta ecológica a la luz y a nutrientes aflorados por movimientos de pequeña escala en vórtices mesoescalares. Específicamente, consideramos un ciclón esférico, en el espacio isotrópico QG, porque nos permite construir un modelo acoplado físico-biológico muy simple con un coste computacional menor que el del modelo acoplado $\mathcal{AB}\varpi$-NPZ. Esto nos posibilita explorar un amplio rango de coeficientes de difusión isopicna κ, intensidades del ciclón, y regímenes tróficos. El capítulo está por tanto diseñado para determinar los valores de κ que maximizan la respuesta planctónica a la luz y nutrientes en diferentes tipos de vórtices.

En el **Capítulo 5** tratamos la interacción vórtice-onda desde un punto de vista físico. Utilizamos el modelo $\mathcal{AB}\varpi$ para investigar la interacción entre monopolos esféricos en el espacio QG y dipolos inmersos en un campo inicial de ondas planas puramente gravitatorias e inerciales. El objetivo del capítulo es relacionar la el campo de velocidad vertical resultante con la VP.

Por último, el **Capítulo 6** contiene una discusión general de los resultados obtenidos y el **Capítulo 7** las principales conclusiones de la tesis.

Capítulo 2. Simulaciones numéricas de distribuciones de nutrientes-fitoplancton-zooplancton fluctuantes forzadas por la velocidad vertical en balance de submesoescala

En este capítulo demostramos primero que las ecuaciones NPZ tienen soluciones en una dimensión estacionarias y continuamente diferenciables en sentido numérico (Figura B.1). No obstante, su correcta discretización requiere altas resoluciones verticales, con un tamaño de malla de pocos centímetros (Figura B.2). Esto representa un obstáculo para la disponibilidad de memoria de acceso aleatorio en los actuales ordenadores que corren modelos acoplados física-ecología en tres dimensiones. Aunque desde una perspectiva numérica este hecho supone una severa limitación computacional, desde una perspectiva más amplia otros obstáculos, como por ejemplo los errores asociados a la parametrización matemática de diferentes procesos NPZ, son probablemente de mayor relevancia (ver Anderson, 2005; Flynn, 2005; Mitra et al., 2007). La exactitud de las soluciones ecológicas modeladas reproducen la dinámica fundamental de los ecosistemas, y que aún cuando la resolución vertical es pobre es posible obtener buenos resultados cualitativos a partir de estos modelos.

Estas soluciones son potencialmente útiles como condiciones iniciales de ecosistemas estacionarios para investigar la importancia de la advección horizontal y vertical en modelos numéricos acoplados física-ecología tridimensionales. Para demostrarlo presentamos como ejemplo, la generación de anomalías plánctonicas debido a un aumento de la velocidad vertical en balance durante un proceso de inestabilidad baroclina (Figura B.3). Debido a este

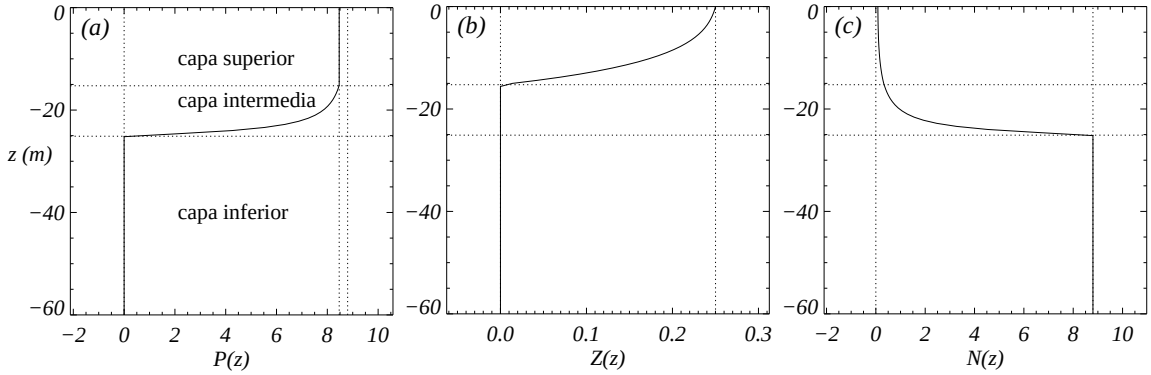

Figura B.1: Perfiles verticales estacionarios de (a) fitoplancton $P(z)$, (b) zooplancton $Z(z)$, y (c) nutrientes $N(z)$ expresados en unidades de mmolN m^{-3}. Estos perfiles diferencian tres capas. Una superior donde fitoplancton y zooplancton coexisten, una intermedia donde sólo existe fitoplancton, y una inferior donde la escasedad de luz no permite el crecimiento del fitoplancton.

hecho las distribuciones de fitoplancton y zooplancton están más relacionadas con los gradientes de VP que con la VP misma. No obstante, estas anomalías planctónicas son posteriormente advectadas lejos de las regiones de afloramiento o subducción. La contribución de la advección horizontal y del cambio local al cambio material del fitoplancton y zooplancton es el doble que la de la velocidad vertical (Figura B.4), hecho que explica que los campos de velocidad vertical y de variables ecológicas estén finalmente descorrelacionados (ver p. ej. Ruiz et al., 2001, para observaciones experimentales in-situ de este proceso). Este proceso,

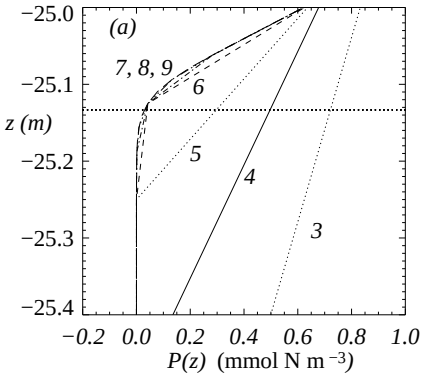

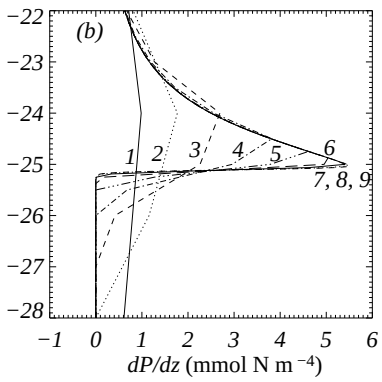

i	resolución (m)
1	4
2	2
3	1
4	0.5
5	0.25
6	0.125
7	0.0625
8	0.03125
9	0.015625

Figura B.2: Visión amplificada alrededor de la profundidad $z \sim -25.1$ m de los perfiles verticales de (a) fitoplancton $P^{(i)}(z)$ y (b) la derivada parcial de P respecto a z, $\partial P^{(i)}/\partial z$, a diferentes resoluciones verticales (i).

junto con la generación de anomalías NPZ por la velocidad vertical de submesoescala, concuerda con Lévy et al. (2001), la cual utilizó un modelo de ecuaciones primitivas con difusión vertical. No obstante, el trabajo experimental de Lévy et al. (2005) cuestiona la contribución de la advección total de submesoescala en la variabilidad de fitoplancton a largo plazo.

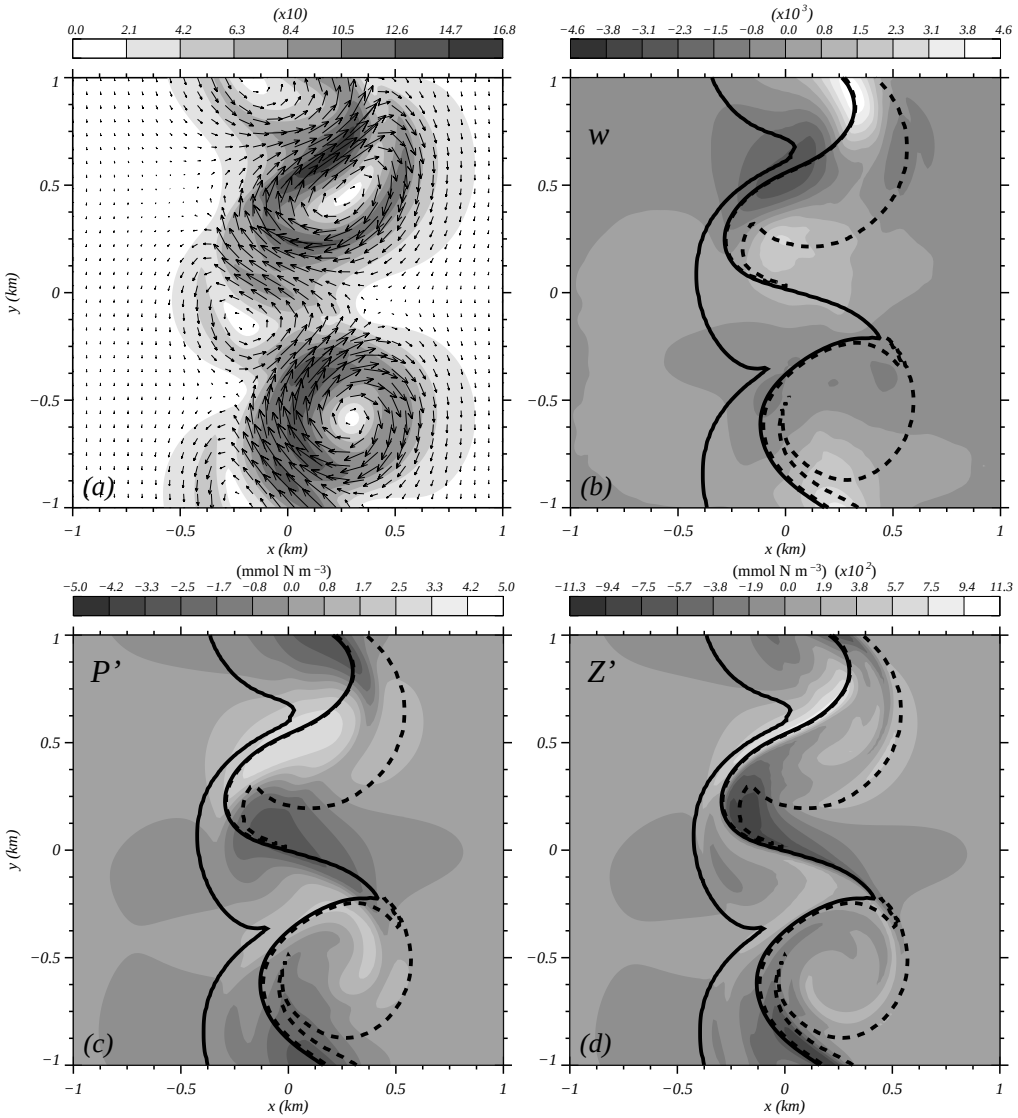

Figura B.3: (a) Distribución de la velocidad horizontal $\mathbf{u}_h = (u, v)$ en la profundidad $z = 0$. Sólo se representa uno de cada cuatro vectores. Los contornos corresponden al módulo de la velocidad horizontal ($\max\{|\mathbf{u}_h|\} = 1.7$). (b) Distribución de la velocidad vertical w en la profundidad $z \simeq -23.4\,\mathrm{m}$ ($w \in [-2.9, 4.5] \times 10^{-3}$). (c) Distribución de la anomalía de fitoplancton P' en $z \simeq -23.4\,\mathrm{m}$ ($P' \in [-3.3, 3.1]\,\mathrm{mmolN\,m^{-3}}$). (d) Distribución de la anomalía de zooplancton Z' en $z = -12.5\,\mathrm{m}$ ($Z' \in [-9.0, 8.3] \times 10^{-2}\,\mathrm{mmolN\,m^{-3}}$). Nótese la correlación inicial de w con P' y en menor grado también con Z'.

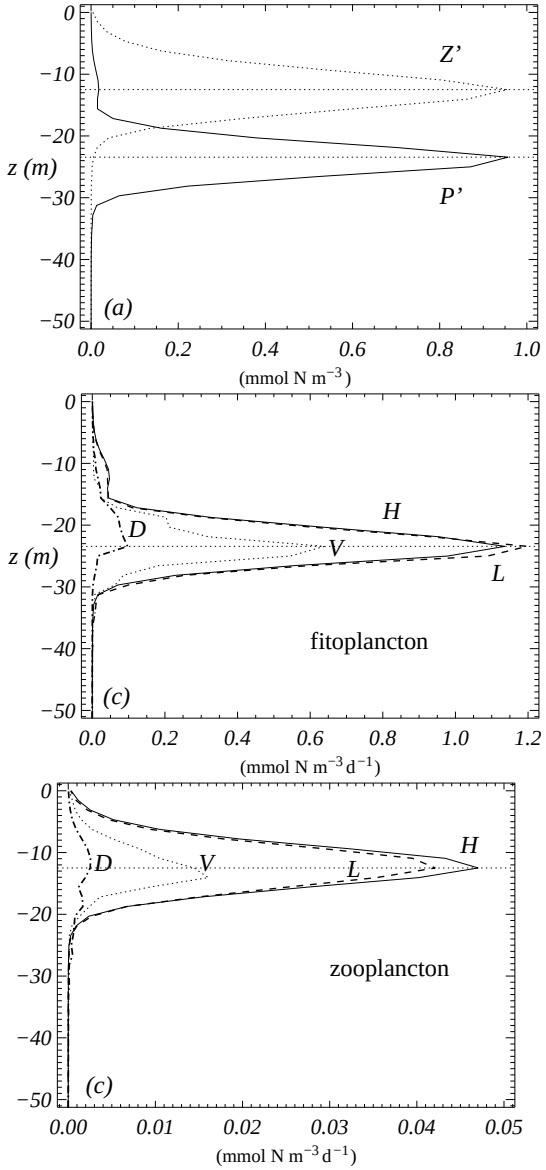

Figura B.4: Perfiles de desviación estandard $\sigma\{\chi\}(z) \equiv (\langle\langle(\chi - \langle\chi\rangle_h)^2\rangle_h)^{1/2}$, donde $\langle\chi\rangle_h$ es el promedio horizontal en función de la profundidad z después de ocho periodos inerciales de simulación de (a) anomalía de fitoplancton P' y zooplancton Z' ($\times 50$), (b) advección horizontal (H), advección vertical (V), cambio local (L), y cambio material (D) de fitoplancton, y (c) para el zooplancton.

Nuestros resultados muestran que el fitoplancton y el zooplancton se comportan aproximadamente como trazadores pasivos cuando los organismos son de hecho trazadores activos. Esto sucede porque los sencillos perfiles NPZ estacionarios que se usan como condiciones iniciales permiten poca interacción entre el fitoplancton y el zooplancton. En un trabajo

futuro investigaremos estas interacciones utilizando perfiles iniciales NPZ más realistas y un modelo biológico más complejo.

Por último, este trabajo representa un primer paso hacía una mejor comprensión de los procesos biológicos forzados por la velocidad vertical de submesoescala. En esta línea, aún existen muchas preguntas abiertas. ¿Cómo la velocidad vertical de submesoescala contribuye a la producción primaria y secundaria en comparación con la de mesoescala? ¿La advección vertical genera diferentes patrones biológicos en regímenes eutróficos y oligotróficos? ¿Es importante la submesoescala en la variación biológica estacional?

Capítulo 3. Incremento de fitoplancton causado por dipolos oceánicos

La distribución tridimensional del plancton ha sido relacionada con la vorticidad potencial utilizando un modelo numérico acoplado físico-biológico que conserva explícitamente la vorticidad potencial en isopicnas. En particular, investigamos cómo la traslación de los vórtices y la acción a distancia de la vorticidad potencial alteran un sistema oligotrófico en estado estacionario. El primer efecto se trató considerando un dipolo maduro inmerso en el ecosistema, mientras que el segundo efecto se analizó inicializando un dipolo subsuperficial y un ecosistema agrupado en superficie.

Constatamos que la separatriz del dipolo, la cual se define mediante los bordes de vorticidad potencial, actuó como una barrera impermeable, generando dos nichos ecológicos diferentes (Figura B.5). En primer lugar, el fitoplancton y el zooplancton quedaron atrapados dentro de los vórtices convergiendo a un estado en equilibrio (Figura B.6), el cual estuvo sustentado por producción regenerada. Esta situación puede explicar la subsistencia de comunidades dentro de vórtices de larga vida que se trasladan en mar abierto (Mackas et al., 2005; Whitney et al., 2005). El estado estacionario observado dependió del desplazamiento vertical de las isopicnas, y por tanto de la vorticidad potencial, y de las condiciones ecológicas iniciales. Estos resultados están en concordancia con trabajos numéricos y experimentales previos que concluyeron que cambios en la geometría del vórtice (Lévy, 2003) y

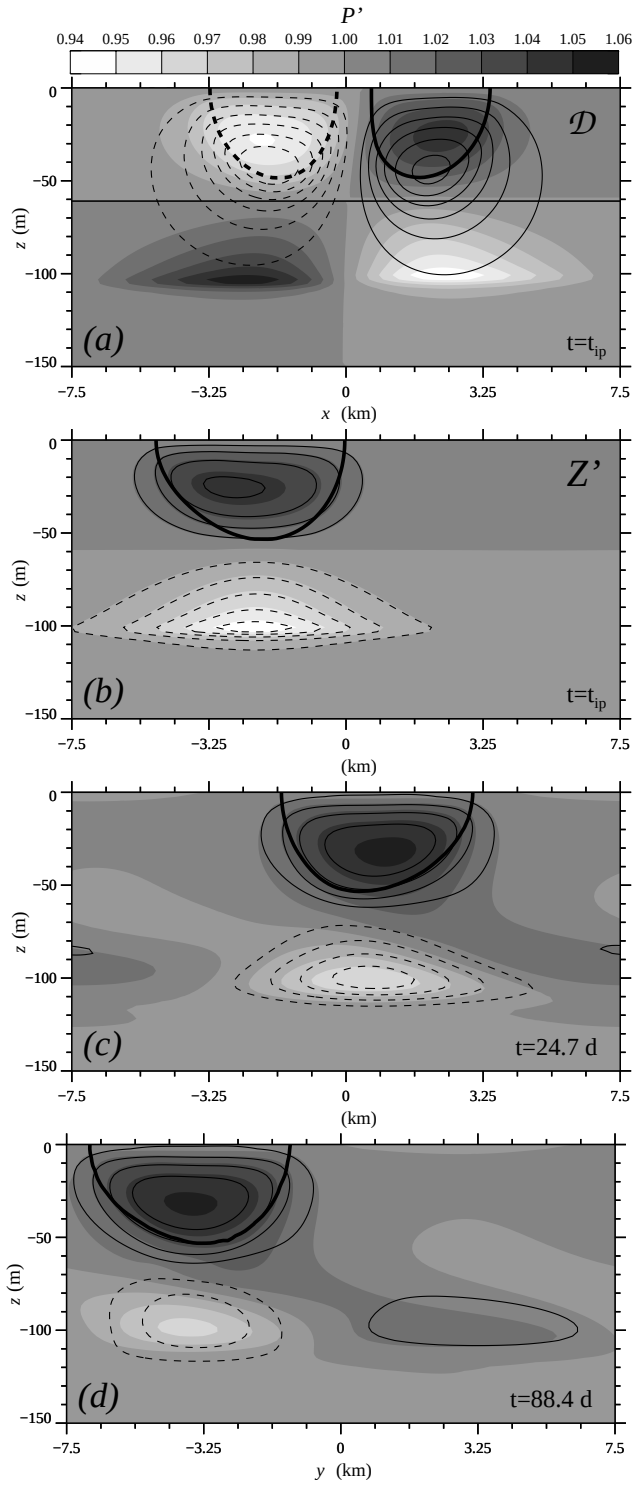

Figura B.5: (a) Sección vertical que intersecta el centro de los vórtices, en $y \cong -2.6\,\mathrm{km}$, ($i_Y = 43$), de $P'(x,z)$ en escala de grises y $\mathcal{D}$ ($|\mathcal{D}| < 4.3\,\mathrm{m}$, intervalo de contorno $\delta\mathcal{D} \simeq 0.6\,\mathrm{m}$) después de la inicialización de VP a $t = t_i$. (b, c, d) Secciones verticales paralelas al eje del dipolo de $P'(y,z)$ y $Z'(y,z)$ en líneas de contorno ($|Z'| < 1.06, \delta Z' = 1\%$) a diferentes tiempos y (b) $x \cong 2.1\,\mathrm{km}$ ($i_X = 83$), (c) $x \cong 2.3\,\mathrm{km}$ ($i_X = 85$), y (d) $x \cong 3.5\,\mathrm{km}$ ($i_X = 95$). Máximo subsuperficial de fitoplancton z_P (línea recta en (a)) y contornos de $\varpi = \pm 0.2$ son incluidos por referencia. Nótese que P' incrementa alrededor de 2% en la estela del ciclón.

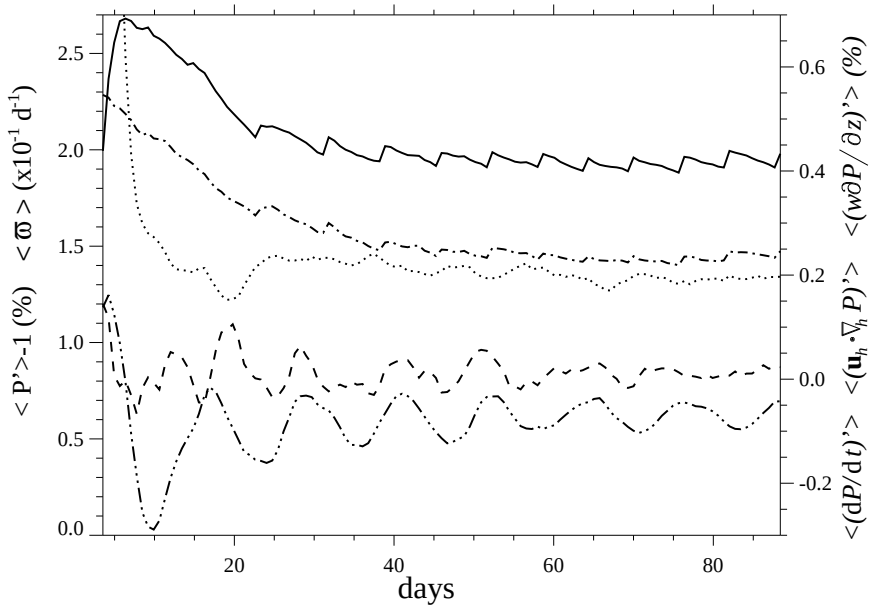

Figura B.6: Evolución temporal de $\langle P' \rangle$ (línea continua), $\langle \varpi \rangle$ (línea discontinua punto-guión), $\langle (\mathrm{d}P/\mathrm{d}t)' \rangle$ (línea de puntos), $\langle (\mathbf{u}_h \cdot \boldsymbol{\nabla}_h P)' \rangle$ (línea discontinua tres puntos-guión) y $\langle (w\, \partial P/\partial z)' \rangle$ (línea discontinua), promediados en el volumen del ciclón. Después de un periodo de ajuste inicial $\langle P' \rangle$ alcanza un estado estacionario cercano a la configuración inicial.

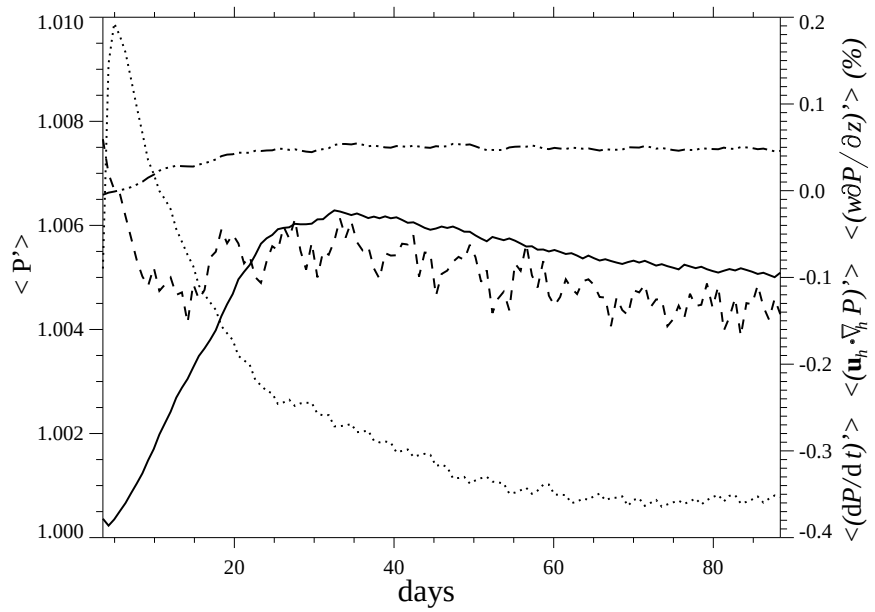

Figura B.7: Evolución temporal de $\langle P' \rangle$ (línea continua), $\langle (\mathrm{d}P/\mathrm{d}t)' \rangle$ (línea de puntos), $\langle (w\, \partial P/\partial z)' \rangle$ (línea discontinua), y $\langle (\mathbf{u}_h \cdot \boldsymbol{\nabla}_h P)' \rangle$ (línea discontinua punto-guión), promediados dentro de la isosuperficie $P' = 1.002$ debajo del borde más profundo del dipolo. Nótese que $\langle P' \rangle$ alcanza un estado casi estacionario, aunque los términos ecológicos no se contrarrestan.

las propiedades biogeoquímicas de las aguas originarias (Thompson et al., 2007), respectivamente, alteran las distribuciones planctónicas.

En segundo lugar, la heterogeneidad planctónica afuera del dipolo se generó por advección vertical y horizontal, las cuales fueron del mismo orden de magnitud que el forzamiento biológico. El aumento del fitoplancton por medio de la advección vertical ocurrió en la estela del dipolo. A medida que el dipolo se trasladaba, las partículas de fluido se desplazaban de la parte frontal de los vórtices a la parte trasera alrededor de los bordes de vorticidad potencial (Figura B.8). Por tanto, éstas se elevaban a profundidades más iluminadas cuando se movían anticiclónicamente y ciclónicamente en dipolos superficiales y subsuperficiales, respectivamente. La respuesta del fitoplancton a este forzamiento tuvo un tiempo de desfase alrededor de $\delta t = 1.4\,\mathrm{d}$ causando un desfase espacial entre el incremento del fitoplancton y el mecanismo causante. Como resultado el fitoplancton se acumuló en la estela de los vórtices. Además, como esta acumulación se movía más lentamente el dipolo con su velocidad de fase, se formó una cola de fitoplancton detrás de éste. La extensión de la cola fue proporcional a la tasa de cambio material del fitoplancton $\mathrm{d}P/\mathrm{d}t$. Por tanto, si se conoce la extensión de la cola de fitoplancton y la velocidad del dipolo, se puede inferir la tasa $\mathrm{d}P/\mathrm{d}t$. La formación de una cola de fitoplancton detrás de los vórtices ya fue conceptualizada por Thompson et al. (2007) En este trabajo, amplia este concepto porque ilustra cómo un solo vórtice es responsable de dos mecanismos de afloramiento diferentes que ocurren simultáneamente.

Un afloramiento permanente de aguas atrapadas dentro de la separatriz del vórtice y un afloramiento transitorio alrededor de la periferia del vórtice (Flierl and McGillicuddy, 2002). Ambos afloramientos pueden explicar la cola de clorofila desarrollada debajo de un pico de clorofila somero (Ning et al., 2004, Figura 9d) observado en la estela de un par de vórtices con anomalías del nivel del mar de signo opuesto (Chang et al., 2010, Figura 10).

También evidenciamos que la advección horizontal causó indirectamente un incremento de fitoplancton cuando existieron gradientes verticales de vorticidad potencial. Para explicar este hecho, investigamos cómo un dipolo subsuperficial de mesoescala alteró un frente de plancton superficial. Como la velocidad horizontal fue máxima a lo largo del eje del dipolo e incrementaba con la profundidad, se formó un filamento a lo largo de la dirección de la trayectoria del dipolo, cuya extensión alcanzó un máximo subsuperficial. Dicha extensión concordó cuantitativamente con una relación analítica entre el desplazamiento de las partículas del fluido y la vorticidad potencial del vórtice utilizando un modelo de dipolo cuasigeostrófico sencillo compuesto por vórtices esféricos de radio y profundidad fijos (Figura B.9). Por tanto, la extensión del filamento se puede aproximar conociendo la geometría e intensidad de la estructura de vorticidad potencial. Como resultado de una cizalla negativa, el fitoplancton incrementó en el frente del filamento debido a una disminución del apantallamiento del fitoplancton que aumentó la irradiancia de la luz. Aunque el cambio luminoso fue pequeño, explicó incrementos significativos de fitoplancton (Figura B.10), como ya se ha observado en anticiclones cuyas aguas superficiales han sido reemplazadas por otras más transparentes

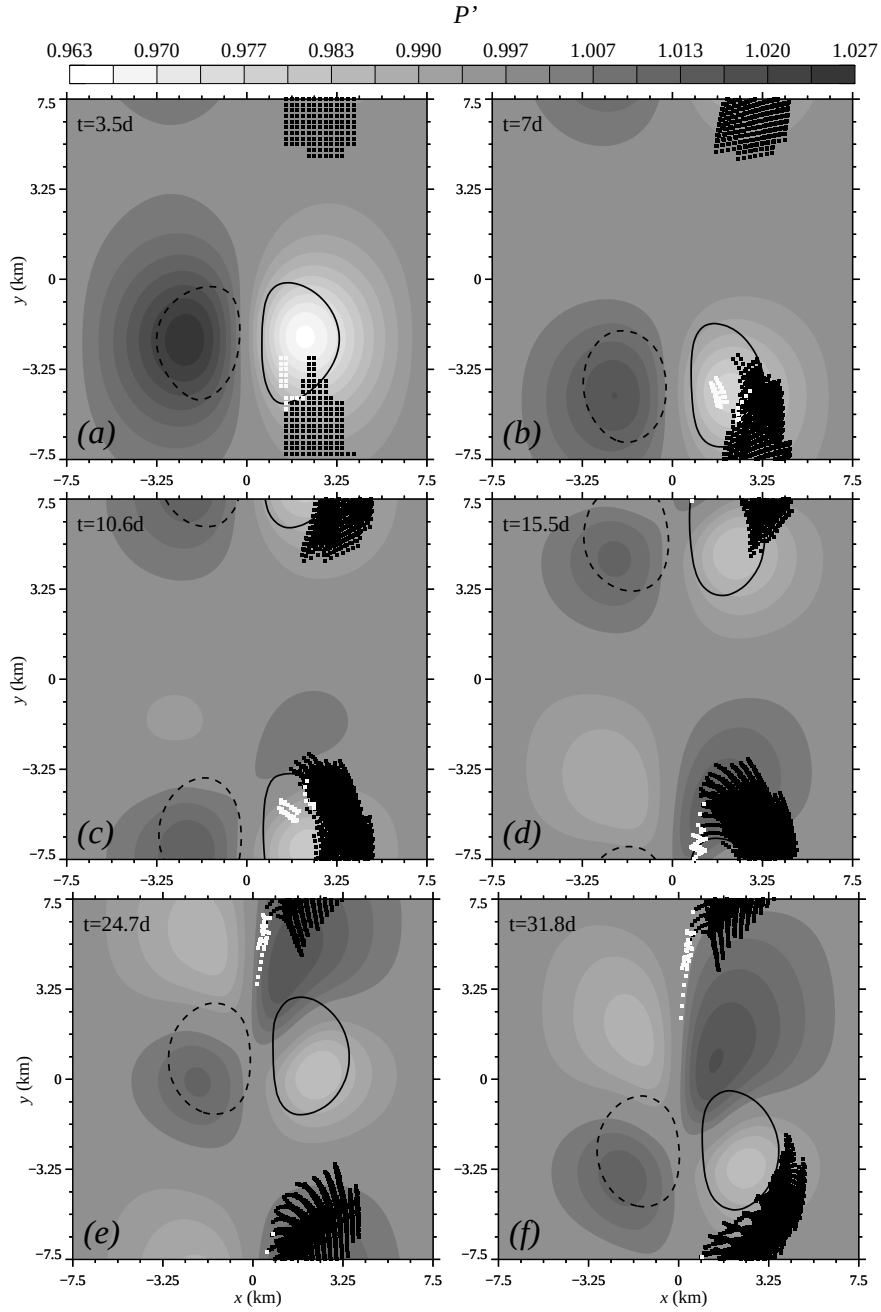

Figura B.8: Evolución temporal de la posición de las partículas de fluido que experimentan un incremento en P' similar al de la cola de P', es decir, $1 < P' < 1.02$, a diferentes tiempos. Los conjuntos de partículas negros ($\mathcal{B}$) y blancos ($\mathcal{W}$) se ilustran con el correspondiente color. Además,, la distribución de P' en $z \simeq -65\,\mathrm{m}$, ($i_Z = 28$) se muestra en contornos grises. Los contornos de VP $\varpi = 0.2$ se incluyen por referencia. Nótese que las partículas seleccionadas se localizan en la estela del ciclón cuando se desarrolla la cola de P'.

(Baird et al., 2011). Por tanto, los dipolos subsuperficiales de mesoescala son responsables tanto del transporte de filamentos superficiales de clorofila de origen costero hacia mar adentro (Serra et al., 2010) como también de un incremento de fitoplancton. El mecanismo que

describimos puede explicar la subsistencia de comunidades subsuperficiales en filamentos planctónicos que penetran en mar abierto, los cuales desaparecerían por la mortalidad y sedimentación del plancton. Finalmente, frentes nítidos de fitoplancton como el que aquí se describe, se asocian frecuentemente a frentes de densidad bien definidos (Jones et al., 1991), en los cuales el afloramiento ocurre a lo largo de los bordes del filamento (Moisan and Hofmann, 1996). La contribución simultánea de un incremento de la irradiancia por luz y un afloramiento localizado a la subsistencia de la comunidad en la evolución a largo plazo de los filamentos costeros será objeto de futuras investigaciones.

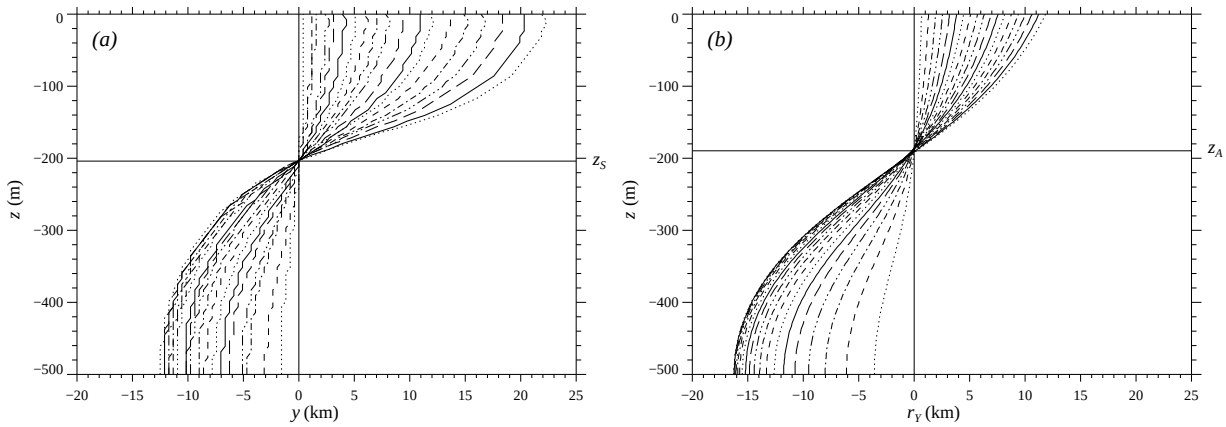

Figura B.9: Posición del borde frontal de N_T a lo largo del eje del dipolo, $x = 0$, centrado en y_1 y relativo al dipolo. Los resultados numéricos (a) son aproximados analíticamente (b) utilizando la velocidad geostrófica exterior de la aproximados QG $\tilde{v}_e^g(r,t)$, ecuación (3.12), donde r_Y es la distancia entre el borde frontal y el centro del dipolo. En ambos casos, la línea vertical inicialmente recta de N_T se inclina gradualmente con el tiempo alrededor del borde superior de la separatriz z_S. Cada línea corresponde a tiempos consecutivos comprendidos entre $t \in (t_i, 15.9)\,\mathrm{d}$ con $\delta t \cong 0.7\,\mathrm{d}$.

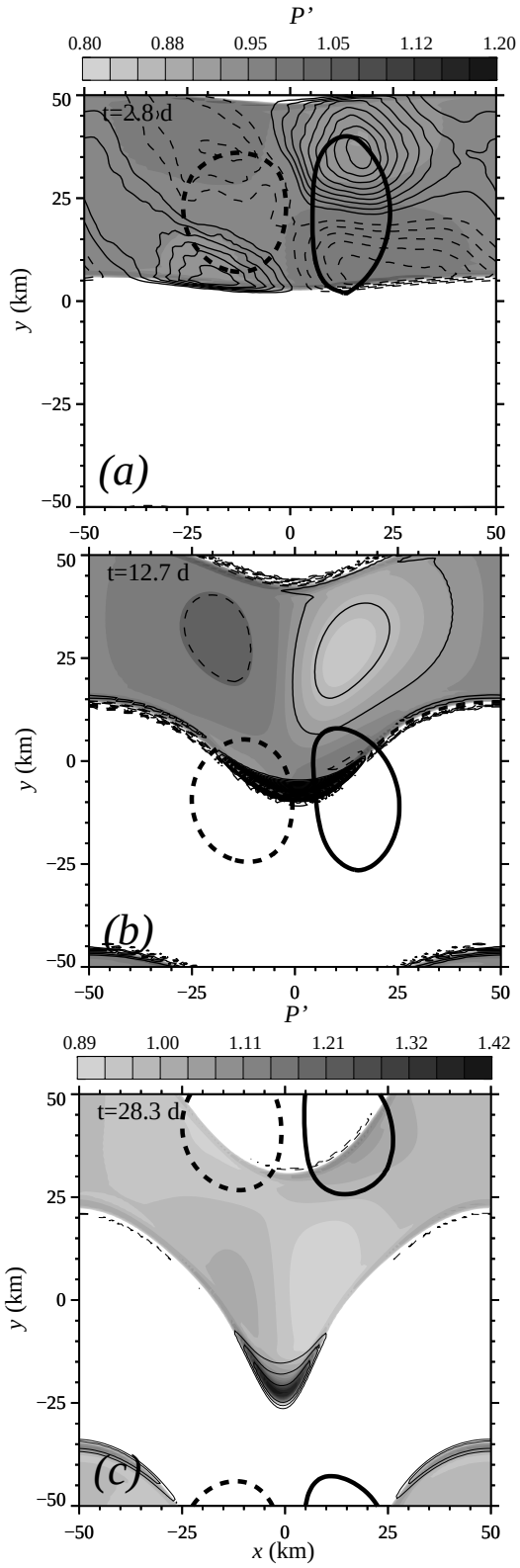

Figura B.10: Distribución horizontal a $z = -125\,\mathrm{m}$ ($i_Z = 112$) en los tiempos indicados de P' (escala de grises) y (a) $(w\,\partial P/\partial z)'$ (el rango de las líneas de contorno es de $(-0.28, 0.48)$ con $\delta = 0.05$), y (b)-(c) $(\mathrm{d}P/\mathrm{d}t)'$ (rango de las líneas de contorno $\in (-0.14, 0.4)$ con $\delta = 0.02$ en b y $\delta = 0.1$ en c). El contorno de VP $\varpi = 0.2$ se incluye por referencia.

Capítulo 4. Respuesta resonántica del plancton a la luz y nutrientes en vórtices de mesoescala

En este capítulo construimos un modelo numérico sencillo para investigar la dinámica de un ecosistema cerrado en vórtices de mesoescala. En particular, nos centramos en ciclones superficiales y anticiclones subsuperficiales porque sus isopicnas están abombadas en la capa superior. Tratamos el impacto del régimen trófico, el movimiento de pequeña escala, y la intensidad de los vórtices en los ecosistemas. En todos los casos explorados, obtuvimos soluciones ecológicas estacionarias numéricamente estables, con coexistencia de fitoplancton y zooplancton.

El régimen trófico, determinado por el máximo de nitrógeno total, caracterizó dos dinámicas ecológicas diferentes. En un régimen oligotrófico, las anomalías de fitoplancton y zooplancton (respecto a un estado de referencia donde las isopicnas son planas como sucede fuera del vórtice) eran de magnitud similar. Estas anomalías se localizaron en el límite inferior del vórtice, donde el flujo de nutrientes era el más grande. Cuando, por el contrario, se inicializó un régimen mesotrófico, las anomalías de zooplancton fueron un orden de magnitud mayor que las de fitoplancton. Ambas anomalías tuvieron su máximo localizado en la isopicna de mayor desplazamiento vertical, y por tanto en aquella que experimenta el mayor cambio de irradiancia (Figura B.11).

El movimiento de pequeña escala, parametrizado como una difusión de tipo Fickiano a lo

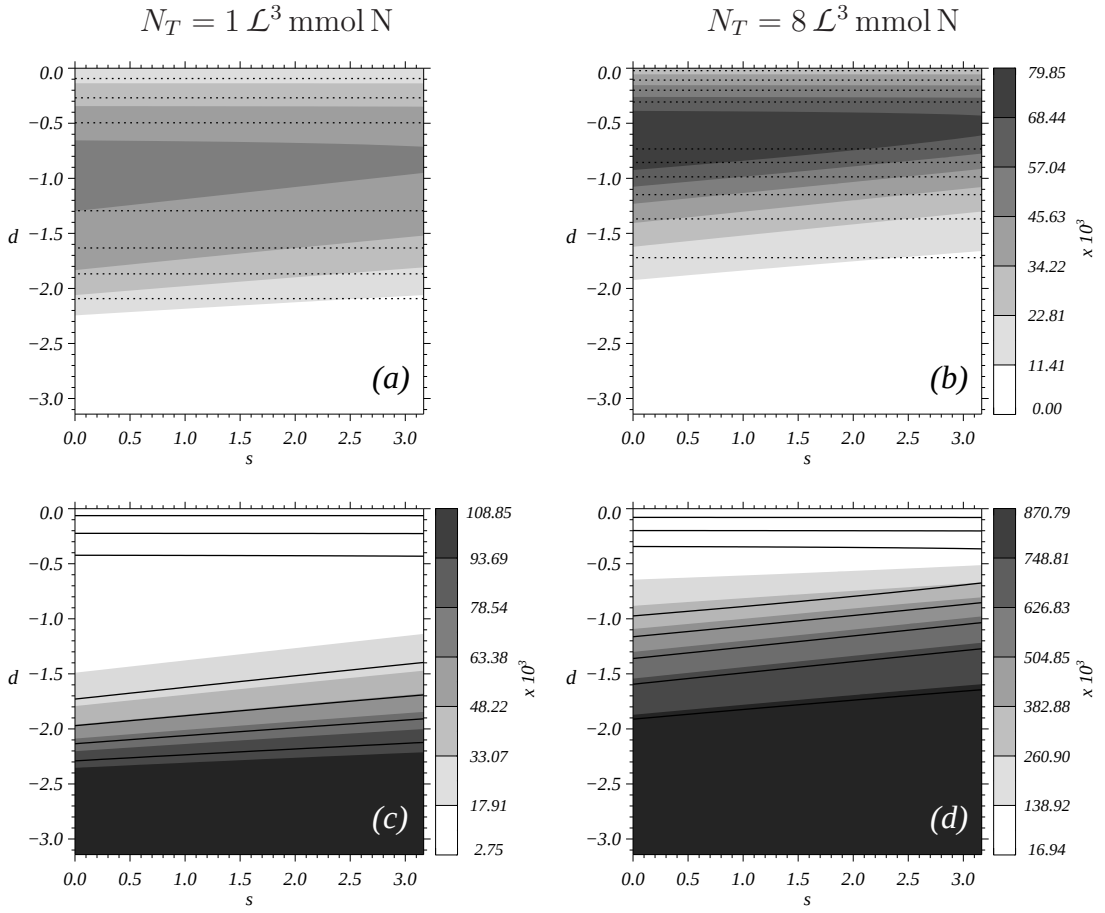

Figura B.11: Distribución vertical con $\mathcal{K} = 0$ y $\mathcal{D}_{\max} = 0.39$ de (a,b) $P(s,d)$ en contornos sombreados y $\hat{P}(d)$ (líneas de puntos, max $\cong 70.5 \times 10^3\,\mathrm{mmol\,N}$, $\delta \simeq 10^5\,\mathrm{mmol\,N}$); y (c,d) $N(s,d)$ y $Z(s,d)$ (líneas continuas, $Z_{\max} \cong 52.79\,(592.57) \times 10^3\,\mathrm{mmol\,N}$, $\delta Z \simeq 10^4\,(10^5)\,\mathrm{mmol\,N}$ en c (d)). Los paneles de la izquierda corresponden a un máximo de N_T $T_1 = 1\,\mathcal{L}^3$ mmol N, mientras que los de la derecha a $T_1 = 8\,\mathcal{L}^3$ mmol N.

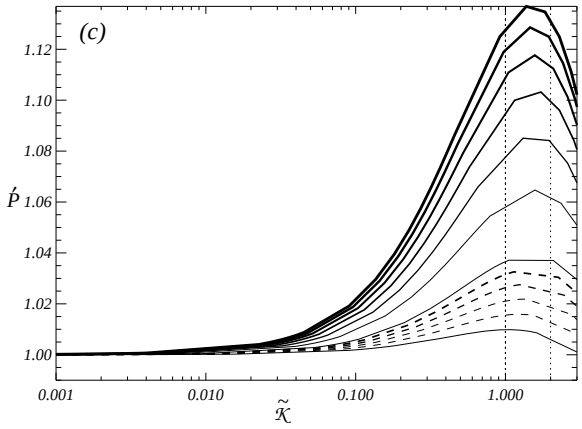

Figura B.12: Distribución de $\acute{P}(\tilde{\mathcal{K}})$ para diferentes condiciones tróficas. Las líneas continuas indican un incremento de $\delta T_1 = 1\,\mathcal{L}^3\,\mathrm{mmol\,N}$, mientras que las discontinuas un incremento de $\delta T_1 = 0.2\,\mathcal{L}^3\,\mathrm{mmol\,N}$.

largo de las isopicnas, incrementó el valor integrado en el espacio de la biomasa de fitoplancton entre un 1% y un 15% según la condición trófica (Figura B.12). Este incremento ocurrió en un coeficiente de difusión característico ($\mathcal{K}^*$) debido a un mecanismo de resonancia entre la escala temporal de difusión y la del fitoplancton. Es decir, cuando la relación entre la tasa de difusión y la del crecimiento del fitoplancton fue cercana a uno. Dos principales mecanismos estuvieron implicados en este incremento de fitoplancton (Figura B.13). En primer lugar, la difusión elevó nutrientes a niveles más luminosos por medio de un flujo de nutrientes hacia adentro que contrarresta el flujo hacia afuera de fitoplancton. En segundo lugar, el zooplancton se desacopló del incremento experimentado por su presa porque el fitoplancton tuvo una tasa de crecimiento mayor que la de zooplancton. Como resultado, el flujo de zooplancton hacia afuera fue mayor que el de fitoplancton y la depredación disminuyó en beneficio del fitoplancton. La contribución mayor de la difusión maximizando el fitoplancton se observó en regímenes mesotróficos. No obstante, grandes valores de $\mathcal{K}^*$ fueron requeridos y se debe tener cierta precaución en su interpretación. Considerando $\mathcal{K}^* = 0.3$ y el límite superior de la parametrización de los movimientos de pequeña escala ($\kappa = 10\,\mathrm{mmol\,N\,m^3}$), resulta una relación de Prandtl $c \cong 20$, la cual está comprendida dentro de la submesoescala. Como nuestras ecuaciones básicas son inapropiadas para similar la dinámica viscosa, restringimos c para el límite inferior de la mesoescala ($c = 35$). En este caso, $\kappa \cong 30\,\mathrm{m^2\,s^{-1}}$, el cual se aproxima a la parametrización del movimiento de mesoescala (Martin et al., 2001; Ledwell et al., 2008). Esto sugiere que la resonancia entre las tasa de crecimiento de plancton y

la advectiva ocurre con vórtices que no son axisimétricos, como ya ha sido constatado por Pasquero (2005).

Finalmente, la intensidad del vórtice, simulada mediante el máximo desplazamiento vertical de las isopicnas, ejerció un efecto antagonico en el ecosistema. Por un lado, éste indujo una respuesta positiva y lineal de fitoplancton debido a que fitoplancton y nutrientes fueron elevados a profundidades más luminosas. El abombamiento de las isopicnas representó un incremento alrededor del 8% y 15% de la biomasa de fitoplancton correspondiente a un escenario con isopicnas planas dependiendo de la condición trófica. Por otro lado, el abombamiento de las isopicnas también incrementó el flujo difusivo ya que aumenta la inclinación de las isopicnas. En consecuencia, $\mathcal{K}^*$ fue casi independiente del desplazamiento vertical de las isopicnas (Figura B.14). Esto sugiere que el factor de incremento del fitoplancton puede ser aproximado por contribuciones aditivas del abombamiento de la isopicnas y la difusión en el coeficiente donde ocurre la resonancia.

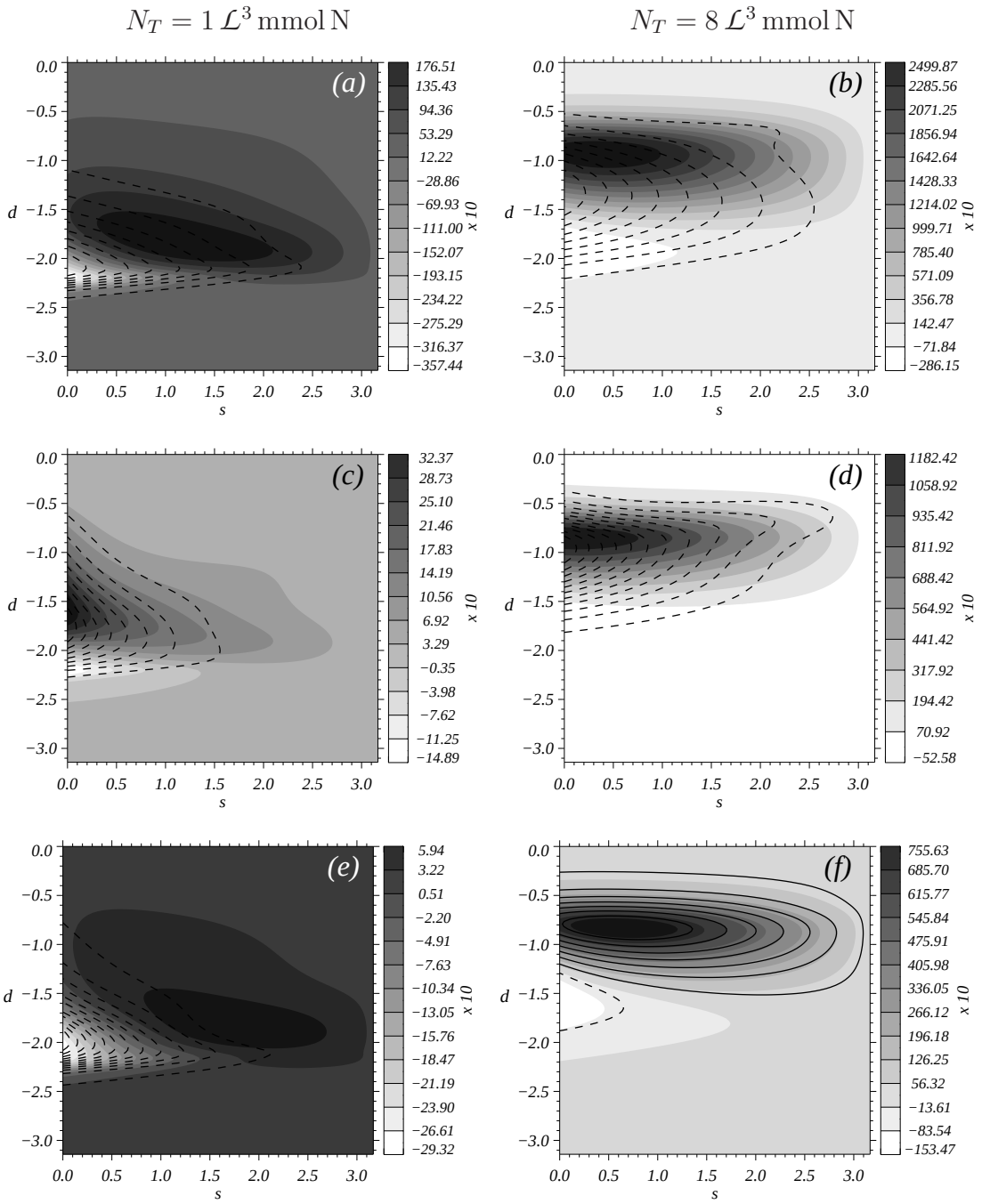

Figura B.13: (a,b) Distribuiones verticales de $P'(s,d)$, en escala de grises, y $Z'(s,d)$, líneas de contorno, para (a) $Z'_{\min} = 8789$ mmol N ($\delta Z' \simeq 10^3$ mmol N), y (b) $Z'_{\min} = -90049$ mmol N ($\delta Z' \simeq 10^4$ mmol N). (c,d) Distribuciones verticales de $G'_P(s,d)$, en escala de grises, y $(\mathcal{K}^*\,\partial^2 P/\partial s^2)(s,d)$, líneas de contorno, para (c) min $= -433$ mmol N ($\delta \simeq 50$ mmol N), y (d) min $= -5909$ mmol N ($\delta \simeq 500$ mmol N). (e,f) Distribuciones verticales de $(G'_P + \mathcal{K}^*\,\partial^2 P/\partial s^2)(s,d)$, en escala de grises, y $R'(s,d)$, líneas de contorno, para (e) $R' \in (-233, 13)$ mmol N ($\delta R'_{\max} \simeq 20$ mmol N), y (f) $R' \in (-1634, 6793)$ mmol N ($\delta R'_{\max} \simeq 10^3$ mmol N).

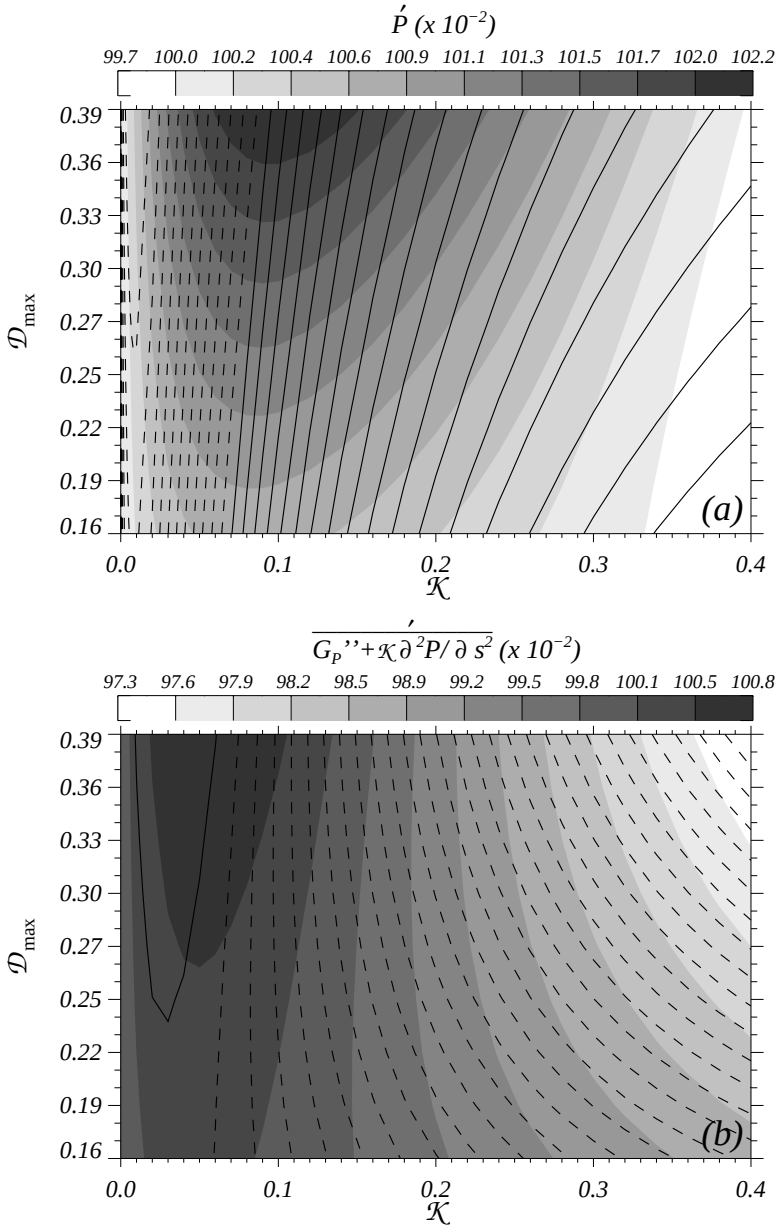

Figura B.14: Distribuciones de (a) $\acute{P}\,(\mathcal{K}, \mathcal{D}_{\max})$ y $\eta' = \eta - 1.08$ (líneas de contorno, $\eta' \in (-0.4, 0.6)$, $\delta\eta' \cong 0.035$), (b) $\overline{G_P'' + \mathcal{K}\acute{\partial}^2 P/\partial s^2}\;(\mathcal{K}, \mathcal{D}_{\max})$ y $\acute{R}''\,(\mathcal{K}, \mathcal{D}_{\max})$ (líneas de contorno, $\in (-4, 0.2) \times 10^{-2}$, $\delta \cong 1.5 \times 10^{-3}$). El régimen trófico es $T_1 = 1.4\,\mathcal{L}^3$ mmol N.

Capítulo 5. La velocidad vertical en la interacción entre ondas inercio–gravitatorias y estructuras vorticales baroclinas de submesoescala

Hemos investigado numéricamente la interacción entre estructuras vorticales baroclinas e idealizadas con ondas inercio–gravitatorias (OIGs) planas y preexistentes que tienen una velocidad horizontal o un desplazamiento vertical de las isopicnas similar. Existen un gran nombre de posibles interacciones diferentes según los parámetros iniciales de las estructuras vorticales y las OIGs, y no nos hemos aventurado a escanear todo el gran espacio paramétrico. Dos principales mecanismos están presentes en esta interacción vórtice-onda. El primer mecanismo es la advección de la vorticidad potencial (VP) por las ondas, la cual causa que la estructura vortical sea inestable forzándola a estar permanentemente en proceso de ajuste geostrófico, al mismo tiempo que modifica los límites superiores e inferiores del rango frecuencial de las OIGs (Figuras B.15, y B.16). El segundo mecanismo es la advección de las ondas por los vórtices, el cual cambia la frecuencia local de las ondas a través de la relación de cambio de frecuencia de Doppler. Estos mecanismos actúan sobre estructuras vorticales de submesoescala con números de Rossby cercanos a la unidad, aunque más pequeños, de manera que éstas permanecen siempre estables a pesar de la gran amplitud de las ondas.

Un resultado notable es el incremento de la velocidad vertical *total* alrededor de un orden de magnitud cuando las ondas inerciales están presentes en los flujos vorticales. Esto es un claro ejemplo de una interacción vórtice-onda no lineal, la cual resulta en la generación de

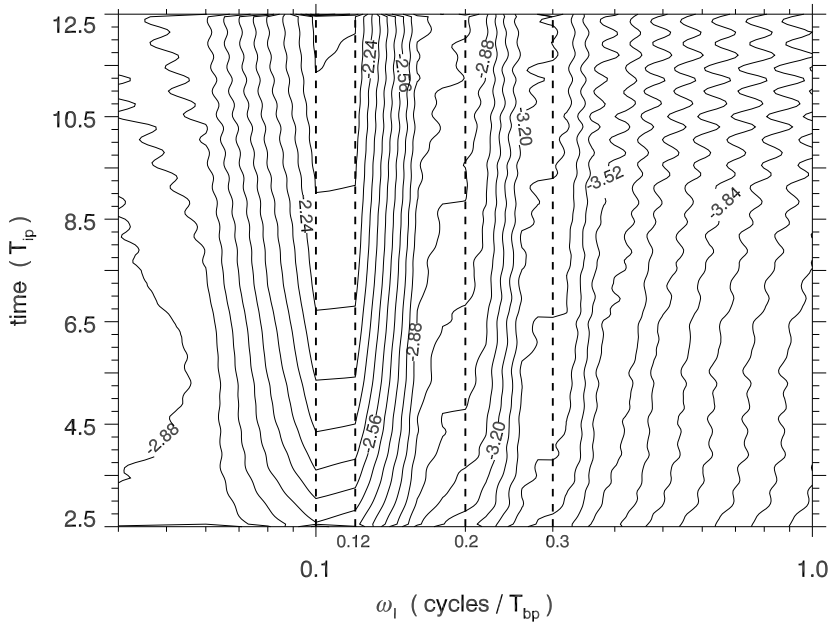

Figura B.15: Espectrograma del promedio espacial de $w(\omega, t_k) \equiv \frac{1}{n}\sum_{j=1}^{n} \hat{w}(\mathbf{x}_j, \omega; t_k)$ desde $t = 0$ hasta $t = 15\,T_{ip}$, donde $\hat{w}(\mathbf{x}_j, \omega; t_k)$ es la transformada de Fourier de las series temporales $w(\mathbf{x}_j, t)$ con $t \in [t_k - \Delta_t/2, t_k + \Delta_t/2]$. El promedio espacial comprendre $n = 8^3$ series temporales igualmente equidistantes en el dominio 3D. La ventana del espectrograma es $\Delta_t = 5T_{ip}$ y el tiempo de desfase $\delta_t = 0.5\,T_{bp}$. Las líneas discontinuas verticales marcan las frecuencias f, $f + \zeta/2 \cong 0.12$, $2f$, y $3f$.

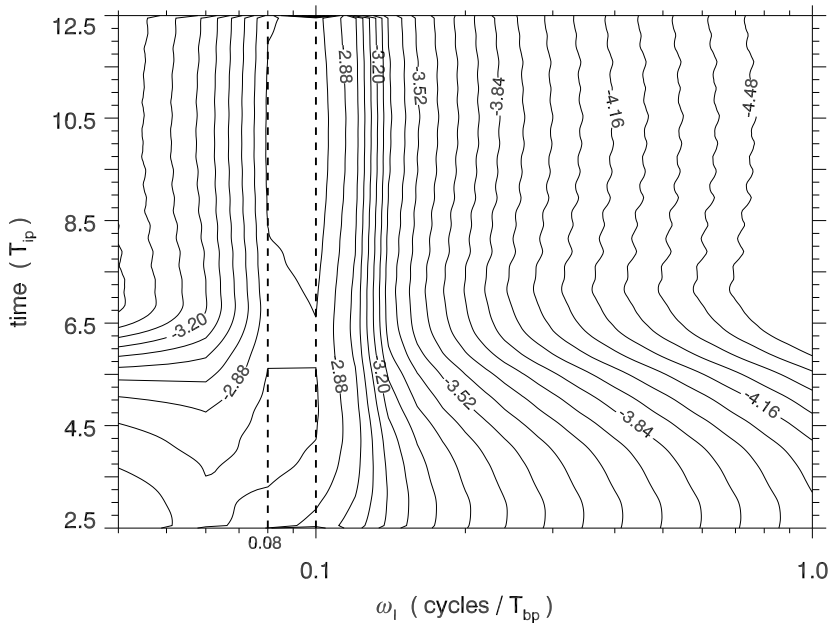

Figura B.16: Espectrograma del promedio espacial $w(\omega, t_k)$. El dominio espacial comprende $n = 9^2$ puntos horizontalmente equidistantes en 17 niveles verticales. Las líneas discontinuas verticales marcan las frecuencias f and $f - \zeta/2 \cong 0.08$.

ondas espirales dextrógiras (Figura B.17). Por tanto, el rango de frecuencia se extiende desde la frecuencia de Coriolis f en tiempos iniciales hasta una frecuencia efectiva f_e y posteriormente hasta una frecuencia suprainercial por medio de mecanismos de resonancia.

Finalmente, hemos considerado sólo interacciones entre dos tipos de estructuras verticales (vórtices monopolares y dipolares) y dos tipos de ondas planas (ondas inerciales y gravitatorias) y muchas otras interacciones son aún desconocidas. Algunos ejemplos son la interacción entre paquetes de OIGs *localizados* y estructuras verticales de submesoescala, y evolución a largo plazo de la inestabilidad vortical de este tipo de flujos en presencia de un campo de ondas inercio–gravitatorias. Otra investigación futura es el papel catalítico de las estructuras verticales desencadenando OIGs.

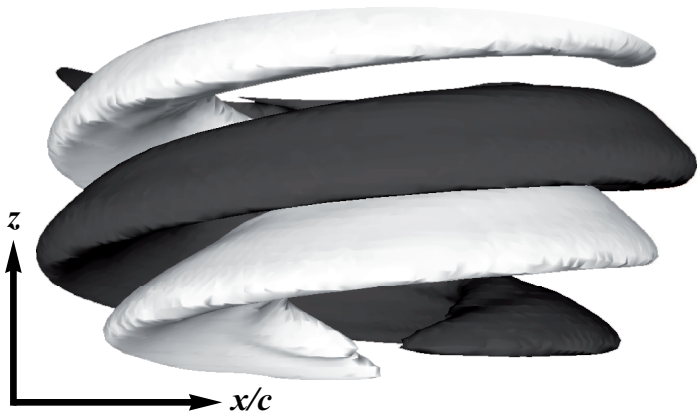

Figura B.17: Isosuperficie de la velocidad vertical *total* ($w = \pm 0.02$) a $t = 5\,T_{ip}$. Vista desde el Sur.

Capítulo 6. Discusión

Esta tesis tiene como objetivo caracterizar patrones de plancton asociados a corrientes de chorro inestables y vórtices de larga vida en mesoescalas y submesoescalas. Específicamente, se investigan numéricamente los efectos de la advección horizontal, vertical, y mezcla isopicna. Además, el flujo resultante de un tipo particular de onda-vórtice también se analiza por su probable implicación en la generación de heterogeneidad planctónica. Seguidamente, se da un resumen de los principales resultados obtenidos en relación a los objetivos de la tesis.

Inicialización ecológica

En primer lugar, tratamos el problema no trivial de la inicialización ecológica usando un modelo ecológico NPZ compuesto por tres variables (Nutrientes-Fitoplancton-Zooplancton, Capítulo 2). Con el fin de cuantificar la respuesta ecológica a perturbaciones físicas buscamos perfiles verticales en equilibrio estable con el fluido en reposo. Para ello, obtuvimos soluciones analíticas estacionarias con un perfil constante de nitrógeno total N_T. Observamos que estos perfiles no son continuamente diferenciables, hecho que supuso una fuente de error cuando se calculan gradientes verticales en el término de advección de las ecuaciones físico-ecológicas. Para solventar dicho error, encontramos soluciones numéricas por integración temporal de perfiles verticales continuamente diferenciables, los cuales convergieron a un estado estacionario y estable. A diferencia de las soluciones analíticas, las numéricas fueron

continuamente diferenciables pero requirieron resoluciones de unos pocos centímetros, las cuales tienen un alto coste computacional. No obstante, el error asociado al disminuir la resolución es menor que el causado por la incertidumbres de la parametrización ecológica. Por tanto, perfiles verticales estacionarios y estables fueron adecuados para inicializar modelos NPZ de una dimensión, pero ¿cómo se implementaron éstos en tres dimensiones? ¿El N_T era homogéneo en niveles horizontales o en isopicnos? ¿Tuvo N_T una distribución dispersa o continúa en el dominio? Observamos que estas condiciones iniciales condujeron a diferentes distribuciones planctónicas (Capítulo 3). En consecuencia, concluimos que las condiciones iniciales más adecuadas tienen que escogerse cuidadosamente según los objetivos específicos de la investigación acoplada físico-ecológica.

Advección horizontal y vertical

El papel de la advección horizontal y vertical en la dinámica planctónica fue investigado inicializando el N_T de tres formas diferentes en tres dimensiones. Cuando el N_T se consideró homogéneo en niveles horizontales pudimos analizar la heterogeneidad planctónica debida a la advección vertical. Cuando por el contrario, el N_T se consideró homogéneo en isopicnas de vórtices completamente desarrollados, se introdujo una heterogeneidad planctónica inicial. Por tanto, pudimos comparar los efectos de la advección vertical y la horizontal sobre esta heterogeneidad inicial. Consideramos primero la inicialización en niveles horizontales con el fin de cuantificar el impacto ecológico de la velocidad vertical generada por una

corriente de chorro baroclínicamente estable (Capítulo 2). Observamos que anomalías de fitoplancton son desarrolladas por la advección horizontal. No obstante, dichas anomalías no se correlacionan con la velocidad vertical porque el fitoplancton responde al afloramiento más lentamente que la acción de la advección horizontal. Basándonos en esto, consideramos un dipolo superficial de submesoescala inicializando N_T constante en isopicnas (Capítulo 3). Este escenario se puede concebir como el resultado de un evento de *bombeo de eddy* y nos permitió investigar su evolución a largo plazo. Observamos dos dinámicas planctónicas diferentes divididas espacialmente por la separatriz del vórtice, y por tanto por las isosuperficies de VP más externas. Dentro de los vórtices, la distribución planctónica estuvo dominada por procesos horizontales. La generación de anomalías planctónicas debido a la advección vertical fue insignificante comparado con las anomalías planctónicas preexistentes, las cuales fueron atrapadas dentro de los vórtices y por tanto transportadas a la velocidad de fase de dipolo. Por el contrario, fuera de los vórtices la heterogeneidad planctónica fue causada por la advección vertical. No obstante, la biomasa planctónica fue transportada lejos de las regiones de afloramiento, análogamente al caso de la corriente de chorro. Como resultado, una cola de fitoplancton se desarrolló en la estela del ciclón. Los elementos del fluido de la zona frontal del dipolo fueron elevados a profundidades más someras cuando circularon anticiclónicamente a la zona posterior. Como el fitoplancton respondió con cierto desfase temporal a la perturbación, la biomasa incrementó en la estela del ciclón. Una

vez allí, decayó con una tasa de mortalidad constante. Dicha tasa se aproximó al valor paramétrico considerando constantes la extensión de la cola y la velocidad de propagación del dipolo. En primer lugar, la dominancia de la advección horizontal sobre la vertical en la dinámica planctónica cuando existen gradientes horizontales de plancton concuerda con Lévy (2003). En segundo lugar, la descorrelación espacial entre la velocidad vertical y el incremento planctónico asociado ha sido observado anteriormente en la mesoescala y la submesoescala (Lévy et al., 2001; Lima et al., 2002). En este trabajo, hemos ido un poco más allá, representando un escenario donde ocurren ambos procesos, y hemos sugerido que los contornos de vorticidad potencial actúan como una barrera espacial entre ellos.

Los resultados arriba mencionados nos ayudaron a comprender la respuesta de una agrupación de fitoplancton a una perturbación causada por un dipolo subsuperficial de mesoescala (Capítulo 3). Observamos que la acción a distancia de la VP deformó la distribución de plancton de manera que un filamento penetró a lo largo del eje del dipolo, donde la velocidad horizontal era máxima. Como esta velocidad incrementaba exponencialmente con la profundidad, la extensión del filamento también. Dicha extensión fue aproximada analíticamente utilizando un modelo casigeostrófico con vórtices de radio y VP constante. Como la cizalla vertical era negativa, una capa arbitraria de fitoplancton estaba más avanzada que otra capa inmediatamente superior, disminuyendo el apantallamiento de fitoplancton en el frente, generando anomalías de plancton. Frecuentemente, se considera que la advección horizontal no puede causar heterogeneidad a menos que ésta exista previamente (ver revisión de Mar-

tin, 2003), como en el caso previo del dipolo. En esta tesis, hemos ampliado este concepto, mostrando una forma indirecta de generación de heterogeneidad planctónica a través de la cizalla vertical de la velocidad horizontal.

Mezcla isopicna en la dinámica ecológica

Hemos observado que los ecosistemas quedan atrapados en el interior del espacio definido por la separatriz del vórtice. Esta fuente inicial de heterogeneidad es a menudo causada por el abombamiento de las isopicnas durante la formación del vórtice, como ocurre en el *bombeo de eddy*. La evolución a largo plazo de este fenómeno es bastante desconocida por lo cual investigamos si ésta alcanza un estado estacionario considerando tres factores: desplazamiento vertical de las isopicnas $\mathcal{D}$, condición trófica, y difusión isopicna (Capítulo 4).

Con el fin de explorar en un amplio rango de los factores mencionados, se construyó un modelo acoplado físico-ecológico en coordenadas isopicnas, menos complejo que el modelo $\mathcal{AB}\varpi$-NPZ. Consideramos un vórtice esférico de mesoescala en el espacio QG, cuyo flujo estaba en balance de gradiente, y por tanto era estacionario y horizontal. Como resultado, la dinámica ecológica dependió sólo de la dimensión vertical, hecho que nos permitió introducir el forzamiento vortical de mesoescala en el modelo NPZ en términos de $\mathcal{D}$. Para ello, encontramos una expresión analítica de $\mathcal{D}$ aproximando una función polinómica a una distribución de $\mathcal{D}$ conocida. Finalmente, inicializamos el modelo acoplado físico-biológico usando perfiles verticales estacionarios y numéricamente estables con el fluido en reposo.

Observamos que estos perfiles siempre convergieron a un estado estacionario con coexistencia de fitoplancton y zooplancton. Cuando no se consideró la mezcla isopicna, la biomasa de fitoplancton incrementó linealmente con $\mathcal{D}$, debido al aumento de la irradiación de la luz, y logarítmicamente con el nitrógeno total, sugiriendo una respuesta de saturación a los nutrientes. Aunque estos resultados se restringen a vórtices esféricos QG, la biomasa de fitoplancton también alcanzó un estado casi-estacionario en el caso del dipolo de submesoescala (Capítulo 3). Por tanto, nos pueden ayudar a comprender casos más complejos en que el movimiento del fluido es tridimensional. Otra limitación a tener en cuenta es que nuestro sistema ecológico es cerrado, cuando en verdad hay pérdidas de nitrógeno a través de los bordes de los vórtices debido a que el fitoplancton sedimenta. La tasa de hundimiento del fitoplancton varia entre $0.5\,\mathrm{m\,d^{-1}}$ y $10\,\mathrm{m\,d^{-1}}$ en experimentos de laboratorio (Smayda, 1970). Este hecho explica el agotamiento de nutrientes dentro de los vórtices al cabo de unos meses.

Cuando se consideró la mezcla isopicna, la biomasa fitoplanctónica fue máxima en un coeficiente de difusión isopicna característico $\mathcal{K}^*$ debido a un mecanismo de resonancia entre la escala temporal de difusión y la ecológica. Dos efectos principales estuvieron implicados. El abombamiento de los isopicnas estimuló el crecimiento del fitoplancton, y por consiguiente la consumición de nutrientes. Ello creó gradientes isopicnos de fitoplancton y zooplancton opuestos a los de los nutrientes, hecho que resultó en un flujo difusivo hacia afuera de los primeros y hacia adentro de los segundos. En consecuencia, la biomasa de fitoplancton incrementó directamente debido a un flujo ascendente de nutrientes, e indirectamente por

una disminución de la herbivoría causada por una difusión de zooplancton más intensa que la difusión de fitoplancton.

La respuesta resonántica del fitoplancton a los nutrientes y la luz ha sido observada considerando difusión horizontal (Pasquero, 2005; McKiver and Neufeld, 2011) y vertical (Huisman et al., 1999; Ghosal and Mandre, 2003) por separado. En este trabajo exploramos diferentes condiciones de nutrientes y tipos de vórtices incluyendo ambas difusiones. Observamos que el régimen trófico determina la magnitud de la respuesta de fitoplancton, la cual es significativa en condiciones mesotróficas, obtuviéndose el mayor $\mathcal{K}^*$. Contrariamente, $\mathcal{K}^*$ fue escasamente modificada por el abombamiento de las isopicnas. En este caso, el crecimiento del fitoplancton causado por la elevación de las isopicnas fue contrarestado por un aumento en el flujo de fitoplancton hacia fuera.

Hemos observado que la mezcla isopicna eleva nutrientes a profundidades más luminosas, pero ¿puede ésta contrarrestar el agotamiento de nutrientes dentro de los vórtices a largo plazo? Para responder esta pregunta podemos comparar las escalas temporales del componente vertical de la difusión isopicna con la tasa de sedimentación constante del plancton. El rango observado del coeficiente no dimensional de difusión isopicna que causa resonancia varia entre 0.06 y 0.3, para condiciones oligotróficas y mesotróficas, respectivamente. Considerando la isopicna con mayor pendiente, este intervalo corresponde a un coeficiente de difusión vertical $\mathcal{K}_z \in [0.35, 1.8] \times 10^{-2}$. La tasa de sedimentación del fitoplancton ha sido estimada alrededor de $w_P = -0.65\,\mathrm{m\,d^{-1}}$ (Spitz et al., 2003). Este valor ha sido calibrado

para un ecosistema costero y es escogido como límite superior de la tasa de sedimentación en ambientes oligotróficos, donde el fitoplancton sedimenta más lentamente que en sistemas costeros. Adimensionalizando apropiadamente w_P en $\mathcal{W}_P$ obtenemos una relación $|\mathcal{K}_z/\mathcal{W}_P|$ comprendida entre $[0.78, 4]$. Por consiguiente, la mezcla isopicna puede explicar la subsistencia del plancton a largo plazo en condiciones mesotróficas. La validación de esta estimación con el sencillo sistema físico-ecológico construido forma parte de una futura investigación.

El papel de la VP en interacciones onda-vórtice

En términos generales, hemos constatado que las distribuciones planctónicas están relacionadas con la VP cuando los procesos horizontales son dominantes, fenómeno que ocurre si ya existen heterogeneidades planctónicas. Dentro de los vórtices las distribuciones de plancton y VP están en fase debido a que ambas se propagan a la velocidad de traslación del vórtice. Fuera de los vórtices, la acción a distancia de la VP deforma las agrupaciones planctónicas de manera no lineal. Por el contrario, el plancton se correlaciona con los gradientes horizontales de VP cuando los procesos verticales son relevantes. No obstante, esta correlación sólo se observa inicialmente ya que las anomalías ecológicas son rápidamente transportadas lejos de su lugar de afloramiento por advección horizontal. Además, la mezcla isopicna incrementa la biomasa planctónica cerca del centro del vórtice. Concretamente donde el desplazamiento vertical de la isopicnas es máximo, y por tanto donde los grandes gradientes verticales de VP son mayores. Para tener una idea de cómo la interacción onda-

vórtice puede afectar la dinámica planctónica investigamos la relación entre la VP y el flujo resultante de un tipo particular de interacción (Capítulo 5).

Consideramos monopolos esféricos, en el espacio QG, y dipolos inmersos en un campo inicial de ondas inerciales y gravitatorias. Cuando se tuvieron en cuenta ondas inerciales, se desarrolló una onda en hélice dextrógira de frecuencia casi-inercial mediante un interacción no lineal onda-vórtice. En primer lugar, los vórtices modificaron la frecuencia inercial a una frecuencia *efectiva* $f_e = f + \zeta/2$ (Mooers, 1975a; Kunze, 1985; Rubenstein and Roberts, 1986), donde ζ es el componente vertical de la vorticidad relativa. Como la distribución inicial de ζ dependía del espacio, se generaron gradientes horizontales de f_e. En segundo lugar, las ondas forzaron a la estructura vortical a estar permanentemente en un proceso de ajuste geostrófico mediante la advección horizontal de VP. En consecuencia, los contornos de VP perdieron la simetría radial inicial y se desarrollaron velocidades verticales de *imbalance*, las cuales se correlacionaron con gradientes horizontales de VP. Cuando se consideraron ondas gravitatorias rápidas, la advección de la onda por el vórtice modificó la frecuencia de onda local ω_l por efecto Doppler. Por tanto, el mayor cambio de ω_l se observó donde las velocidades horizontales fueron máximas, y por tanto donde existían grandes gradientes horizontales de VP.

Las ondas inercio–gravitatorias (OIGs) tienen escalas de minutos a horas, a menudo más pequeñas que el período de crecimiento del fitoplancton, el cual varía entre medio día y un par de días. No obstante, la combinación de advección horizontal y vertical puede permitir

que el plancton se acople a las OIGs (Franks, 1995b). De hecho, algunas observaciones in-situ evidencian el papel de las OIGs como generadores de heterogeneidad (Franks, 1995a; Granata et al., 1995). El impacto en la dinámica planctónica de la onda en espiral observada será objeto de una investigación próxima.

En general, el trabajo presentado contribuye a la caracterización de la estructura tridimensional del plancton asociada a vórtices de mesoescala y submesoescala mediante la VP. Esta concebido más como una investigación heurística que un intento de simular un tipo particular de ecosistema. Nuestros resultados son consecuencia de unas suposiciones numéricas iniciales, las cuales han sido diseñadas para incrementar la comprensión de la dinámica planctónica en un océano estratificado y en rotación, que son las características de la dinámica en el mar abierto.

Capítulo 7. Conclusiones

1. Perfiles verticales ecológicos estacionarios y numéricamente estables son adecuados para inicializar modelos físico-ecológicos acoplados en su descripción Euleriana.

2. La inicialización de dichos perfiles, homogéneos en niveles horizontales o isopicnos en todo el dominio o en agrupaciones, condujo a diferentes distribuciones planctónicas. Por tanto, las condiciones iniciales en tres dimensiones tienen que escogerse cuidadosamente según los objetivos de la investigación.

3. La separatriz del vórtice dividió dos dinámicas planctónicas diferentes. Dentro de la separatriz, la distribución de plancton fue dominada por la advección horizontal y estuvo en fase con la vorticidad potencial (VP) debido a que ambas variables se trasladaron a la velocidad de fase del vórtice. Por el contrario, fuera de la separatriz, la advección horizontal y vertical del plancton fueron del mismo orden de magnitud que el forzamiento ecológico. La advección vertical generó anomalías de plancton que fueron inmediatamente transportadas lejos del lugar de afloramiento por la advección horizontal. En consecuencia, el plancton se correlacionó inicialmente con la velocidad vertical, y por tanto con gradientes horizontales de VP.

4. Una cola de fitoplancton se desarrolló en la estela de un ciclón en traslación por advección horizontal, advección vertical, y las escalas temporales intrínsecas al fitoplanc-

ton. La extensión horizontal de esta cola es casi estacionaria y depende linealmente de la velocidad de propagación del vórtice y de la tasa de mortalidad del fitoplancton.

5. Un dipolo baroclino subsuperficial deformó una distribución superficial de plancton de forma que un filamento penetró a lo largo del eje del dipolo. La extensión horizontal de dicho filamento incrementó con la profundidad porque la cizalla vertical de la velocidad horizontal era negativa. En consecuencia, el apantallamiento del fitoplancton disminuyó en el frente del filamento y la biomasa de fitoplancton incrementó. Por tanto, la advección horizontal podría ser indirectamente un generador de heterogeneidad planctónica mediante la modulación del régimen lumínico.

6. Se construyó un modelo físico-ecológico sencillo considerando monopolos baroclinos de mesoescala, esféricos en el espacio cuasigeostrófico (QG, que tiene la dimensión vertical alargada) y movimientos de pequeña escala. El forzamiento de mesoescala se introdujo en el modelo ecológico en términos del desplazamiento vertical de las isopicnas, mientras que el forzamiento de pequeña escala se parametrizó como una difusión Fickiana.

7. Distribuciones de fitoplancton y zooplancton estacionarias y numéricamente estables fueron posibles considerando vórtices de intensidad variable en diferentes condiciones tróficas y un amplio rango de coeficientes de difusión isopicna.

8. La difusión isopicna incrementó la biomasa de fitoplancton por un mecanismo de reso-

nancia entre escalas de tiempo físicas y ecológicas. Este incremento fue significativo en condiciones mesotróficas. En este caso, el máximo de fitoplancton se localizó en profundidad donde el desplazamiento vertical de las isopicnas fue mayor, cercano a los mayores gradientes verticales de VP. Sugerimos que la difusión isopicna puede contribuir a la subsistencia de plancton a largo plazo dentro de vórtices coherentes.

9. La advección de VP por ondas inercio–gravitatorias de gran amplitud inestabiliza las estructuras vorticales, forzándolas a estar permanente en un proceso de ajuste geostrófico. Además, la advección de VP modifica los límites superiores e inferiores del rango de frecuencia de la onda inercio–gravitatoria. La advección de las ondas por los vórtices modificó la frecuencia de onda local por efecto Doppler.

10. Una interacción no lineal entre vórtices esféricos (en el espacio QG) y ondas puramente inerciales generó una onda en hélice dextrógira de frecuencia casi-inercial que incrementó la velocidad vertical total alrededor de un orden de magnitud.

Bibliography

Abraham, E. R., 1998: The generation of plankton patchiness by turbulent stirring. *Nature*, **391**, 577–580.

Anderson, T. R., 2005: Plankton functional type modelling: running before we can walk? *J. Plankton. Res.*, **27**, 1073–1081, doi:10.1093/plankt/fbi076.

Arístegui, J., P. Tett, A. Hernández-Guerra, G. Basterretxea, M. F. Montero, K. Wild, P. Sangrà, S. Hernández-León, M. Canton, J. A. García-Braun, M. Pacheco, and E. D. Barton, 1997: The influence of island-generated eddies on chlorophyll distribution: a study of mesoscale variation around Gran Canaria. *Deep-Sea Res. I*, **44 (1)**, 71–96.

Arnone, R. A. and P. E. LaViolette, 1986: Satellite definition of the bio-optical and thermal variation of coastal eddies associated with the African Current. *J. Geophys. Res.*, **91(C2)**, 2351–2364, doi:10.1029/JC091iC02p02 351.

Atwood, E., J. T. Duffy-Anderson, J. K. Horne, and C. Ladd, 2010: Influence of mesoscale eddies on ichthyoplankton assemblages in the Gulf of Alaska. *Fish. Oceanogr.*, **19 (6)**, 493–507.

Baird, M. E., I. M. Suthers, D. A. Griffin, B. Hollings, C. Pattiaratchi, J. D. Everett, M. Roughan, K. Oubelkheir, and M. Doblin, 2011: The effect of surface flooding on the physical–biogeochemical dynamics of a warm-core eddy off southeast Australia. *Deep-Sea Res.II*, **58**, 592–605.

Barton, E. D., J. Arístegui, P. Tett, M. Canton, J. A. García-Braun, S. Hernández-León, L. Nykjaer, C. Almeida, J. Almunia, S. Ballesteros, G. Basterretxea, J. Escánez, L. García-Weill, A. Hernández-Guerra, F. López-Laatzen, R. Molina, M. F. Montero, E. Navarro-Pérez, J. M. Rodríguez, K. van Lenning, H. Vélez, and K. Wild, 1998: The transition zone of the Canary Current upwelling region. *Prog. Oceanogr.*, **41 (4)**, 455–504.

Batten, S. D. and W. R. Crawford, 2005: The influence of coastal origin eddies on oceanic plankton distributions in the eastern Gulf of Alaska. *Deep-Sea Res. II*, **52**, 991–1009.

Bibby, T. S., M. Y. Gorbunov, K. W. Wyman, and P. G. Falkowski, 2008: Photosynthetic community responses to upwelling in mesoscale eddies in the subtropical North Atlantic and Pacific Oceans. *Deep-Sea Res. II*, **55**, 1310–1320.

Bracco, A., S. Clayton, and C. Pasquero, 2009: Horizontal advection, diffusion, and plankton spectra at the sea surface. *J. Geophys. Res.*, **114**, C02 001, doi:10.1029/2007JC004 671.

Brown, S. L., M. R. Landry, K. E. Selph, E. J. Yang, Y. M. Rii, and R. R. Bidigare, 2008: Diatoms in the desert: Plankton community response to a mesoscale eddy in the subtropical North Pacific. *Deep-Sea Res. II*, **55 (10–13)**, 1321–1333.

Bühler, O. and M. E. McIntyre, 2005: Wave capture and wave-vortex duality. *J. Fluid Mech.*, **534**, 67–95.

Busenberg, S., S. K. Kumar, P. Austin, and G. Wake, 1990: The dynamics of a model of a plankton-nutrient interaction. *Bull. Math. Biol.*, **52**, 677–696.

Capet, X., J. C. McWilliams, M. J. Molemaker, and A. F. Shchepetkin, 2008: Mesoscale to submesoscale transition in the California Current System. Part I: Flow structure, eddy flux, and observational tests. *J. Phys. Oceanogr.*, **38**, 29–43.

Chang, Y.-T., T. Y. Tang, S.-Y. Chao, M.-H. Chang, D. S. Ko, Y. J. Yang, W.-D. Liang, and M. J. McPhaden, 2010: Mooring observations and numerical modeling of thermal structures in the South China Sea. *J. Geophys. Res.*, **115**, C10 022, doi:10.1029/2010JC006 293.

Cullen, J. J. and M. R. Lewis, 1988: The kinetics of algal photoadaptation in the context of vertical mixing. *J. Plankton Res.*, **10 (5)**, 1039–1063.

Danioux, E. and P. Klein, 2008a: Propagation of wind energy into the deep ocean through a fully turbulent mesoscale eddy field. *J. Phys. Oceanogr.*, **38**, 2224–2241.

———, 2008b: A resonance mechanism leading to wind-forced motions with a $2f$ frequency. *J. Phys. Oceanogr.*, **38**, 2322–2329.

Denman, K. L. and A. E. Gargett, 1995: Biological-physical interactions in the upper ocean: The role of vertical and small scale transport processes. *Annu. Rev. Fluid Mech.*, **27**, 225–256.

Doney, S. C., D. M. Glover, S. J. McCue, and M. Fuentes, 2003: Mesoscale variability of Sea-viewing Wide Field-of-view Sensor (SeaWiFS) satellite ocean color: Global patterns and spatial scales. *J. Geophys. Res.*, **108 (C2)**, 3024, doi:10.1029/2001JC000 843.

Dritschel, D. G. and A. Viúdez, 2003: A balanced approach to modelling rotating stably stratified geophysical flows. *J. Fluid Mech.*, **488**, 123–150.

Dubosq, S. and A. Viúdez, 2007: Three-dimensional mesoscale dipole frontal collisions. *J. Phys. Oceanogr.*, **37**, 2331–2344.

Dugdale, R. C., 1967: Nutrient limitation in the sea: Dynamics, identification, and significance. *Limnol. Oceanogr.*, **12**, 685–695.

Durran, D. R., 1998: *Numerical Methods for Wave Equations in Geophysical Fluid Dynamics*. Springer.

Edwards, A. M. and A. Yool, 2000: The role of higher predation in plankton population models. *J. Plankton Res.*, **22 (6)**, 1085–1112.

Edwards, C. A., T. A. Powell, and H. P. Batchelder, 2000: The stability of an NPZ model subject to realistic levels of vertical mixing. *J. Mar. Res.*, **58**, 37–60.

Falkowski, P. G., 1983: Light-shade adaptation and vertical mixing of marine phytoplankton: A comparative field study. *J. Mar. Res.*, **41 (2)**, 215–237.

Falkowski, P. G., D. Zieman, Z. Kolber, and P. K. Bienfang, 1991: Role of eddy pumping in enhancing primary production in the ocean. *Nature*, **352**, 55–58.

Fedorov, K. N. and A. I. Ginzburg, 1986: Mushroom-like currents (vortex dipoles) in the ocean and in a laboratory tank. *Ann. Geophys. B-Terr. P.*, **4**, 507–516.

Fernández, C., P. Raimbault, G. Caniaux, N. Garcia, and P. Rimmelin, 2005: Influence of mesoscale eddies on nitrate distribution during the POMME program in the northeast Atlantic Ocean. *J. Mar. Sys.*, **55**, 155–175.

Flierl, G. R. and D. J. McGillicuddy, 2002: Mesoscale and submesoscale physical-biological interactions. *Biological-Physical Interactions in the Sea*, Robinson, A., J. McCarthy, and B. Rothschild, Eds., John Wiley and Sons, Inc., New York, The Sea, Vol. 12, 152–153.

Flynn, K. J., 2005: Castles built on sand: Dysfunctionality in plankton models and the inadequacy of dialogue between biologists and modellers. *J. Plankton. Res.*, **27**, 1205–1210, doi:10.1093/plankt/fbi099.

Frajka-Williams, E., P. B. Rhines, and C. C. Eriksen, 2009: Physical controls and mesoscale variability in the Labrador Sea spring phytoplankton bloom observed by Seaglider. *Deep Sea Res. II*, **56 (12)**, 2144–2161.

Franks, P. J. S., 1995a: Thin layers of phytoplankton: A model of formation by near-inertial wave shear. *Deep-Sea Res. I*, **42 (1)**, 75–91.

———, 1995b: Thin layers of phytoplankton: a model of formation by near-inertial wave shear. *Deep Sea Res. I*, **42 (1)**, 75–91.

———, 2002: NPZ models of plankton dynamics: Their construction, coupling to physics, and application. *J. Oceanogr.*, **58**, 379–387.

———, 2005: Plankton patchiness, turbulent transport and spatial spectra. *Mar. Ecol. Prog. Ser.*, **294**, 295–309.

Franks, P. J. S., J. S. Wroblewski, and G. R. Flierl, 1986a: Behavior of a simple plankton model with food-level acclimation by herbivores. *Mar. Biol.*, **91**, 121–129.

———, 1986b: Prediction of phytoplankton growth in response to the frictional decay of a warm-core ring. *J. Geophys. Res.*, **91(C6)**, 7603–7610, doi:10.1029/JC091iC06p07 603.

Friedrichs, M. A. M., R. R. Hood, and J. D. Wiggert, 2006: Ecosystem model complexity versus physical forcing: Quantification of their relative impact with assimilated Arabian Sea data. *Deep-Sea Res. II*, **53**, 576–600.

Gammaitoni, L., P. Hänggi, P. Jung, and F. Marchesoni, 1998: Stochastic resonance. *Rev. Mod. Phys.*, **70 (1)**, 224–285.

Garrett, C. and W. Munk, 1979: Internal waves in the ocean. *Ann. Rev. Fluid Mech.*, **11**, 339–369.

Gascard, J. C., A. J. Watson, M. J. Messias, K. A. Olsson, T. Johannessen, and K. Simonsen, 2002: Long-lived vortices as a mode of deep ventilation in the Greenland Sea. *Nature*, **416**, 525–527.

Ghosal, S. and S. Mandre, 2003: A simple model illustrating the role of turbulence on phytoplankton blooms. *J. Math. Biol.*, **46**, 333–346.

Gill, A. E., 1984: *Atmosphere-Ocean Dynamics*. Acad. Press, pp. 568–571.

Gómez, F., G. Gorsky, L. Striby, J. M. Vargas, N. González, M. Picheral, J. García-Lafuente, M. Varela, and M. Goutx, 2001: Small-scale temporal variations in biogeochemical features in the Strait of Gibraltar, Mediterranean side—the role of NACW and the interface oscillation. *J. Mar. Sys.*, **30**, 207–220.

Gordon, H. R., D. K. Clark, J. L. Mueller, and W. A. Hovis, 1980: Phytoplankton pigments from the Nimbus-7 Coastal Zone Color Scanner: Comparisons with surface measurements. *Science*, **210 (4465)**, 63–66.

Gower, J. F. R., K. L. Denman, and R. J. Holyer, 1980: Phytoplankton patchiness indicates the fluctuation spectrum of mesoscale oceanic structure. *Nature*, **288**, 157–159.

Granata, T., J. Wiggert, and T. Dickey, 1995: Trapped, near-inertial waves and enhanced chlorophyll distributions. *J. Geophys. Res.*, **100 (C10)**, 20 793–20 804.

Haury, L. R., J. A. McGowan, and P. H. Wiebe, 1978: Patterns and processes in the time-space scales of plankton distributions. *Spatial pattern in plankton communities*, Steele, J. H., Ed., Plenum Press, 277–327.

Holton, J. R., 2004: *An Introduction to Dynamic Meteorology*. Elsevier.

Hoskins, B. J. ., M. E. McIntyre, and A. W. Robertson, 1985: On the use and significance of isentropic potential vorticity maps. *Quart. J . R . Met. Soc.*, **111**, 877–946.

Hoskins, B. J., I. Draghici, and H. C. Davies, 1978: A new look at the ω-equation. *Quart. J. Roy. Meteor. Soc.*, **104**, 31–38.

Huang, B., J. Hu, H. Xu, Z. Cao, and D. Wang, 2010: Phytoplankton community at warm eddies in the northern South China Sea in winter 2003/2004. *Deep-Sea Res. II*, **57**, 1792–1798.

Huisman, J., P. van Oostveen, and F. J. Weissing, 1999: Critical depth and critical turbulence: Two different mechanisms for the development of phytoplankton blooms. *Limnol. Oceanogr.*, **44 (7)**, 1781–1787.

Jassby, A. and T. Platt, 1976: Mathematical formulation of the relationship between photosynthesis and light for phytoplankton. *Limnol. Oceanogr.*, **21**, 540–547.

Jones, B. H., C. N. K. Mooers, M. M. Rienecker, T. Stanton, and L. Washburn, 1991: Chemical and biological structure and transport of a cool filament associated with a jet-eddy system off northern California in July 1986 (OPTOMA21). *J. Geophys. Res*, **96(C12)**, 22 207–22 225, doi:10.1029/91JC02 146.

Kahru, M., B. G. Mitchell, S. T. Gille, C. D. Hewes, and O. Holm-Hansen, 2007: Eddies enhance biological production in the Weddell-Scotia Confluence of the Southern Ocean. *Geophys. Res. Lett.*, **34**, L14 603, doi:10.1029/2007GL030 430.

Kasajima, Y., K. A. Olsson, T. Johannessen, M. J. Messias, E. Jeansson, R. G. J. Bellerby, and I. Skjelvan, 2006: A submesoscale coherent eddy in the Greenland Sea in 2003. *J. Geophys. Res.*, **111**, C07 013, doi:10.1029/2005JC003 130.

Klein, P. and G. Lapeyre, 2009: The oceanic vertical pump induced by mesoscale turbulence. *Annu. Rev. Mar. Sci.*, **1**, 351–75.

Kunze, E., 1984: Observations of near-inertial waves in a front. *J. Phys. Oceanogr.*, **14**, 566–581.

———, 1985: Near-inertial wave propagation in geostrophic shear. *J. Phys. Oceanogr.*, **15**, 544–565.

———, 1986: The mean and near-inertial velocity fields in a warm-core ring. *J. Phys. Oceanogr*, **16**, 1444–1461.

Ladd, C., N. B. Kachel, and C. W. Mordy, 2005: Observations from a Yakutat eddy in the northern Gulf of Alaska. *J. Geophys. Res.*, **110**, C03 003, doi:10.1029/2004JC002 710.

Lawson, L. M., E. E. Hofmann, and Y. H. Spitz, 1996: Time series sampling and data assimilation in a simple marine ecosystem model. *Deep-Sea Res. II*, **43 (2–3)**, 625–651.

Ledwell, J. R., D. J. McGillicuddy, and L. A. Anderson, 2008: Nutrient flux into an intense deep chlorophyll layer in a mode-water eddy. *Deep-Sea Res. II*, **55**, 1139–1160.

Ledwell, J. R., A. J. Watson, and C. S. Law, 1998: Mixing of a tracer in the pycnocline. *J. Geophys. Res.*, **103 (C10)**, 21,499–21,529.

Lehahn, Y., F.d'Ovidio, M. Lévy, and E. Heifetz, 2007: Stirring of the northeast Atlantic spring bloom: A Lagrangian analysis based on multisatellite data. *J. Geophys. Res.*, **112**, C08 005, doi:10.1029/2006JC003 927.

Lévy, M., 2003: Mesoscale variability of phytoplankton and of new production: Impact of the large-scale nutrient distribution. *J. Geophys. Res.*, **108(C11)**, 3358, doi:10.1029/2002JC001 577.

Lévy, M., M. Gavart, L. Mémery, G. Caniaux, and A. Paci, 2005: A four-dimensional mesoscale map of the spring bloom in the northeast Atlantic (POMME experiment): Results of a prognostic model,. *J. Geophys. Res.*, **110**, C07S21, doi:10.1029/2004JC002 588.

Lévy, M., P. Klein, and A.-M. Treguier, 2001: Impact of sub-mesoscale physics on production and subduction of phytoplankton in an oligotrophic regime. *J. Mar. Res.*, **59**, 535–565.

Lima, I. D., D. B. Olson, and S. C. Doney, 2002: Biological response to frontal dynamics and mesoscale variability in oligotrophic environments: Biological production and community structure. *J. Geophys. Res.*, **107 (C8)**, 3111, doi:10.1029/2000JC000 393.

Mackas, D. L., M. Tsurumi, M. D. Galbraith, and D. R. Yelland, 2005: Zooplankton distribution and dynamics in a North Pacific eddy of coastal origin: II. Mechanisms of eddy colonization by and retention of offshore species. *Deep-Sea Res. II*, **52**, 1011–1035.

Mahadevan, A., 2006: Modeling vertical motion at ocean fronts: Are nonhydrostatic effects relevant at submesoscales? *Ocean Model.*, **14**, 222–240.

Mahadevan, A. and D. Archer, 2000: Modeling the impact of fronts and mesoscale circulation on the nutrient supply and biogeochemistry of the upper ocean. *J. Geophys. Res.*, **105 (C1)**, 1209–1225.

Mahadevan, A. and J. W. Campbell, 2002: Biogeochemical patchiness at the sea surface. *Geophys. Res. Lett.*, **29 (19)**, 1926, doi:10.1029/2001GL014 116.

Mahadevan, A., L. N. Thomas, and A. Tandon, 2008: Comment on "eddy/wind interactions stimulate extraordinary mid-ocean plankton blooms". *Science*, **320 (5875)**, 448.

Mann, K. H. and J. R. N. Lazier, 1991: *Dynamics of Marine Ecosystems*. Blackwell Publishing.

Martin, A. P., 2003: Phytoplankton patchiness: The role of lateral stirring and mixing. *Prog. Oceanogr.*, **57**, 125–174.

Martin, A. P. and P. Pondaven, 2003: On estimates for the vertical nitrate flux due to eddy pumping. *J. Geophys. Res.*, **108 (C11)**, 3359, doi:10.1029/2003JC001 841.

Martin, A. P. and K. J. Richards, 2001: Mechanisms for vertical nutrient transport within a North Atlantic mesoscale eddy. *Deep-Sea Res. II*, **48**, 757–773.

Martin, A. P., K. J. Richards, A. Bracco, and A. Provenzale, 2002: Patchy productivity in the open ocean. *Global Biogeochem. Cycles*, **16 (2)**, 1025, doi:10.1029/2001GB001 449.

Martin, A. P., K. J. Richards, C. S. Law, and M. Liddicoat, 2001: Horizontal dispersion within an anticyclonic mesoscale eddy. *Deep-Sea Research II*, **48**, 739–755.

McGillicuddy, D. J. and L. A. Anderson, 2003: Eddy-driven sources and sinks of nutrients in the upper ocean: Results from a 0.1° resolution model of the North Atlantic. *Glob. Geochem. Cycles*, **17 (2:1035)**, doi:10.1029/2002GB001 987.

McGillicuddy, D. J., R. Johnson, D. A. Siegel, A. F. Michaels, N. R. Bates, and A. H. Knap, 1999: Mesoscale variations of biogeochemical properties in the Sargasso Sea. *J. Geophys. Res.*, **104 (C6)**, 13,381–13,394.

McIntyre, M. E. and W. A. Norton, 2000: Potential vorticity inversion on a hemisphere. *J. Atmos. Sci.*, **57**, 1214–1235.

McKiver, W. J. and Z. Neufeld, 2011: Resonant plankton patchiness induced by large-scale turbulent flow. *Phys. Rev. E*, **83 (016303)**, 1–9.

McWilliams, J. C., 1985: Submesoscale, coherent vortices in the ocean. *Rev. Geophys.*, **23**, 165–182.

Menkes, C. E., S. C. Kennan, P. Flament, Y. Dandonneau, S. Masson, B. Biessy, E. Marchal, G. Eldin, J. Grelet, Y. Montel, A. Morlière, A. Lebourges-Dhaussy, C. Moulin, G. Champalbert, and A. Herbland, 2002: A whirling ecosystem in the equatorial Atlantic. *Geophys. Res. Lett.*, **29 (11)**, 1553, doi:10.1029/2001GL014 576.

Miropol'sky, Y. Z., 2001: *Dynamics of Internal Gravity Waves in the Ocean*. Kluwer Academic Publishers, Dordrecht, 406 pp.

Mitra, A., K. J. Flynn, and M. J. R. Fasham, 2007: Accounting for grazing dynamics in nitrogen-phytoplankton-zooplankton models. *Limnol. Oceanogr.*, **52**, 649–661.

Mizobata, K., S. I. Saitoh, A. Shiomoto, T. Miyamura, N. Shiga, K. Imai, M. Toratani, Y. Kajiwara, and K. Sasaoka, 2002: Bering Sea cyclonic and anticyclonic eddies observed during summer 2000 and 2001. *Prog. Oceanogr.*, **55**, 65–75.

Moisan, J. R. and E. E. Hofmann, 1996: Modeling nutrient and plankton processes in the California coastal transition zone 1. A time- and depth-dependent model. *J. Geophys. Res.*, **101(C10)**, 22 647–22 676, doi:10.1029/96JC01 718.

Molemaker, M. J., J. C. McWilliams, and I. Yavneh, 2005: Baroclinic instability and loss of balance. *J. Phys. Oceanogr.*, **35**, 1505–1517.

Mooers, C. N. K., 1975a: Several effects of a baroclinic current on the cross-stream propagation of inertial-internal waves. *Geophys. Fluid Dyn.*, **6**, 245–275.

———, 1975b: Several effects of baroclinic currents on the three-dimensional propagation of inertial-internal waves. *Geophys. Fluid Dyn.*, **6**, 277–284.

Morán, X. A. G., I. Taupier-Letage, E. Vázquez-Domínguez, S. Ruiz, L. Arin, P. Raimbault, and M. Estrada, 2001: Physical-biological coupling in the Algerian Basin (SW Mediterranean): Influence of mesoscale instabilities on the biomass and production of phytoplankton and bacterioplankton. *Deep-Sea Res. I*, **48**, 405–437.

Munk, W., L. Armi, K. Fischer, and F. Zachariasen, 2000: Spirals on the sea. *Proc. R. Soc. Lond. A.*, **456**, 1217–1280.

Navarro, G., J. Ruiz, I. E. Huertas, C. M. García, F. Criado-Aldeanueva, and F. Echevarría, 2006: Basin-scale structures governing the position of the deep fluorescence maximum in the Gulf of Cádiz. *Deep-Sea Res. II*, **53**, 1261–1281.

Newberger, P. A., J. S. Allen, and Y. H. Spitz, 2003: Analysis and comparison of three ecosystem models. *J. Geophys. Res.*, **108(C3)**, 3061, doi:10.1029/2001JC001 182.

Nieves, V., C. Llebot, A. Turiel, J. Solé, E. García-Ladona, M. Estrada, and D. Blasco, 2007: Common turbulent signature in sea surface temperature and chlorophyll maps. *Geophys. Res. Lett.*, **34**, L23 602, doi:10.1029/2007GL030 823.

Niewiadomska, K., H. Claustre, L. Prieur, and F. d'Ortenzio, 2008: Submesoscale physical-biogeochemical coupling across the Ligurian Current (northwestern Mediterranean) using a bio-optical glider. *Limnol. Oceanogr.*, **53 (5)**, 2210–2225.

Ning, X., F. Chai, H. Xue, Y. Cai, C. Liu, and J. Shi, 2004: Physical-biological oceanographic coupling influencing phytoplankton and primary production in the South China Sea. *J. Geophys. Res.*, **109**, C10 005, doi:10.1029/2004JC002 365.

Niwa, Y. and T. Hibiya, 1999: Response of the deep ocean internal wave field to traveling midlatitude storms as observed in long-term current measurements. *J. Geophys. Res.*, **104 (C5)**, 10 981–10 989.

Ohman, M. D. and H. J. Hirche, 2001: Density-dependent mortality in an oceanic copepod population. *Nature*, **412**, 638–641.

Ohman, M. D., J. A. Runge, E. G. Durbin, D. B. Field, and B. Niehoff, 2002: On birth and death in the sea. *Hydrobiologia*, **480**, 55–68.

Olaizola, M., D. A. Ziemann, P. K. Bienfang, W. A. Walsh, and L. D. Conquest, 1993: Eddy-induced oscillations of the pycnocline affect the floristic composition and depth distribution of phytoplankton in the subtropical pacific. *Marine Biology*, **116 (4)**, 533–542, doi:10.1007/BF00355 471.

Oschlies, A., 2008: Eddies and upper-ocean nutrient supply. *Ocean Modeling in an Eddying Regime, Geophys. Monogr. Ser., 177*, Hecht, M. W. and H. Hasumi, Eds., AGU, 115–130.

Oschlies, A. and V. Garçon, 1998: Eddy-induced enhancement of primary production in a model of the North Atlantic Ocean. *Nature*, **394**, 266–269.

Pallàs-Sanz, E. and A. Viúdez, 2005: Diagnosing mesoscale vertical motion from horizontal velocity and density data. *J. Phys. Oceanogr.*, **35**, 1744–1762.

———, 2007: Three-dimensional ageostrophic motion in mesoscale vortex dipoles. *J. Phys. Oceanogr.*, **37**, 84–105.

Parsons, T. R., R. J. LeBrasseur, and J. D. Fulton, 1967: Some observations on the dependence of zooplankton grazing on the cell size and concentration of phytoplankton blooms. *J. Oceanogr. Soc. Japan*, **23 (1)**, 10–17.

Pasquero, C., 2005: Differential eddy diffusion of biogeochemical tracers. *Geophys. Res. Lett.*, **32**, L17 603, doi:10.1029/2005GL023 662.

Pedlosky, J., 1987: *Geophysical Fluid Dynamics*. Springer-Verlag, 705 pp.

———, 2003: *Waves in the Ocean and Atmosphere*. Springer, Berlin, 260 pp.

Pelegrí, J. L., J. Arístegui, L. Cana, M. González-Dávila, A. Hernández-Guerra, S. Hernández-León, A. Marrero-Díaz, M. F. Montero, P. Sangrà, and M. Santana-Casiano, 2005: Coupling between the open ocean and the coastal upwelling region off northwest Africa: Water recirculation and offshore pumping of organic matter. *J. Mar. Sys.*, **54 (1–4)**, 3–37.

Pelegrí, J. L., A. Marrero-Díaz, and A. W. Ratsimandresy, 2006: Nutrient irrigation of the North Atlantic. *Prog. Oceanogr.*, **70 (2–4)**, 66–406.

Perkins, H., 1976: Observed effect of an eddy on inertial oscillations. *Deep-Sea Res.*, **23**, 1037–1042.

Pitchford, J. and J. Brindley, 1998: Intratrophic predation in simple predator-prey models. *Bull Math. Biol.*, **60**, 937–953.

Polzin, K. and R. Ferrari, 2004: Isopycnal dispersion in NATRE. *J. Phys. Oceanogr.*, **34 (1)**, 247–257.

Provenzale, A., 1999: Transport by coherent barotropic vortices. *Ann. Rev. Fluid Mech.*, **31**, 55–93.

Read, J. F., R. T. Pollard, and U. Bathmann, 2002: Physical and biological patchiness of an upper ocean transect from South Africa to the ice edge near the Greenwich Meridian. *Deep-Sea Res. II*, **49**, 3713–3733.

Richardson, P. L., A. S. Bower, and W. Zenk, 2000: A census of Meddies tracked by floats. *Prog. Oceanogr.*, **45**, 209–250.

Rodríguez-Marroyo, R. and A. Viúdez, 2009: Vortex Rossby waves in mesoscale dipoles. *J. Geophys. Res.*, **114**, C10 009, doi:10.1029/2009JC005 339.

Rubenstein, D. M. and G. O. Roberts, 1986: Scattering of inertial waves by an ocean front. *J. Phys. Oceanogr.*, **16**, 121–131.

Rudnick, D. L. and J. R. Luyten, 1996: Intensive surveys of the Azores Front 1. Tracers and dynamics. *J. Geophys. Res.*, **101 (C1)**, 923–939.

Ruiz, J., F. Echevarría, J. Font, S. Ruiz, E. García, J. M. Blanco, F. Jiménez-Gómez, L. Prieto, A. González-Alaminos, C. M. García, P. Cipollini, H. Snaith, A. Bartual, A. Reul, and V. Rodríguez, 2001: Surface distribution of chlorophyll, particles and gelbstoff in the Atlantic jet of the Alboran Sea: From submesoscale to subinertial scales of variability. *J. Mar. Sys.*, **29**, 277–292.

Sangrà, P., G. Basterretxea, J. L. Pelegrí, and J. Arístegui, 2001: Chlorophyll increase due to internal waves on the shelf break of Gran Canaria (Canary Islands). *Sci. Mar.*, **65 (Suppl. 1)**, 89–97.

Sangrà, P., J. L. Pelegrí, A. Hernández-Guerra, I. Arregui, J. M. Martín, A. Marrero-Díaz, A. Martínez, A. W. Ratsimandresy, and A. Rodríguez-Santana, 2005: Life history of an anticyclonic eddy. *J. Geophys. Res*, **110**, C03 021, doi:10.1029/2004JC002 526.

Serra, N., I. Ambar, and D. Boutov, 2010: Surface expression of mediterranean water dipoles and their contribution to the shelf/slope – open ocean exchange. *Ocean Sci.*, **6**, 191–209.

Shay, L. K., T. M. Cook, and P. E. An, 2003: Submesoscale coastal ocean flows detected by very high frequency radar and autonomous underwater vehicles. *J. Atmos. Oceanic Technol.*, **20**, 1583–1599.

Siegel, D. A., D. B. Court, D. W. Menzies, P. Peterson, S. Maritorena, and N. B. Nelson, 2008: Satellite and in situ observations of the bio-optical signatures of two mesoscale eddies in the Sargasso Sea. *Deep-Sea Res. II*, **55**, 1218–1230.

Siegel, D. A., D. J. McGillicuddy, and E. A. Fields, 1999: Mesoscale eddies, satellite altimetry, and new production in the Sargasso Sea. *J. Geophys. Res.*, **104 (C6)**, 13,359–13,379.

Siegel, D. A., P. Peterson, D. J. McGillicuddy, S. Maritorena, and N. B. Nelson, 2011: Bio-optical footprints created by mesoscale eddies in the Sargasso Sea. *Geophys. Res. Lett.*, **38**, L13 608, doi:10.1029/2011GL047 660.

Smayda, T. J., 1970: The suspension and sinking of phytoplankton in the sea. *Oceanogr. Mar. Biol. Ann. Rev.*, **8**, 353–414.

Smith, E. L., 1936: Photosynthesis in relation to light and carbon dioxide. *Proc. Nat. Acad. Sci. U.S.A.*, **22**, 504–511.

Spitz, Y. H., P. A. Newberger, and J. S. Allen, 2003: Ecosystem response to upwelling off the Oregon coast: Behavior of three nitrogen-based models. *J. Geophys. Res.*, **108(C3)**, 3062, doi:10.1029/2001JC001 181.

Stapleton, N. R., W. T. Aicken, P. R. Dovey, and J. C. Scott, 2002: The use of radar altimeter data in combination with other satellite sensors for routine monitoring of the ocean: Case study of the northern Arabian Sea and Gulf of Oman. *Can. J. Remote Sensing*, **4**, 567–572.

Steele, J. H., 1978: *Spatial Pattern in Plankton Communities*. Plenum Press.

Steffen, E. L. and E. A. D'Asaro, 2004: Meso- and submesoscale structure of a convecting field. *J. Phys. Oceanogr.*, **34**, 44–60.

Strass, V. and J. D. Woods, 1987: Horizontal and seasonal variation of density and chlorophyll profiles between the Azores and Greenland. *Toward a theory on biological-physical interactions in the world ocean*, Rothschild, B. J., Ed., Kluwer Academic Publishers, 113–136.

Sur, H. İ., E. Özsoy, Y. P. Ilyin, and U. Ünlüata, 1996: Coastal/deep ocean interactions in the Black Sea and their ecological/environmental impacts. *J. Mar. Sys.*, **7**, 293–320.

Testor, P. and J. C. Gascard, 2003: Large-scale spreading of deep waters in the Western Mediterranean Sea by submesoscale coherent eddies. *J. Phys. Oceanogr.*, **33 (1)**, 75–87.

Tew-Kai, E. and M. Francis, 2009: Patterns of variability of sea surface chlorophyll in the Mozambique Channel: A quantitative approach. *J. Marine Syst.*, **77 (1-2)**, 77–88.

Thomas, L. N., A. Tandon, and A. Mahadevan, 2008: Sub-mesoscale processes and dynamics. *Ocean Modeling in an Eddying Regime, Geophys. Monogr. Ser., 177*, Hecht, M. W. and H. Hasumi, Eds., AGU, Washington DC, USA, 17–38.

Thompson, P. A., S. Pesant, and A. M. Waite, 2007: Contrasting the vertical differences in the phytoplankton biology of a dipole pair of eddies in the south-eastern Indian Ocean. *Deep-Sea Res. II*, **54**, 1003–1028.

Thorpe, A. J. and C. H. Bishop, 1994: Potential vorticity and the electrostatics analogy: Quasi-geostrophic theory. *Quart. J. Roy. Met. Soc.*, **120**, 713–731.

van Meurs, P., 1998: Interactions between near-inertial mixed layer currents and the mesoscale: The importance of spatial variabilities in the vorticity field. *J. Phys. Oceanogr.*, **28**, 1363–1388.

Viúdez, A., 2001: The relation between Beltrami's material vorticity and Rossby-Ertel's potential vorticity. *J. Atmos. Sci.*, **58 (17)**, 2509–2517.

———, 2008a: The piecewise constant symmetric potential vorticity vortex in geophysical flows. *J. Fluid Mech.*, **614**, 145–172.

———, 2008b: The stationary frontal wave packet spontaneously generated in mesoscale dipoles. *J. Phys. Oceanogr.*, **38**, 243–256.

Viúdez, A. and D. G. Dritschel, 2003: Vertical velocity in mesoscale geophysical flows. *J. Fluid Mech.*, **483**, 199–223.

———, 2004a: Optimal potential vorticity balance of geophysical flows. *J. Fluid Mech.*, **521**, 343–352.

———, 2004b: Potential vorticity and the quasigeostrophic and semigeostrophic mesoscale vertical velocity. *J. Phys. Oceanogr.*, **33**, 865–887.

Voropayev, S. I. and Y. A. D. Afanasyev, 1994: *Vortex Structures in a Stratified Fluid*. Chapman and Hall, 230 pp.

Weller, R. A., 1982: The relation of near-inertial motions observed in the mixed layer during the JASIN (1978) experiment to the local wind stress and to quasi-geostrophic flow field. *J. Phys. Oceanogr.*, **12**, 1122–1136.

Whitney, F., W. Crawford, and P. Harrison, 2005: Physical processes that enhance nutrient transport and primary productivity in the coastal and open ocean of the subarctic NE Pacific. *Deep-Sea Res. II*, **52**, 681–706.

Woods, J. D., 1987: Scale upwelling and primary production. *Toward a theory on biological-physical interactions in the world ocean*, Rothschild, B. J., Ed., Kluwer Academic Publishers, 7–38.

Wroblewski, J. S., 1977: A model of phytoplankton plume formation during variable Oregon upwelling. *J. Mar. Res.*, **35**, 357–394.

Yoder, C., C. McClain, G. Feldman, and W. Esaias, 1993: Annual cycles of phytoplankton chlorophyll concentrations in the global ocean: A satellite view. *Global Biogeochem. Cycles*, **7 (1)**, 181–193.

Yoshimori, A. and M. J. Kishi, 1994: Effects of interaction between two warm-core rings on phytoplankton distribution. *Deep-Sea Res. I*, **41 (7)**, 1039–1052.

Young, W. R. and M. B. Jelloul, 1997: Propagation of near-inertial oscillations through a geostrophic flow. *J. Mar. Res.*, **55**, 735–766.

Agraïments/Agradecimientos/Acknowledgements

Quanta raó tenien aquells que hem deien d'escriure els agraïments abans de patir símptomes crònics de *tesisitis* [1]!!! Quan un acaba amb un PhD (Permanent head Damage) sembla impossible escriure amb certa gràcia les pàgines que seran més llegides de la tesis. La veritat és que me falten paraules per explicar que ha significat per jo. Ella té ses dues cares de sa lluna. Una obscura, de paraules difàcils *remolí* i difícils *vòrtex*. I s'altra blanca, amb paraules de nimfes d' *Hespèrides* per tots els que heu fet realitat aquest somni.

Tot va començar el setembre'06. Vaig entrar al ICM amb la idea de veure el mar i en vaig sortir convençuda que havia modelitzar. El què? No m'havia quedat molt clar... Com? Amb ordenadors... amb ordenadors ?¿? Arj!!! M'havien tornat a vendre la motooo!!! El venedor s'amagava llavors darrera un dibuix de mariner i va acabar sent el director d'aquesta tesis. A l'*Álvaro* li estic infinitament agraïda per tot temps i paciència que m'ha dedicat en transmetre'm el seu coneixement. El que em va convèncer a treballar amb ell va ser la passió amb que viu la ciència. D'ell he aprés rigor, eficiència, capacitat crítica, i també literatura. Admiro la seva lucidesa a l'hora d'afrontar els problemes i la claredat amb que els resol. ¡Gracias por darme la oportunidad de poner un poco de vida a los remolinos! This thesis wouldn't have been either possible without *Yvette*. I really enjoyed the discussions in her blackboard. She was sharp asking me the questions that unveiled the flaws of my homemade hypothesis or let me know what to do. Thanks for your valuable comments and for let me fill your disks at a distance!!! I am also indebted to *Tim Cowles* who introduced me to Yvette and took care with *Susan* that my Oregonian dream was a success.

Aquests cinc anys com a ice-eme han donat per quatre sortides amb el Departament que Organitza més Festes (DOF), tres campanyes (no creuers), algunes activitats de VIPs (Voluntaris Incondicionals d'en Pelegrí), uns quants congresos, molts croissanets del Beltrán, incontables cafès... Representa tot un repte mencionar totes les cares que hi han estat

[1] Malaltia diagnosticada per la Dra. Pastor

presents i segur que me'n deixo més d'una, per tant gràcies, gràcies a tots per cinc anys inoblidables!

Començaré pel departament i particularment per dues persones ben especials. Una d'elles és la *Rocío*. Lluitadora innata, noble, divertida, incombustible, sempre disposada a donar-te un cop de mà (que no un golpe de mano...) ¡Gracias por dejarme conocerte un poco! Aún nos quedan 22km por correr, ¿eh? L'altre és la *Marieta* de l'ull viu, amb qui poques paraules calen. Un aflorament de sensibilitat, delicadesa, i respecte. Gràcies per totes les xerraetes, viatges, i sandwiches que han fluït!

Amb el temps les taules del B6 han canviat de propietari excepte una, la de la *Maria Rosa*, gran observadora i sempre a punt per qualsevol imprevist. Gràcies per donar vidilla al despatx! I resisteix la invasió masculina que s'aproxima! *Suso, Miquel, Miguel, y Pedro* cuidad de MRosa y ¡adelante con las tesis! En el passadís de la Corrent Polar també trobem el *Jordi Salat*, qui en una aparent posició de despistat sempre troba els punts febles dels meus models, el *Jordi Font*, la primera persona en rebre'm, l'*Emili*, un irresponsable molt eficient, i l'*Antonio García-Olivares*, un científic que parla tan ràpid com pensa. *Josep Lluís*! Gràcies per ser tan entranyable, somrient, i haver-me portat al mig del Atlàntic!

De camí cap a un passadís paral·lel tenim el *Kintxo*, un gran cor sota una llarga barba, la *Maribel*, qui sempre m'arranca un somriure, i l'omnipresent *Agustí* amb les seves històries de pirates. L' *Antonio Turiel*, segur que baixaràs el 100% d'error de la chl-a!, el comandant *Emelianov*, qui em va convidar a una caça de meddies, i al *Jerôme Gourrion*, cavil·lant com llançar més simulacions a gaia. Al B36 hi ha les millors terapeutes per la *tesisitis*! La *Paola*, la meva consciència els últims mesos, ¡gracias por transportarme a tu latitud! La *Carmen* amb el seu leitmotif *Disfruta la tesis*, i la *Patricia*, la bondat i dolcesa personificades.

En una altra òrbita tenim a la *Vero*, companya de riures neuròtics, la *María Piles*, aconseguirem patinar algun dia!, la *Caro*, i el *Sébastien*. Gràcies al *Fernando, Justino, i Javier* pel vostre inestimable suport tècnic! En la mateixa planta trobem a l'*Ismael*, a qui no se li escapa detall, al *Marc*, qui plasma l'oceanografia en imatges i dibuixos com ningú, l'*assimilation team*, Quim encara que siguis ute-eme que no decaiguin les calçotades!, i al *Jordi Solé*, en ROMS man.

Fora del DOF però dins l'ICM... gràcies a la *peña del bankito* per salpebrar l'hora del taper. A *Clarekens* por apadrinarme y sacar siempre punta al lado positivo, a *AnaMariKbyo* por ser ella misma, a *Aránzazuuu* por disfrutar de las pequeñas cosas ¡cualquiera se atreve a defender después de ti!, a *Pati* per obrir-me les portes de casa seva, a *Sara* i als ping-y-pongs, *Sr.Castell*, *Guillem*, i *Joan Ignasi*, ¿qué pauer? ¡ping-pong peras cuando me ganéis dos partidas seguidas! A *Martí*, l'home orquestra, i a *Raquel* per la morcilla que espera al congelador, ¡Ánimos que la tesis también tiene final! A *Marta Ribó* pels matins al sol, tuperless i esdeveniments varis, y al *Jaume, Ben*, *Sergio, Cristina, Máximo, Rachelle, Sarah-Jeanne, Bea Thomas...* per les converses dins i fora els passadissos.

I gràcies als que ja no hi sou però hi heu estat. A la *Clara Llebot*, amb qui puc parlar el mateix llenguatge en codi, per tot el que hem compartit. Al *Marco* pel seu *savoir faire*, al *Rob* per les repesques, a la *Vero*, de qui vaig heredar la taula amb vistes, pels savis consells, a la *Jaime* for a decisive Barceloneta tapeo, i a la *Sofi*, la *Maricel* i l'*Enric*. Thanks to the *veggies & Co.* for the *veggie tales* in Corvallis. Finalment, gràcies a la *Natalia*, per aconseguir-me els articles més històrics, a la *Loli, Rosario* i *Raquel*, por hacer brillar el despacho, y al *Aridane* por chivarme todos los intríngulis de *Cómo depositar una tesis*.

En els afers exteriors... gràcies al *pare* pel seu amor incondicional i la paciència infinita. A la *Juani* per tenir la fonda oberta 24h tots els dies de la setmana, però sobretot per ser més mare que tieta. Als *tiets* per aparèixer sempre en moments clau. Al *padrí*, per la seva estimació i recolzament en la distància, a la *Rosa*, per passar-me la llavor que tot ho pregunta, a la *Joana*, pels emails de les 8am, a l'*Eulàlia*, la hippie més divertida de la família, i a l'*Alicia* per posar cortines a Joanetes.

A la *Nurieta*, una amiga molt humanament sensible i a més a més companya de pis. Gràcies per la teva alegria contagiosa, per la teva comprensió i respecte els últims mesos, per apostar per les persones, per poder parlar de tot i res. I a la *Silvia*, font inesgotable d'energia positiva. Gràcies per la teva sinceritat i espontaneïtat, per estar sempre al peu del canó, per tot el que hem rigut i plorat. Com més et conec, més em sorprens.

A la *Mar*, una petita Amélie, per deixar-me endinsar en el seu món interior, a la *Bet* per totes les filosofades i películes fins la matinada ;p. Perquè malgrat la distància cada cop que ens veiem sembla ahir. A l' *Enric* per aguantar els efectes a tercers de la *tesisitis*.

Als del *Casal* per fer créixer arrels i als *Estupendus* pels moments esporàngics, carnavals... *Silvi* gràcies per la teva energia constant! A les *Empanadilles*, per tots els gols marcats i que ens queden per marcar! A la *Rosa Surinach*, per la seva sensibilitat en captar l'estat de les persones, i a una veïna recuperada l'*Elena*, ¡aún me falta el Kodak rosa! A la *MARta*, *Lluís*, *Benji*, i *Cristina*, pels viatges Wa Yeah!

Gràcies a tots per inspirar-me dia rera dia!

This thesis has been funded by the
Spanish *Ministerio de Educación, Cultura,
y Deporte* through a Ph.D. scholarship to
Mariona Claret Cortés, under the program
Formación de Profesorado Universitario
(ref. AP200604635).